THE UNIVERSITY OF QUEENSLAND

AUSTRALIA

New insights into experiments on unconventional superconductors: The influence of symmetry and the superconducting gap of κ-(BEDT-TTF)$_2$Cu[N(CN)$_2$]Br

David Cavanagh

B.Sc. (Hons)

A thesis submitted for the degree of Doctor of Philosophy at

The University of Queensland in 2018

School of Mathematics and Physics

Abstract

The question of the mechanism giving rise to unconventional superconductivity has been the focus for countless experimental and theoretical efforts for the past three decades. In this thesis, I report on our efforts to better understand the superconducting gap structure in one particular organic unconventional superconductor, κ-(BEDT-TTF)$_2$Cu[N(CN)$_2$]Br, and the insights regarding this question that can be gained from the study of previously performed experiments in these materials. Understanding the gap structure in these unconventional superconducting materials is of significant importance, due to the lack of a 'smoking gun' experiment to differentiate between proposed mechanisms. The only method by which the superconductivity can be probed, therefore, is via the properties of the superconducting order parameter, the superconducting gap.

I demonstrate that the low symmetry common to many unconventional superconductors can be used to establish classes of superconducting gaps based on the symmetry properties of the gap function. Superconducting gaps with symmetry required node placement and those with accidental nodes, I find, can be distinguished reliably via the nuclear magnetic relaxation. If the gap has accidental nodes, the relaxation rate $1/T_1$ displays a pronounced peak, similar in origin to the Hebel-Slichter peak in a conventional superconductor. In κ-(BEDT-TTF)$_2$Cu[N(CN)$_2$]Br, this helps us to distinguish between the many proposed gap structures.

This peak in $1/T_1$, similar to the Hebel-Slichter peak in conventional superconductors, arises due to a logarithmic divergence in a clean, non-interacting model, and is controlled in real systems by disorder, electron-electron interactions and bandstructure effects. I have investigated these effects on the numerically calculated peak in a low symmetry toy model and a number of proposed effective models for the bandstructure of κ-(BEDT-TTF)$_2$Cu[N(CN)$_2$]Br. While the influence of electron-electron interactions on the susceptibility, via random phase approximation vertex corrections, is sufficient to suppress the peak even in a model of conventional s-wave superconductivity, I find that even when all of these controlling effects are present, only gaps with symmetry required nodes provide reasonable fits to experimental data.

I further discuss the quasiparticle scattering rate, as can be measured in a superconductor via the microwave conductivity or measurements of the penetration depth. After discussing how the phase space available for momentum relaxing umklapp processes is influenced by the Fermi surface geometry, in a Fermi liquid, and nodal positioning, in a superconductor with a nodal gap, I again consider the proposed gap functions for κ-(BEDT-TTF)$_2$Cu[N(CN)$_2$]Br. The observed cubic temperature dependence of the scattering rate, as opposed to the exponentially activated behaviour seen in cuprate superconductors, is enough to further constrain the form of the superconducting gap, and distinguish between proposed gap functions with symmetry required nodes.

In the organic BEDT-TTF based materials, it has become convention to label the superconducting gaps in terms of axes rotated 45° from the crystal axes. On the basis of these results, I show that the gap function for κ-(BEDT-TTF)$_2$Cu[N(CN)$_2$]Br must be of a '$d_{x^2-y^2}$-wave' form, in this labelling convention, with symmetry required nodes aligned with the crystal axes and on the boundaries of the

first Brillouin zone.

Declaration by author

This thesis is composed of my original work, and contains no material previously published or written by another person except where due reference has been made in the text. I have clearly stated the contribution by others to jointly-authored works that I have included in my thesis.

I have clearly stated the contribution of others to my thesis as a whole, including statistical assistance, survey design, data analysis, significant technical procedures, professional editorial advice, financial support and any other original research work used or reported in my thesis. The content of my thesis is the result of work I have carried out since the commencement of my higher degree by research candidature and does not include a substantial part of work that has been submitted to qualify for the award of any other degree or diploma in any university or other tertiary institution. I have clearly stated which parts of my thesis, if any, have been submitted to qualify for another award.

I acknowledge that an electronic copy of my thesis must be lodged with the University Library and, subject to the policy and procedures of The University of Queensland, the thesis be made available for research and study in accordance with the Copyright Act 1968 unless a period of embargo has been approved by the Dean of the Graduate School.

I acknowledge that copyright of all material contained in my thesis resides with the copyright holder(s) of that material. Where appropriate I have obtained copyright permission from the copyright holder to reproduce material in this thesis and have sought permission from co-authors for any jointly authored works included in the thesis.

Publications included in this thesis

1. [1] **D.C. Cavanagh**, and B.J. Powell, *Nuclear magnetic resonance in low-symmetry superconductors*, *Physical Review B* 97(2): 024509, 2018

Submitted manuscripts included in this thesis

No manuscripts submitted for publication

Other publications during candidature

Peer-reviewed publications

1. [2] **D.C. Cavanagh**, A. C. Jacko and B.J. Powell, *Breakdown of the universality of the Kadowaki-Woods Ratio in multi-band metals*, *Physical Review B* 92(19): 195138, 2015

Contributions by others to the thesis

My primary supervisor, Professor Ben Powell, has contributed to the conception and design of this work, and provided ongoing support and advice during my candidacy and the writing of this thesis.

Statement of parts of the thesis submitted to qualify for the award of another degree

No works submitted towards another degree have been included in this thesis.

Research involving human or animal subjects

No animal or human subjects were involved in this research.

Acknowledgments

This thesis, like any significant work, is the product of one person but the result of a hugely supportive network of people. In the interest of brevity, I will try to limit my thanks to the most important people, without whom I would never have completed this.

My primary supervisor, Ben Powell, has given me a tremendous amount of support, direction and advice, for which I am deeply grateful. Ben has consistently motivated and believed in me, even (especially) when I have found myself frustrated with a lack of progress and full of doubt, and I couldn't have asked for a better supervisor.

I owe a special thanks to my close friends, office mates and proofreaders, Marco Ho and Amie Khosla, who have helped contribute to my procrastination and excessive caffeination, patiently withstood my complaints any time something went wrong over the past four years, and somehow still offered to proofread this thesis.

Thanks as well to my family. You have been unwaveringly supportive of me during my PhD candidature, understanding of how much of my time and concentration has been taken up with this, and infinitely patient with my fumbling attempts at explaining what I've been doing.

Most of all, thank you to my partner Sarah Warren. You have been there for me through every day of stress, insecurity, frustration and exhaustion. This process has been at least as stressful for you as for me and you haven't complained about it once. Without your love and support, I couldn't have done any of this. I owe you more gratitude than I can ever hope to show, but I'll keep trying.

Financial support

This research was supported by an Australian Government Research Training Program Scholarship

Keywords

Unconventional superconductivity, κ-(BEDT-TTF)$_2$Cu[N(CN)$_2$]Br, superconductivity, organic superconductivity, superconducting gap, low-symmetry superconductivity

Australian and New Zealand Standard Research Classifications (ANZSRC)

ANZSRC code: 020404 Electronic and Magnetic Properties of Condensed Matter; Superconductivity 100%

Fields of Research (FoR) Classification

FoR code: 0204, Condensed Matter Physics, 100%

Contents

List of figures

List of tables

List of abbreviations and symbols

Abbreviations	
AF	Antiferromagnet
AFM	Antiferromagnetic metal
BCS	Bardeen, Cooper and Schrieffer
BEDT-TTF	bis(ethylenedithio)tetrathiafulvalene
CO	Charge order
DFT	Density functional theory
dmit	1,3-dithiole-2-dithione-4,5-dithiolate
FL	Fermi liquid
κ-Br	κ-(BEDT-TTF)$_2$Cu[N(CN)$_2$]Br
NFL	non-Fermi liquid
NMR	Nuclear magnetic resonance
RPA	Random phase approximation
STM	Scanning tunnelling microscopy
SC	Superconductor
SDW	Spin density wave
TMTSF	tetramethyltetraselenafulvalen
TMTTF	tetramethyltetrathiafulvalene
YBCO	$YBa_2Cu_3O_{6+x}$

Symbols	
$A_{\boldsymbol{k}}(E)$	Spectral density function
A_H	Hyperfine coupling parameter
α	Isotropic component of a gap with accidental nodes
$c_i^{(\dagger)}$	Annihilation (creation) operator for state i
C_s	Heat capacity in the superconducting state
$\chi_{+-}(\boldsymbol{q},\omega)$	Transverse spin susceptibility
$\chi_0(\boldsymbol{q},\omega)$	Non-interacting transverse spin susceptibility
$\chi_{RPA}(\boldsymbol{q},\omega)$	RPA-dressed transverse spin susceptibility

$\chi_{SC}(\boldsymbol{q}, \omega)$	Non-interacting transverse spin susceptibility in the superconducting state
$\Delta_{\boldsymbol{k}}$	Superconducting gap
Δ_0	Maximum superconducting gap magnitude
$D(E)$, $N(E)$, $\rho(E)$	Quasiparticle density of state
d_{xy}	Anisotropic 'd-wave' gap function, with nodes at $x = 0$ and $y = 0$
$\mathrm{d}_{x^2-y^2}$	Anisotropic 'd-wave' gap function, with nodes at $\lvert x\rvert = \lvert y\rvert$
E_F, μ	Fermi energy, chemical potential
$E_{\boldsymbol{k}}$	Superconducting quasiparticle energy at momentum $\boldsymbol{k}$, $E_{\boldsymbol{k}} = \sqrt{\xi_{\boldsymbol{k}}^2 + \lvert\Delta_{\boldsymbol{k}}\rvert^2}$
η	Lorentzian broadening
$G_{\boldsymbol{k}}^{(0)}(\omega)$	Non-interacting (bare) Green's function at momentum $\boldsymbol{k}$ and frequency ω
$G_{\boldsymbol{k}}(\omega)$	Interacting (dressed) Green's function at momentum $\boldsymbol{k}$ and frequency ω
γ_e	Electron gyromagnetic ratio
H, $\mathcal{H}$	Hamiltonian
$\hbar$	Reduced Planck constant
$i\omega_n$	Matsubara frequency
$\boldsymbol{k}$	Crystal momentum
k_B	Boltzmann constant
λ_L	London penetration depth
$\boldsymbol{p}$	Momentum, $\boldsymbol{p} = \hbar\boldsymbol{k}$
ρ_s	Superfluid density
$\Sigma_{\boldsymbol{k}}(\omega)$	Quasiparticle self-energy at momentum $\boldsymbol{k}$ and frequency ω
t, t_x, t_y, t', $t2'$, δ_t	Tight binding parameters
$1/T_1$	Nuclear magnetic relaxation rate
τ^{-1}	Quasiparticle scattering rate
T_c	Superconducting critical temperature
T_c^-	T_c as approached from below
U	Hubbard interaction strength
U_c	Critical interaction strength in the RPA
$v_\Delta(\boldsymbol{k})$	Gradient of the superconducting gap, at momentum $\boldsymbol{k}$
$v_F(\boldsymbol{k})$	Fermi velocity, at momentum $\boldsymbol{k}$
$\xi_{\boldsymbol{k}}$	Electron dispersion at momentum $\boldsymbol{k}$
Z	Quasiparticle weight
Z_s	Surface impedance

Chapter 1

Introduction

The study of superconductivity is one of the most fascinating and active areas of condensed matter physics research. While conventional, phonon-mediated, superconductivity is well explained by the theory of Bardeen, Cooper and Schrieffer (BCS) [3, 4], there is no consensus on an underlying mechanism giving rise to superconductivity in unconventional superconductors such as the cuprate, organic, heavy fermion and iron pnictide families of materials [5–9]. The difficulty in identifying the mechanism of superconductivity in these materials arises from the fact that there exists no way to directly measure this mechanism. Experiments are limited to probing the order parameter of the resulting superconducting state, with the mechanism only examinable via inference [5, 10].

I will give a brief overview of conventional superconductivity, and the successes of BCS theory, before discussing the various difficulties in deriving a similar microscopic theory for unconventional superconductors. There exist numerous excellent introductory texts to conventional superconductivity and BCS theory [11–13] and it is not the aim of this introduction to attempt to reproduce them. Rather, the aim is to highlight the great successes and insight of BCS theory, before discussing why such successes have not yet been possible with regards to unconventional superconductors. Specifically, I wish to highlight the fact that there exists no 'smoking gun' experiment that identifies the pairing mechanism in unconventional superconductors, which has limited insight into these materials to that which can be inferred from the behaviour of the superconducting order parameter, the superconducting gap. The problem of identifying the mechanism of superconductivity then requires an understanding of how the form of the superconducting gap influences experimental properties, which forms the focus of this thesis.

1.1 Conventional superconductivity

In a conventional superconductor, electrons form Cooper pairs at low temperature due to an attractive, phonon-mediated interaction [14]. This interaction is local in space but retarded in time, resulting in an attractive force despite the direct, repulsive electron-electron interaction [15]. In a BCS superconductor, this interaction pairs time reversed states within some energy range, given by the 'superconducting gap'

Δ, of the Fermi energy (see Fig. 1.1), removing the low energy excitations from the system [11, 12, 16]. One of the successes of BCS theory is the explanation of this gap in the density of states (see Fig. 1.2), seen experimentally, as a result of the attractive Bardeen-Pines interaction, which cannot be probed directly [11, 15].

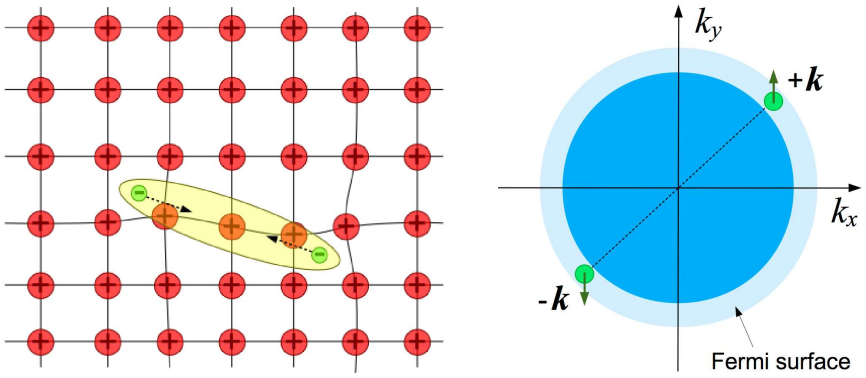

Figure 1.1: Schematic representations of the Bardeen-Pines interaction (left) and the destabilisation of the Fermi surface due to Cooper pairing (right), reproduced from Ref. [17]. The Bardeen-Pines interaction can be understood heuristically as the influence of a lattice distortion on the electrons. As one electron moves through the crystal lattice, it attracts ions, resulting in a slightly enhanced positive charge density, which in turn attracts a second electron. The slow relaxation of the lattice (phonons) relative to the electron velocity results in an interaction that is local in space but retarded in time. The Fermi surface then becomes unstable to the formation of Cooper pairs due to the interaction, which gives rise to the superconducting ground state wherein all electrons at the Fermi surface have undergone pairing.

The formation of Cooper pairs destabilises the Fermi liquid ground state, giving rise to a new phase of matter characterised by a broken 'gauge' symmetry. More accurately, in a superconductor the ground state is a state in which quasiparticles close to the Fermi energy not only undergo pairing, but in which there exists a phase coherence between these pairs [12]. The broken symmetry is then the global U(1) phase symmetry, not the local gauge symmetry [19]. As a result of this global phase invariance, the electromagnetic field couples directly to the phase of the coherent ground state, which exhibits a phase stiffness that gives rise to the Meissner effect, the definitive signature of superconductivity [11, 20].

The Meissner effect is the spontaneous expulsion of magnetic flux from a material on transition to a superconducting state. Unlike dissipationless transport of electricity, which may arise in other systems (for example, due to a vanishing scattering rate) the Meissner effect is a direct consequence of the global gauge invariance of the system, unique to the superconducting state [11, 16]. BCS theory is then capable of explaining the connection between the microscopic Bardeen-Pines interaction and the key experimental signature of superconductivity, the Meissner effect.

While BCS theory was the first comprehensive microscopic theory of the superconducting transition, the relationship between the Meissner effect and the broken global gauge symmetry had already been established by Ginzburg and Landau [21]. Ginzburg and Landau developed an effective theory for superconductivity, which explained the macroscopic phenomena but made no assumptions about the

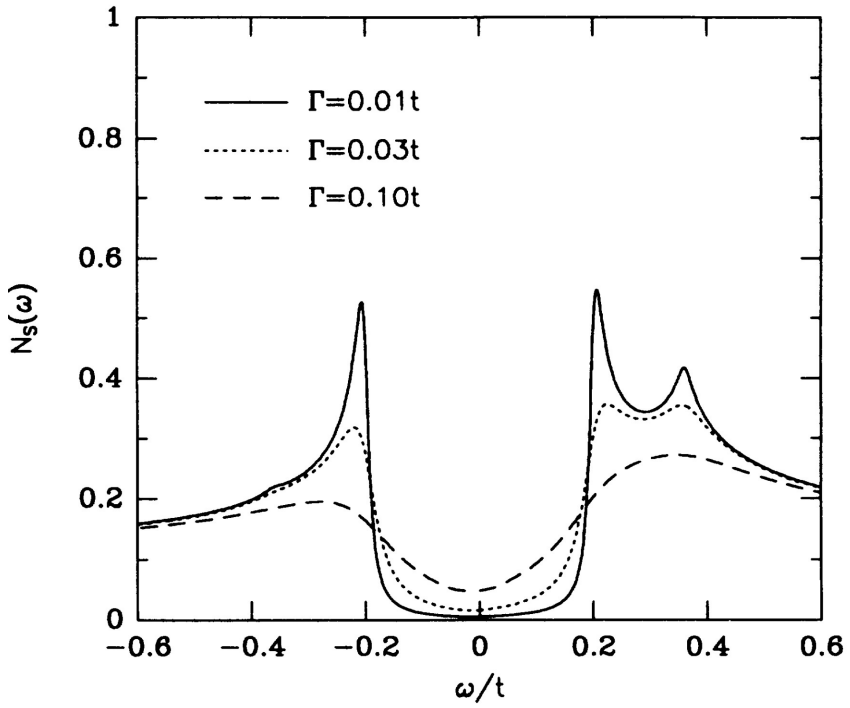

Figure 1.2: The density of states of a conventional 's-wave' superconducting state, calclated for a model bandstructure of the high-temperature cuprate superconductor $YBa_2Cu_3O_7$, reproduced from Ref. [18]. Γ here is a single particle lifetime introduced by scattering from impurities. For small Γ, the density of states shows the effects of BCS superconductivity. The formation of Cooper pairs from the states at the Fermi surface results in the exponential suppression of low energy excitations, with the spectral weight of these states shifted to the pronounced 'coherence peaks' at the energy large enough to break Cooper pairs, the superconducting gap (here $\Delta_0 = 0.2t$, with t the largest tight-binding hopping parameter). The secondary peak at $\omega \sim 0.4t$ is due to bandstructure effects, namely the presence of a significant enhancement of the density of states at this energy in the non-superconducting model bandstructure.

underlying microscopic mechanism. Gor'kov [22] later demonstrated that the parameters used by Ginzburg and Landau in their effective theory could in fact be derived from the BCS theory. This lent further support to the microscopic BCS model, and identified the superconducting gap with the macroscopic order parameter of the phase.

The success of Ginzburg and Landau's theory highlights an important difficulty that BCS overcame in the development of their theory, that the experimental signatures of superconductivity could be explained completely from a macroscopic, effective theory, with no way to directly determine the underlying microscopic mechanism. Understanding the microscopic mechanism required further insight. For BCS theory, this insight came from the isotope effect [23], where it was found that the superconducting transition temperature, T_c, varied with the mass of the ions in the material in the same way as did the Debye frequency, the characteristic energy scale associated with phonons. This led Bardeen and Pines [15] to examine the phonon-mediated electronic interaction ultimately responsible for Cooper pairing in conventional superconductors [3, 4, 14].

1.2 Unconventional superconductors

The link between the microscopic, phonon-mediated, interaction and the macroscopic Meissner effect is now well established in conventional superconductors, but these materials make up only a fraction of all superconductors. In the various families of unconventional superconductors, the cuprate, organic, heavy fermions and iron pnictides, there exists no consensus on the mechanism of superconductivity, though there exists some evidence of similarities between the various families of materials [6, 8, 9, 24–26], as can be seen in Figs. 1.3 and 1.4. Despite the uncertainty regarding the microscopic origins of superconductivity in these materials, and the inability of BCS theory to describe them, they are still well explained, at macroscopic scales, by a generalisation of the Ginzburg-Landau theory.

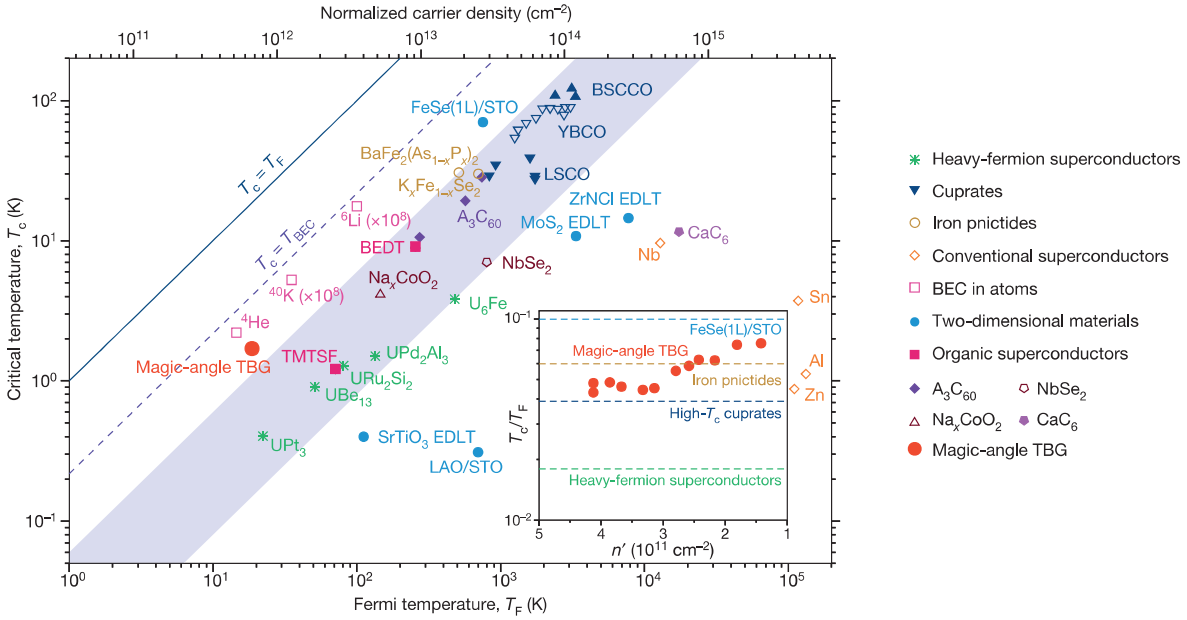

Figure 1.3: Hints of similarities between unconventional superconductors, reproduced from Ref. [26]. An update, and extension, of the 'Uemura plot' [24] displaying a correlation between the critical (T_c) and Fermi (T_F) temperatures of a range of unconventional superconductors, including the cuprate, organic, heavy fermion and iron pnictide superconductors, as well as a number of conventional superconductors and atomic Bose-Einstein condensates and the newly discovered superconducting phase in magic angle twisted bilayer graphene (TBG) [26, 27]. While there is no apparent correlation between the Fermi and critical temperatures for the conventional superconductors (diamonds), the vast majority of the unconventional superconductors share a similar value of the ratio T_c/T_F (the shaded region of the figure). This consistency is suggestive of some similarity in the mechanism of superconductivity in these materials, potentially due to electron-electron (as opposed to electron-phonon) interactions, in the same way that the isotope effect in conventional superconductors is suggestive of the influence of phonons on the superconductivity mechanism.

As is typical of emergent phenomena, there is no way to directly extract the details of the microscopic mechanism from the emergent properties of the superconductor, which can be explained entirely on the basis of effective parameters defined phenomenologically [5, 10, 28]. The problem of understanding the mechanism of superconductivity in these materials is then, from a practical standpoint, a problem of understanding the macroscopic order parameter, the superconducting gap, and attempting to infer information about the mechanism from this. This problem is made more difficult by the lack of a

'smoking gun' experiment that would unambiguously confirm an underlying mechanism, which has lead to a number of theorised possibilities that cannot be distinguished or falsified experimentally [8, 29–31].

In the simple case studied by Bardeen, Cooper and Schrieffer, the attractive interaction is assumed to be isotropic, and dominates between quasiparticle states related by time reversal symmetry [3, 4]. The isotropy of the interaction results in a superconducting gap that is likewise isotropic, $\Delta_{\boldsymbol{k}} = \Delta_0$, with no dependence on momentum $\boldsymbol{k}$. The interaction also results in a singlet superconducting state, wherein pairs carrying zero total momentum are formed by time reversed quasiparticles, with opposite spin and momentum. BCS theory is also a weak-coupling approximation [32], though the more general theory developed by Eliashberg [33, 34] can account for a wider range of interaction strengths, leading to a ground state of the same form as the BCS state.

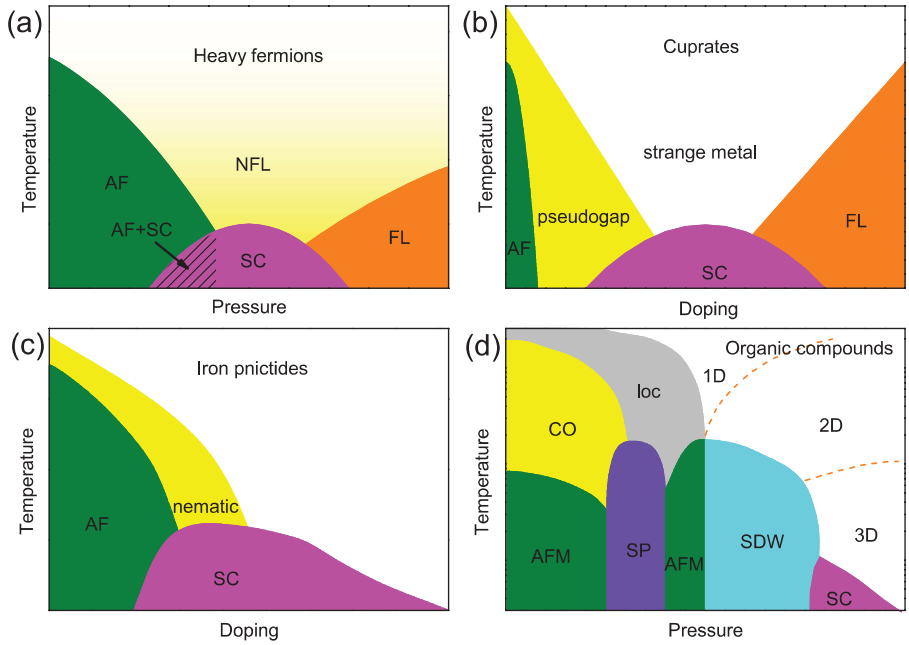

Figure 1.4: Schematic phase diagrams for a number of unconventional superconductors, reproduced from Ref. [35]. Each phase diagram exhibits a number of common features: the existence of a dome-like superconducting transition which extends over multiple normal phases, the presence of both Fermi liquid (FL) and non-Fermi liquid (NFL) normal phases above T_c (including the strange metal, pseudogap, nematic and antiferromagnetic [AF] phases), and a number of other exotic phases related to strong electronic correlations (including AF phases as well as the spin-Peierls [SP], charge-order [CO], antiferromagnetic metal [AFM], localised [loc] and spin density wave [SDW] phases). The focus of this thesis is an organic superconductor belonging to the κ-(BEDT-TTF)$_2X$ family of organic superconductors, while (d) here refers to the superconducting Bechgaard/Fabre salts.

The successes of BCS (and Eliashberg) theory additionally rest heavily on the assumption of a Fermi liquid ground state above the critical temperature T_c, upon which the derivation of the theory depends (see Sec. 1.5 for more details). In many unconventional superconductors, however, the normal (i.e. high temperature) state is not a simple Fermi liquid, and the overall phase diagram is often complicated, with many competing phases (see Fig. 1.4). In some unconventional superconductors, there exists a region of the phase diagram where a Fermi liquid is seen at high temperatures and the superconducting state at low temperatures, but this only accounts for some subsection of the

superconducting transition. For example, in the cuprate family of superconductors, often referred to as high-temperature superconductors, the phase of the material may be controlled via chemical doping. The normal state of these materials may be tuned by increasing the chemical doping, changing it from a Mott insulator (low doping and temperature), through a number of exotic phases (often including pseudogap and strange metal phases), to a Fermi liquid (high levels of doping), all of which may transition to an unconventional superconducting state at low temperatures [8]. Similar complex phase diagrams are present for a number of organic [6, 7], heavy fermion [36–38], and iron-based [31, 39, 40] superconductors. Interestingly, it is rare in these materials to observe a phase transition within the superconducting state, even as an external parameter (e.g., chemical doping, or pressure) is varied, and the corresponding normal state undergoes a transition.

As is the case in the assumption of a Fermi liquid ground state, any and all of the assumptions and restrictions of BCS theory may be invalid in unconventional superconductors. A more complex pairing interaction than the phonon-mediated interaction in BCS theory may lead to a situation where the valid order parameter of the Ginzburg-Landau theory, the superconducting gap, differs from that of the BCS state [9]. The symmetry of the order parameter may then provide some insight into the mechanism of superconductivity on the microscopic scale, which cannot be probed directly [5, 10]. As such, the determination of the exact form of the superconducting gap is of significant importance.

Superconducting states can be classified by their symmetry [5, 9, 10]. Generally, unconventional superconductivity is defined by the breaking of an additional symmetry beyond the global gauge invariance [5, 9, 10], most frequently a reduction of the point group symmetry. Other possibilities include breaking time reversal or, for triplet superconductors, spin rotation symmetries [41].

Starting from the SO(3)×SO(3)×U(1) symmetry of superfluid ^{3}He [41], the discussion of unconventional superconductivity has focused on superconductivity in high symmetry environments. In such an isotropic system, with SO(3) rotational symmetry, the spherical harmonics form a complete basis for the possible gap functions. The gaps, and the corresponding superfluidity, may then be labelled by the orbital angular momentum, as s-, p-, d-wave etc. This nomenclature, while reasonable for the p-wave symmetry of the superfluid state in ^{3}He [41], has also been applied to superconducting states in crystals, where the symmetry is generally significantly reduced from the isotropic rotational symmetry of ^{3}He. As a result, it has become common practice to carry over the s-, p-, d-wave etc. notation from the SO(3) case when labelling superconducting states. In a crystalline material, however, the spherical symmetry is no longer relevant and the point group of the crystal constrains the symmetry distinct solutions of the Schrödinger equation. Thus, formally the possible superconducting gaps should be classified by the irreducible representations of the point group of the crystal. It is common, however, to refer to the cuprates as d-wave superconductors, rather than as having superconductivity described by, say, the B_{1g} representation of D_{4h} [10, 42]. I continue this abuse of notation below, but will attempt to make clear, where possible, the representation of the material point group that the superconducting gap belongs to.

Superconductivity in materials such as the cuprate, organic, heavy fermion and iron-based families of unconventional superconductors, is widely believed to arise from electronic correlations. These

unconventional superconductors share many similar properties, including complex phase diagrams with multiple phases and (spin singlet) superconductivity in particular proximity to some magnetically ordered phase. While the order parameter is believed to be anisotropic in the majority of these materials, disagreement remains over the exact form of the gap function in many materials. In the iron-based superconductors both 'd-wave' (nodal) gap structures and nodeless '$s_{\pm}$-wave' structures, with band-dependent magnitudes, have been proposed for various materials [43, 44], while in some heavy fermion superconductors a band-dependent gap symmetry has been discussed [45, 46] (i.e. with nodes present on some bands and isotropic gap magnitude on others).

One surprisingly common feature of unconventional superconductivity is the observation of such states in many materials with rather low point group symmetries. Non-centrosymmetric materials are a prominent example. Here spin-orbit coupling can mix singlet and triplet superconducting states [47]. Many organic superconductors, e.g., those based on the BEDT-TTF, $Pd(dmit)_2$, TMTSF, or TMTTF molecules, form monoclinic or orthorhombic crystals [48]. This means that superconducting symmetries that are distinct on the square lattice (see Table 1.1) such as s-wave, d_{xy}, or $d_{x^2-y^2}$ often belong to the same irreducible representation [25, 42] (see Table 1.2). Similarly, a number of transition metal oxides with orthorhombic crystal structures superconduct [49–52]. In some cuprates, chemical doping results in a distortion of the lattice, reducing the rotational symmetry to C_2, similar to that of the organic and transition metal oxide superconductors (i.e., orthorhombic as opposed to tetragonal). This distortion is on the order of $< 10\%$ of the lattice spacing [51, 52].

Irreducible representation	Required nodes	Example basis functions	Gap states
A_{1g}	None	$1_{\boldsymbol{k}}$	s
A_{2g}	Line	$X_{\boldsymbol{k}}Y_{\boldsymbol{k}}\left(X_{\boldsymbol{k}}^2 - Y_{\boldsymbol{k}}^2\right)$	'g-wave'
B_{1g}	Line	$X_{\boldsymbol{k}}^2 - Y_{\boldsymbol{k}}^2$	$d_{x^2-y^2}$
B_{2g}	Line	$X_{\boldsymbol{k}}Y_{\boldsymbol{k}}$	d_{xy}
E_g	Line	$(X_{\boldsymbol{k}}Z_{\boldsymbol{k}}, Y_{\boldsymbol{k}}Z_{\boldsymbol{k}})$	'$d_{xz} + id_{yz}$'-wave

Table 1.1: Even parity irreducible representations, and the corresponding basis functions and gap structures, for the D_{4h} (square lattice) point group relevant to the cuprate superconductors [10]. The two 'd-wave' gap functions in this system belong to different irreducible representations of the point group. Additionally, there exists a two-dimensional representation (E_g) with a two component order parameter, which would break time-reversal symmetry [53]. The functions $1_{\boldsymbol{k}}$, $X_{\boldsymbol{k}}$ and $Y_{\boldsymbol{k}}$ are any generic functions that transform as 1, k_x and k_y, respectively, and determine which gap function states belong to each irreducible representation.

Emergent physics can also lower the symmetry of a material, for example, via electronic 'nematicity'. Indeed, in some cuprates, even if the crystal lattice is constrained to reduce this distortion, evidence of electronic nematicity has been observed in transport properties [52], while nematic phases (with reduced rotational symmetry) have been theorised, resulting from spin or charge density wave order [54]. Evidence of such phases and their connection to the pseudogap phase has been observed in some cuprate materials from magnetic torque measurements [55]. Additionally, nematic phases arise in iron-based superconductors [56, 57] (for example, as temperature is lowered, FeSe undergoes a structural transition

Irreducible representation	Required nodes	Example basis functions	Gap states
A_{1g}	None	$1_{\boldsymbol{k}}$, $X_{\boldsymbol{k}}^2$, $Y_{\boldsymbol{k}}^2$, $Z_{\boldsymbol{k}}^2$	s, $d_{x^2-y^2}$
B_{1g}	Line	$X_{\boldsymbol{k}} Z_{\boldsymbol{k}}$	d_{xz}
B_{2g}	Line	$X_{\boldsymbol{k}} Y_{\boldsymbol{k}}$	d_{xy}
B_{3g}	Line	$Y_{\boldsymbol{k}} Z_{\boldsymbol{k}}$	d_{yz}

Table 1.2: Even parity irreducible representations, and the corresponding basis functions and gap structures, for the D_{2h} point group relevant to κ-(BEDT-TTF)$_2$Cu[N(CN)$_2$]Br (κ-Br), reproduced from Ref. [42]. In an isotropic system, each 'd-wave' gap transforms as a different irreducible representation, while here the '$d_{x^2-y^2}$-wave' state belongs to the trivial representation, as does the isotropic 's-wave' gap. The functions $1_{\boldsymbol{k}}$, $X_{\boldsymbol{k}}$, $Y_{\boldsymbol{k}}$ and $Z_{\boldsymbol{k}}$ are any generic functions that transform as 1, k_x, k_y and k_z, respectively, and determine which gap function states belong to each irreducible representation. In the κ-(BEDT-TTF)$_2X$ organics, the convention has arisen to define the x and y directions in the highly conducting $(a-c)$ plane at 45° to the a and c crystal axes. The labelling of the d_{xy} and $d_{x^2-y^2}$ states is then swapped in this convention, where the 'd_{xy}'-wave gap has accidental nodes and is in the trivial A_{1g} representation.

to an orthorhombic state well above the superconducting critical temeprature [58]) and strong anisotropy has been observed in resistivity measurements of the heavy-fermion superconductor $CeRhIn_5$ [59], indicating the presence of some nematic order.

1.2.1 Accidental and symmetry required nodes of the superconduting gap

If a superconducting order parameter is described by a non-trivial representation of the point group, this can imply the presence of nodes. For example, consider a superconductor on a square lattice with D_{4h} symmetry. Let us examine the case where the superconducting gap is a representation of B_{1g}, often called a $d_{x^2-y^2}$ gap (see Table 1.1). This implies, among other things, that the superconducting gap changes sign under rotations by $\pi/2$ out of the plane and reflections through the diagonals of the square. Together these symmetries imply that the superconducting gap must vanish along the diagonals of the Brillouin zone. These zeros are thus symmetry required nodes. They exist for any B_{1g} gap and can only be moved or lifted at a phase transition. In contrast accidental nodes are not enforced by any symmetry of the order parameter. As external parameters, such as temperature, pressure, or field are varied, accidental nodes are free to move around the Fermi surface and even disappear without a phase transition.

There are important differences between accidental nodes and those required by symmetry. In the latter case, as in the discussion of a $d_{x^2-y^2}$ (B_{1g}) gap on a square (D_{4h}) lattice, the location of the nodes is restricted to satisfy a symmetry constraint, because the gap function transforms as a non-trivial representation of the point group. Such a restriction may be enforced, for example, by the symmetry requirement that the gap is odd under a reflection through the plane of the node line. In the case of accidental nodes, the positioning of the nodes is unrestricted by symmetry requirements. In low symmetry superconductors, this allows the possibility of a mixed symmetry 's+d-wave' state [62, 63]. For example, the 'd_{xy}-wave' and '$d_{x^2-y^2}$-wave' gaps both belong to nontrivial representations of

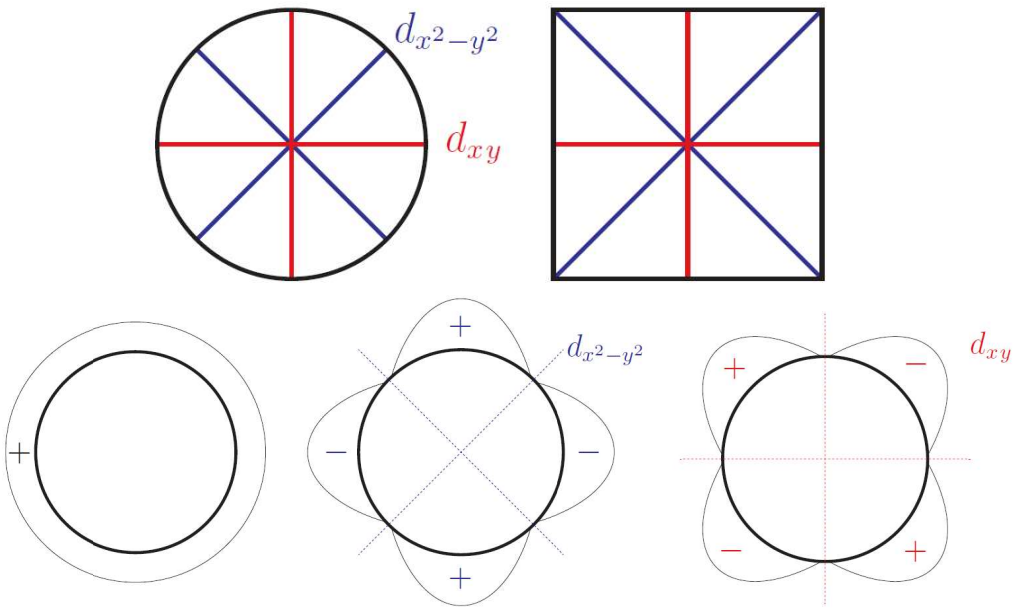

Figure 1.5: Two gaps, both termed 'd-wave', on a square (D_{4h}) lattice (unit cell top right), have nodes lying on axes of high symmetry, making these nodes symmetry required. In the bottom row, the gap function and Fermi surface (at low filling) is shown, and it is clear that in the case of the two d-wave gaps (bottom middle and bottom right), the gap function is odd under reflections about the nodal axes, indicating that the gap transforms as a non-trivial representation of the point group. In the case of the isotropic gap (bottom left), the gap is odd under no transformations, as it belongs to the trivial representation of the point group. As in the case of a spherically symmetric material (top left), the two d-wave gaps are indistinguishable by most experimental probes. This indistinguishablity lead to the use of extremely sensitive tunnelling probes to identify the gap symmetry in the cuprate superconductors, which have close to square crystal lattices [60, 61].

the D_{4h} point group (B_{2g} and B_{1g}, respectively) and will have symmetry required nodes (see Fig. 1.5 for a schematic representation of the gap magnitude on the Fermi surface of such a material). For a rectangular lattice, however, the relevant point group is the D_{2h} group, and the 'd_{xy}-wave' and '$\mathrm{d}_{x^2-y^2}$-wave' gaps belong respectively to the B_{2g} and A_{1g} (trivial) representation of this point group [42], and nodes of the '$\mathrm{d}_{x^2-y^2}$-wave' gap will be accidental (see Fig. 1.6). As many models find $\mathrm{d}_{x^2-y^2}$ superconductivity on the square lattice one expects that, at least for small rectangular distortions, this will also be the dominant superconducting channel for similar models with D_{2h} point group symmetry. However, generically a real material with this symmetry will be able to lower its energy by producing an admixture of isotropic (s-wave) superconductivity, e.g., via sub-dominant interactions. If this admixture is small it will not remove the nodes, but will move them (note that an admixture with a complex phase, which would lift the nodes, additionally breaks time reversal symmetry, and will be measurable by probes sensitive to time reversal symmetry [53]).

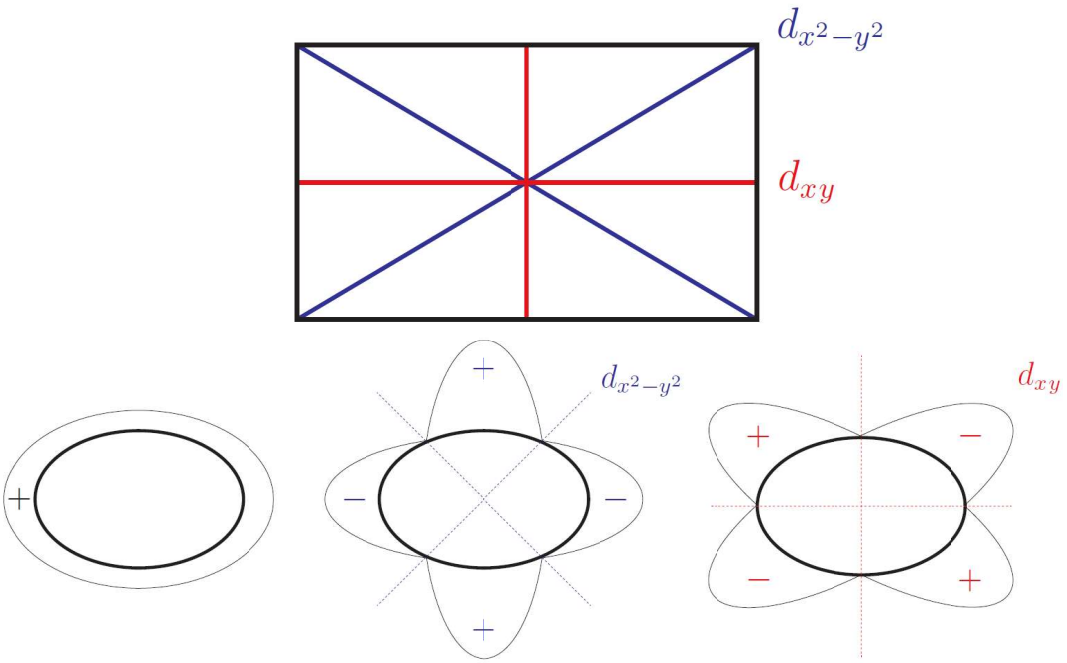

Figure 1.6: Unlike the case of Fig. 1.5, the d_{xy} and $d_{x^2-y^2}$ -wave superconducting gaps in a system with orthorhombic (D_{2h}) symmetry. Only the d_{xy}-wave gap has nodes lying on high symmetry axes in this case. As a consequence, the $d_{x^2-y^2}$-wave gap on the Fermi surface is no longer odd under reflections through the nodal axes (bottom middle) and therefore no longer transforms as a nontrivial representation of the point group, making the nodes formally accidental as they are not constrained by symmetry. Since both the isotropic (bottom left) and $d_{x^2-y^2}$-wave gaps belong to the trivial representation of the point group, the mixing of these two gap functions is allowed by symmetry, which would result in a repositioning of the gap nodes on the Fermi surface.

1.3 Experimental probes of the superconducting gap

Understanding the exact form of the superconducting gap is of considerable importance, however, it is often far from straightforward in practice. The Josephson interference experiments responsible for unambiguously identifying the '$d_{x^2-y^2}$-wave' symmetry of the cuprates [60, 61] have not been possible in many materials. The interpretation of other experimental results can be ambiguous.

It is possible to classify superconductivity as either singlet (as in the BCS case) or triplet on the basis of measurements of the Knight shift. For a singlet superconductor, Cooper pairs have zero total spin and the Knight shift, the amount by which a signal in a nuclear magnetic resonance experiment is shifted by the electronic environment, tends to zero at zero temperature. In a triplet superconductor, however, Cooper pairs are in the triplet state, and the gap is a more complex (vector) function. The Knight shift then tends to a finite value at zero temperature, as the spin susceptibility (which shifts the NMR signal) becomes a tensor, rather than scalar, property [5].

The limiting low temperature behaviours of many experimental probes (e.g., heat capacity, thermal conductivity, nuclear magnetic relaxation rate, or the superfluid density, via the penetration depth) can, in principle, determine the form of the gap, distinguishing between a fully gapped state, line nodes (where the gap vanishes along some line on the Fermi surface), and point nodes (where the gap vanishes at a single point on the Fermi surface). As shown in Fig. 1.7, a fully gapped superconductor

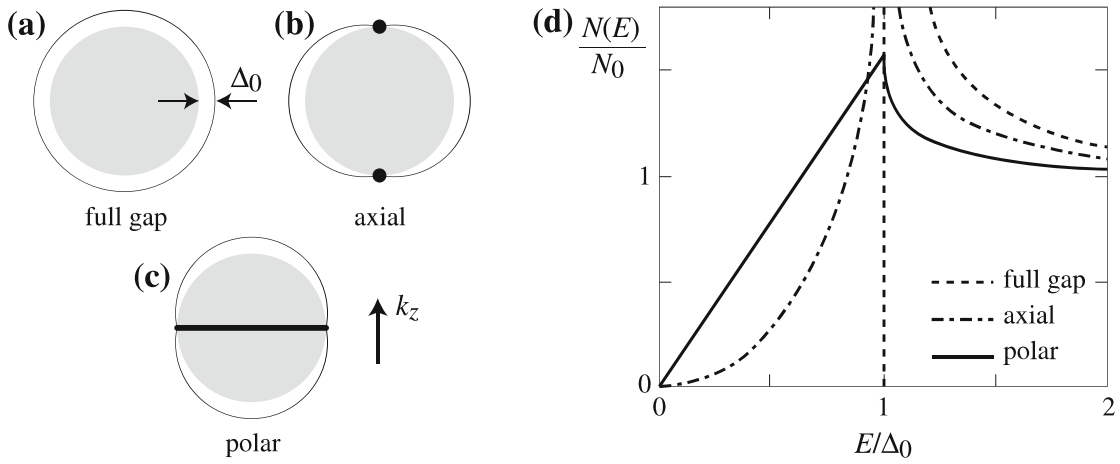

Figure 1.7: The gap function on a spherical Fermi surface for an isotropic, s-wave gap (a), a gap with point (axial) nodes (b) and line (polar) nodes (c), and the low energy density of states for each case (d), normalised to the Fermi liquid value, reproduced from Ref. [64]. For the fully gapped superconductor, the low energy excitations are exponentially suppressed, while the line nodes have a linear density of states at low energy, and the point nodes have a quadratic low energy form. In experimental probes, such as the heat capacity, the temperature dependence at low temperatures will reflect the low energy form of the density of states.

has no low energy ($E < \Delta_0$) states available in the system, as all quasiparticles near the Fermi surface have taken part in pairing. As a result, any property that depends on the density of states at low energies then displays the exponential suppression of these states, with an exponential temperature dependence reflecting the energy required to excite quasiparticles. Conversely, if there are nodes in the gap function then no activated (exponential) behaviour is necessary. The form of the low energy density of states depends on the nature of the nodes (point or line) and the particular temperature dependence of these experimental probes, for example, the heat capacity (see Fig. 1.8) of superfluid density (see Fig. 1.9) at low temperatures, can be used to extract the nature of the nodes in the gap function [5, 65].

The results of low temperature probes, however, are often controversial [25, 65, 67], and can be technically difficult to perform for materials with low critical temperatures. Additionally, such experiments cannot, even in principle, differentiate between different gap symmetries with the same class of nodes (point or line), as they probe only the effect of the node on the density of states. This has led to the study of directional probes, such as thermal conductivity [68, 69].

Techniques such as scanning tunneling microscopy (STM) have also been used to probe the density of states more directly. In an STM experiment, an electrode measures the tunneling of electrons from the surface of a material, by recording the differential conductance of the surface as the applied voltage is varied [71]. As the differential conductance due to the quasiparticle tunneling is directly related to the surface density of states, this allows the probe to determine the form of the density of states. Such an experiment is, however, extremely sensitive to surface effects, due to the presence of impurities or inconsistencies in the cleaving of the crystal surface (see Fig. 1.10). The results of such scanning tunneling spectroscopy experiments, especitally on unconventional superconductors, have therefore often been subject to interpretation [71].

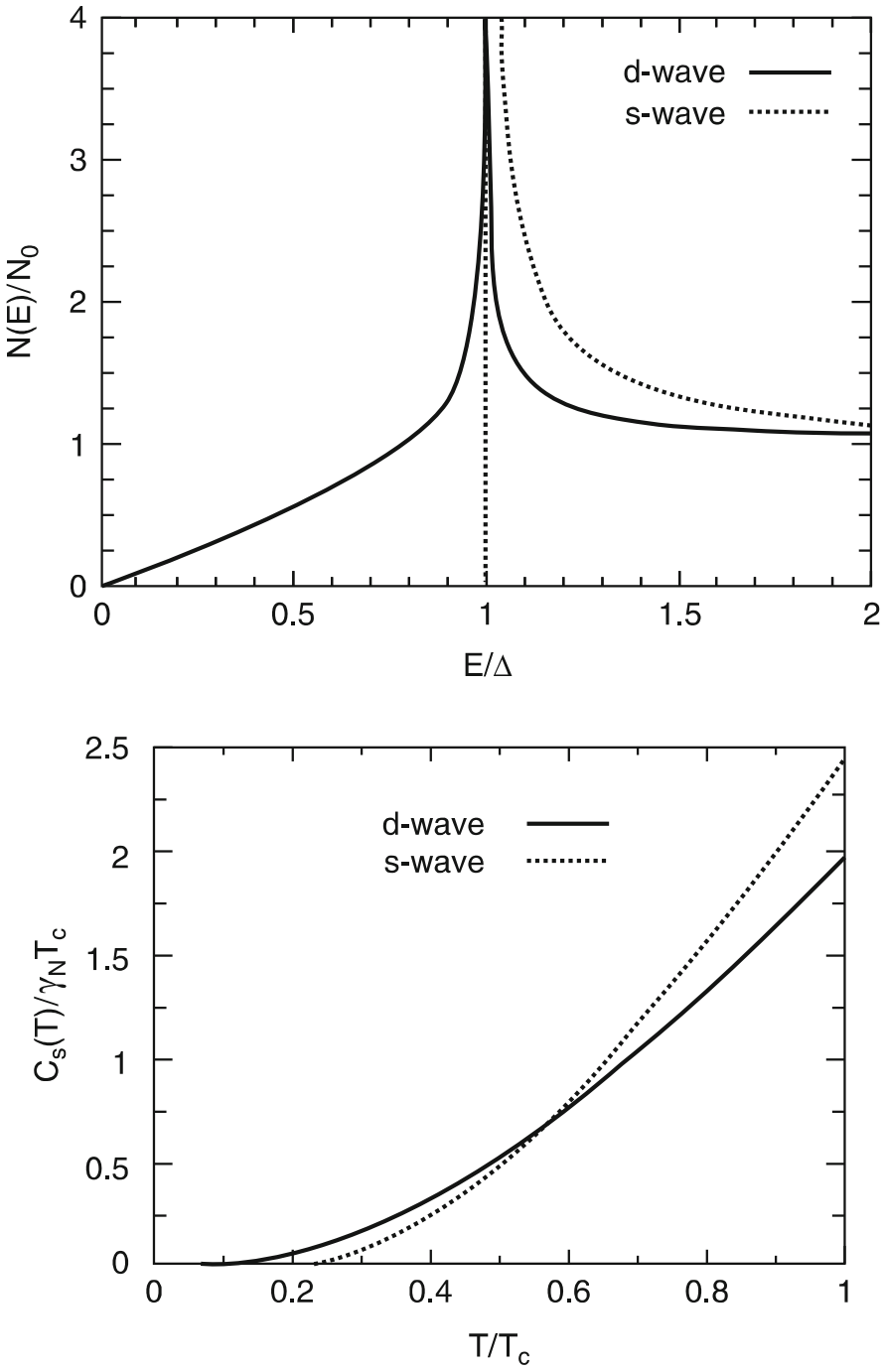

Figure 1.8: The density of states (top) influences the temperature dependence of the heat capacity at low temperatures (bottom, normalised by the value at T_c), reproduced from Ref. [66]. At low temperatures, the heat capacity for the model with an isotropic gap (dashed) increases exponentially with temperature, due to the exponential supression of low energy excitations. The nodal 'd-wave' gap, on the other hand, results in a low temperature heat capacity that varies as a power law (approximately quadratically). In this case, the nodes of the 'd-wave' gap are line nodes. If the nodes were instead point nodes, the low temperature heat capacity would be expected to obey a higher power law (cubic rather than quadratic [9]).

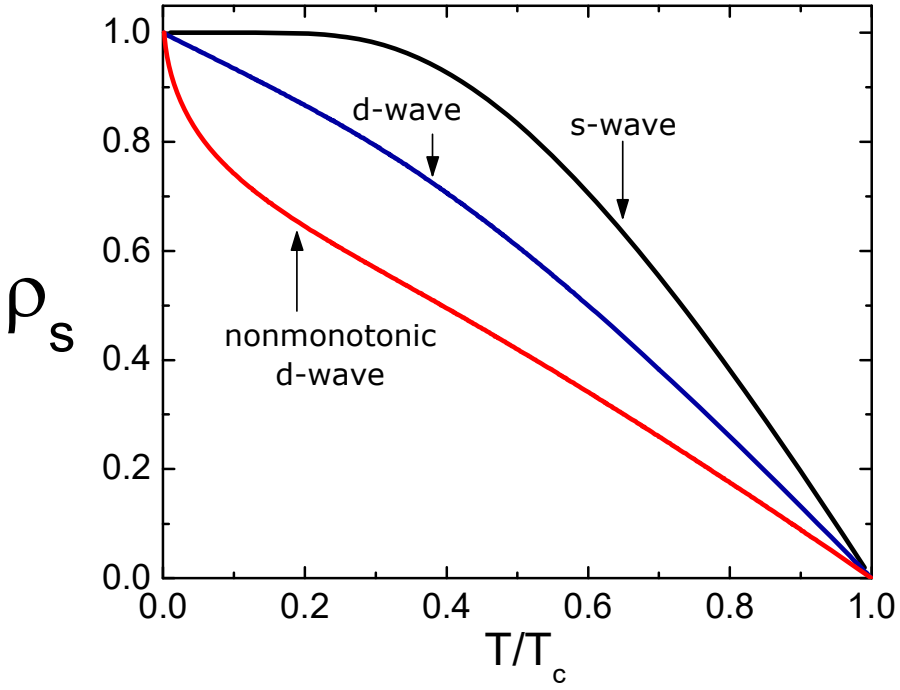

Figure 1.9: The superfluid density, measurable via the London penetration depth ($\rho_s = 1/\lambda_L^2$), is also strongly influenced by the superconducting density of states, reproduced from Ref. [70]. The superfluid density is reduced from the zero temperature value due to the existence of low energy excitations, which remove states from the superfluid. For a conventional 's-wave' superconductor, the exponential suppression of low energy excitations is clearly visible here, as the exponential temperature dependence of the reduction of the superfluid density, while for the two 'd-wave' cases, the existence of low energy quasiparticles results in a superfluid density that rapidly decreases as temperature is raised. In the simple 'd-wave' case, the linearity of the low energy density of states is expressed by the linear temperature dependence of the deviation form the zero temperature value of the superfluid density. The low energy density of states for the 'nonmonotonic d-wave' superconductor varies more strongly with energy, resulting in the more rapid reduction of the superfluid density. The influence of the detailed gap structure on measurements of the superfluid density will be revisited in more detail in Chapter 5.

1.4 Unconventional superconductivity in κ-Br

The focus of this thesis is an organic superconductor, κ-(BEDT-TTF)$_2$Cu[N(CN)$_2$]Br (κ-Br), in which the identification of the gap function has been particularly contentious. The exact form of the superconducting gap in this material has been a matter of considerable disagreement for several decades [42, 62, 63, 74–82]. This material has the highest critical temperature (at ambient pressure) of the BEDT-TTF based superconductors [65] (see Fig. 1.11), and as such has been the focus of a wide variety of experimental probes to determine the properties of superconductivity in this family of materials.

While Knight shift measurements on κ-Br consistently indicate singlet pairing [84, 85], due to the vanishing of the Knight shift at zero temperature, interpretations of the results of other experiments have been inconsistent. There has been evidence from the temperature dependence of low temperature

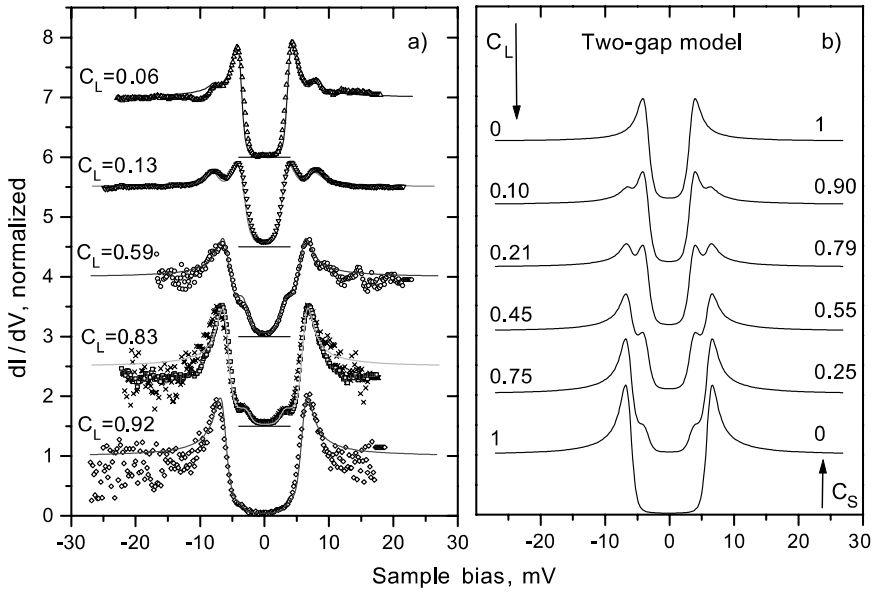

Figure 1.10: Scanning tunnelling spectroscopy of MgB_2, with fits to a two-gap model, reproduced from Ref. [72]. The spectra obtained show considerable variation across the surface (left), with different values of the relative strength of the two gaps (C_L/C_S) required to fit the data at different locations. This highlights the sensitivity of scanning tunnelling spectroscopy to surface effects, as well as its usefulness as a potential direct probe of the density of states. In this material, low temperature probes are sensitive only to the exponential suppression of low energy excitations, and the double gap structure is not evident [73]. A similar multi-peak structure seen in the spectrum of κ-(BEDT-TTF)$_2$Cu[N(CN)$_2$]Br has been considered evidence of a proposed complicated gap function [63].

specific heat measurements taken to indicate nodeless ('s-wave') superconductivity [79, 80, 86] while other experiments indicate the presence of nodes of the gap function [87–89]. Similarly, penetration depth measurements were inconclusive [90–92] until recently, with more precise measurements showing a power law temperature dependence suggestive of a nodal superconducting state [82]. Recent measurements of the low temperature thermal conductivity have been taken as an indication of a fully gapped superconducting state [81], while the nuclear magnetic relaxation, which will be discussed in more detail in Chapter 2, has consistently indicated nodal superconductivity [84, 85]. The density of states from the surface tunneling spectroscopy has been found to show some indication of multiple coherence peaks, which has been linked to a complicated mixed order parameter [63], though similar signals have been observed in other multi-band materials with a superconducting gap magnitude that varies between bands [72]. This ongoing disagreement has led both theorists [42, 62, 74, 77, 93] and experimentalists [63, 94] to discuss the possibility of a variety of superconducting gaps, including those with both symmetry required and accidental nodes in organic superconductors.

For the most part, early measurements of many properties have indicated nodeless superconductivity while later experiments with higher resolution have generally indicated nodal superconductivity. One notable exception to this pattern is a recent measurement of the thermal conductivity, which was found to vanish at zero temperature, consistent with the suppression of low energy quasiparticles in a nodeless superconductor [81]. In this work, I will consider a variety of gaps, including those without nodes,

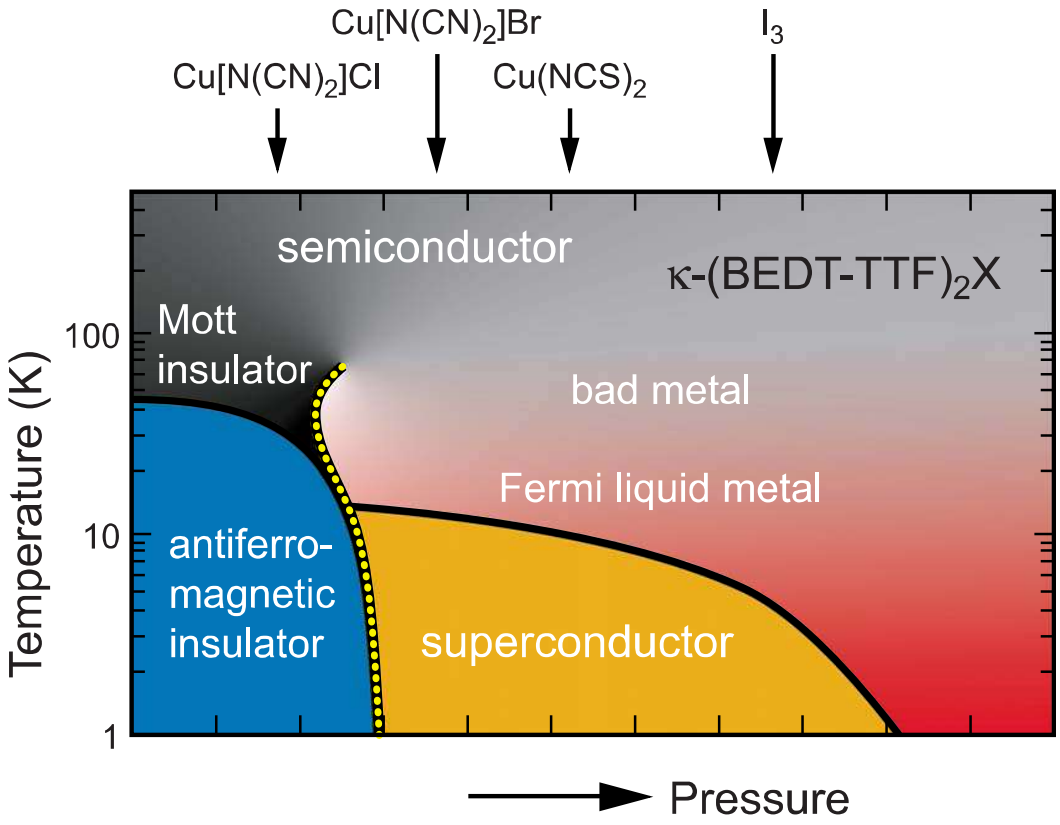

Figure 1.11: Schematic phase diagram for the κ-(BEDT-TTF)$_2X$ family of superconductors, reproduced from Ref. [83]. In these systems, pressure controls the transitions between a number of exotic states that arise from strong electronic correlations, as does the choice of the anion X, much as chemical doping does in the cuprates. Like many unconventional superconductors, these materials form a layered structure, with alternating layers of the anion X and layers made up of BEDT-TTF dimers, and conduction primarily in the BEDT-TTF layers. At ambient pressure, κ-(BEDT-TTF)$_2$Cu[N(CN)$_2$]Br has the highest critical temperature, with a Fermi liquid state immediately above T_c that crosses over into a bad metal as temperature is increased.

and those with symmetry required or accidental nodes, and the predictions of experimental properties arising from them.

Among the proposed superconducting gaps for κ-Br, there has arisen a common convention, when referring to superconducting gaps, to label the 'd-wave' states in a way consistent with the unit cell of the simpler β-(BEDT-TTF)-based materials. In this convention, the momentum axes are taken to be rotated 45° from the crystal axes of the material [42, 62, 77]. The relevant point group for κ-Br is the D_{2h} group, in which case the '$d_{x^2-y^2}$-wave' state (in this labelling convention) has symmetry required nodes and transforms as the B_{2g} representation of the group (see Table 1.2 for contrast), while the 'd_{xy}-wave state transforms as the trivial A_{1g} representation [42]. I discuss this convention further in Chapters 3 and 4.

One of the key goals of this thesis is to understand how the various proposed gaps for κ-Br influence experimental probes of the superconducting state. I will also demonstrate how this understanding of the influence of the gap symmetry on these properties may be of use in studying the superconductivity observed in other materials in which the form of the superconducting gap is unknown. The focus is on two properties in particular: the $1/T_1$ nuclear magnetic relaxation rate (in Chapters 2, 3 and 4),

and the quasiparticle scattering rate τ^{-1} (in Chapter 5), which may be determined from penetration depth experiments. Both of these properties have a long history as probes of superconductivity, but, as I shall demonstrate, have potential as more detailed probes of the gap structure than previously considered. To help in later understanding how the gap affects these properties, I now introduce some general background theory that will be relevant in the following chapters.

1.5 The Nambu quantum many-body formalism for superconductivity

In the following chapters, I will treat the superconductivity in κ-Br on the basis of a generalisation of the BCS theory that includes an anisotropic gap [9, 20]. I make no assumptions regarding the pairing mechanism, aside from that it gives rise to a potentially anisotropic gap, presumably due to some microscopic interaction arising from the strong electronic correlations. While the details of the mechanism of the superconducting transition are not fully understood, close to the transition the normal state of κ-Br is in fact a Fermi liquid (see Fig. 1.11) [7, 25, 65]. As such, I make use of Nambu's formalism [19] for the superconducting transition, where a Fermi liquid evolves into a superconductor due to the influence of the superconducting order parameter, $\Delta_{\boldsymbol{k}}$, which I take to be momentum dependent.

One of the great insights of Eliashberg [33, 34] and Nambu [16, 19] was in devising a method of expressing the quantum field theoretic properties of the normal (Fermi liquid) state in such a way that the diagrams contributing to the normal state may be extended to account for interactions in the superconducting state and, for a conventional superconductor, the transition itself. This then establishes a connection between the superconducting and normal states, allowing the treatment of the transition diagrammatically. In a general quantum many body problem, the renormalisation of the single-particle properties is taken into account via Dyson's equation (shown diagrammatically in Fig. 1.12),

$$G_{\boldsymbol{k}}(\omega) = G^{(0)}_{\boldsymbol{k}}(\omega) + G^{(0)}_{\boldsymbol{k}}(\omega)\,\Sigma_{\boldsymbol{k}}(\omega)\,G_{\boldsymbol{k}}(\omega), \tag{1.1}$$

where $G^{(0)}_{\boldsymbol{k}}(\omega)$ is the unrenormalised (bare) propagator, or Green's function, at momentum $\boldsymbol{k}$ and frequency ω, $G_{\boldsymbol{k}}(\omega)$ is the renormalised (dressed) propagator and $\Sigma_{\boldsymbol{k}}(\omega)$ is the self-energy, which takes into account all one particle irreducible interactions. Dyson's equation is shown diagrammatically in Fig. 1.12, and some diagrams contributing to the self-energy (in a Fermi liquid) are shown in Fig. 1.13.

A significant aspect of the superconducting state is that the fundamental single particle excitations are no longer purely electronic, but consist of broken Cooper pairs, with some character of the two time reversed particles (electron and hole) that make up the Cooper pair. Nambu showed that excitations of the superconducting state may be considered as two-dimensional spinors in a (Nambu) spinor space, where one element of the spinor corresponds to the electron-like component of the quasiparticle and the other element corresponds to the hole-like component [19].

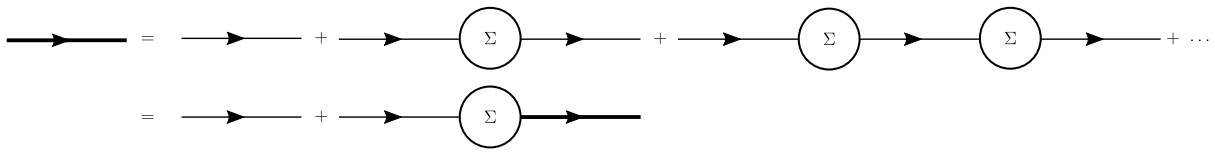

Figure 1.12: Diagrammatic form of Dyson's equation. Here the bold lines denote the dressed Green's function, which is renormalised from the bare Green's function due to repeated interactions described by the self energy.

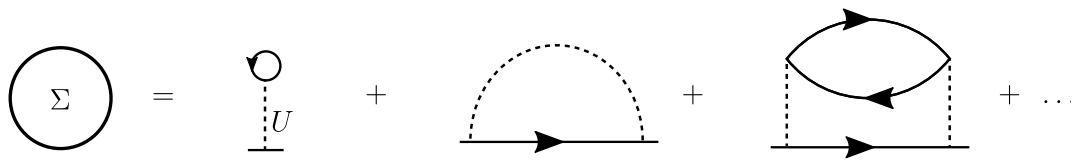

Figure 1.13: Diagrams contributing to the self-energy. Here, a solid line with an arrow indicates the propagator (or Green's funuctions), while a dashed line denotes an interaction (in this case a Hubbard-like point contact interaction of strength U). The diagrams contributing to the self-energy are one particle irreducible, and cannot be divided into self-energy like diagrams by cutting a single propagator line.

The Hamiltonian of a Fermi liquid state may be expressed as a diagonal matrix in the Nambu spinor space,

$$H = \sum_{\boldsymbol{k},\sigma} \begin{pmatrix} c^\dagger_{\boldsymbol{k},\sigma} & c_{-\boldsymbol{k},-\sigma} \end{pmatrix} \begin{bmatrix} \xi_{\boldsymbol{k}} & 0 \\ 0 & -\xi_{\boldsymbol{k}} \end{bmatrix} \begin{pmatrix} c_{\boldsymbol{k},\sigma} \\ c^\dagger_{-\boldsymbol{k},-\sigma} \end{pmatrix}, \tag{1.2}$$

where $\xi_{\boldsymbol{k}}$ is the electronic dispersion, measured from the Fermi energy(i.e. $\xi_{\boldsymbol{k}} = \varepsilon_{\boldsymbol{k}} - \mu$) and $c^{(\dagger)}_{\boldsymbol{k},\sigma}$ destroys (creates) an electron state with momentum $\boldsymbol{k}$ and spin σ. The creation (destruction) of an electron state can also be interpreted as the destruction (creation) of a hole state, a distinction that becomes relevant in the superconducting phase, where excitations are given by linear combinations of electron and hole states. On transition to a superconducting state, the Hamiltonian is altered by the introduction of off-diagonal terms responsible for hybridising the electron and hole components, resulting in the composite quasiparticles of the superconductor (sometimes referred to as 'bogoliubons'). The effective Hamiltonian can be expressed [16, 19] via

$$H = \sum_{\boldsymbol{k},\sigma} \begin{pmatrix} c^\dagger_{\boldsymbol{k},\sigma} & c_{-\boldsymbol{k},-\sigma} \end{pmatrix} \begin{bmatrix} \xi_{\boldsymbol{k}} & \Delta_{\boldsymbol{k}} \\ \Delta^\star_{\boldsymbol{k}} & -\xi_{\boldsymbol{k}} \end{bmatrix} \begin{pmatrix} c_{\boldsymbol{k},\sigma} \\ c^\dagger_{-\boldsymbol{k},-\sigma} \end{pmatrix} = \sum_{\boldsymbol{k},\sigma} \begin{pmatrix} c^\dagger_{\boldsymbol{k},\sigma} & c_{-\boldsymbol{k},-\sigma} \end{pmatrix} \mathcal{H}_{\boldsymbol{k}} \begin{pmatrix} c_{\boldsymbol{k},\sigma} \\ c^\dagger_{-\boldsymbol{k},-\sigma} \end{pmatrix}, \tag{1.3}$$

where $\Delta_{\boldsymbol{k}}$ is the (momentum-dependent) superconducting gap, which I have assumed to be independent of spin. The eigenstates of Eq. (1.3) then give the elementary excitations of the system, which, due to

the inclusion of the superconducting gap $\Delta_{\boldsymbol{k}}$, are given by linear combinations of electron ($c^{\dagger}_{\boldsymbol{k},\sigma}$) and hole ($c_{-\boldsymbol{k},-\sigma}$) excitations.

The Green's functions of the superconductor are defined, in the Nambu space, by [16, 19, 33, 34]

$$G_{\boldsymbol{k}}\left(i\omega_n\right) = \frac{1}{i\omega_n \mathbb{I} - \mathcal{H}_{\boldsymbol{k}}}, \tag{1.4}$$

where $i\omega_n = (2n+1)\,\pi k_B T$ is a Matsubara (thermal) frequency, given by the location of poles of the distribution function [95] and $\mathbb{I}$ is the identity matrix in the Nambu space. This expression defines a matrix of functions termed the Nambu-Gor'kov Green's function,

$$G_{\boldsymbol{k}}\left(i\omega_n\right) = \frac{1}{\left(i\omega_n - E_{\boldsymbol{k}}\right)\left(i\omega_n + E_{\boldsymbol{k}}\right)} \begin{bmatrix} i\omega_n - \xi_{\boldsymbol{k}} & \Delta^{\star}_{\boldsymbol{k}} \\ \Delta_{\boldsymbol{k}} & i\omega_n + \xi_{\boldsymbol{k}} \end{bmatrix}, \tag{1.5}$$

where the prefactor comes from the determinant of $\mathcal{H}\left(\boldsymbol{k}\right)$, and $E_{\boldsymbol{k}} = \sqrt{\xi^2_{\boldsymbol{k}} + \left|\Delta_{\boldsymbol{k}}\right|^2}$ is the quasiparticle (bogoliubon) energy. The diagonal terms in the Nambu-Gor'kov Green's function matrix correspond to the Green's functions of electron and hole states, while the off-diagonal terms correspond to the 'anomalous' (pairing) Green's functions. In the limit $\Delta_{\boldsymbol{k}} = 0$, the anomalous Green's functions vanish and the electron and hole Green's functions become completely independent, and the system is in a Fermi liquid state.

The superconducting gap arises, at low temperatures, as a consequence of interactions and therefore must be taken into account by the self-energy. More complex interactions are neglected in conventional phonon-mediated superconductivity, justified by Migdal's theorem [96]. Migdal's theorem demonstrates that higher-order interactions (vertex corrections) as irrelevant by noting that the interaction scales with the ratio of the electron and ion masses (typically on the order of 10^{-3} or smaller). However, for other, non-phonon mediated, pairing mechanisms, there is no general reason to neglect vertex corrections.

Dyson's equation for the superconducting state is given by a matrix equation of the form of Eq. (1.1), with the self-energy a 2×2 matrix in the Nambu spinor space. The self-energy can then be expanded in terms of the identity matrix and the Pauli matrices,

$$\begin{aligned} \sigma_1 &= \begin{bmatrix} 0 & 1 \\ 1 & 0 \end{bmatrix} \\ \sigma_2 &= \begin{bmatrix} 0 & -i \\ i & 0 \end{bmatrix} \\ \sigma_3 &= \begin{bmatrix} 1 & 0 \\ 0 & -1 \end{bmatrix}, \end{aligned} \tag{1.6}$$

which form a basis for a 2×2 matrix space. The self-energy is then

$$\Sigma_{\boldsymbol{k}}\left(i\omega_n\right) = \mathbb{I}\,\Sigma^{(\mathbb{I})}_{\boldsymbol{k}}\left(i\omega_n\right) + \sigma_1\Sigma^{(1)}_{\boldsymbol{k}}\left(i\omega_n\right) + \sigma_2\Sigma^{(2)}_{\boldsymbol{k}}\left(i\omega_n\right) + \sigma_3\Sigma^{(3)}_{\boldsymbol{k}}\left(i\omega_n\right), \tag{1.7}$$

where the diagonal elements are responsible for renormalisation of the energy spectrum ($\Sigma^{(\mathbb{I})}$) and shifting the electron and hole energies ($\Sigma^{(3)}$), while the off-diagonal elements ($\Sigma^{(1)}$ and $\Sigma^{(2)}$) result in the (complex) pairing function $\Delta_{\boldsymbol{k}}$.

In a conventional superconductor, the Eliashberg theory proceeds by evaluating the self-energy elements self-consistently, using an electronic interaction screened by the phonon propagator [32–34,97], yielding an expression for the gap function and quasiparticle lifetime, and can be used to predict the critical temperature for the system. This approach relies heavily on both the assumption that the normal state of the system is a Fermi liquid, and the use of Migdal's theorem to neglect electron-phonon vertex corrections. In unconventional superconductors, there is generally no reason for either of these assumptions to hold, one of the many difficulties present in attempts to understand the mechanism of superconductivity in these materials.

1.5.1 The susceptibility in a superconductor and coherence functions

The properties I will investigate in this report, the $1/T_1$ relaxation rate and the quasiparticle scattering rate τ^{-1}, are both many-particle properties, as opposed to single-particle properties such as the heat capacity. As such, it is necessary to understand how the coherence of the ground state enters into these properties. Both $1/T_1$ and τ^{-1} depend on correlation functions (susceptibilities). In particular, the nuclear magnetic relaxation rate is defined in terms of the low frequency limit of the transverse spin susceptibility [98,99], $\chi_{+-}(\boldsymbol{q},\omega) = \chi'_{+-}(\boldsymbol{q},\omega) + i\chi''_{+-}(\boldsymbol{q},\omega)$,

$$\frac{1}{T_1 T} \propto \lim_{\omega\to 0}\sum_{\boldsymbol{q}} \frac{\chi''_{+-}(\boldsymbol{q},\omega)}{\omega}.$$

The quasiparticle scattering rate can be related, by the fluctuation dissipation theorem, to the charge susceptibility [16,95,100], though this will not be central to the discussion.

The susceptibility is defined in the superconducting state, as in a Fermi liquid, via a bubble diagram [101] (see Chap 3 for further details on the diagrammatic form of correlation functions)

$$\chi_{SC}(\boldsymbol{q},i\omega_n) = \frac{1}{2\beta}\mathrm{Tr}\left\{\sum_{\boldsymbol{k},ik_n} G(\boldsymbol{k},ik_n)\,G(\boldsymbol{k}+\boldsymbol{q},ik_n+i\omega_n)\right\}, \tag{1.8}$$

where $G(\boldsymbol{k},i\omega_n)$ is the Green's function of the superconducting quasiparticle found in Eq. (1.5). For the purposes of performing the sum over Matsubara frequencies, it is useful to separate the Green's function into two terms, with positive and negative energy poles,

$$G_{\boldsymbol{k}}(i\omega_n) = \frac{1}{i\omega_n - E_{\boldsymbol{k}}}\begin{bmatrix} \frac{1}{2}\left(1+\frac{\xi_{\boldsymbol{k}}}{E_{\boldsymbol{k}}}\right) & \frac{1}{2}\frac{\Delta^\star_{\boldsymbol{k}}}{E_{\boldsymbol{k}}} \\ \frac{1}{2}\frac{\Delta_{\boldsymbol{k}}}{E_{\boldsymbol{k}}} & \frac{1}{2}\left(1-\frac{\xi_{\boldsymbol{k}}}{E_{\boldsymbol{k}}}\right)\end{bmatrix} + \frac{1}{i\omega_n + E_{\boldsymbol{k}}}\begin{bmatrix} \frac{1}{2}\left(1-\frac{\xi_{\boldsymbol{k}}}{E_{\boldsymbol{k}}}\right) & -\frac{1}{2}\frac{\Delta^\star_{\boldsymbol{k}}}{E_{\boldsymbol{k}}} \\ -\frac{1}{2}\frac{\Delta_{\boldsymbol{k}}}{E_{\boldsymbol{k}}} & \frac{1}{2}\left(1+\frac{\xi_{\boldsymbol{k}}}{E_{\boldsymbol{k}}}\right)\end{bmatrix}. \tag{1.9}$$

The sum over Matsubara frequencies is then performed in the usual manner, via a contour integral in the complex plane [95]. The resulting expression gains factors of the electron (hole) occupation

function, $f(E)$ [$\bar{f}(E)$], for each positive (negative) pole,

$$\begin{aligned}\chi_{SC}(\boldsymbol{q}, i\omega_n) &= \frac{1}{4}\sum_{\boldsymbol{k}}\left\{\left[1+\frac{\xi_{\boldsymbol{k}}\xi_{\boldsymbol{k}+\boldsymbol{q}}+\Delta_{\boldsymbol{k}}\Delta_{\boldsymbol{k}+\boldsymbol{q}}}{E_{\boldsymbol{k}}E_{\boldsymbol{k}+\boldsymbol{q}}}\right]\frac{f\left(E_{\boldsymbol{k}+\boldsymbol{q}}\right)-f\left(E_{\boldsymbol{k}}\right)}{i\omega_n-\left(E_{\boldsymbol{k}+\boldsymbol{q}}-E_{\boldsymbol{k}}\right)}\right.\\ &+\left[1-\frac{\xi_{\boldsymbol{k}}\xi_{\boldsymbol{k}+\boldsymbol{q}}+\Delta_{\boldsymbol{k}}\Delta_{\boldsymbol{k}+\boldsymbol{q}}}{E_{\boldsymbol{k}}E_{\boldsymbol{k}+\boldsymbol{q}}}\right]\frac{\bar{f}\left(E_{\boldsymbol{k}+\boldsymbol{q}}\right)-f\left(E_{\boldsymbol{k}}\right)}{i\omega_n+\left(E_{\boldsymbol{k}+\boldsymbol{q}}+E_{\boldsymbol{k}}\right)}\\ &+\left[1-\frac{\xi_{\boldsymbol{k}}\xi_{\boldsymbol{k}+\boldsymbol{q}}+\Delta_{\boldsymbol{k}}\Delta_{\boldsymbol{k}+\boldsymbol{q}}}{E_{\boldsymbol{k}}E_{\boldsymbol{k}+\boldsymbol{q}}}\right]\frac{f\left(E_{\boldsymbol{k}+\boldsymbol{q}}\right)-\bar{f}\left(E_{\boldsymbol{k}}\right)}{i\omega_n-\left(E_{\boldsymbol{k}+\boldsymbol{q}}+E_{\boldsymbol{k}}\right)}\\ &\left.+\left[1+\frac{\xi_{\boldsymbol{k}}\xi_{\boldsymbol{k}+\boldsymbol{q}}+\Delta_{\boldsymbol{k}}\Delta_{\boldsymbol{k}+\boldsymbol{q}}}{E_{\boldsymbol{k}}E_{\boldsymbol{k}+\boldsymbol{q}}}\right]\frac{\bar{f}\left(E_{\boldsymbol{k}+\boldsymbol{q}}\right)-\bar{f}\left(E_{\boldsymbol{k}}\right)}{i\omega_n+\left(E_{\boldsymbol{k}+\boldsymbol{q}}-E_{\boldsymbol{k}}\right)}\right\}. \end{aligned} \tag{1.10}$$

The prefactors in each term of this expression are known as the coherence factors, and arise due to the different combinations of terms in the initial Green's functions. These coherence factors demonstrate the influence of the superconducting gap directly on the susceptibility, beyond the influence of the density of states.

The final term in Eq. (1.10) may be combined with the first by expressing the occupation factor part as

$$\sum_{\boldsymbol{k}}\frac{\bar{f}\left(E_{\boldsymbol{k}+\boldsymbol{q}}\right)-\bar{f}\left(E_{\boldsymbol{k}}\right)}{i\omega_n+\left(E_{\boldsymbol{k}+\boldsymbol{q}}-E_{\boldsymbol{k}}\right)} = \sum_{\boldsymbol{k}}\frac{1-f\left(E_{\boldsymbol{k}+\boldsymbol{q}}\right)-[1-f\left(E_{\boldsymbol{k}}\right)]}{i\omega_n+\left(E_{\boldsymbol{k}+\boldsymbol{q}}-E_{\boldsymbol{k}}\right)} = \sum_{\boldsymbol{k}}\frac{f\left(E_{\boldsymbol{k}}\right)-f\left(E_{\boldsymbol{k}+\boldsymbol{q}}\right)}{i\omega_n+\left(E_{\boldsymbol{k}+\boldsymbol{q}}-E_{\boldsymbol{k}}\right)} \tag{1.11}$$

and making the change of variables $\boldsymbol{k}\rightarrow-(\boldsymbol{k}+\boldsymbol{q})$. Noting that the quasiparticle energy is even with respect to the wavevector $\boldsymbol{k}$ (if the system has time reversal or parity symmetry), this term can be expressed as

$$\sum_{\boldsymbol{k}}\frac{f\left(E_{\boldsymbol{k}}\right)-f\left(E_{\boldsymbol{k}+\boldsymbol{q}}\right)}{i\omega_n+\left(E_{\boldsymbol{k}+\boldsymbol{q}}-E_{\boldsymbol{k}}\right)} = \sum_{\boldsymbol{k}}\frac{f\left(E_{-\boldsymbol{k}-\boldsymbol{q}}\right)-f\left(E_{-\boldsymbol{k}}\right)}{i\omega_n+\left(E_{-\boldsymbol{k}}-E_{-\boldsymbol{k}-\boldsymbol{q}}\right)} = \sum_{\boldsymbol{k}}\frac{f\left(E_{\boldsymbol{k}+\boldsymbol{q}}\right)-f\left(E_{\boldsymbol{k}}\right)}{i\omega_n-\left(E_{\boldsymbol{k}+\boldsymbol{q}}-E_{\boldsymbol{k}}\right)} \tag{1.12}$$

This allows the superconducting susceptibility to be simplified yet further [102–104],

$$\begin{aligned}\chi_{SC}(\boldsymbol{q}, i\omega_n) &= \sum_{\boldsymbol{k}}\left\{\frac{1}{2}\left[1+\frac{\xi_{\boldsymbol{k}}\xi_{\boldsymbol{k}+\boldsymbol{q}}+\Delta_{\boldsymbol{k}}\Delta_{\boldsymbol{k}+\boldsymbol{q}}}{E_{\boldsymbol{k}}E_{\boldsymbol{k}+\boldsymbol{q}}}\right]\frac{f\left(E_{\boldsymbol{k}+\boldsymbol{q}}\right)-f\left(E_{\boldsymbol{k}}\right)}{i\omega_n-\left(E_{\boldsymbol{k}+\boldsymbol{q}}-E_{\boldsymbol{k}}\right)}\right.\\ &+\frac{1}{4}\left[1-\frac{\xi_{\boldsymbol{k}}\xi_{\boldsymbol{k}+\boldsymbol{q}}+\Delta_{\boldsymbol{k}}\Delta_{\boldsymbol{k}+\boldsymbol{q}}}{E_{\boldsymbol{k}}E_{\boldsymbol{k}+\boldsymbol{q}}}\right]\frac{\bar{f}\left(E_{\boldsymbol{k}+\boldsymbol{q}}\right)-f\left(E_{\boldsymbol{k}}\right)}{i\omega_n+\left(E_{\boldsymbol{k}+\boldsymbol{q}}+E_{\boldsymbol{k}}\right)}\\ &\left.+\frac{1}{4}\left[1-\frac{\xi_{\boldsymbol{k}}\xi_{\boldsymbol{k}+\boldsymbol{q}}+\Delta_{\boldsymbol{k}}\Delta_{\boldsymbol{k}+\boldsymbol{q}}}{E_{\boldsymbol{k}}E_{\boldsymbol{k}+\boldsymbol{q}}}\right]\frac{f\left(E_{\boldsymbol{k}+\boldsymbol{q}}\right)-\bar{f}\left(E_{\boldsymbol{k}}\right)}{i\omega_n-\left(E_{\boldsymbol{k}+\boldsymbol{q}}+E_{\boldsymbol{k}}\right)}\right\}. \end{aligned} \tag{1.13}$$

Performing the analytic continuation to real frequencies ($i\omega_n\rightarrow\omega+i\eta$), with the limit $\eta\rightarrow0$ implied) gives the familiar generalisation of the BCS susceptibility [101] (for a momentum dependent gap),

$$\begin{aligned}\chi_{SC}(\boldsymbol{q}, \omega) &= \sum_{\boldsymbol{k}}\left\{\frac{1}{2}\left[1+\frac{\xi_{\boldsymbol{k}}\xi_{\boldsymbol{k}+\boldsymbol{q}}+\Delta_{\boldsymbol{k}}\Delta_{\boldsymbol{k}+\boldsymbol{q}}}{E_{\boldsymbol{k}}E_{\boldsymbol{k}+\boldsymbol{q}}}\right]\frac{f\left(E_{\boldsymbol{k}+\boldsymbol{q}}\right)-f\left(E_{\boldsymbol{k}}\right)}{\omega+i\eta-\left(E_{\boldsymbol{k}+\boldsymbol{q}}-E_{\boldsymbol{k}}\right)}\right.\\ &+\frac{1}{4}\left[1-\frac{\xi_{\boldsymbol{k}}\xi_{\boldsymbol{k}+\boldsymbol{q}}+\Delta_{\boldsymbol{k}}\Delta_{\boldsymbol{k}+\boldsymbol{q}}}{E_{\boldsymbol{k}}E_{\boldsymbol{k}+\boldsymbol{q}}}\right]\frac{\bar{f}\left(E_{\boldsymbol{k}+\boldsymbol{q}}\right)-f\left(E_{\boldsymbol{k}}\right)}{\omega+i\eta+\left(E_{\boldsymbol{k}+\boldsymbol{q}}+E_{\boldsymbol{k}}\right)}\\ &\left.+\frac{1}{4}\left[1-\frac{\xi_{\boldsymbol{k}}\xi_{\boldsymbol{k}+\boldsymbol{q}}+\Delta_{\boldsymbol{k}}\Delta_{\boldsymbol{k}+\boldsymbol{q}}}{E_{\boldsymbol{k}}E_{\boldsymbol{k}+\boldsymbol{q}}}\right]\frac{f\left(E_{\boldsymbol{k}+\boldsymbol{q}}\right)-\bar{f}\left(E_{\boldsymbol{k}}\right)}{\omega+i\eta-\left(E_{\boldsymbol{k}+\boldsymbol{q}}+E_{\boldsymbol{k}}\right)}\right\}. \end{aligned} \tag{1.14}$$

The superconducting gap then influences the susceptibility not only by altering the density of states, an effect which enters the expression via the occupation factors, but also by the coherence factors. While the effect of the density of states is well understood, with relation to the low temperature limit of $1/T_1$ [11, 12, 20], discussion of the influence of the coherence factors on the relaxation rate has largely been limited to the case of conventional (fully gapped) superconductivity [11, 105, 106]. This is another example where ideas have been carried over from high symmetry environments (such as that of ^{3}He), wherein the coherence factors of a nodal gap must vanish due to the symmetry of the gap function. As I shall discuss in more detail in the following chapters, this assumption is only true for gaps with symmetry required nodes, with dramatic consequences for $1/T_1$ in gaps with accidental nodes.

1.6 Thesis outline

In Chapter 2, I investigate how the symmetry properties of the superconducting gap affects the nuclear magnetic relaxation rate $1/T_1$. I focus particularly on the difference between symmetry required and accidental nodes, in a toy model with D_{2h} symmetry, showing that there are distinct differences in the relaxation rate between the two cases, with a prominent Hebel-Slichter-like peak present in the latter case. I also examine how factors such as the presence of impurities, bandstructure effects and electronic interactions influence the form of the relaxation rate.

Chapter 3 examines, in greater detail, how the inclusion of vertex corrections, in the form of the random phase approximation (RPA), influences the nuclear magnetic relaxation. I also introduce effective models for the BEDT-TTF based family of superconductors and discuss the various gap symmetries proposed for them, before examining how the relaxation rate behaves for these models and gap functions.

A more thorough discussion of the effective models proposed for κ-(BEDT-TTF)$_2$Cu[N(CN)$_2$]Br is presented in Chapter 4, before I make a detailed comparison between experimental data and the $1/T_1$ relaxation rates predicted for the various gap functions.

Finally, in Chapter 5 I turn my attention to the penetration depth, and discuss how measurements of the relaxation rate may be used to probe the structure of the gap function. I also discuss, in this chapter, current relaxation in Fermi liquids and superconductors more generally, and how umklapp scattering should influence the relaxation rates measured in both cases. The gap structure in κ-(BEDT-TTF)$_2$Cu[N(CN)$_2$]Br is revisited in light of the scattering rate, and I determine which of the proposed gap functions are consistent with the measured rate.

Chapter 6 summarises these results and conclusions.

The following publication has been incorporated as Chapter 2.

1. [1] **D.C. Cavanagh**, and B.J. Powell, *Nuclear magnetic resonance in low-symmetry superconductors*, *Physical Review B* 97(2): 024509, 2018

Contributor	Statement of contribution	%
D.C. Cavanagh	writing of text	90
	proof-reading	60
	theoretical derivations	90
	numerical calculations	100
	preparation of figures	100
	initial concept	20
B.J. Powell	writing of text	10
	proof-reading	40
	supervision, guidance	100
	theoretical derivations	10
	initial concept	80

Chapter 2

Nuclear Magnetic Resonance in Low-Symmetry Superconductors

2.1 Introduction

In this chapter, I consider the nuclear spin-lattice relaxation rate $1/T_1$ in superconductors with accidental nodes, the positions of which are not constrained by symmetry. In superconductors with isotropic gaps $1/T_1T$ increases to a peak below T_c. This peak, first observed by Hebel and Slichter [105, 106], is a direct consequence of the quasiparticle coherence in the superconducting state and the resulting enhancement of the density of states at the gap [12, 98]. I investigate the existence of an analogous peak in the relaxation rate for anisotropic gaps with accidental nodes. I first show that in models without disorder or electronic interactions (beyond those involved in the pairing) there is a logarithmic divergence in $1/T_1T$ as $T \to T_c$ from below. This divergence exists even if there is no isotropic component of the gap, $\Delta_{\boldsymbol{k}}$, i.e. $\int d^3\boldsymbol{k}\Delta_{\boldsymbol{k}} = 0$. I show, numerically in a D_{2h} symmetric model – similar to those discussed above – that this divergence is controlled but not removed entirely by either disorder or electron-electron interactions, giving rise to a Hebel-Slichter-like peak. However, it shows some subtle differences from the true Hebel-Slichter peak both in its microscopic origin and in that it is not controlled by gap anisotropy. Furthermore, the peak occurs at T_c^- (immediately below the critical temperature, $T_c^- = \lim_{\delta\to 0}(T_c - \delta)$) for a superconductor with accidental nodes rather than when $T \sim \Delta$ as in a true Hebel-Slichter peak.

2.2 Nuclear magnetic resonance and the relaxation rate $1/T_1T$

The spins of atomic nuclei relax by exchanging energy with their environment. In the case of a metal or superconductor this means the conduction electrons. Thus the relaxation rate of nuclei in an electronic environment is related to the transverse dynamic susceptibility of the quasiparticles,

$\chi_{+-}(\boldsymbol{q},\omega) = \chi'_{+-}(\boldsymbol{q},\omega) + i\chi''_{+-}(\boldsymbol{q},\omega)$, via [12,98,99]

$$\frac{1}{T_1 T} = \lim_{\omega\to 0} \frac{2k_B}{\gamma_e^2 \hbar^4} \sum_{\boldsymbol{q}} |A_H(\boldsymbol{q})|^2 \frac{\chi''_{+-}(\boldsymbol{q},\omega)}{\omega}, \tag{2.1}$$

where γ_e is the (electron) gyromagnetic ratio and $A_H(\boldsymbol{q})$ is the hyperfine coupling, which is approximated by a point contact interaction [$A_H(\boldsymbol{q}) = A_H$] for simplicity.

The susceptibility itself is given by the transverse spin correlation function [16,100]

$$\chi_{+-}(\boldsymbol{q},\omega) = \lim_{i\omega_n\to\omega+i\eta} \int_0^\beta d\tau e^{i\omega_n\tau} \left\langle T_\tau S_{\boldsymbol{q}}^{(+)}(\tau) S_{\boldsymbol{q}}^{(-)}(0) \right\rangle, \tag{2.2}$$

where $i\omega_n$ is a (bosonic) Matsubara frequency, τ is the imaginary time, $\beta = 1/k_B T$ and $S_{\mathbf{q}}^{(\pm)}$ is the Fourier transform of the spin raising (lowering) operator, at wavevector $\mathbf{q}$. Eq. (2.2) can be expressed in terms of the Green's function of quantum many body theory, $G_{\mathbf{k},\sigma}(i\omega_n)$ and appropriate vertex functions, [16]

$$\chi_{+-}(\boldsymbol{q},\omega) = \lim_{i\omega_n\to\omega+i\eta} \sum_{i\omega_m,\sigma,\sigma'} \sum_{\boldsymbol{k}} \gamma_{\boldsymbol{q}}^{(+)}(i\omega_n) G_{\boldsymbol{k},\sigma}(i\omega_m + i\omega_n) G_{\boldsymbol{k}+\boldsymbol{q},\sigma'}(i\omega_m) \Gamma_{\boldsymbol{q}}^{(-)}(i\omega_n), \tag{2.3}$$

where $\gamma^{(\pm)}$ represents the bare interaction vertex for raising (lowering) the spin and Γ represents the fully renormalised vertex (including all vertex corrections). Neglecting vertex corrections, which will be revisited in Chapter 3, and using the vertices to constrain the spin indices,

$$\chi_{+-}(\boldsymbol{q},\omega) = \lim_{i\omega_n\to\omega+i\eta} 2 \sum_{i\omega_m} \sum_{\boldsymbol{k}} G_{\boldsymbol{k},\uparrow}(i\omega_m + i\omega_n) G_{\boldsymbol{k}+\boldsymbol{q},\downarrow}(i\omega_m), \tag{2.4}$$

where the overall factor of two arises due to the possible spin orientations. We can then express the renormalised Green's functions in this expression in terms of the spectral density function, [16]

$$G_{\boldsymbol{k}}(i\omega_n) = \int_{-\infty}^{\infty} \frac{dE}{2\pi} \frac{A_{\boldsymbol{k}}(E)}{i\omega_n - E}, \tag{2.5}$$

resulting in the expression

$$\chi_{+-}(\boldsymbol{q},\omega) = \lim_{i\omega_n\to\omega+i\eta} 2 \sum_{i\omega_m} \sum_{\boldsymbol{k}} \int \frac{dE_1 dE_2}{(2\pi)^2} \frac{A_{\boldsymbol{k}}(E_1) A_{\boldsymbol{k}+\boldsymbol{q}}(E_2)}{(i\omega_m + i\omega_n - E_1)(i\omega_m - E_2)}, \tag{2.6}$$

$$= 2 \sum_{\boldsymbol{k}} \int \frac{dE_1 dE_2}{(2\pi)^2} \frac{f(E_2) - f(E_1)}{\omega + i\eta - (E_2 - E_1))} A_{\boldsymbol{k}}(E_1) A_{\boldsymbol{k}+\boldsymbol{q}}(E_2), \tag{2.7}$$

where $f(E)$ is the Fermi-Dirac distribution factor, and in the final line I have performed the sum over Matsubara frequencies and the analytical continuation, $i\omega_n \to \omega + i\eta$. In the clean, weakly interacting limit, the (Fermi liquid) spectral density function takes the approximate form [16,100]

$$A_{\boldsymbol{k}}(E) = Z\pi\delta(\xi_{\boldsymbol{k}} - E), \tag{2.8}$$

with Z the quasiparticle weight (responsible for the renormalisation of the quasiparticle energy), resulting in an expression for the dressed Green's function as a linear combination of noninteracting Green's functions.

In the superconducting state, the Green's functions appearing in Eq. (2.3) are replaced by matrix Green's functions spanning the Hilbert space of both electrons and holes, as discussed in Chapter 1. The anomalous (off-diagonal) components of these Green's functions give rise to superconductivity. In this case, Eq. (2.7) is modified to include a trace over the Nambu-Gor'kov pseudospin indices, which label the quasiparticle and hole contributions to each Green's function, [101]

$$\chi_{+-}(\boldsymbol{q},\omega) = \lim_{i\omega_n\to\omega+i\eta} 2\sum_{i\omega_m}\sum_{\boldsymbol{k}} \mathrm{Tr}\left\{G_{\boldsymbol{k}}\left(i\omega_m+i\omega_n\right)G_{\boldsymbol{k}+\boldsymbol{q}}\left(i\omega_m\right)\right\}. \tag{2.9}$$

The anomalous components of the Green's functions are the source of the coherence effects that can be probed directly in the NMR relaxation rate, $1/T_1T$.

In terms of the spectral density function, $A_{\boldsymbol{k}}(E)$, the transverse spin susceptibility for a generalised BCS superconductor is [16, 98, 101, 107]

$$\begin{aligned}\chi''_{+-}(\boldsymbol{q},\omega) = & \sum_{\boldsymbol{k}}\int_{-\infty}^{\infty}\frac{dE_1dE_2}{4\pi^2} \\ & \times\left\{\frac{1}{2}\left[1+\frac{\xi_{\boldsymbol{k}}\xi_{\boldsymbol{k}+\boldsymbol{q}}+\Delta_{\boldsymbol{k}}\Delta_{\boldsymbol{k}+\boldsymbol{q}}}{E_{\boldsymbol{k}}E_{\boldsymbol{k}+\boldsymbol{q}}}\right]\left[f(E_2)-f(E_1)\right]\delta\left[\omega-(E_2-E_1)\right]A_{\boldsymbol{k}}(E_1)A_{\boldsymbol{k}+\boldsymbol{q}}(E_2)\right. \\ & +\frac{1}{4}\left[1-\frac{\xi_{\boldsymbol{k}}\xi_{\boldsymbol{k}+\boldsymbol{q}}+\Delta_{\boldsymbol{k}}\Delta_{\boldsymbol{k}+\boldsymbol{q}}}{E_{\boldsymbol{k}}E_{\boldsymbol{k}+\boldsymbol{q}}}\right]\left[\bar{f}(E_2)-f(E_1)\right]\delta\left[\omega+(E_2+E_1)\right]A_{\boldsymbol{k}}(E_1)A_{\boldsymbol{k}+\boldsymbol{q}}(E_2) \\ & \left.+\frac{1}{4}\left[1-\frac{\xi_{\boldsymbol{k}}\xi_{\boldsymbol{k}+\boldsymbol{q}}+\Delta_{\boldsymbol{k}}\Delta_{\boldsymbol{k}+\boldsymbol{q}}}{E_{\boldsymbol{k}}E_{\boldsymbol{k}+\boldsymbol{q}}}\right]\left[f(E_2)-\bar{f}(E_1)\right]\delta\left[\omega-(E_2+E_1)\right]A_{\boldsymbol{k}}(E_1)A_{\boldsymbol{k}+\boldsymbol{q}}(E_2)\right\},\end{aligned} \tag{2.10}$$

where $\xi_{\boldsymbol{k}}$ is the single particle dispersion, measured from the chemical potential,

$$E_{\boldsymbol{k}} = \sqrt{\xi_{\boldsymbol{k}}^2+|\Delta_{\boldsymbol{k}}|^2}, \tag{2.11}$$

and $\bar{f}(E)=1-f(E)$. The coherence factors (i.e., the terms in square brackets) in Eq. (2.10) arise naturally from the trace over Nambu spinors. For a superconductor with an isotropic gap, these coherence factors are responsible for the existence of the Hebel-Slichter peak [12, 98].

From Eq. (2.10) I consider three approximations: (i) The clean, BCS limit, where interactions are limited to those giving rise to superconductivity and no disorder is present. (ii) Uncorrelated disorder, where electron-impurity interactions result in a broadening of the peak in the spectral function (i.e. give rise to a finite quasiparticle lifetime). The strong disorder regime is irrelevant as strong disorder suppresses unconventional superconductivity [20]. And (iii) disorder and electron-electron interactions, with the latter taken into account via the random phase approximation (RPA). In the following analysis I will treat the clean BCS limit analytically, then extend the results to account for disorder and electron-electron interactions numerically. The effects of electron-electron interactions via the random phase approximation will be explored further in the following chapter.

2.3 The clean limit

Inserting Eq. (2.10) for the dynamic susceptibility into the expression for the relaxation rate, Eq. (2.1),

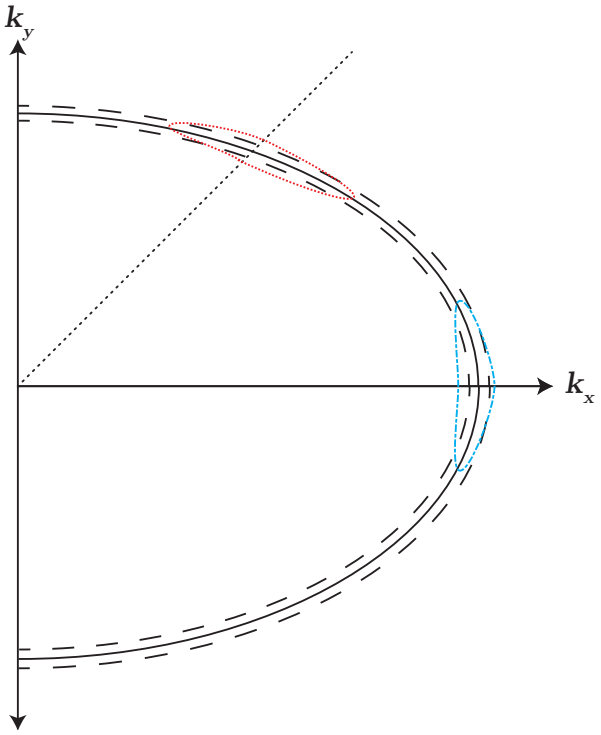

Figure 2.1: Contours of constant energy for an isotropic gap (black dashed lines), symmetry required nodes (blue dot dashed line) and accidental nodes (red dotted line), sketched for an elliptical Fermi surface. The black dotted line indicates the position of the accidental node, while the symmetry required nodes reside on the axes (with the contour around the k_x-axis highlighted).

$$\begin{aligned}\frac{1}{T_1T} \propto \lim_{\omega\to 0}\sum_{\boldsymbol{k},\boldsymbol{q}}\int_{-\infty}^{\infty}\frac{dE_1\,dE_2}{4\omega}\\ \times\Bigg\{&\frac{1}{2}\left[1+\frac{\xi_{\boldsymbol{k}}\xi_{\boldsymbol{k}+\boldsymbol{q}}+\Delta_{\boldsymbol{k}}\Delta_{\boldsymbol{k}+\boldsymbol{q}}}{E_{\boldsymbol{k}}E_{\boldsymbol{k}+\boldsymbol{q}}}\right]\left[f\left(E_2\right)-f\left(E_1\right)\right]\delta\left[\omega-\left(E_2-E_1\right)\right]A_{\boldsymbol{k}}\left(E_1\right)A_{\boldsymbol{k}+\boldsymbol{q}}\left(E_2\right)\\ &+\frac{1}{4}\left[1-\frac{\xi_{\boldsymbol{k}}\xi_{\boldsymbol{k}+\boldsymbol{q}}+\Delta_{\boldsymbol{k}}\Delta_{\boldsymbol{k}+\boldsymbol{q}}}{E_{\boldsymbol{k}}E_{\boldsymbol{k}+\boldsymbol{q}}}\right]\left[\bar{f}\left(E_2\right)-f\left(E_1\right)\right]\delta\left[\omega+\left(E_2+E_1\right)\right]A_{\boldsymbol{k}}\left(E_1\right)A_{\boldsymbol{k}+\boldsymbol{q}}\left(E_2\right)\\ &+\frac{1}{4}\left[1-\frac{\xi_{\boldsymbol{k}}\xi_{\boldsymbol{k}+\boldsymbol{q}}+\Delta_{\boldsymbol{k}}\Delta_{\boldsymbol{k}+\boldsymbol{q}}}{E_{\boldsymbol{k}}E_{\boldsymbol{k}+\boldsymbol{q}}}\right]\left[f\left(E_2\right)-\bar{f}\left(E_1\right)\right]\delta\left[\omega-\left(E_2+E_1\right)\right]A_{\boldsymbol{k}}\left(E_1\right)A_{\boldsymbol{k}+\boldsymbol{q}}\left(E_2\right)\Bigg\}\end{aligned} \tag{2.12}$$

Performing the integration over E_2 and setting $E_1 = E$, I obtain,

$$\begin{aligned}
\frac{1}{T_1T} &= \lim_{\omega\to 0}\sum_{\boldsymbol{k},\boldsymbol{q}}\int_{-\infty}^{\infty}\frac{dE}{4\omega}\left\{\frac{1}{2}\left[1+\frac{\xi_{\boldsymbol{k}}\xi_{\boldsymbol{k}+\boldsymbol{q}}+\Delta_{\boldsymbol{k}}\Delta_{\boldsymbol{k}+\boldsymbol{q}}}{E_{\boldsymbol{k}}E_{\boldsymbol{k}+\boldsymbol{q}}}\right]\left[f\left(E+\omega\right)-f\left(E\right)\right]A_{\boldsymbol{k}}\left(E\right)A_{\boldsymbol{k}+\boldsymbol{q}}\left(E\right)\right.\\
&\quad+\frac{1}{4}\left[1-\frac{\xi_{\boldsymbol{k}}\xi_{\boldsymbol{k}+\boldsymbol{q}}+\Delta_{\boldsymbol{k}}\Delta_{\boldsymbol{k}+\boldsymbol{q}}}{E_{\boldsymbol{k}}E_{\boldsymbol{k}+\boldsymbol{q}}}\right]\left[\bar{f}\left(-E-\omega\right)-f\left(E\right)\right]A_{\boldsymbol{k}}\left(E\right)A_{\boldsymbol{k}+\boldsymbol{q}}\left(-E\right)\\
&\quad\left.+\frac{1}{4}\left[1-\frac{\xi_{\boldsymbol{k}}\xi_{\boldsymbol{k}+\boldsymbol{q}}+\Delta_{\boldsymbol{k}}\Delta_{\boldsymbol{k}+\boldsymbol{q}}}{E_{\boldsymbol{k}}E_{\boldsymbol{k}+\boldsymbol{q}}}\right]\left[f\left(E\right)-\bar{f}\left(-E+\omega\right)\right]A_{\boldsymbol{k}}\left(-E\right)A_{\boldsymbol{k}+\boldsymbol{q}}\left(E\right)\right\}\\
&\propto \sum_{\boldsymbol{k},\boldsymbol{q}}\int_{-\infty}^{\infty}\frac{dE}{4}\left\{\frac{1}{2}\left[1+\frac{\xi_{\boldsymbol{k}}\xi_{\boldsymbol{k}+\boldsymbol{q}}+\Delta_{\boldsymbol{k}}\Delta_{\boldsymbol{k}+\boldsymbol{q}}}{E_{\boldsymbol{k}}E_{\boldsymbol{k}+\boldsymbol{q}}}\right]\left[-\frac{df}{dE}\right]A_{\boldsymbol{k}}\left(E\right)A_{\boldsymbol{k}+\boldsymbol{q}}\left(E\right)\right.\\
&\quad+\frac{1}{4}\left[1-\frac{\xi_{\boldsymbol{k}}\xi_{\boldsymbol{k}+\boldsymbol{q}}+\Delta_{\boldsymbol{k}}\Delta_{\boldsymbol{k}+\boldsymbol{q}}}{E_{\boldsymbol{k}}E_{\boldsymbol{k}+\boldsymbol{q}}}\right]\left[-\frac{df}{dE}\right]A_{\boldsymbol{k}}\left(E\right)A_{\boldsymbol{k}+\boldsymbol{q}}\left(-E\right)\\
&\quad\left.+\frac{1}{4}\left[1-\frac{\xi_{\boldsymbol{k}}\xi_{\boldsymbol{k}+\boldsymbol{q}}+\Delta_{\boldsymbol{k}}\Delta_{\boldsymbol{k}+\boldsymbol{q}}}{E_{\boldsymbol{k}}E_{\boldsymbol{k}+\boldsymbol{q}}}\right]\left[-\frac{df}{dE}\right]A_{\boldsymbol{k}}\left(-E\right)A_{\boldsymbol{k}+\boldsymbol{q}}\left(E\right)\right\},
\end{aligned}\tag{2.13}$$

where I also use $\bar{f}\left(-E\right) = f\left(E\right)$ to take the limit $\omega \to 0$, leading to the derivative of the Fermi function in each of the three terms. Combining the contributions from each of the three terms in Eq. (2.13) and rearranging this expression gives

$$\frac{1}{T_1T} \propto \frac{1}{4\pi^2}\int_{-\infty}^{\infty}dE\left[-\frac{df}{dE}\right]\sum_{n=1}^{3}\left[\mathcal{K}_n\left(E\right)\right]^2,\tag{2.14}$$

where

$$\mathcal{K}_1\left(E\right) = \sum_{\boldsymbol{k}}A_{\boldsymbol{k}}\left(E\right),\tag{2.15a}$$

$$\mathcal{K}_2\left(E\right) = \sum_{\boldsymbol{k}}\frac{\xi_{\boldsymbol{k}}}{E_{\boldsymbol{k}}}A_{\boldsymbol{k}}\left(E\right),\tag{2.15b}$$

$$\mathcal{K}_3\left(E\right) = \sum_{\boldsymbol{k}}\frac{\Delta_{\boldsymbol{k}}}{E_{\boldsymbol{k}}}A_{\boldsymbol{k}}\left(E\right).\tag{2.15c}$$

Each term in Eq. (2.14) represents the average of a function over a contour of approximately constant energy $E_{\boldsymbol{k}}$, due to the peak in $A_{\boldsymbol{k}}(E)$ at $E \simeq E_{\boldsymbol{k}}$. These averages are then integrated over energy, with the integral restricted by the derivative of the Fermi function to a range of order k_BT. For an s-wave superconductor, this contour will wrap around the entire Fermi surface, while for a gap with nodes, the contour will form closed surfaces around the nodes (for energies smaller than the maximum gap). Examples of these contours are shown in Fig. 2.1.

2.3.1 Anisotropic gap with accidental nodes

In the clean, BCS limit, the spectral functions are given by Dirac delta functions,

$$A_{\boldsymbol{k}}\left(E\right) = \pi\delta\left(E_{\boldsymbol{k}}-E\right),\tag{2.16}$$

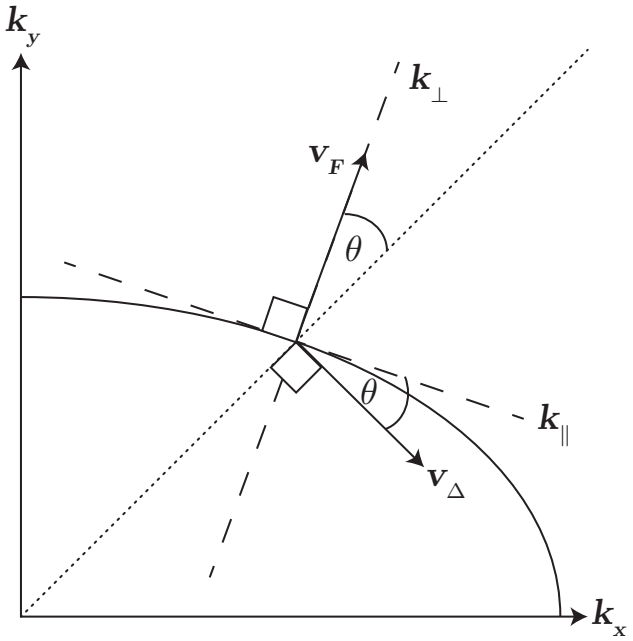

Figure 2.2: The geometry of a system with accidental nodes. Arrows denote the gradients of the normal dispersion (v_F) and the gap function (v_Δ), in the local co-ordinate system defined at the node. The solid line denotes the Fermi surface and the dotted line the node location, while $k_\parallel$ and $k_\perp$ respectively denote the coordinates parallel and perpendicular to the Fermi surface.

each of which can be decomposed [100, 108] into delta functions acting on a local coordinate $\boldsymbol{k}_\perp$, the component of $\boldsymbol{k}$ perpendicular to the Fermi surface,

$$\delta\left(E_{\boldsymbol{k}} - E\right) = \sum_{k_\perp(E)} \left|\frac{\partial E_{\boldsymbol{k}}}{\partial k_\perp}\right|^{-1} \delta\left[k_\perp - k_\perp\left(E\right)\right]. \tag{2.17}$$

These delta functions then constrain the magnitude of $\boldsymbol{k}_\perp$ to the value corresponding to the constant energy surface, $\boldsymbol{k}_\perp\left(E\right)$. For a Fermi liquid (or a s-wave superconductor), such a constraint would yield an energy surface parallel to the Fermi surface, corresponding to a shift in the chemical potential. For a superconductor with an anisotropic gap, this constraint will yield contours similar to those in Fig. (2.1), with the value of $\boldsymbol{k}_\perp$ varying around the Fermi surface. The gradient of the gap function is then, in terms of $\boldsymbol{k}_\perp$ and a local $(D-1)$-dimensional manifold parallel to the Fermi surface, $\{\boldsymbol{k}_i\}$, given by

$$\boldsymbol{v}_\Delta\left(\boldsymbol{k}\right) \equiv \boldsymbol{\nabla}_{\boldsymbol{k}}\Delta_{\boldsymbol{k}} = \sum_{i=1}^{D-1} \hat{\boldsymbol{k}}_i \left[v_\Delta\left(\boldsymbol{k}\right)\right]_i + \hat{\boldsymbol{k}}_\perp v_\perp\left(\boldsymbol{k}\right), \tag{2.18}$$

where $\left[v_\Delta\left(\boldsymbol{k}\right)\right]_i = \boldsymbol{v}_\Delta\left(\boldsymbol{k}\right)\cdot\hat{\boldsymbol{k}}_i$ is the projection of $\boldsymbol{\nabla}_{\boldsymbol{k}}\Delta_{\boldsymbol{k}}$ onto $\boldsymbol{k}_i$, the ith dimension on the manifold parallel to the Fermi surface, $v_\perp\left(\boldsymbol{k}\right) = \boldsymbol{v}_\Delta\left(\boldsymbol{k}\right)\cdot\hat{\boldsymbol{k}}_\perp$ is the projection of $\boldsymbol{\nabla}_{\boldsymbol{k}}\Delta_{\boldsymbol{k}}$ onto $\boldsymbol{k}_\perp$, $\hat{\boldsymbol{k}}_\mu = \boldsymbol{k}_\mu/k_\mu$, and $k_\mu = |\boldsymbol{k}_\mu|$ for any subscript μ including none. In general, the $[v_\Delta(\boldsymbol{k})]_i$ and $v_\perp(\boldsymbol{k})$ are functions of the position on the manifold. For a symmetry required gap function, the perpendicular component of the gap gradient. $v_\perp\left(\boldsymbol{k}\right)$ will vanish at the node, while an accidental symmetry gap is under no such constraint.

In the simplest, two dimensional, case (with $\boldsymbol{k}_i = \boldsymbol{k}_\parallel$), this gives, near the nodes,

$$\boldsymbol{v}_\Delta\left(\boldsymbol{k}\right) = \hat{\boldsymbol{k}}_\parallel v_\Delta\left(\boldsymbol{k}\right)\cos\left[\theta\left(\boldsymbol{k}\right)\right] + \hat{\boldsymbol{k}}_\perp v_\Delta\left(\boldsymbol{k}\right)\sin\left[\theta\left(\boldsymbol{k}\right)\right], \tag{2.19}$$

where $\theta(\boldsymbol{k})$ parametrises the local co-ordinate system. At the momentum where the node crosses the Fermi surface, $\boldsymbol{k}_{\mathrm{F}}^{\mathrm{node}}$, $\theta = \theta\left(\boldsymbol{k}_{\mathrm{F}}^{\mathrm{node}}\right)$ is the angle between the nodal line and the normal to the Fermi surface (see Fig. 2.2). In the absence of a lattice potential, the Fermi surface has full rotational symmetry and $\theta(\boldsymbol{k})$ will be constant over the Fermi surface. Whereas, in lattice models, which necessarily have lower symmetry, it can be understood as a parameter defined by a local coordinate transformation performed at each point on the energy contour. For small energies, this angle can be approximated by the value at the node.

Near a node, the gap function will be independent of the coordinate parallel to the node line. Importantly, in the accidental case this is not required to be normal to the Fermi surface. This angle is defined by

$$\sin\theta = \frac{\boldsymbol{v}_F \cdot \boldsymbol{v}_\Delta}{|\boldsymbol{v}_F|\,|\boldsymbol{v}_\Delta|}, \tag{2.20}$$

where $\boldsymbol{v}_\Delta = \boldsymbol{v}_\Delta\left(\boldsymbol{k}_{\mathrm{F}}^{\mathrm{node}}\right)$, and $\boldsymbol{v}_F = \boldsymbol{\nabla}_{\boldsymbol{k}}\xi_{\boldsymbol{k}}|_{\boldsymbol{k}=\boldsymbol{k}_{\mathrm{F}}^{\mathrm{node}}}$ is the Fermi velocity at the node. (For simplicity I assume θ is the same for all nodes in the analytical treatment, below.) Note that $\theta = \phi + \pi/2$, where ϕ is the angle between $\boldsymbol{v}_\Delta$ and $\boldsymbol{v}_F$. Near the node the energy is then

$$E_{\boldsymbol{k}} \sim \sqrt{\left[\boldsymbol{v}_F \cdot \left(\boldsymbol{k} - \boldsymbol{k}_{\mathrm{F}}^{\mathrm{node}}\right)\right]^2 + \left[\boldsymbol{v}_\Delta \cdot \left(\boldsymbol{k} - \boldsymbol{k}_{\mathrm{F}}^{\mathrm{node}}\right)\right]^2}, \tag{2.21}$$

where both the gap, $\Delta_{\boldsymbol{k}}$, and the electron dispersion $\xi_{\boldsymbol{k}}$ have been approximated by Taylor series' about the node.

The delta function in Eq. (2.16) then constrains the component perpendicular to the Fermi surface, allowing the simplification,

$$\begin{aligned}
\sum_{k_\perp(E)} \left|\frac{\partial E_{\boldsymbol{k}}}{\partial k_\perp}\right|^{-1} \delta\left[k_\perp - k_\perp(E)\right] &= \sum_{k_\perp(E)} \left|\frac{\partial E_{\boldsymbol{k}}}{\partial \varepsilon_{\boldsymbol{k}}}\frac{\partial \varepsilon_{\boldsymbol{k}}}{\partial k_\perp} + \frac{\partial E_{\boldsymbol{k}}}{\partial \Delta_{\boldsymbol{k}}}\frac{\partial \Delta_{\boldsymbol{k}}}{\partial k_\perp}\right|^{-1} \delta\left[k_\perp - k_\perp(E)\right] \\
&= \sum_{k_\perp(E)} \left|\frac{\varepsilon_{\boldsymbol{k}}\frac{\partial \varepsilon_{\boldsymbol{k}}}{\partial k_\perp} + \Delta_{\boldsymbol{k}}\frac{\partial \Delta_{\boldsymbol{k}}}{\partial k_\perp}}{E_{\boldsymbol{k}}}\right|^{-1} \delta\left[k_\perp - k_\perp(E)\right] \\
&= \sum_{k_\perp(E)} \left|\frac{E}{v_F\sqrt{E^2 - |\Delta_{\boldsymbol{k}}|^2} + \Delta_{\boldsymbol{k}} v_\Delta \sin\theta}\right| \delta\left[k_\perp - k_\perp(E)\right].
\end{aligned} \tag{2.22}$$

Previous analyses [12, 109] have primarily focused on the symmetry required case. A symmetry required node must reside on an axis of symmetry, to which the Fermi surface must be perpendicular; thus $\theta = 0$. In fact, the vanishing of this angle is responsible for the lack of analytical divergences encountered in the symmetry required case, see Section 2.3.2.

As a first approximation, I perform a binomial expansion in $\Delta_{\boldsymbol{k}} v_\Delta \sin\theta / v_F\sqrt{E^2 - |\Delta_{\boldsymbol{k}}|^2}$ in the denominators in Eqs. (2.15). Such an approximation is valid for $T \sim T_c$, where $\Delta_{\boldsymbol{k}} \to 0$ provided v_Δ/v_F is not too large; i.e., away from van Hove singularities, where v_F vanishes. Additionally, for sufficiently small $\sin\theta$, such an expansion will be reasonable at all temperatures given the same caveat.

Performing the expansion gives

$$\mathcal{K}_1(E) = \int_E d\boldsymbol{k}_\parallel \frac{E}{v_F\sqrt{E^2-\Delta_{\boldsymbol{k}}^2}+\Delta_{\boldsymbol{k}} v_\Delta \sin\theta} \approx \int_E d\boldsymbol{k}_\parallel \left[\frac{E}{v_F\sqrt{E^2-\Delta_{\boldsymbol{k}}^2}} - \frac{E\Delta_{\boldsymbol{k}} v_\Delta \sin\theta}{v_F^2\left(E^2-\Delta_{\boldsymbol{k}}^2\right)}\right] \tag{2.23a}$$

$$\mathcal{K}_2(E) = \int_E d\boldsymbol{k}_\parallel \frac{\sqrt{E^2-\Delta_{\boldsymbol{k}}^2}}{v_F\sqrt{E^2-\Delta_{\boldsymbol{k}}^2}+\Delta_{\boldsymbol{k}} v_\Delta \sin\theta} \approx \int_E d\boldsymbol{k}_\parallel \left[\frac{1}{v_F} - \frac{\Delta_{\boldsymbol{k}} v_\Delta \sin\theta}{v_F^2\sqrt{E^2-\Delta_{\boldsymbol{k}}^2}}\right] \tag{2.23b}$$

$$\mathcal{K}_3(E) = \int_E d\boldsymbol{k}_\parallel \frac{\Delta_{\boldsymbol{k}}}{v_F\sqrt{E^2-\Delta_{\boldsymbol{k}}^2}+\Delta_{\boldsymbol{k}} v_\Delta \sin\theta} \approx \int_E d\boldsymbol{k}_\parallel \left[\frac{\Delta_{\boldsymbol{k}}}{v_F\sqrt{E^2-\Delta_{\boldsymbol{k}}^2}} - \frac{\Delta_{\boldsymbol{k}}^2 v_\Delta \sin\theta}{v_F^2\left(E^2-\Delta_{\boldsymbol{k}}^2\right)}\right], \tag{2.23c}$$

where $\int_E d\boldsymbol{k}_\parallel$ denotes the integral over the $(D-1)$-dimensional surface in momentum space at energy E.

In the terms depending on the gap, I approximate the gap function by a Taylor series in the momentum components parallel to the Fermi surface, near the node. In D-dimensions this is given by

$$\Delta_{\boldsymbol{k}} = \sum_{i=1}^{D-1} (v_\Delta)_i \left(k_\parallel^i - k_\parallel^{i(0)}\right) + O\left(k_\parallel^i - k_\parallel^{i(0)}\right)^2, \tag{2.24}$$

where $\boldsymbol{k}_\parallel^{(0)} = \hat{\boldsymbol{k}}_\parallel^{(0)} k_\parallel^{(0)}$ denotes the position of the node. In the case of $D = 2$ this gives

$$\Delta_{\boldsymbol{k}} = v_\Delta \cos\theta \left(k_\parallel - k_\parallel^{(0)}\right) + O\left(k_\parallel - k_\parallel^{(0)}\right)^2. \tag{2.25}$$

Under this approximation for the gap, I arrive at

$$\mathcal{K}_1(E) = \lim_{\delta\to 0} \frac{E}{2} \left\langle \frac{\operatorname{sgn}(\Delta)}{v_F\cos\theta}\left[\frac{\pi}{v_\Delta} + \frac{\sin\theta}{v_F}\ln(\delta)\right]\right\rangle_E \tag{2.26a}$$

$$\mathcal{K}_2(E) = \left\langle v_F^{-1}\right\rangle_E \tag{2.26b}$$

$$\mathcal{K}_3(E) = \lim_{\delta\to 0} \frac{E}{2} \left\langle \frac{\tan\theta}{v_F^2}\right\rangle_E \ln(\delta), \tag{2.26c}$$

where $\langle \ldots \rangle_E$ denotes the average over the contour(s) of energy E, across which the magnitude of v_F and v_Δ may in principle vary, as may the angle θ. Note that $\mathcal{K}_1(E)$ depends on the difference between the averages taken on the segments of the energy contour with positive and negative superconducting gap, while $\mathcal{K}_2$ and $\mathcal{K}_3$ depend only on averages over the entire energy contour. The logarithmically divergent contributions arise due to the vanishing denominators in the second terms on the right hand side of Eqs. (2.23a) and (2.23c), while the terms with square roots in the denominator give a convergent contribution.

In the general case of accidental node placement, the velocity magnitudes $v_\Delta(\boldsymbol{k})$ and $v_F(\boldsymbol{k})$ vary across the energy surface, but as a demonstrative example, consider the simplest case where they are constant near the node, *i.e.*, $v_F(\boldsymbol{k}) = v_F$ and $v_\Delta(\boldsymbol{k}) = v_\Delta$. In this case, only the factor of $\operatorname{sgn}(\Delta)$ varies

across the contour, changing sign and resulting in the cancellation of the logarithmic divergence, giving

$$\mathcal{K}_1(E) = 0 \tag{2.27a}$$
$$\mathcal{K}_3(E) = E\frac{\tan\theta}{v_F^2}\lim_{\delta\to 0}\ln(\delta)\,. \tag{2.27b}$$

Both the linear correction to Eq. (2.23b) and the zero order contribution to Eq. (2.23c) vanish as the gap function is odd with respect to the position of the node, but higher order corrections will diverge, similar to the divergence encountered in Eq. (2.26c).

In a more general model, the velocities $v_F(\boldsymbol{k})$ and $v_\Delta(\boldsymbol{k})$ depend on $\boldsymbol{k}$, and so $\mathcal{K}_1(E)$ may also be nonvanishing and divergent [cf. Eq. (2.26a)]. In general, the node in an anisotropic gap function is not required to be near a portion of the gap function where a linear expansion in $k_\parallel$ is valid, in particular the presence of an isotropic component of the gap will shift the node position. Including higher order terms in either the Taylor series for the gap or the expansions of the $\mathcal{K}_i$ is, however, insufficient to remove these divergences.

2.3.2 Anisotropic gap with symmetry required nodes

If $\Delta_{\boldsymbol{k}}$ transforms as a non-trivial representation of the point group, the nodes are required by symmetry. This implies that θ vanishes, as the gap function near the node is independent of the direction perpendicular to the Fermi surface. Further, as the node in this case is required to reside on a symmetry axis for the material, $\mathcal{K}_3$ must vanish, given that an equal length of the contour is on either side of the node where the gap changes sign. In this case, $\mathcal{K}_2$ [Eq. (2.23b)] again gives a non-divergent contribution with the form of the density of states, as the surface integral over the energy contour; and Eq. (2.23a) reduces to $\mathcal{K}_1(E) = \pi E/\langle v_\Delta v_F\rangle$. In this way, I recover the well known result [11, 16] that no Hebel-Slichter peak is observed.

2.3.3 Isotropic gap

To better understand the divergence found for the gap with accidental nodes, it is helpful to consider the differences between the origin of this divergence and the divergence responsible for the Hebel-Slichter peak in conventional s-wave superconductors.

In a superconductor with a purely isotropic gap, which necessarily belongs to the trivial representation of the point group, the gap function is independent of momentum, so $\boldsymbol{v}_\Delta = 0$ and $\Delta_{\boldsymbol{k}} = \Delta_0$, and the energy is only dependent on $\boldsymbol{k}_\parallel$ through $v_F(\boldsymbol{k})$. The momentum sums in the relaxation rate, with Eq.

(2.11), give the constant energy surface integral $S(E) = \sum_{\boldsymbol{k}_\parallel, \boldsymbol{k}_\perp(E)} [v_F(\boldsymbol{k})]^{-1} \delta[\boldsymbol{k}_\perp - \boldsymbol{k}_\perp(E)]$,

$$\mathcal{K}_1(E) = \int_E d\boldsymbol{k}_\parallel \frac{E}{v_F\sqrt{E^2-\Delta_0^2}} = \frac{E}{\sqrt{E^2-\Delta_0^2}} S(E) \tag{2.28a}$$

$$\mathcal{K}_2(E) = \int_E d\boldsymbol{k}_\parallel \frac{\sqrt{E^2-\Delta_0^2}}{v_F\sqrt{E^2-\Delta_0^2}} = S(E) \tag{2.28b}$$

$$\mathcal{K}_3(E) = \int_E d\boldsymbol{k}_\parallel \frac{\Delta_0}{v_F\sqrt{E^2-\Delta_0^2}} = \frac{\Delta_0}{\sqrt{E^2-\Delta_0^2}} S(E)\,. \tag{2.28c}$$

Thus, $\mathcal{K}_2$ is once more non-divergent. The energy integrals over $\mathcal{K}_1^2$ and $\mathcal{K}_3^2$ result in a logarithmic divergence in the energy domain when $T \simeq E = \Delta$, giving rise to the Hebel-Slichter peak. Thus, one expects the maximum of the Hebel-Slichter peak to occur somewhat below T_c. This divergence is in general controlled in a real material by one or more of gap anisotropy, the presence of impurities or strong coupling effects [11, 12, 109].

This is in marked contrast to the accidental node case, where the peak results from a divergence in the momentum integral, independently of the energy value. The Hebel-Slichter peak observed in the isotropic case arises due to a divergence at a particular energy, as can also be seen in the density of states.

While the Hebel-Slichter peak seen for isotropic gaps is a direct result of the enhancement of the density of states at the gap, in the accidental node case, the effect is more subtle. For accidental nodes the gap velocity is not, in general, along the direction of the node (Fig. 2.2). This leads to additional terms in the spectral function and hence the density of states. These terms lead to the logarithmic divergence in $1/T_1T$ at $T \to T_c^-$. Thus the temperature dependence of the divergence for superconductors with accidental nodes is somewhat different from that of the true Hebel-Slichter peak.

2.4 Disorder and Electron-Electron Interactions

The classical s-wave Hebel-Slicter peak is controlled by disorder, electron-electron interactions, and gap anisotropy. These effects reduce the logarithmic divergence found analytically in the clean limit to a peak in the relaxation rate observed in conventional superconductors. Anisotropy in the gap function is necessarily present in the case of accidental nodes. Therefore, it is important to understand the effects of the former two effects in the current context.

If the energy integrals in Eq. (2.10) are evaluated, first using the delta function to constrain E_2 before using the strongly peaked nature of the spectral function to evaluate $E_1 \approx E_{\boldsymbol{k}}$,

$$\begin{aligned}\chi''_{+-}(\boldsymbol{q},\omega) = \sum_{\boldsymbol{k}} \Bigg\{ &\frac{1}{2}\left[1 + \frac{\xi_{\boldsymbol{k}}\xi_{\boldsymbol{k}+\boldsymbol{q}} + \Delta_{\boldsymbol{k}}\Delta_{\boldsymbol{k}+\boldsymbol{q}}}{E_{\boldsymbol{k}}E_{\boldsymbol{k}+\boldsymbol{q}}}\right][f(E_{\boldsymbol{k}}+\omega) - f(E_{\boldsymbol{k}})]\, A_{\boldsymbol{k}+\boldsymbol{q}}(E_{\boldsymbol{k}}+\omega) \\ &+\frac{1}{4}\left[1 - \frac{\xi_{\boldsymbol{k}}\xi_{\boldsymbol{k}+\boldsymbol{q}} + \Delta_{\boldsymbol{k}}\Delta_{\boldsymbol{k}+\boldsymbol{q}}}{E_{\boldsymbol{k}}E_{\boldsymbol{k}+\boldsymbol{q}}}\right][f(E_{\boldsymbol{k}}+\omega) - f(E_{\boldsymbol{k}})]\, A_{\boldsymbol{k}+\boldsymbol{q}}(-E_{\boldsymbol{k}}-\omega) \\ &+\frac{1}{4}\left[1 - \frac{\xi_{\boldsymbol{k}}\xi_{\boldsymbol{k}+\boldsymbol{q}} + \Delta_{\boldsymbol{k}}\Delta_{\boldsymbol{k}+\boldsymbol{q}}}{E_{\boldsymbol{k}}E_{\boldsymbol{k}+\boldsymbol{q}}}\right]\left[f(\omega-E_{\boldsymbol{k}}) - \bar{f}(E_{\boldsymbol{k}})\right] A_{\boldsymbol{k}+\boldsymbol{q}}(\omega-E_{\boldsymbol{k}})\Bigg\}, \end{aligned} \tag{2.29}$$

where the remaining spectral function is evaluated numerically by introducing a finite Lorentzian broadening, of width η,

$$A_{\boldsymbol{k}}(E) = \frac{\eta}{\eta^2 + (E_{\boldsymbol{k}} - E)^2}. \tag{2.30}$$

This is equivalent to introducing a finite quasiparticle lifetime to the familiar BCS susceptibility [11, 16, 104]

To evaluate the relaxation rate, Eq. (2.1), each of the nested momentum integrals (over $\boldsymbol{k}$ and $\boldsymbol{q}$) are performed numerically on a discrete grid, with a small finite frequency, which is then reduced until further variations no longer affect the result, allowing the limit $\omega \to 0$ to be approximated numerically.

In all of the following calculations, I take the temperature dependence of the gap to be given by the strong coupling BCS form:

$$\Delta_0(T) = \frac{\Delta_0}{2} \tanh\left(3\sqrt{\frac{T_c}{T} - 1}\right) \tag{2.31}$$

with $\Delta_0/2 = 2.5 k_B T_c = 0.25t$, typical of a number of unconventional superconductors [82, 102].

2.4.1 Orthorhombic model

In order to investigate this behaviour numerically, I consider a simple tight-binding model on an orthorhombic lattice, with nearest neighbour couplings (t_x and t_y) allowed to vary independently. The dispersion relation is thus

$$\varepsilon_{\boldsymbol{k}} = t_x \cos k_x + t_y \cos k_y, \tag{2.32}$$

with $a_x = a_y = 1$ (where a_x and a_y are the lattice constants in the x and y directions, respectively).

I consider two different symmetry states, a $\mathrm{d}_{x^2-y^2}$ gap, with nodes located at $k_y = \pm k_x$, given by

$$\Delta_{\boldsymbol{k}}^{(x^2-y^2)} = \frac{\Delta_0}{2}\left(\cos k_x - \cos k_y\right), \tag{2.33}$$

and a d_{xy} gap, with nodes located on the axes ($k_x = 0$ and $k_y = 0$)

$$\Delta_{\boldsymbol{k}}^{(xy)} = \Delta_0 \sin k_x \sin k_y. \tag{2.34}$$

In both cases, the maximum magnitude of the gap is $|\Delta_0|$. The model described by Eq. (2.32) has reflection symmetry about the k_x and k_y axes, making the nodes of the d_{xy} gap symmetry required and those of the $\mathrm{d}_{x^2-y^2}$ accidental. The presence or absence of a divergent peak in the $1/T_1T$ relaxation rate is dependent on the angle between the quasiparticle group velocity and the 'gap velocity' at the position of the node on the Fermi surface. In a material with symmetry required nodes, the angle vanishes ($\theta^{(xy)} = 0$ for this model) as does the average of the gap, resulting in an absence of the Hebel-Slichter peak.

For this model, the group velocity is given by

$$\mathbf{v}_{\boldsymbol{k}} = \begin{bmatrix} -t_x \sin(k_x) \\ -t_y \sin(k_y) \end{bmatrix}, \tag{2.35}$$

while, for the accidental node gap, the gradient gives

$$\boldsymbol{v}_{\boldsymbol{k}}^{(x^2-y^2)} = \begin{bmatrix} -\frac{\Delta_0}{2}\sin(k_x) \\ \frac{\Delta_0}{2}\sin(k_y) \end{bmatrix}. \tag{2.36}$$

Near the $k_x = k_y$ node of the $\mathrm{d}_{x^2-y^2}$ symmetry gap, I find, from Eq. (2.20),

$$\sin\theta^{(x^2-y^2)} = \frac{(t_x - t_y)}{\sqrt{2}\sqrt{t_x^2 + t_y^2}}, \tag{2.37}$$

which vanishes for $t_x = t_y$, because for a Fermi surface with C_{4v} symmetry the $\mathrm{d}_{x^2-y^2}$ gap has symmetry required nodes.

The above calculations estimate the parameters relevant to the divergence for specific 'd-wave' gap symmetries, as these are the focus in many families of unconventional superconductor, especially the cuprate and organic superconductors. If the nodes of the gap are accidental, by definition there is no preferred node placement on the Fermi surface and the above case is fine tuned. To explore the possibilities of other node locations, I include a finite isotropic component into the gap function. This results in a shift of the node position on the Fermi surface, while retaining the symmetry properties of the fully anisotropic gap. Additionally, such an isotropic component will alter the magnitude of the average gap on the Fermi surface, unless such effects are negated by the shifted node position. As an example, I consider a $\mathrm{d}_{x^2-y^2}$-wave gap with an isotropic component parametrised by a real coefficient, α, given by

$$\Delta_{\boldsymbol{k}}(\alpha) = \Delta_0\left[\alpha + (1-|\alpha|)\frac{\cos k_x - \cos k_y}{2}\right], \tag{2.38}$$

where $\alpha = \pm 1$ corresponds to the conventional isotropic gap, $\alpha = 0$ corresponds to the situations described in the previous section, and the absolute value of α is taken in the prefactor to the second term so that the magnitude of the maximum gap remains constant. A complex α is not considered, as this would break time reversal symmetry, which would be detectable by other methods [9, 42]. Hence,

$$\sin\left[\theta_\alpha(k_y)\right] = \frac{(t_x - t_y)\sin^2 k_y - \frac{4t_x\alpha}{|\alpha|-1}\left[\frac{\alpha}{|\alpha|-1} - \cos k_y\right]}{\sqrt{2}\sqrt{\left[(t_x^2+t_y^2)\sin^2 k_y - \frac{4t_x\alpha}{|\alpha|-1}\left(\frac{\alpha}{|\alpha|-1} - \cos k_y\right)\right]\left[\sin^2 k_y - \frac{2\alpha}{|\alpha|-1}\left(\frac{\alpha}{|\alpha|-1} - \cos k_y\right)\right]}}. \tag{2.39}$$

Notably, this expression is now explicitly dependent on k_y, and therefore the shape and size of the Fermi surface, unlike in the $\alpha = 0$ case considered previously. Additionally, it can be seen that, while the isotropic component may enhance the peak in the accidental node case, it can also potentially reduce the peak, depending on the relative magnitudes of the anisotropy t_y/t_x, the isotropic component α and the size and position of the Fermi surface, via k_y.

Eq. (2.39) also indicates that, even in the limit of vanishing anisotropy in the hopping parameters ($t_x \to t_y$), there arises a divergence in the relaxation rate due to the second term in the numerator for

$\alpha \neq 0$. This is entirely expected, as the gap has a non-zero average value over the Fermi surface for non-zero α. In terms of the angle θ, this can be interpreted as the isotropic component altering the nodal structure of the gap in the Brillouin zone, deforming the surface upon which nodes exist.

2.4.2 Robustness of the Hebel-Slichter-like peak

In Fig. 2.3, I show the results of the numerical calculations for the above model with $t_y = 0.4t_x$ for various gap symmetries at quarter filling. As expected, in the symmetry required ($\theta = 0$) case, $1/T_1T$ decreases immediately below T_c, never increasing above the Fermi liquid value. For the isotropic gap ($\alpha = 1$) and gaps with accidental nodes ($-1/2 \leq \alpha \leq 1/2$) the logarithmic divergence found in the pure case is controlled by the introduction of disorder for all gaps studied. Nevertheless, I find clear Hebel-Slichter-like peaks for all of the gaps with accidental nodes studied, indicating that the essential physics of this effect survives even quite strong disorder.

It is interesting to note that the size of the peak varies smoothly with α, cf. Eq. (2.38). In particular the case $\alpha = 0$, where there is no isotropic component in the gap, is not special. Indeed the peak is smaller for $\alpha < 0$ than it is for $\alpha = 0$. This is a straightforward consequence of the anisotropy of the Fermi surface. For $\alpha = -1/4$ the average gap over Fermi surface is less than the average for $\alpha = 0$. As α is further decreased this average must vanish and then increase again with the peak for $\alpha = -1$ being identical to that for $\alpha = 1$.

To better understand the dependence of the peak magnitude on the Fermi surface anisotropy I show the $\alpha = 0$ accidental node case for varying hopping anisotropy in Fig. 2.4. These numerical results should be compared to the analytical prediction that $\sin\theta \propto t_x - t_y$, Eq. (2.37).

At low temperatures increasing the anisotropy always increases $1/T_1T$, consistent with the changes in θ. For weak anisotropies the peak grows, consistent with this prediction. However, a maximum is reached at $t_y = 0.4t_x$, further increasing the anisotropy (decreasing t_y) decreases the peak immediately below T_c. This behaviour is not explained by the variation of θ.

The supression of the Hebel-Slichter-like peak for $t_y < 0.4t_x$ is due to the presence of a van Hove singularity in the density of states which approaches the the Fermi energy at quarter filling as t_y is reduced. Close to T_c the gap is small, $k_BT \gtrsim \Delta_0(T)$, and contours with energy $\sim \mu \pm k_BT$ wrap around a large segment of the Fermi surface. As a result, such contours include the region of the Fermi surface where the van Hove singularity is relevant, enhancing the spectral weight (density of states) in this region. This, in turn, affects the average of the gap within $\sim k_BT$ of the Fermi surface. In the example considered here, the superconducting gap in the vicinity of the van Hove singularity is of the minority sign of the gap, and thus the van Hove singularity reduces the average gap value over the Fermi surface. In the orthorhombic model, the van Hove singularity arises as the Fermi surface crosses the Brillouin zone boundary ($k_y = \pm\pi$), enhancing the contribution for $\Delta_{\boldsymbol{k}} < 0$. As the accidental nodes are on the $k_x = \pm k_y$ diagonals, the average of the gap within $\sim k_BT$ of the Fermi surface $\langle\Delta_{\boldsymbol{k}}\rangle_{\mu\pm k_BT} > 0$ is then reduced by the contribution due to the van Hove singularity.

Thus, for temperatures close to T_c, the enhancement of the spectral density at the van Hove point

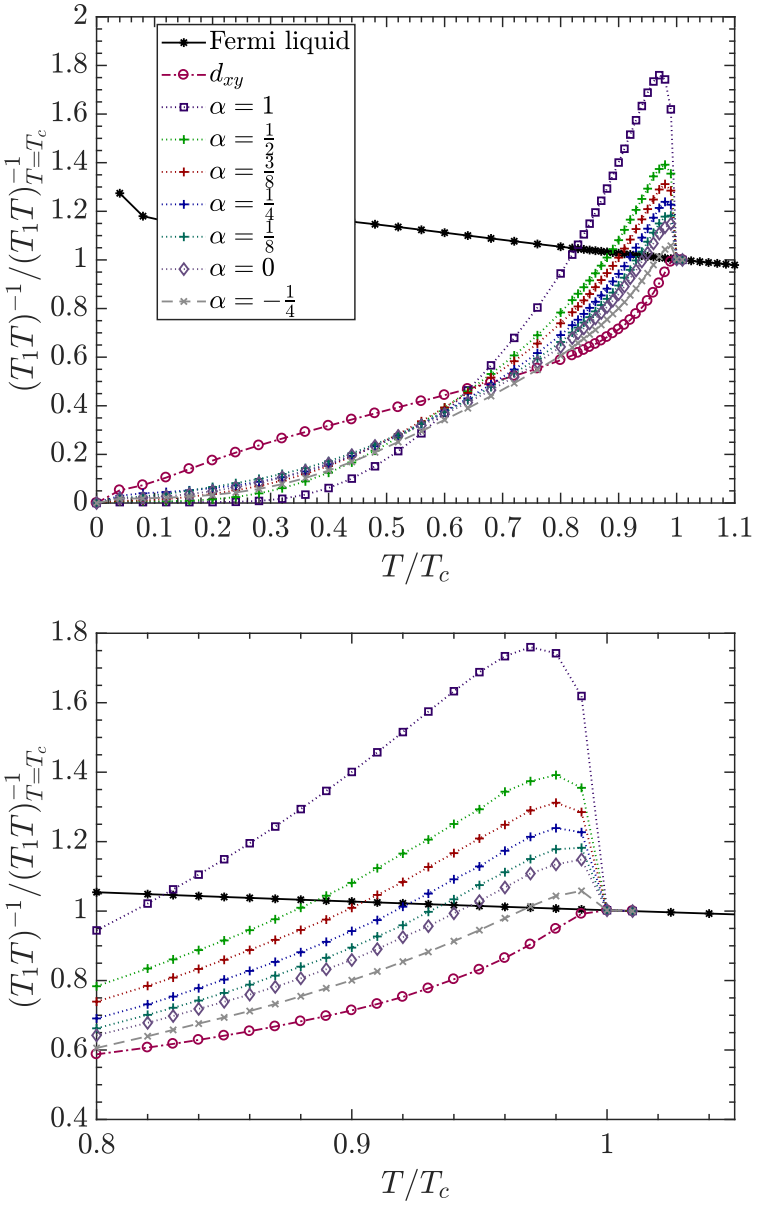

Figure 2.3: Peak structure in the presence of disorder. The divergence observed in the clean limit, Eq. (2.26a-2.26c), is controlled by the introduction of disorder, but a clear peak remains even in the limit of large disorder. Top: Orthorhombic model, Eq. (2.32), with $t_y = 0.4t_x$. The relaxation rates in both the isotropic s-wave ($\alpha = 1$) and symmetry required (d_{xy}) gap cases match conventional expectations with a Hebel-Slichter peak and its absence, respectively. In the accidental node case, a peak is present at $\alpha = 0$, which grows smoothly to the s-wave magnitude with increasing isotropic component. Furthermore, the variation of the peak is also smooth for $\alpha < 0$. Interestingly this decreases the peak magnitude, as the angle is decreased in this case, cf. Eq. (2.39). Bottom: The same data, close to T_c, highlighting the peak structure. For these plots, frequency $\omega = 5 \times 10^{-3}t$, Lorentzian broadening $\eta = 10^{-3}t$ (corresponding to a residual resistivity of order $\sim 10\ \Omega\,\mathrm{cm}$ for $a_x, a_y \sim 3$ Å, relevant to cuprates and other transition metal oxides, up to $\sim 100\ \Omega\,\mathrm{cm}$ for organic materials, with $a_x, a_y \sim 10$ Å, well above measured values in irradiated crystals [110]), number of grid points $N = 300^4$ (300 per dimension in the $\boldsymbol{q}$ and $\boldsymbol{k}$ integrals) and $\langle n \rangle = 0.5$ (quarter filling).

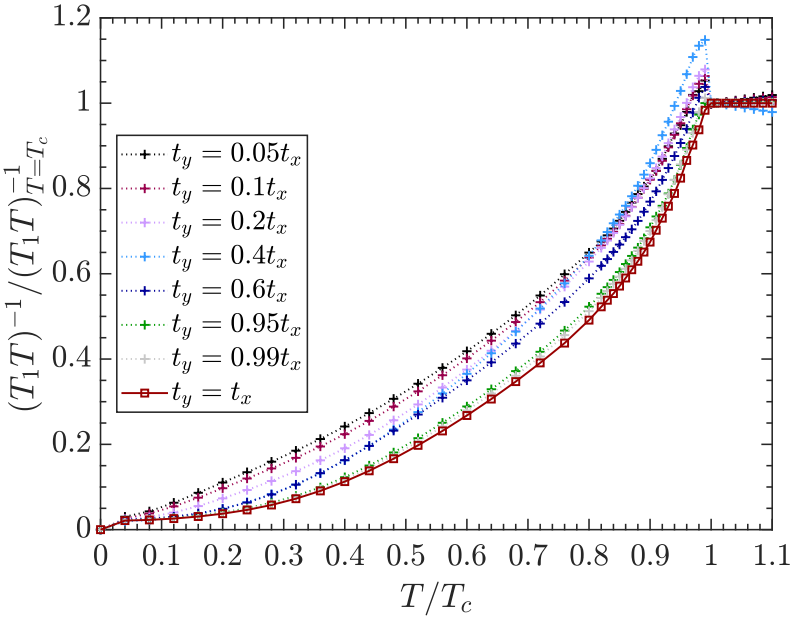

Figure 2.4: The effect of bandstructure anisotropy on the relaxation rate $1/T_1T$. Here I plot the calculated $1/T_1T$ for the orthorhombic model, Eq. (2.32), for various values of t_y/t_x for the case of accidental nodes with no isotropic component ($\alpha = 0$). The magnitude of the peak initially grows with increasing anisotropy, reaching a maximum value for $t_y = 0.4t_x$, before decreasing again. The initial growth arises from the increase in $\theta^{(x^2-y^2)}$, cf. Eq. (2.37). The suppression of the Hebel-Slichter-like peak for $t_y < 0.4t_x$ is caused by the proximity to a van Hove singularity when the Fermi surface crosses the Brillouin zone boundary. Notably, this behaviour is only seen close to T_c, where contours with energy $\sim k_BT$ wrap around a significant portion of the Fermi surface. At sufficiently low temperatures $1/T_1T$ also increases monotonically with increasing anisotropy (decreasing t_y/t_x). Note that in the normal state $1/T_1T$ depends on the hopping anisotropy, as visible from the spread of the data above T_c. Parameters: $\omega = 5 \times 10^{-3}t$, $\eta = 10^{-3}t$, $N = 300^4$ and $\langle n \rangle = 0.5$.

becomes significant, while it is less relevant at lower temperatures where the contours of energy $\sim k_BT$ are further from the van Hove point. Such behaviour is not apparent from variation of θ (see Sec. 2.3.1), as the binomial expansion in the derivation of Eqs. (2.23) fails due to the divergence of $1/v_F$ near the van Hove point. The importance of such singularities are, however, apparent from Eqs. (2.15).

In the low temperature regime, where the gap is maximal, the relevant contours are restricted to be near the nodes, well away from the van Hove singularity, and thus the relaxation rate increases smoothly as a function of decreasing t_y. In the regime of smaller anisotropy ($t_y \geq 0.4t_x$), the effects of the van Hove singularity are not strong enough to overwhelm the effects due to the variation of θ, and the peak size increases smoothly with decreasing t_y.

For all levels of anisotropy ($t_y < t_x$), the qualitative features observed in the $t_y = 0.4t_x$ case are largely unchanged, though at very low anisotropy ($t_y \gtrsim 0.95t_x$) the $\alpha = 0$ peak is strongly suppressed and not clearly resolved in the numerics. As stated above, in the limit $t_x = t_y$, the $d_{x^2-y^2}$ symmetry state possesses symmetry required, rather than accidental, nodes, and the peak vanishes. Fig. 2.5 displays a variety of gap functions in the square lattice at quarter filling, showing that both purely anisotropic

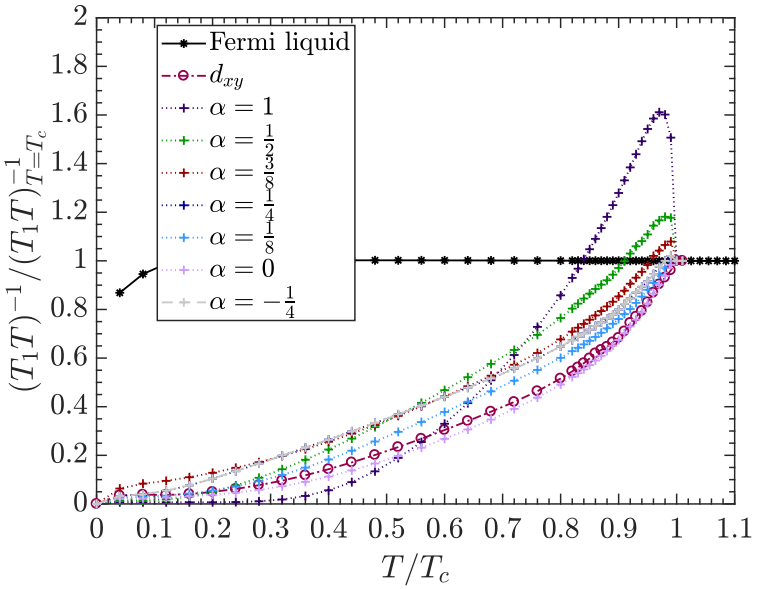

Figure 2.5: $1/T_1T$ in the square limit of the orthorhombic model, Eq. (2.32), $t_x = t_y$ at quarter filling. In this case, both the $d_{x^2-y^2}$ and d_{xy} gaps have symmetry required nodes, and the two symmetries are indistinguishable, with no peak is present for either case. Further, as can be seen in Eq. (2.39), a peak is only produced by introducing an isotropic component to the gap function.

gaps have symmetry required nodes, evidenced by the lack of a peak in $1/(T_1T)$ in either case.

Finally, to investigate the effects of including electron-electron interactions (which will be revisited in more detail in the following chapter), I present results for the random phase approximation. The RPA for the magnetic susceptibility is the sum over ladder diagrams [111], therefore this treatment includes the vertex corrections that are neglected above. Explicitly, I replace the magnetic susceptibility by

$$\chi_{RPA}(\boldsymbol{q},\omega) = \frac{\chi_{+-}(\boldsymbol{q},\omega)}{1 - U\chi_{+-}(\boldsymbol{q},\omega)},$$

where $\chi_{+-}(\boldsymbol{q},\omega)$ is the magnetic susceptibility (in either the superconducting or normal state, as appropriate) in the absence of these electron-electron interactions. For simplicity the treatment is limited to a Hubbard-like model with a contact interaction, U. The imaginary part of the RPA susceptibility is given by

$$\chi''_{RPA}(\boldsymbol{q},\omega) = \frac{\chi''_{+-}(\boldsymbol{q},\omega)}{\left[1 - U\chi'_{+-}(\boldsymbol{q},\omega)\right]^2 + \left[U\chi''_{+-}(\boldsymbol{q},\omega)\right]^2}, \tag{2.40}$$

As shown in Fig. 2.6, the qualitative features of the relaxation rate survive the inclusion of vertex corrections via the RPA susceptibility. Nevertheless it is important to note that the RPA treatment predicts that electron-electron interactions tend to suppress the Hebel-Slichter-like peak.

Beyond vertex corrections electron-electron interactions lead to a temperature dependence for the quasiparticle lifetime. Including such effects, for example via the phenomenological form described in [112], does not lead to significant changes in $1/T_1T$.

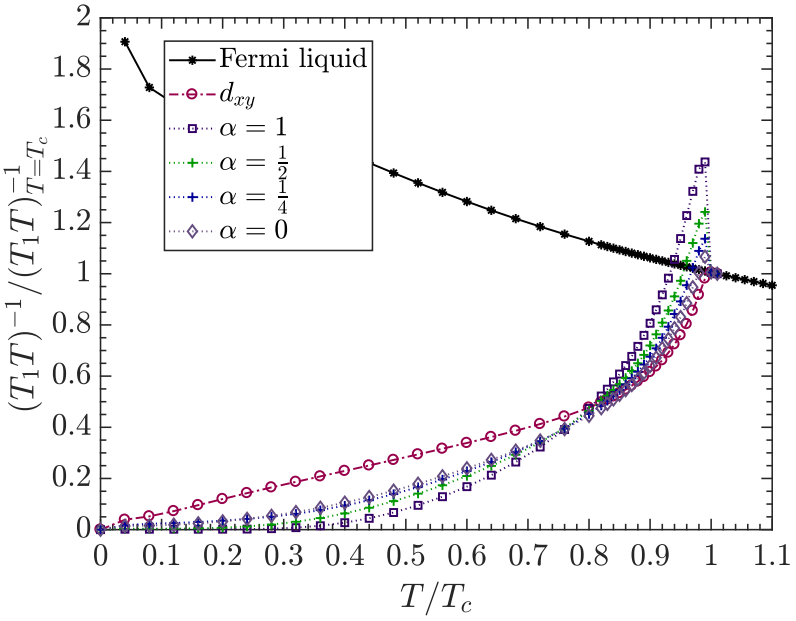

Figure 2.6: Robustness of the accidental node peak to electron-electron interactions. Orthorhombic model, Eq. (2.32), with $t_y = 0.4t_x$, and $U = 2t$. It is apparent here that the inclusion of electron-electron interactions via the RPA susceptibility does not alter the qualitative features of the previous figures. A clear Hebel-Slichter-like peak is still apparent for all values of α in the accidental node case, though the width of said peaks is reduced, even in the s-wave case ($\alpha = 1$). The Fermi liquid relaxation rate also acquires a much stronger temperature dependence. Parameters: $\omega = 5 \times 10^{-3}t$, $\eta = 10^{-3}t$, $N = 300^4$ and $\langle n \rangle = 0.5$.

2.5 Conclusions

I have shown that there is a logarithmic divergence in $1/T_1T$ in superconductors with accidental nodes as $T \to T_c$ from below. This contrasts with the true Hebel-Slichter peak that when $\Delta \sim T$, i.e. somewhat below T_c. The microscopic origin of this divergence is distinct from that of the Hebel-Slichter peak familiar from s-wave superconductors. One signature of this is that the observed peak is not controlled by the anisotropy in the gap, as it is in the Hebel-Slichter case. Indeed, I have shown that the peak is observed in a purely anisotropic gap. I have confirmed that both impurities and electron-electron interactions can control the divergence, but for reasonable values these effects do not completely suppress the effect.

Thus, I predict a Hebel-Slichter-like peak should be observed in superconductors with accidental nodes. This provides an important test for theories of superconductivity in low symmetry materials that predict the presence of accidental nodes.

Chapter 3

Vertex Corrections and NMR in Low-Symmetry Superconductors

As has been shown in the previous chapter, in a simple toy model including both self-energy (via a finite quasiparticle lifetime) and vertex corrections, up to a reasonable value of the interaction strength, does not drastically alter the form of the $1/T_1T$ relaxation rate. Specifically, I showed that both the Hebel-Slichter peak and its analogue in the presence of accidental nodes persistent in the presence of vertex corrections. In this chapter, I will explore how interactions, may remove prominent features of the relaxation rate, such as the Hebel-Slichter peak in a superconductor with an isotropic gap. I will also investigate the dependence of these characteristic features on the strength of the vertex corrections, within the random phase approximation (RPA).

3.1 Self-Energy, Vertex Corrections and Nuclear Magnetic Resonance

In order to discuss how vertex corrections affect the $1/T_1$ relaxation rate, it is important first to highlight why such effects are distinct from those arising due to the self energy and why such effects may remove the Hebel-Slichter peak. To this end, I will first highlight the different ways in which interactions enter into the calculation of material properties. In quantum many-body calculations, interactions can be broadly divided into two classes: those giving rise to the self-energy, and those responsible for vertex corrections [16, 95, 113]. The focus of this chapter is the effect of vertex corrections, but I will first discuss the self-energy, the influence of which is somewhat simpler conceptually.

In the language of diagrammatic perturbation theory (or quantum field theory), the self-energy accounts for renormalisation of the single particle propagator (Green's function) and is given by the sum of all one particle irreducible diagrams, i.e. all diagrams that cannot be split into smaller diagrams by the cutting of a single propagator line [95]. Vertex corrections, on the other hand, renormalise the interaction vertex, given by two particle irreducible diagrams, which cannot be divided into other

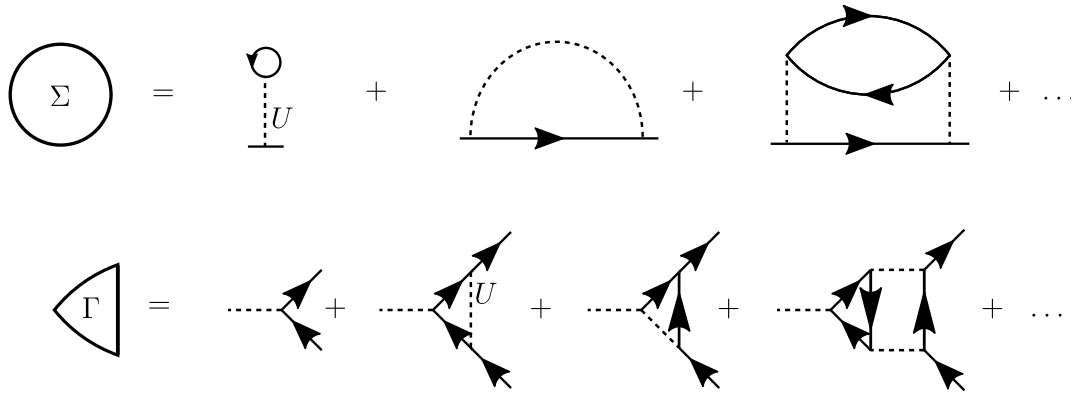

Figure 3.1: Diagrams contributing to the self-energy (top) and renormalised interaction vertex (bottom). Here, a solid line with an arrow indicates the propagator (or Green's funuctions), while a dashed line denotes an interaction (in this case a Hubbard-like point contact interaction of strength U). The diagrams contributing to the self-energy are one particle irreducible, and cannot be divided into self-energy like diagrams by cutting a single propagator line, while those contributing to the vertex corrections (the right three diagrams in the bottom line) cannot be divided into vertex-like diagrams by cutting two propagator lines. Note, the first diagram on the right side of the equation for the renormalised vertex is that of the unrenormalised (or bare) interaction vertex, with the following diagrams giving the vertex corrections.

diagrams by the cutting of any two propagator lines. Examples of these two classes of diagrams are shown in Fig. 3.1.

The spin susceptibility, which is central to the relaxation rate $1/T_1$, is given diagrammatically by a bubble diagram, with two propagator lines joined by interaction vertices (see Fig. 3.2) [16, 111]. In order to account for interactions in the susceptibility, both the self-energy (in the propagator lines) and vertex corrections (in one of the interaction vertices) must be included in the bubble diagram for the susceptibility [95, 111], as shown in the right hand diagram of Fig. 3.2. I will discuss, in the following, both of these effects and how they affect the properties of a Fermi liquid, before generalisation to the superconducting state, which is accomplished by replacing the scalar propagators of the Fermi liquid with Nambu-Gor'kov spinor propagators in the superconductor [20], as discussed in the introduction, Chapter 1.

3.1.1 Interactions in Fermi liquid theory

In the absence of interactions, the single particle propagator (Green's function), for a Fermi liquid, is given by [16, 95, 111, 113]

$$G_{\boldsymbol{k}}^{(0)}(\omega) = \frac{1}{\omega + i\eta - E_{\boldsymbol{k}}}, \tag{3.1}$$

where $E_{\boldsymbol{k}}$ is the energy of a quasiparticle with (crystal) momentum $\boldsymbol{k}$, and the limit $\eta \to 0^+$ is implied, which results in the imaginary part of the Green's function taking the form of a Dirac delta function,

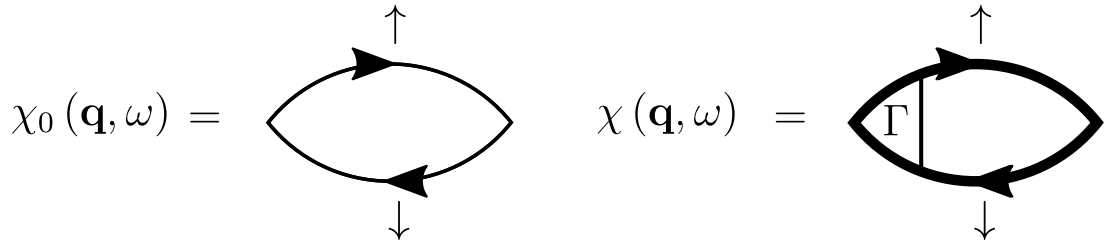

Figure 3.2: The diagrammatic form of the transverse spin susceptibility, which takes the form of a bubble diagram. On the left, the bare (non-interacting) susceptibility is given by a bubble made of two bare (electron) propagators (with the left and right vertices representing spin raising and lowering operators, respectively), while on the right the fully dressed susceptibility includes both self-energy effects, due to the renormalised (bold) propagators, and vertex corrections via the dressed vertex Γ (note, only one of the vertices is dressed by interactions to avoid double counting of contributions). The arrows indicate the spin states of the propagators, which has been omitted in the text for clarity.

peaked at $\omega = E_{\boldsymbol{k}}$. The susceptibility, in the absence of interactions, is given by [111]

$$\chi_0(\boldsymbol{q},\omega) = \lim_{i\omega_n\to\omega+i\eta}\sum_{\boldsymbol{k},i\Omega_m}\gamma^{i\omega_n,i\Omega_m}_{\boldsymbol{k},\boldsymbol{q}}G^{(0)}_{\boldsymbol{k}+\boldsymbol{q}}(i\omega_n)\,G^{(0)}_{\boldsymbol{k}}(i\omega_n+i\Omega_m)\,\gamma^{i\omega_n,-i\Omega_m}_{\boldsymbol{k},-\boldsymbol{q}}, \tag{3.2}$$

where the $i\omega_n$ are Matsubara frequencies, $G^{(0)}_{\boldsymbol{k}}(i\omega_n)$ is the thermal (Matsubara) Green's function, related to the real-frequency (retarded) Green's function by the analytical continuation $i\omega_n \to \omega + i\eta$, and $\gamma^{i\omega_n,i\Omega_m}_{\boldsymbol{k},\boldsymbol{q}}$ are the bare vertices (for the spin susceptibility $\gamma = S^{\pm}$, with subscripts and superscripts suppressed for clarity).

The influence of the self-energy on the Green's function is given by Dyson's equation, shown diagrammatically in Fig. 1.12, a recursive equation that takes into account multiple (one particle irreducible) interactions via the self-energy [95]. Algebraically, this equation is given by

$$\begin{aligned} G_{\boldsymbol{k}}(\omega) &= G^{(0)}_{\boldsymbol{k}}(\omega) + G^{(0)}_{\boldsymbol{k}}(\omega)\,\Sigma_{\boldsymbol{k}}(\omega)\,G_{\boldsymbol{k}}(\omega) \\ &= \frac{1}{\left[G^{(0)}_{\boldsymbol{k}}(\omega)\right]^{-1} - \Sigma_{\boldsymbol{k}}(\omega)}, \end{aligned} \tag{3.3}$$

where $\Sigma_{\boldsymbol{k}}(\omega) = \Sigma'_{\boldsymbol{k}}(\omega) + i\Sigma''_{\boldsymbol{k}}(\omega)$ is the self-energy and $G_{\boldsymbol{k}}(\omega)$ is the renormalised (dressed) Green's function. The dressed Green's function, including self-energy effects, is then

$$G_{\boldsymbol{k}}(\omega) = \frac{1}{\left[\omega - E_{\boldsymbol{k}} - \Sigma'_{\boldsymbol{k}}(\omega)\right] + i\left[\eta - \Sigma''_{\boldsymbol{k}}(\omega)\right]}. \tag{3.4}$$

The real part of the self-energy is responsible for the renormalisation of the single particle spectrum, while the imaginary part of the self-energy broadens the Green's function, resulting in a finite

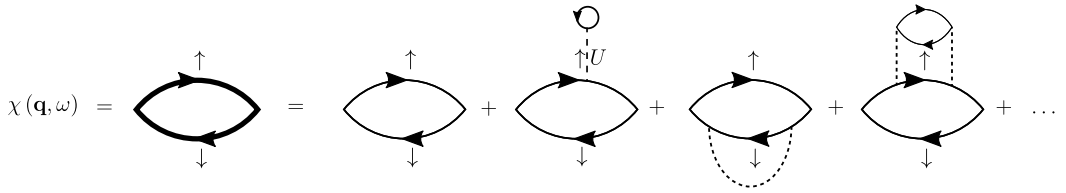

Figure 3.3: The spin susceptibility in the presence of self-energy effects due to interactions. In this case, the bare Green's functions in the non-interacting susceptibility, χ_0, are renormalised by interactions and replaced by dressed (renormalised) Green's functions.

quasiparticle lifetime (in the non-interacting case, the limit $\eta \to 0^+$ results in a propagtor with an infinite lifetime at $\omega = E_{\boldsymbol{k}}$ and vanishing lifetime otherwise) [113].

Lifetime effects on $1/T_1T$ have already been investigated to a degree in the previous chapter, where a finite quasiparticle lifetime was introduced into the numerical calculations. This served the purpose of both investigating the contribution of impurity effects on the Hebel-Slichter-like peaks and ensuring the stability of the numerical calculations. Including electronic interactions in the quasiparticle lifetime is not expected to alter the picture dramatically, introducing a temperature dependence to the lifetime but not significantly influencing the stability of the peak structure. In the presence of such effects, the spin susceptibility is given by diagrams such as those in Fig. 3.3, where incorporating self-energy effects has the overall effect of replacing the bare Green's functions in the bubble diagram defining χ_0 (the first diagram on the right hand side of the equality) with their dressed counterparts.

Vertex corrections, on the other hand, renormalise the coupling constants of the system, causing higher order corrections to experimental properties than those accounted for by the self-energy. Additionally, the algebraic form of such effects is more complicated. The Dyson equation that relates the dressed and bare Green's functions is replaced in the calculation of the renormalised interaction vertex by the Bethe-Salpeter equation, an integral equation which must be solved anew in each specific case, as it lacks a closed form solution like that given for the Dyson equation by Eq. (3.4). As such, it is a fairly common practice to neglect vertex corrections in low order calculations of system properties. For example, dynamical mean field theory, an extremely popular approximation scheme that successfully describes many phenomena in strongly correlated materials, famously neglects all vertex corrections in the conductivity by construction. Such neglect, however, is not well justified in any finite dimension, as highlighted by Baym and Kadanoff [114, 115], for physical conservation laws to be satisfied, vertex corrections must be taken into account.

In order to satisfy conservation laws, which take the form of Ward identities in quantum field theory [116], vertex corrections must be taken into account. It has been shown, for example, that neglect of the current vertex correction in calculations of the conductivity, is equivalent to taking a relaxation time approximation [95, 117]. While this approach is not inherently invalid, it neglects the structure of the scattering rate, and therefore the conductivity, with regards to direction, which may lead to inaccurate results. For the $1/T_1$ relaxation rate, there is a similar possibility, that neglecting vertex corrections may mask effects that lead to the destruction of the Hebel-Slichter peak for a fully

gapped superconductor [118, 119] or the related peak found in the previous chapter for a gap with accidental nodes.

The analysis in the previous chapter relied on the expression of the transverse spin susceptibility in terms of a convolution of single-particle propagators,

$$\chi_{+-}(\boldsymbol{q},\omega) = \lim_{i\omega_n\to\omega+i\eta} \sum_{\boldsymbol{k},i\Omega_m\bar{\sigma}\neq\sigma} G^{(0)}_{\boldsymbol{k}+\boldsymbol{q},\sigma}(i\omega_n)\, G^{(0)}_{\boldsymbol{k},\bar{\sigma}}(i\omega_n + i\Omega_m), \tag{3.5}$$

in which case the the relaxation rate can be expressed with the influence of the two Green's functions separated, due to a property of the convolution, $\sum_{\boldsymbol{q},\boldsymbol{k}} f(\boldsymbol{k}+\boldsymbol{q}) f(\boldsymbol{k}) = [\sum_{\boldsymbol{k}} f(\boldsymbol{k})]^2$,

$$\frac{1}{T_1 T} \propto \lim_{\omega\to 0} \frac{1}{\omega} \sum_{\boldsymbol{q}} \chi_{+-}(\boldsymbol{q},\omega) = \lim_{\omega\to 0} \frac{1}{\omega} \left[\sum_{\boldsymbol{k}} G^{(0)}_{\boldsymbol{k},\bar{\sigma}}(\omega) \right]^2 . \tag{3.6}$$

When the coherence factors of the Green's functions are taken into account, the sum $\sum_{\boldsymbol{k}} G^{(0)}_{\boldsymbol{k},\bar{\sigma}}(\omega)$ includes a term that gives the Fermi surface average of the superconducting gap, from which the Hebel-Slichter peak arises (as does the peak for a gap with accidental nodes). This argument hinges on the fact that the susceptibility depends on the momentum $\boldsymbol{q}$ solely through the convolution of the two Green's function. In the presence of vertex corrections, the susceptibility can no longer be expressed as a convolution of two Green's functions, due to the momentum dependence of the renormalised vertex. This vertex replaces one of the bare vertices in Eq. (3.2) (see Fig. 3.2 for a comparison of the diagrammatic forms of the bare and fully renormalised susceptibilities), where in Eq. (3.5) both bare vertices were given by the raising and lowering spin operators (with no momentum or frequency dependence).

Additionally, vertex corrections and strong coupling effects have previously, in the context of the cuprate high-temperature superconductors, been found capable of removing the Hebel-Slichter peak in a fully gapped superconductor [118–122], and the possibility of such effects must also be examined. In the context of the BEDT-TTF-based organic superconductors, this is particularly important, as there remains controversy over the gap symmetry, due to conflicting evidence found in different experiments [42, 63, 68, 76, 80–82, 87–89, 94], and electron-electron interactions are expected to be extremely strong. As a first approximation, I investigate the possibility of these effects by including vertex corrections via the random phase approximation.

3.1.2 Vertex Corrections via The Random Phase Approximation

The random phase approximation (RPA) is a form of generalised Hartree-Fock theory, with the dressed susceptibility given by a sum of ladder diagrams [111], as shown in Fig. 3.4. Algebraically, the

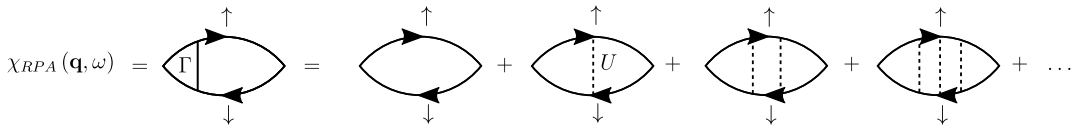

Figure 3.4: Diagrams contributing to the RPA dressed susceptibility. In these diagrams the vertices of the bubbles on the right of the equality are given by the spin raising and lowering operators $S^{\pm}$, and the ladder sum can be replaced by the closed form solution Eq. (3.7). Note that the algebraic form for the susceptibility is identical to that for the charge susceptibility, which is given diagrammatically by a sum of bubble diagrams rather than ladder diagrams [111].

approximation is given, for a Hubbard (i.e. momentum independent) interaction, by the infinite sum

$$\begin{aligned}
\chi_{\mathrm{RPA}}(\boldsymbol{q},\omega) &= \chi_0(\boldsymbol{q},\omega) + \chi_0(\boldsymbol{q},\omega)\,U\chi_0(\boldsymbol{q},\omega) + \chi_0(\boldsymbol{q},\omega)\,U\chi_0(\boldsymbol{q},\omega)\,U\chi_0(\boldsymbol{q},\omega) + \ldots \\
&= \chi_0(\boldsymbol{q},\omega)\left(1 + \sum_{i=1}^{\infty}\left[U\chi_0(\boldsymbol{q},\omega)\right]^i\right) \\
&= \chi_0(\boldsymbol{q},\omega)\left(1 + U\chi_{\mathrm{RPA}}(\boldsymbol{q},\omega)\right) \\
&= \frac{\chi_0(\boldsymbol{q},\omega)}{1 - U\chi_0(\boldsymbol{q},\omega)}.
\end{aligned} \tag{3.7}$$

The RPA is, by definition, a weak-coupling approximation, being a perturbative expenasion in the interaction [16, 111]. As such, some care must be taken to restrict use of the approximation to within the range of its validity. In particular, the denominator of Eq. (3.7) is only nonzero, for all momenta $\boldsymbol{q}$ for interaction strengths U below some upper limit U_c . If the interaction strength is sufficiently large, the susceptibility will diverge when $[1 - U\chi_0(\boldsymbol{q},\omega)] = 0$, undergoing a Stoner instability. In the low frequency regime in which the relaxation rate $1/T_1T$ is defined, this condition is dominated by the real part of the bare susceptibility, which tends to a constant value as $\omega \to 0$, while the imaginary part vanishes [100]. The susceptibility will then diverge when $\chi_0'(\boldsymbol{q},\omega) = 1/U$, allowing a definition of the critical value for the interaction strength as $U_c = 1/\max\left[\chi_0'(\boldsymbol{q},\omega)\right]$ and the RPA will be invalid for interaction strengths equal to or greater than this critical value, and less reliable in the vicinity of this critical interaction strength. This critical U would indicate a transition to an ordered state, typically an antiferromagnet [111].

More Sophisticated Approximations

It is worth noting, briefly, that there exists a vast zoo of approximation schemes for diagrammatic perturbation theory, with many such schemes taking vertex corrections into account in a more complex or sophisticated manner. The RPA explicitly neglects vertex corrections other than those given by ladder diagrams, neglecting, for example, diagrams including crossed interaction lines. In this simplest case of the RPA, any momentum dependence to the electronic interaction is also explicitly neglected (though this can be remedied by replacing U by some momentum dependent interaction $U_{\boldsymbol{q}}$ without altering the form of the susceptibility further). More sophisticated approximations may also take self-consistent effects into account, by utilising the dressed vertex, obtained from including the vertex corrections,

in calculating the self-energy, which may itself then be used to calculate the vertex corrections, until some self-consistency criteria is satisfied [123, 124].

In such approximation schemes, the divergence observed in the RPA dressed susceptibility at $U \sim 1/\max\left(\chi_0'\right)$ may be shifted to a different value of the interaction strength or even removed entirely, resulting in the possibility of much stronger interactions (relative to the material's bandwidth). However, any relevant effects due to vertex corrections that are observable in the RPA are representative, and likely to be relevant in more complicated approximation schemes. Thus, for the sake of simplicity, the discussion of vertex corrections is limited to the RPA.

3.1.3 Effects on the $1/T_1$ relaxation rate

As I have previously stated, the relaxation rate in the presence of vertex corrections is no longer given by a convolution of Green's functions, as it was in the previous chapter. When the susceptibility is dressed by vertex corrections due to the RPA, the relaxation rate, $1/T_1T$ is given by,

$$\begin{aligned}\frac{1}{T_1T} &= \lim_{\omega\to 0}\frac{2k_B}{\gamma_e^2\hbar^4}\sum_{\boldsymbol{q}}\left|A_H\left(\boldsymbol{q}\right)\right|^2\frac{\chi''_{RPA}\left(\boldsymbol{q},\omega\right)}{\omega}\\ &\propto \lim_{\omega\to 0}\sum_{\boldsymbol{q}}\frac{\chi''_{RPA}\left(\boldsymbol{q},\omega\right)}{\omega},\end{aligned} \tag{3.8}$$

where again, as in the previous chapter, the hyperfine interaction is approximated by a point contact interaction $[A_H\left(\boldsymbol{q}\right) = A_H]$ for simplicity. To fully understand the effects of vertex corrections on this calculation, it is necessary to resort to numerical calculations, but some insight may still be gained analytically. In the limit $\omega \to 0$, the nature of the Kramers-Kronig relation linking the real and imaginary parts of the susceptibility implies that the real part of the susceptibility is even with respect to frequency and the imaginary part odd [108], allowing the two to be approximated, at low frequencies by

$$\begin{aligned}\chi'_{+-}\left(\boldsymbol{q},\omega\right) &= B_{\boldsymbol{q}} + O\left(\omega\right),\\ \chi''_{+-}\left(\boldsymbol{q},\omega\right) &= C_{\boldsymbol{q}}\omega + O\left(\omega^2\right),\end{aligned} \tag{3.9}$$

in which case the relaxation rate is given by

$$\begin{aligned}\frac{1}{T_1T} &\propto \lim_{\omega\to 0}\sum_{\boldsymbol{q}}\frac{1}{\omega}\frac{\chi''_{+-}\left(\boldsymbol{q},\omega\right)}{\left[1-U\chi'_{+-}\left(\boldsymbol{q},\omega\right)\right]^2+\left[U\chi''_{+-}\left(\boldsymbol{q},\omega\right)\right]^2}\\ &= \lim_{\omega\to 0}\sum_{\boldsymbol{q}}\frac{C_{\boldsymbol{q}}}{\left[1-UB_{\boldsymbol{q}}\right]^2+\left[UC_{\boldsymbol{q}}\omega\right]^2}.\end{aligned} \tag{3.10}$$

Taking the limit $\omega \to 0$ gives

$$\frac{1}{T_1T} \propto \sum_{\boldsymbol{q}}\frac{C_{\boldsymbol{q}}}{\left[1-UB_{\boldsymbol{q}}\right]^2}, \tag{3.11}$$

which, if $U = 0$, reduces to the non-interacting result of the previous chapter, and, as expected, the divergence of the susceptibility is controlled by the real part of the susceptibility. In this case, the features relevant to the non-interacting result, which are given by the form of $C_{\boldsymbol{q}}$, are influenced by features of the static real part of the susceptibility. In particular, since the static susceptibility is bounded from below by $\chi'_{+-}(\boldsymbol{q}, \omega = 0) = B_{\boldsymbol{q}} = 0$, whenever $B_{\boldsymbol{q}}$ is large, the contribution to the relaxation rate is enhanced, while for $B_{\boldsymbol{q}}$ small, the contribution to the relaxation rate will be largely unchanged from the non-interacting contribution.

The static part of the susceptibility is given by

$$\begin{aligned} B_{\boldsymbol{q}} = \chi'_{+-}(\boldsymbol{q}, \omega = 0) \quad = \quad & \sum_{\boldsymbol{k}} \left\{ \frac{1}{2} \left[1 + \frac{\xi_{\boldsymbol{k}} \xi_{\boldsymbol{k}+\boldsymbol{q}} + \Delta_{\boldsymbol{k}} \Delta_{\boldsymbol{k}+\boldsymbol{q}}}{E_{\boldsymbol{k}} E_{\boldsymbol{k}+\boldsymbol{q}}} \right] \frac{f\left(E_{\boldsymbol{k}+\boldsymbol{q}}\right) - f\left(E_{\boldsymbol{k}}\right)}{E_{\boldsymbol{k}} - E_{\boldsymbol{k}+\boldsymbol{q}}} \right. \\ & + \frac{1}{4} \left[1 - \frac{\xi_{\boldsymbol{k}} \xi_{\boldsymbol{k}+\boldsymbol{q}} + \Delta_{\boldsymbol{k}} \Delta_{\boldsymbol{k}+\boldsymbol{q}}}{E_{\boldsymbol{k}} E_{\boldsymbol{k}+\boldsymbol{q}}} \right] \frac{\bar{f}\left(E_{\boldsymbol{k}+\boldsymbol{q}}\right) - f\left(E_{\boldsymbol{k}}\right)}{E_{\boldsymbol{k}} + E_{\boldsymbol{k}+\boldsymbol{q}}} \\ & \left. + \frac{1}{4} \left[1 - \frac{\xi_{\boldsymbol{k}} \xi_{\boldsymbol{k}+\boldsymbol{q}} + \Delta_{\boldsymbol{k}} \Delta_{\boldsymbol{k}+\boldsymbol{q}}}{E_{\boldsymbol{k}} E_{\boldsymbol{k}+\boldsymbol{q}}} \right] \frac{\bar{f}\left(E_{\boldsymbol{k}}\right) - f\left(E_{\boldsymbol{k}+\boldsymbol{q}}\right)}{E_{\boldsymbol{k}} + E_{\boldsymbol{k}+\boldsymbol{q}}} \right\}, \end{aligned} \tag{3.12}$$

and the structure of $B_{\boldsymbol{q}}$ can be seen to depend in a complicated manner on the bandstructure and gap symmetry, particularly with regards to approximate nesting of the Fermi surface (which may enhance the first term).

While the effect of the real part of the susceptibility can, in principle, enhance the features dominating the form of the relaxation rate (i.e. if $C_{\boldsymbol{q}}$ and $B_{\boldsymbol{q}}$ have similar structure, large contributions to the relaxation rate will be enhanced while smaller contributions will be unaffected), there is no *a priori* reason to expect such an arrangement, as the structures of $C_{\boldsymbol{q}}$ and $B_{\boldsymbol{q}}$ may differ drastically.

Additionally, it was established early in the study of unconventional cuprate superconductivity that a combination of strong coupling [120, 121] and RPA-like vertex corrections [118, 119] is capable of supressing the Hebel-Slichter peak in a conventional superconductor. It was later demonstrated, however, that such effects are not sufficient to match the low temperature behaviour of the relaxation rate [18, 104]. It is possible that, close to T_c, while the magnitude of the gap is small and the behaviour of the susceptibility dominated by the first term in Eq. (3.12), the nesting of the Fermi surface is sufficient to suppress the imaginary part of the susceptibility. In the low temperature limit, where the gap has reached its maximum magnitude, the enhancement of the first term may no longer dominate Eq. (3.12), allowing the temperature dependence at low temperatures to be determined by the imaginary part of the bare susceptibility, and therefore unaltered (beyond an overall factor) from the exponential temperature dependence of the non-interacting case for a fully gapped superconductor. This then is why the introduction of vertex corrections was insufficient, in the case of the cuprate high-temperature superconductors, to explain the temperature dependence of $1/T_1T$ with an isotropic superconducting gap.

While the destruction of the Hebel-Slichter peak is by no means an entirely new phenomenon, it has not, to our knowledge, been discussed in the context of the organic superconductors. This is of particular interest due to the long standing conflicts between the gap structures extracted from different experiments [63, 80–82, 94], as well as first principles theoretical calculations [62, 74, 75, 78], on these

materials. Additionally, the strength of electronic interactions in these materials is, to a degree, tunable by the application of external pressure. In such materials, it may be possible to alter the interaction strength and determine the gap structure by measuring $1/T_1T$ and comparing both the temperature and interaction dependence of the relaxation rate to predictions.

3.2 Effective models

In this section, I briefly review the various effective models and gap functions used to numerically examine the effects of the RPA vertex corrections on $1/T_1T$.

3.2.1 The orthorhombic model and Van Hove singularities

In the previous chapter, a tight-binding model for an orthorhombic lattice was introduced, with dispersion given by

$$\xi_{\boldsymbol{k}} = t_x \cos(k_x) + t_y \cos(k_y) - \mu. \tag{3.13}$$

This model was used to test the robustness of the Hebel-Slichter-like peak due to the presence of accidental nodes in the superconducting gap, finding it resilient to disorder and intermediate strength electron-electron interactions (as quantified by the RPA vertex corrections). In this chapter, the effects of the RPA on the relaxation rate will be examined in more detail.

3.2.2 Effective models for single band β-(BEDT-TTF)$_2X$

In the single band BEDT-TTF-based organic superconductors, the band structure is well approximated by a tight binding model with next-nearest-neighbour hopping along a single diagonal [125–128], as a result of the arrangement of dimer sites in the unit cell (see Fig. 3.5),

$$\xi_{\boldsymbol{k}} = t_x \cos(k_x) + t_y \cos(k_y) + t' \cos(k_x - k_y), \tag{3.14}$$

where the dispersion is measured relative to the chemical potential. The inequivalent next-nearest neighbour couplings give rise to the anisotropy of the model, reducing the rotational symmetry to C_2 from the C_4 symmetry of the square lattice.

3.2.3 Multiple bands: κ-(BEDT-TTF)$_2X$

In the the multi-band (κ polymorph) organic superconductors, an additional energy scale is introduced, which arises from the more complicated structure of the hopping integrals. In these materials, the orientation of the dimer units results in an alternating pattern of nearest neighbour hopping integrals in both the x and y directions, which causes the magnetic breakdown observed in cyclotron orbits under high magnetic fields [125, 128]. As a result, the unit cell of the single band model for the β polymorph is doubled, halving the Brillouin zone and giving rise to the second Fermi surface sheet (this can be

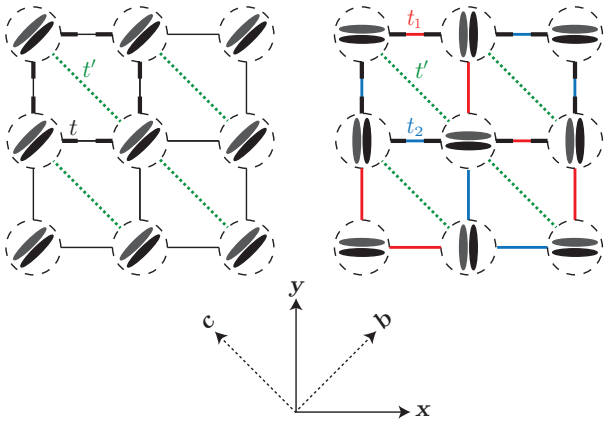

Figure 3.5: Left: model for β-(BEDT-TTF)$_2X$. Right: κ-(BEDT-TTF)$_2X$. Bottom: Alignment of axes. b (a) and c here are crystallographic axes for the monoclinic (orthorhombic) organic materials, with the model axes x and y rotated by 45 degrees. The thick dashed line represents the unit cell, the size of which is doubled in the κ model relative to the β model due to the rearrangement of the dimer orientations.

interpreted as a result of the new Brillouin zone boundary intersecting the original β polymorph Fermi surface) [75, 128]. This new sheet is concave, or hole-like, as opposed to the original convex sheet. The quasiparticle dispersion is given by

$$\xi_{\boldsymbol{k},\pm} = t' \cos\left(k_x - k_y\right) \pm t\sqrt{\left[\cos\left(k_x\right) + \cos\left(k_y\right)\right]^2 + \left(\frac{\delta_t}{t}\right)^2 \left[\sin\left(k_x\right) + \sin\left(k_y\right)\right]^2}\,, \tag{3.15}$$

where $t = t_x = t_y = (t_1 + t_2)/2$ and $\delta_t = (t_1 - t_2)/2$. The band structure of these materials may be reasonably well approximated by a model with the pattern of hopping elements seen on the right in Fig. 3.6. In this model, the new parameter δ_t controls the magnitude of the magnetic field required to induce the 'magnetic breakdown' cyclotron orbit. Additionally, an increase in this parameter can increase the nesting of the quasi-one-dimensional sheets in κ-(BEDT-TTF)$_2X$ Fermi surface seen in Fig. 3.6, by reducing the curvature of these sheets, as shown in Fig. 3.7

3.2.4 Gap Symmetries

In the previous chapter, I made use of simple models of the superconducting gap symmetry, focusing on the pure 'd-wave' states, the d_{xy} symmetry

$$\Delta_{\boldsymbol{k}}^{(\mathrm{xy})} = \Delta_0 \sin\left(k_x\right) \sin\left(k_y\right), \tag{3.16}$$

and $\mathrm{d}_{x^2-y^2}$ symmetry states

$$\Delta_{\boldsymbol{k}}^{(\mathrm{x^2-y^2})} = \frac{\Delta_0}{2}\left[\cos\left(k_x\right) - \cos\left(k_y\right)\right]. \tag{3.17}$$

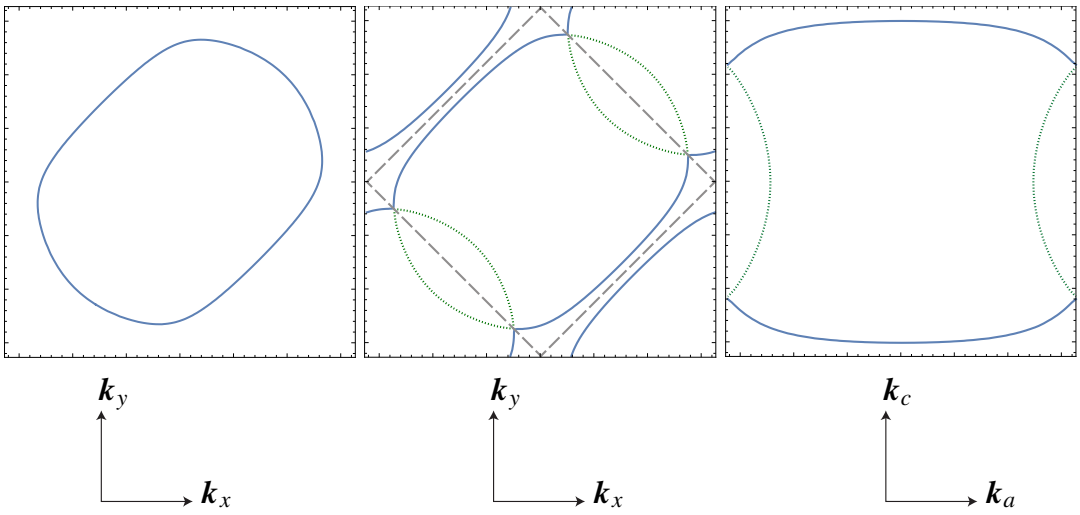

Figure 3.6: Left: Fermi surface for the effective model of β-(BEDT-TTF)$_2X$ in Fig. 3.5. Middle: Fermi surface for the effective model of κ-(BEDT-TTF)$_2X$ in Fig. 3.5, with dotted lines showing the second band arising due to the doubled unit cell. Right: the Fermi surface for κ-(BEDT-TTF)$_2X$ in the reduced Brillouin zone. The doubling of the unit cell in the κ polymorph results in a reduction of the first Brillouin zone, shown by the dashed lines in the middle figure, giving the two band Fermi surface even in the limit $\delta_t \rightarrow 0$.

In the case of the orthorhombic model, the '$d_{x^2-y^2}$-wave' state transforms as the trivial representation of the point group, and as such is able to mix freely with the isotropic 's-wave' gap, leading to a general form of the gap function in the presence of accidental nodes

$$\Delta_{\boldsymbol{k}}^{(\mathrm{x^2-y^2})}(\alpha) = \Delta_0 \left[\alpha + (1 - |\alpha|) \frac{\cos(k_x) - \cos(k_y)}{2} \right]. \tag{3.18}$$

In the case of the effective models described above for the BEDT-TTF based organic superconductors, the C_4 symmetry is lowered to C_2 by the anisotropy of the next nearest neighbour hopping t', and as such, the high-symmetry axes of the model lie on the diagonals. Thus, for these models, the '$d_{x^2-y^2}$-wave' state has the symmetry required nodes, and the general form of the gap with accidental nodes ('s+d_{xy}-wave' symmetry) is given by

$$\Delta_{\boldsymbol{k}}^{(\mathrm{xy})}(\alpha) = \Delta_0 \left[\alpha + (1 - |\alpha|) \sin(k_x) \sin(k_y) \right]. \tag{3.19}$$

Schmalian [74] has proposed, on the basis of self-consistent RPA calculations of the gap function in κ-(BEDT-TTF)$_2X$, an anisotropic gap with symmetry required nodes. To maintain the periodic translational invariance, the $d_{x^2-y^2}$-wave gap (with symmetry required nodes) above, must possess nodes on the boundary of the reduced Brillouin zone (giving a total of eight nodes on the Fermi surface). Strictly speaking, such a gap is more readily defined as the d_{xy}-wave state in the reduced Brillouin zone (the rightmost panel of Fig. 3.6). I will however, attempt to use consistent notation between the β and κ polymorphs and therefore define our labels as those in the extended Brillouin zone, where the Fermi surface has axes of reflection symmetry along the diagonals. As such, the symmetry required gap in the extended Brillouin zone is given by

$$\Delta_{\boldsymbol{k}}^{(\mathrm{x^2-y^2})} = \Delta_0 \frac{\cos(2k_x) - \cos(2k_y)}{2}, \tag{3.20}$$

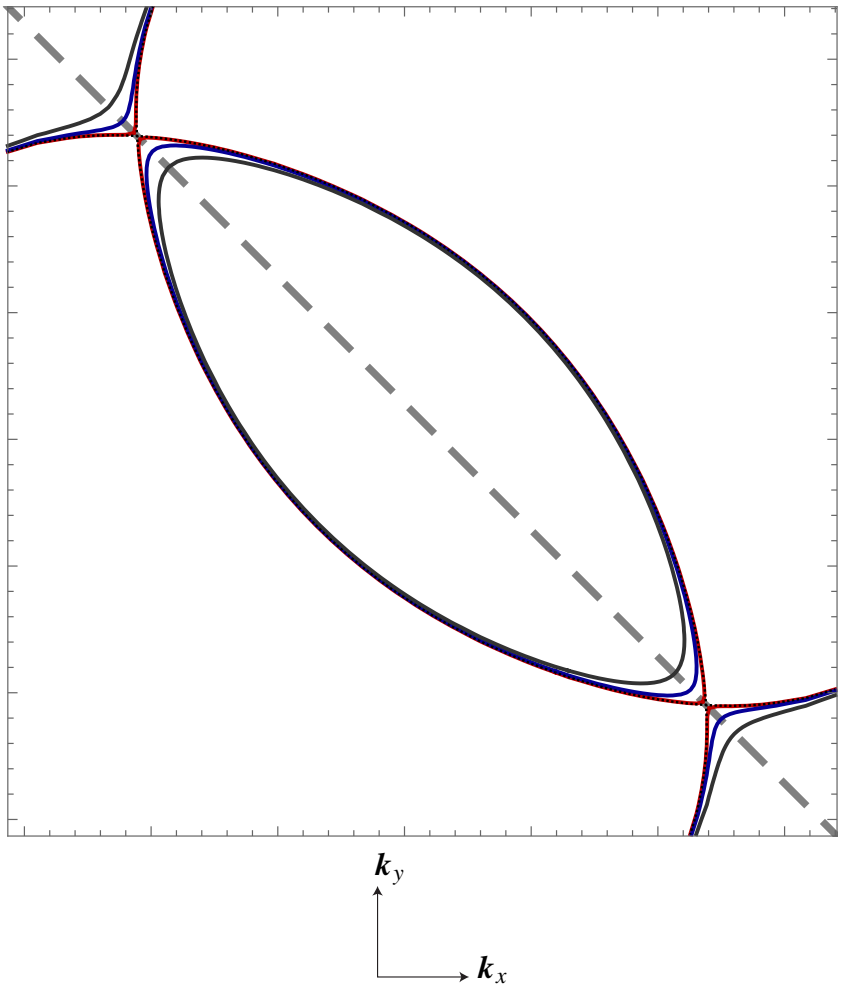

Figure 3.7: Fermi surface for the effective model of κ-(BEDT-TTF)$_2X$ in Fig.3.5, near the boundary of the reduced Brillouin zone (grey, dashed) for $\delta_t = 0$ (black, dotted) $\delta_t = 0.01t$ (red), $\delta_t = 0.05t$ (blue) and $\delta_t = 0.1t$ (black, solid). As the magnitude of δ_t is increased, the gap between bands at the reduced Brillouin zone boundary increases, as does the nesting of the quasi-one-dimensional Fermi surface sheets, as a result of the decreasing curvature of these sheets.

where the additional factors of two in the cosine functions are responsible for the nodes on the boundary of the reduced Brillouin zone (given by $k_x \pm k_y = \pm\pi$ in the extended Brillouin zone). The gap proposed independently not only by Schmalian [74], but also Kondo and Moriya [129] and Kino and Kontani [127], is defined, however, in the expanded Brillouin zone, and does not possess these additional nodes (see Fig. 3.8 for a comparison of these two gap functions). Additionally, the sign of the gap varies between the two bands, ensuring the gap preserves the periodicity of the Brillouin zone only when the β-like larger Fermi surface is considered (i.e. when travelling across a boundary on the Fermi surface, one must change bands). Such a gap function is given by

$$\Delta_{\boldsymbol{k},i}^{\left(\bar{x}^2-\bar{y}^2\right)} = \gamma_i \Delta_0 \frac{\cos\left(k_x\right) - \cos\left(k_y\right)}{2}, \tag{3.21}$$

where $\gamma_i = \pm 1$ changes the sign of the gap dependent on the band index i. It is important to note that this gap maintains the periodicity of the reduced Brillouin zone only when the gap between the Fermi surface sheets at the boundary is very small, and is therefore unlikely to be applicable when the

parameter δ_t is nonzero, as it is in most real materials.

Kuroki *et al.* [75] highlighted the fact that such a gap, when viewed in the reduced Brillouin zone, results in a discontinuous change in the sign of the superconducting gap across the (reduced) Brillouin zone boundary, while remaining on a single band. The authors went on to highlight the importance of the choice of effective model in determining the gap function from RPA-like approximations, finding a gap with accidental nodes when making use of a model based on the BEDT-TTF monomers, rather than effective models like those above based on a dimerised picture. The distinction between the two effective models will be revisited in more detail in Chapter 4.

Recently, Guterding *et al.* [62, 63] utilised a combination of *ab initio* methods and fitting to experimental tunnelling spectra to propose a more complicated gap symmetry with eight accidental nodes, consisting of a combination of a d_{xy} component and extended s-wave components,

$$\Delta_{\boldsymbol{k}} = \Delta_0 \left\{ c_{s_1} \left[\cos\left(k_x\right) \cos\left(k_y\right) \right] + c_{s_2} \left[\cos\left(2k_x\right) + \cos\left(2k_y\right) \right] + c_d \left[\sin\left(k_x\right) \sin\left(k_y\right) \right] \right\}, \quad (3.22)$$

where the coefficients denoting the various components are allowed to vary with temperature, and extracted from a fit to scanning tunnelling spectroscopy measurements.

It is worth noting that a gap with symmetry required nodes has been predicted in a number of strongly correlated models for superconductivity in the organic superconductors. A resonating valence bond theory calculation of the superconductivity in an anisotropic triangular lattice model (i.e. $\delta_t = 0$) found a gap with symmetry required nodes in a realistic parameter regime for the BEDT-TTF superconductors [7, 25, 77]. In such a model, increasing the frustration, t'/t, drives the superconductivity into first a mixed symmetry state with a complex order parameter (termed 'd+*i*d'-wave) as the frustration approaches $t'/t = 1$ and the d_{xy}-wave gap component becomes finite. If the frustration is increased further, with $t'/t \gtrsim 1.1$, the $d_{x^2-y^2}$ component becomes suppressed, with the gap purely consisting of the d_{xy} (+ s) -wave component. For the superconducting κ-(BEDT-TTF)$_2X$ materials, the anisotropy is typically on the order of $t'/t \leq 0.7$ [130], placing them firmly within the regime where calculations predict a $d_{x^2-y^2}$-wave gap, with symmetry required nodes [77].

For ease of reference, in Appendix A, I provide a summary of the parameters of the effective models considered in this chapter and Chapter 4, along with the critical interaction strength for each model, which has been calculated numerically during the analysis. Additionally, in Appendix A, I list the models and the relevant labels for gap functions with accidental and symmetry required nodes.

3.3 Numerical Results

In this section, I report numerical calculations of the $1/T_1$ relaxation rate in the models discussed in the previous section for a variety of gap symmetries.

3.3.1 Fully gapped superconductors

The central result of this chapter is highlighted in Fig. 3.9, in which the temperature dependence of $1/T_1T$ is plotted for an effective model of κ-(BEDT-TTF)$_2X$ with isotropic s-wave superconductivity,

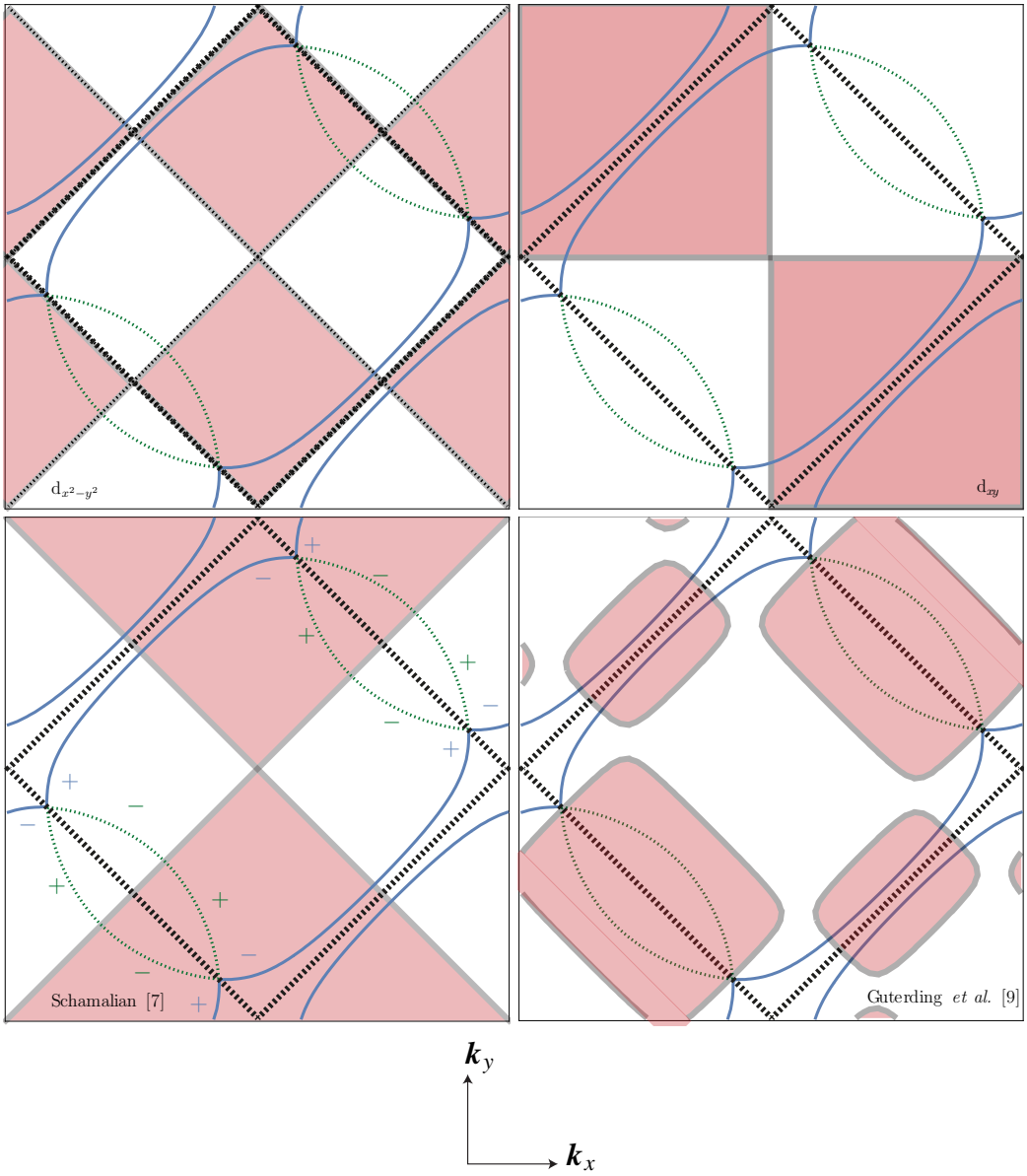

Figure 3.8: Gap functions in κ-(BEDT-TTF)$_2X$, with nodes given by black dotted lines. Top left: symmetry required '$d_{x^2-y^2}$-wave' gap with nodes on the boundary of the reduced Brillouin zone (grey dashed line). Top right: d_{xy}-wave anisotropic gap with accidental nodes. Bottom left: the gap function proposed by Schamalian [74], a '$d_{x^2-y^2}$-wave' gap without nodes on the boundary of the reduced Brillouin zone, and changing sign between bands (blue solid and green dotted lines). Bottom right: the complicated gap function proposed by Guterding *et al.* [62, 63] with eight accidental nodes.

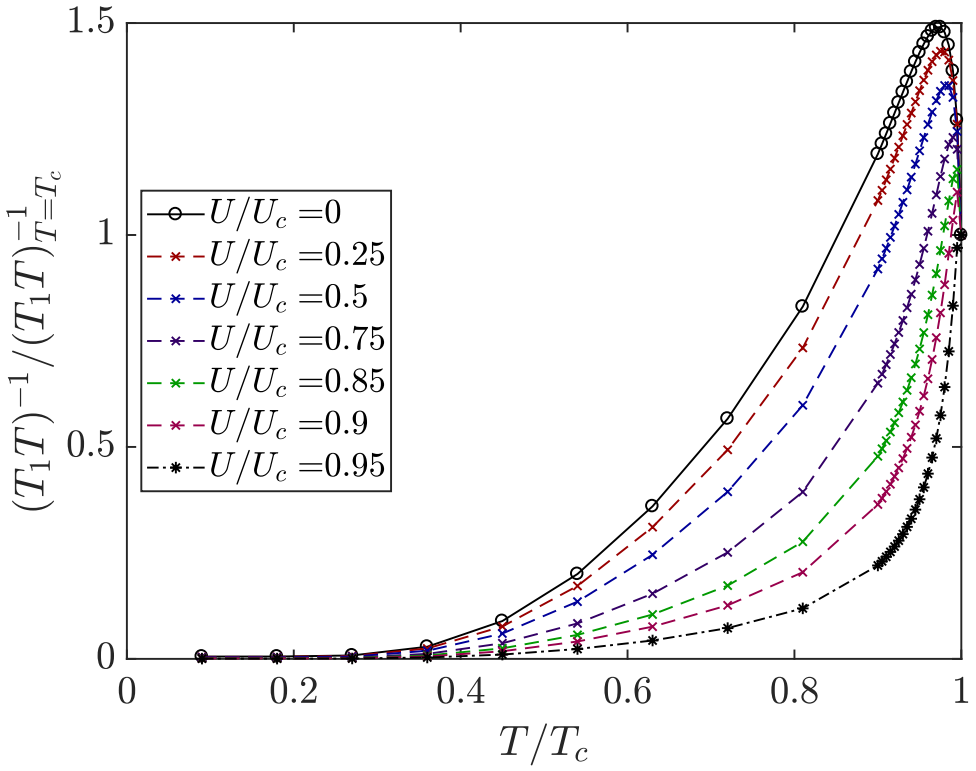

Figure 3.9: The temperature dependence of $1/T_1T$, with increasing interaction strength in a dimerised model of s-wave superconductivity in κ-(BEDT-TTF)$_2X$, with $t' = 0.5t$, $\delta_t = 0.05t$. In the limit of strong vertex corrections, the peak narrows and eventually vanishes entirely. While the peak only disappears for $U \geq 0.9U_c$ (see Fig. 3.11), the narrowing and suppression of the peak at lower interaction strengths may be sufficient to disguise the Hebel-Slichter peak in experiments. In these calculations, $U_c \sim 12.4t$, $\eta = 5 \times 10^{-3}t$, and $\Delta_0/2 = 2.5k_BT_c$. The critical interaction strengths for the all of the models considered in this chapter can all be found in Appendix A.

for various interaction strengths. As the interaction strength is increased, the clear Hebel-Slichter peak observed in the non-interacting limit is suppressed and ultimately vanishes near the critical interaction strength, U_c. Even for interaction strengths well below this limit, the vertex corrections narrow the peak, as well as reduce the peak magnitude. Depending on the sensitivity of the experiment, as well as the stability and range of temperatures, this narrowing alone may be sufficient to obscure the presence of such a peak in real materials.

Additional figures, showing the temperature dependence of $1/T_1T$ for a variety of effective models and gap functions, can be found in Appendix B. In all cases, the vertex corrections are sufficient, for large interaction strengths, to suppress any peaks in the relaxation rate, but do not significantly alter the temperature dependence at low temperatures. A conclusive determination of the gap structure based on the $1/T_1$ relaxation rate then requires a comparison between experiment and theory for both at the behaviour of $1/T_1$ at low temperatures and the presence or absence of a peak immediately below T_c. A detailed comparison with experimental $1/T_1$ data for κ-Br at all temperatures below T_c is the focus of the next chapter.

Understanding how bandstructure effects, particularly the anisotropy and the presence of Van Hove singularities, affect the Hebel-Slichter peak and its destruction by vertex corrections is also of interest.

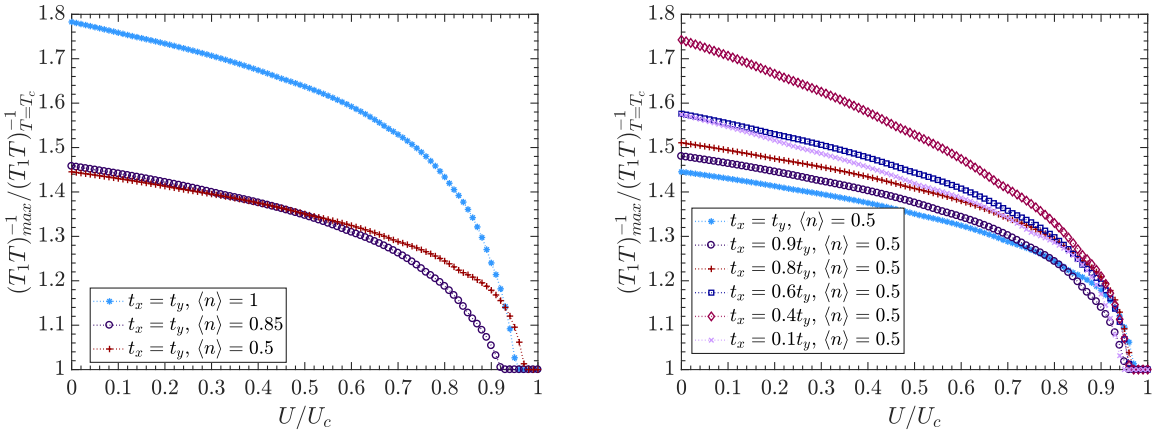

Figure 3.10: The influence of anisotropy and Van Hove singularities on the peak value of the $1/T_1$ relaxation rate in a fully gapped superconductor, in the presence of vertex corrections. Left: the relaxation rate calculated for a square lattice at various fillings, $\langle n\rangle = 0.5$, $\langle n\rangle = 0.85$, and $\langle n\rangle = 1$, at which point the Van Hove singularity is at the Fermi energy. Right: the relaxation rate for the orthorhombic model with $\langle n\rangle = 0.5$ at various levels of anisotropy. Clearly, the proximity of the Van Hove singularity to the Fermi surface influences the magnitude of the peak, with a significant enhancement when $\langle n\rangle = 1$ (half-filling). Additionally, the proximity of the singularity seems to influence the robustness of the peak to the effects of the RPA vertex corrections in a complex manner. The anisotropy of the model, on the other hand, has a minimal effect on the relaxation rate. In such a system, where the superconducting gap, being isotropic, has the effect of suppressing the influence of the band structure and Fermi surface symmetry. In all cases here, the Hebel-Slichter peak vanishes close to U_c. In these calculations, $\eta = 5 \times 10^{-3}t$ and $\Delta_0/2 = 2.5k_BT_c$. For the Van Hove calculations $U_c \sim 18.9t$, $9.2t$ and $6.2t$ in order of increasing filling, while for the orthorhombic model $U_c \sim 18.9t$, $17.7t$, $16.5t$, $14.0t$, $11.5t$ and $10.4t$ in order of decreasing anisotropy t_y/t_x.

In Fig. 3.10, I investigate how the magnitude of the Hebel-Slichter peak (measured by the maximum value of $1/T_1T$ for $T \leq T_c$) varies with these parameters.

The overall magnitude of the Hebel-Slichter peak, at all interaction strengths, displays a non-monotonic dependence on the anisotropy. As in the case of the peak seen in the previous chapter for an anisotropic gap with accidental nodes, this is largely due to the influence of Van Hove singularities that approach the Fermi energy as the anisotropy is increased. In contrast, the resilience of the peak to vertex corrections is largely independent of anisotropy. In all cases, the peak is reduced at a similar rate and vanishes around $U \gtrsim 0.95U_c$.

The proximity of Van Hove singularities to the Fermi surface has a more dramatic influence on the Hebel-Slichter peak, with the peak enhanced at half-filling ($\langle n\rangle = 1$), when the Van Hove resides at the Fermi energy. Additionally, proximity to the Van Hove singularity affects the magnitude of the interaction strength at which the peak vanishes in a non-monotonic way, with the peak vanishing at a weaker interaction strength for $\langle n\rangle = 0.85$ than for quarter filling ($\langle n\rangle = 0.5$) or the Van Hove filling ($\langle n\rangle = 1$). The critical value of the interaction strength does appear to vary simply with the proximity to the Van Hove singularity, however, decreasing significantly as the singularity approaches the Fermi energy.

In Fig. 3.11 I examine the effects of vertex corrections on the Hebel-Slichter peak in effective models for BEDT-TTF based organic superconductors. In these models, the magnitude of the peak

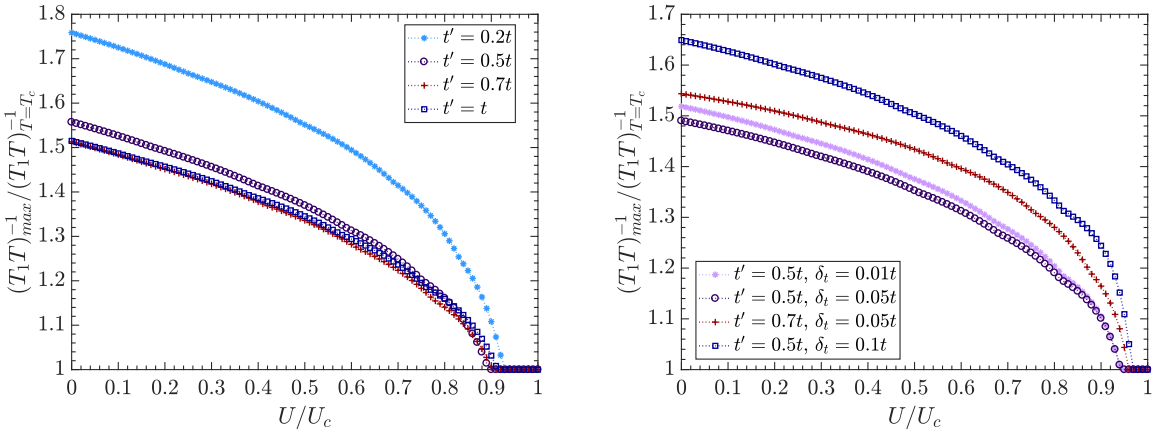

Figure 3.11: The maximal value of $1/T_1T$, with increasing interaction strength in a dimerised model of s-wave superconductivity in BEDT-TTF based superconductors for various model parameters. Left: the relaxation rate in the single band β-(BEDT-TTF)$_2X$ for varying levels of anisotropy. Right: the relaxation rate in the two band κ-(BEDT-TTF)$_2X$, varying anisotropy and the magnetic breakdown energy scale δ_t. As in Fig. 3.10, the effects of anisotropy on the relaxation rate are minimal, though the interaction strength required to remove the Hebel-Slichter peak does vary non-monotonically as a function of the next-nearest neighbour coupling t'. The influence of the magnetic breakdown gap energy scale on the behaviour of the relaxation rate is less significant than the anisotropy t', with the Hebel-Slichter peak proving robust to RPA vertex corrections up to $U \geq 0.9U_c$ in all cases. In these calculations, $\eta = 5 \times 10^{-3}t$ and $\Delta_0/2 = 2.5k_BT_c$. For the β polymorph calculations $U_c \sim 4.5t$, $6.0t$, $7.3t$ and $8.7t$, in order of increasing t'/t, while for the κ polymorph $U_c \sim 12.4t$ for $t' = 0.5t$ and $U_c \sim 13.2t$ for $t' = 0.7t$ (δ_t does not significantly influence U_c).

again depends on the model parameters in a non-trivial way, but the behaviour of the peak as vertex corrections become stronger is not influenced dramatically by these parameters. Compared to the simple models in Fig. 3.10, the Hebel-Slichter peak vanishes at a somewhat lower interaction strength, around $U \sim 0.9U_c$, and the additional energy scale δ_t arising in the two band κ polymorphs has a small influence on the vanishing of the peak, though it does influence the magnitude of the peak.

3.3.2 Anisotropic gaps with accidental nodes

In addition to the Hebel-Slichter peak seen in fully gapped superconductors, the effects of vertex corrections on the peak found in superconductors with accidental nodes is of particular interest when considering the BEDT-TTF-based superconductors. In these materials, a number of gaps with accidental nodes have been proposed, and the presence of strong electronic interactions raises the question of whether the the peak found in the previous chapter will be observable in these or other unconventional superconductors.

To this end I present, in Fig. 3.12, the magnitude of the peak due to a gap with accidental nodes and its evolution with interaction strength in the orthorhombic model. In models with low levels of anisotropy, the peak is not pronounced enough to be visible even in the non-interacting case, $U = 0$. In the more strongly anisotropic bandstructures, however, the influence of the anisotropy on the robustness of the peak to vertex corrections can be observed. As in the previous chapter, the maximum magnitude of the peak is found at an intermediate level of anisotropy, due to a combination of the changing Fermi

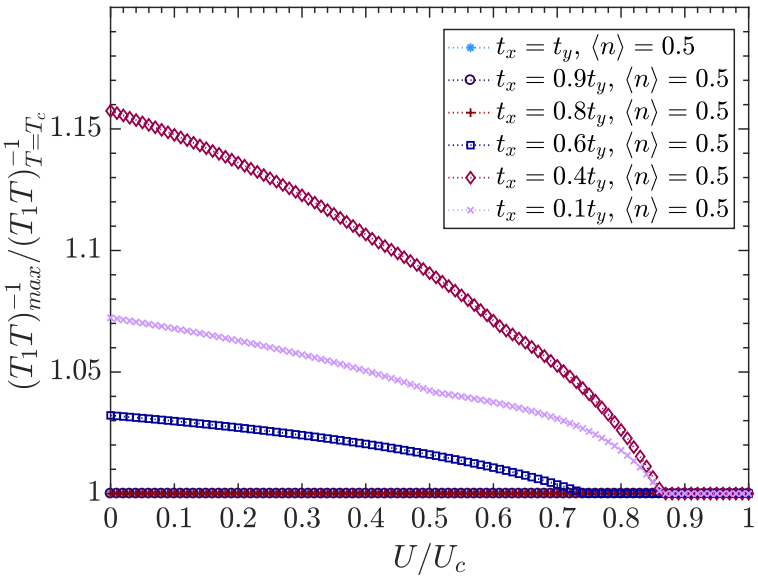

Figure 3.12: The maximal value of $1/T_1T$ in an orthorhombic superconductor with accidental nodes, for various levels of anisotropy and the dependence of this Hebel-Slichter-like peak on interaction strength. As in the non-interacting case, the magnitude of the Hebel-Slichter-like peak is enhanced by increasing anisotropy (decreasing t_y/t_x) for large t_y before the peak is reduced again at high anisotropy (low t_y) by a combination of the influence of Van Hove singularities and the reduction of $\langle \Delta_{\boldsymbol{k}} \rangle$ due to the open Fermi surface sheets. In all cases, the peak (when clearly defined) is robust against RPA vertex corrections up to large interaction strengths.

surface shape and proximity of Van Hove singularities for $t_y < 0.4t_x$. Additionally, here the interaction strength at which the peak vanishes seems to converge to a value ($U \sim 0.85U_c$) for large anisotropy. In all cases, the peak is robust to weak vertex corrections, but vanishes at an interaction strength somewhat below that necessary to remove the Hebel-Slichter peak in the s-wave case.

The effects of vertex corrections on the Hebel-Slichter-like peak due to a gap with accidental nodes in effective models for BEDT-TTF based organic superconductors are shown in Fig. 3.13. The bandstructure has a much more dramatic effect on the behaviour than in the orthorhombic model of Fig. 3.12, with both the magnitude and interaction dependence of the gap varying non-linearly with the bandstructure parameters, t'/t and δ_t/t.

Interestingly, for the single band β models, the peak has a greater magnitude for lower levels of anisotropy (measured by the magnitude of t'/t) while in the limit $t' = t$ (i.e. the isotropic triangular lattice) the peak magnitude is quite small and not very robust to vertex corrections. For smaller t'/t (larger peak magnitudes) the peak is robust to vertex corrections up to an interaction strength comparable to that found for the isotropic gap case in Fig. 3.11.

In the two band κ polymorphs, the model parameters have an additional effect on the U dependence of the peak magnitude. For larger values of δ_t, it can be seen that the magnitude of the peak actually increases with interaction strength, rather than decreasing. The magnitude of this increase is controlled by δ_t, as is the overall height of the peak. It is worth noting that, for larger δ_t, the curvature of the open (quasi-1D) bands of the Fermi surface is decreased, especially near to the boundary of the reduced Brillouin zone. This increases the nesting of these Fermi surface sheets, which may explain

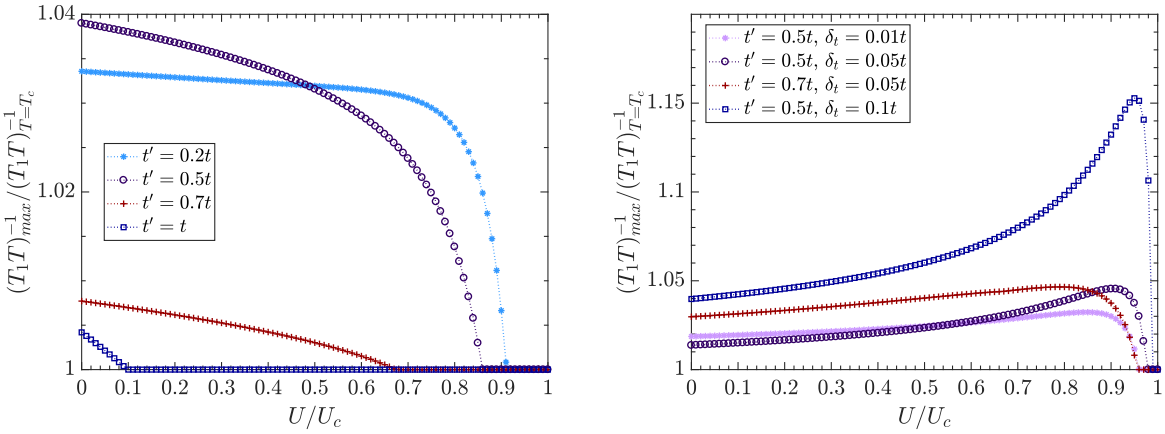

Figure 3.13: The magnitude of the Hebel-Slichter-like peak in $1/T_1T$, with increasing interaction strength in a model of BEDT-TTF based superconductors with anisotropic (d_{xy}-wave) gaps exhibiting accidental nodes for various model parameters. Left: the relaxation rate in the single band β-(BEDT-TTF)$_2X$ for varying levels of anisotropy. Right: the relaxation rate in the two band κ-(BEDT-TTF)$_2X$, varying anisotropy and the magnetic breakdown energy scale δ_t. Unlike in the fully gapped s-wave case, δ_t has a dramatic influence on the dependence on the peak on the interaction strength, with vertex corrections enhancing the peak magnitude for $\delta_t \geq 0.05t$ up to very large interaction strengths. Additionally, the peak observed here is somewhat more robust to vertex corrections than the true Hebel-Slichter peak of the s-wave case.

the enhancement of the peak. Additionally, in all of the cases investigated, the peak is found to be considerably more robust to vertex corrections than in the single band β models, in some cases persisting to $U > 0.95U_c$, beyond the interaction strength sufficient to remove the Hebel-Slichter peak in Fig. 3.11.

Non-zero s-wave component

In Fig. 3.14 I examine the effects of introducing a non-zero isotropic component to the anisotropic gap with accidental nodes. In this case, as the isotropic component is increased, the enhancement of the peak due to larger values of δ_t is gradually suppressed, with the overall U dependence of the relaxation rate approaching that of the Hebel-Slichter peak in the fully gapped case, as the isotropic component approaches the full gap magnitude. The introduction of the isotropic component additionally has little effect on the value of the interaction strength at which the peak vanishes, beyond reducing the differences in this value between to the different bandstructures.

3.3.3 A more complicated gap function: the gap of Guterding *et al.*

As a final discussion, I turn to the complicated gap symmetry proposed by Guterding *et al.* [62, 63], as shown in Eq. (3.22).

In Fig. 3.15 I examine how the temperature of this gap function evolves under increasing interaction strength. The left panel displays the gap for parameters extracted at $T \sim 0.5T_c$, while the right uses parameters extracted at $T \sim T_c$. While vertex corrections do not dramatically alter the form of the gap fit to low temperature parameters, the gap with parameters from $T \sim T_c$ exhibits a noticeable

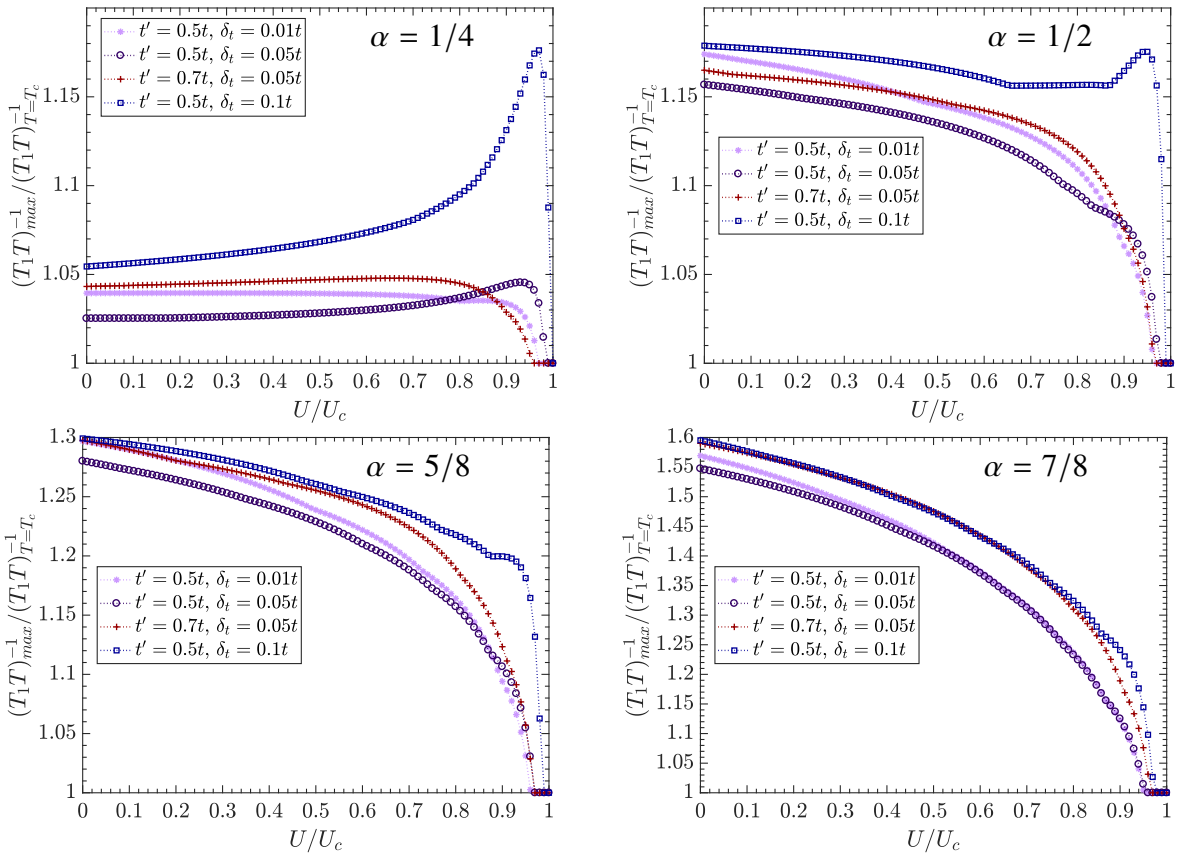

Figure 3.14: The magnitude of the Hebel-Slichter-like peak in $1/T_1T$, with increasing interaction strength in models of κ-(BEDT-TTF)$_2X$ based superconductors with anisotropic gaps and accidental nodes for various model parameters, with non-zero isotropic gap component α. As the s-wave component of the gap, α, is increased, the positive gradient of the peak with respect to interaction strength is gradually decreased until, in the absence of nodes, the interaction dependence of the peak magnitude smoothly transitions to that observed in the s-wave case. Top left: $\alpha = 1/4$. Top right: $\alpha = 1/2$, at which point the accidental nodes vanish. Bottom left: $\alpha = 5/8$. Bottom right: $\alpha = 7/8$.

Hebel-Slichter-like peak, robust to vertex corrections up to $U \sim 0.95U_c$. While, as discussed above, such an interaction strength is not unreasonable for BEDT-TTF based superconducting materials, it does impose some constraints on the validity of this gap structure.

This particular gap function arises as a combination of *ab initio* electronic structure calculations and fluctuation exchange (a generalisation of the RPA) calculations of the superconducting properties, which give an estimate of the interaction strength while self-consistently determining the superconducting gap. Zantout *et al.* [78] extend this approach, applying it to a number of BEDT-TTF based superconductors. They find that, in all the materials studied, the self-consistent determination of the gap results in a gap function of the form of Eq. (3.22). There is some dependence of the predicted gap function on the level of approximation used in determining the model, which will be discussed in more detail in Chapter 4. The interaction strengths obtained in these materials are typically $\lesssim 0.7U_c$ (for the κ-(BEDT-TTF)$_2X$ models studied here, the critical interaction strength is typically around $U_c \sim 12t$, while Zantout *et al.* find interaction strengths up to 0.7eV [78], with $t \approx 0.17$eV [62]). For the parameters extracted close to T_c, the peak persists up to $U \sim 0.95U_c$, well above the interaction strengths estimated in Ref. [78]. Such a peak should then be observable experimentally. The fact that this peak is not evident

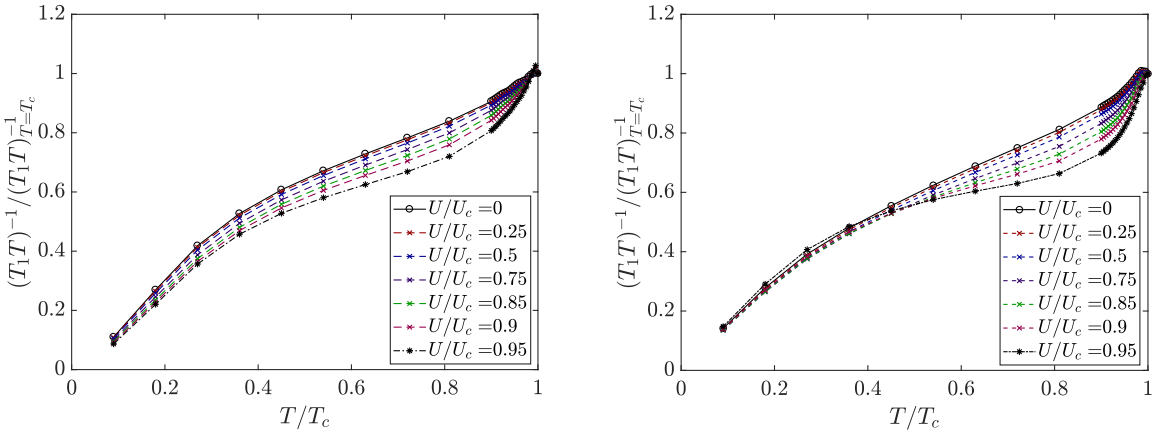

Figure 3.15: $1/T_1T$ in a dimerised model of superconductivity in the two band κ-(BEDT-TTF)$_2X$ for $t' = 0.5t$, $\delta_t = 0.05t$, with the mixed symmetry gap proposed in [62]. Left: gap parameters calculated in Ref. [62] by fitting to tunnelling spectra at low temperatures ($T \leq T_c$). Right: gap parameters calculated just below T_c. In both cases, there is a peak evident close to $T = T_c$, the existence of which is contradicted by experiment [85].

experimentally [85] is a major shortcoming of this proposed gap symmetry.

3.4 Application to other materials

As I have shown in this chapter, while the robustness of the Hebel-Slichter peak in an s-wave superconductor is largely independent of the anisotropy, the Hebel-Slichter like peak for a gap with accidental nodes is highly dependent on anisotropy. Another particularly interesting material is λ-(BETS)$_2$GaCl$_4$, which has a two-fold rotational symmetry but no reflection symmetry [131]. In this material, any nodes of the superconducting gap must by definition be accidental. Given that a nodal gap is predicted in this material [131], and that the material is highly anisotropic, measurement of $1/T_1T$ in this material offers the possibility of an additional experimental verification of the findings of this chapter, as a Hebel-Slichter like peak is likely to be present and robust to strong interactions.

3.5 Conclusions

Vertex corrections, described by the random phase approximation, can suppress the Hebel-Slichter peak in a fully gapped superconductor, and the similar peak found for gaps with accidental nodes, only for significantly strong interactions. When the peak is suppressed by vertex corrections, near $U/U_c \approx 1$, the influence of the RPA does not significantly alter the low temperature behaviour of the nuclear magnetic relaxation rate.

The suppression of a Hebel-Slichter (or Hebel-Slichter-like) peak in the BEDT-TTF based organic superconductors is therefore not sufficient to reconcile the $1/T_1$ measurements with thermodynamic probes [79, 80, 86] argued to indicate an s-wave gap. A definitive determination of the gap structure from $1/T_1$ therefore requires a comparison between experiment and theory at all temperatures, which forms the focus of the following chapter.

In the organic superconductors, the application of pressure can be used to decrease the effective interaction strength, which will influence the magnitude of any peak in $1/T_1T$. This allows for an additional experimental probe of the superconducting gap in these materials, by measuring the temperature and pressure (and therefore U/U_c) dependence of the relaxation rate to give further insight into the gap symmetry

Chapter 4

NMR in the organic superconductor κ-(BEDT-TTF)$_2$Cu[N(CN)$_2$]Br

In this chapter, I present a more concrete discussion of the $1/T_1$ relaxation rate measured in nuclear magnetic resonance experiments on the quasi-two-dimensional BEDT-TTF based superconductors. The primary focus of this chapter is to identify which, if any, of the gap functions considered thus far account for the behaviour of the experimentally observed relaxation rate. To this end, the focus will be on κ-(BEDT-TTF)$_2$Cu[N(CN)$_2$]Br [85], which has been characterised in the greatest detail among the BEDT-TTF superconductors, largely due to its relatively high critical temperature. In the process of this evaluation, I will also discuss and contrast various effective and *ab initio* models put forth to describe the bandstructure of this and other BEDT-TTF based materials, with particular regards to disagreements found between models that treat the dimerised BEDT-TTF molecules as a single effective molecule, and those that treat each BEDT-TTF molecule individually [62, 63, 75, 78, 130].

4.1 Models for BEDT-TTF based organic superconductors

In the BEDT-TTF based organic superconductors, the BEDT-TTF molecules are strongly dimerised, and form two-dimensional layers, separated by layers of the anion (the X in κ-(BEDT-TTF)$_2X$), with the electronic conduction strongly confined to the BEDT-TTF layers [7, 25, 65, 67]. This structure led to the proposal, early in the study of such materials, of effective models which consider BEDT-TTF dimers as a single site in a tight-binding model [125, 128, 132, 133]. While such models accurately reproduce features found in cyclotron resonance experiments [125, 128], there has long been disagreement over the validity of the use of such models for prediction of properties such as the superconducting gap structure [62, 74, 75, 78].

The earliest predictions of the gap structure for the κ-(BEDT-TTF)$_2X$ materials were made by Jörg Schamalian [74], Kino and Kontani [127], and Kondo and Moriya [129]. All three studies made use of such a dimerised model for the material bandstructure, and all independently found an anisotropic gap with symmetry required nodes, of a $d_{x^2-y^2}$-wave form over the extended (β) Brillouin zone, as discussed

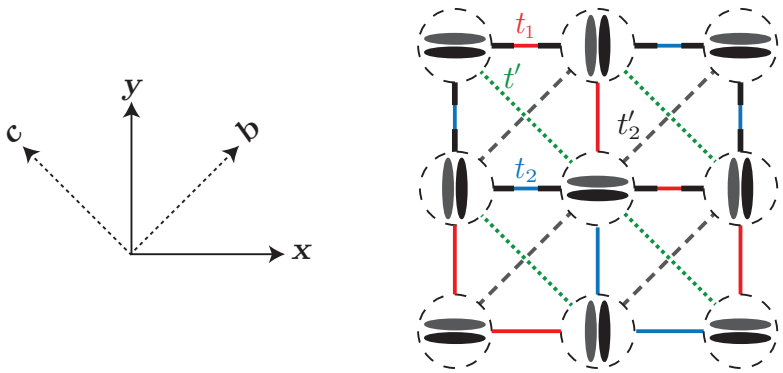

Figure 4.1: Model for dimerised κ-(BEDT-TTF)$_2X$, from Ref. [130], which differs from the model discussed in the previous chapter by the inclusion of an additional next-nearest neighbour coupling, t'_2, weaker than the next-nearest neighbour t' already included due to the orientation of the relevant dimers.

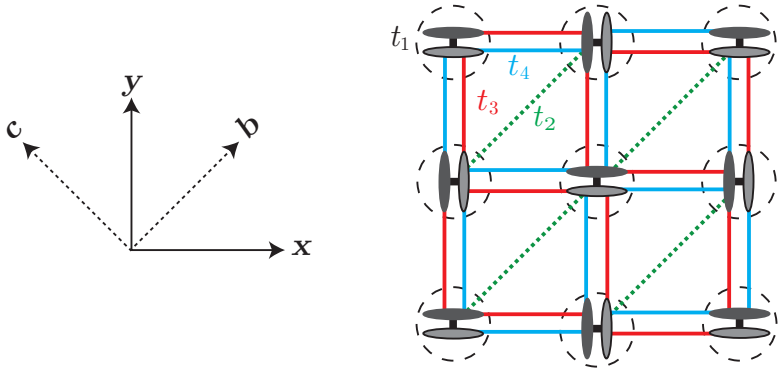

Figure 4.2: Model for κ-(BEDT-TTF)$_2X$, from Ref. [130]. This differs from the model shown in Fig. 4.1 in that the dimerisation of the BEDT-TTF molecules is not assumed *a priori*, but given by the large value for the t_1 hopping element. The monomer model shown here gives a bandstructure with four bands, at $\frac{3}{4}$ filling, while the dimerised model has two bands at half filling.

in the previous chapter. Later, Kuroki *et al.* [75] argued that the result of Schmalian was an artefact of the dimerised model used, showing that a similar calculation utilising a model treating the BEDT-TTF monomers individually produced a gap with accidental nodes, while a dimerised model reproduced Schmalian's result. Interestingly, in the gap function Kuroki *et al.* calculated in the monomer model, the node positioning coincided with the gap between Fermi surface sheets that opens on the boundary of the reduced Brillouin zone in the κ polymorphs, though their model neglects the alternating hopping elements that give rise to such a separation. Examples of the dimer and monomer tight-binding models are shown in Figs. 4.1 and 4.2, respectively, with the relevant tight binding parameters indicated.

In recent years, there have been a number of attempts to develop more accurate models for material bandstructures, based on first principles (or *ab initio*) methods [78, 130, 134]. The details and history of such methods are not the focus of this work and, as such, I will only review them briefly[1].

[1] A more comprehensive review of such methods, and their application to organic molecular crystals, can be found in Ref. [134]

Broadly speaking, such methods aim to parametrise effective low energy Hamiltonians based on first principles bandstructure calculations, performed via density functional theory (DFT). These methods proceed by taking the momentum-space Bloch wavefunctions output from the DFT calculation and constructing from these a physically-motivated basis set of real-space wavefunctions, specifically maximally localised Wannier functions. These real-space wavefunctions are then used to determine tight binding parameters by calculating the overlap of Wannier functions localised on neighbouring molecules. This then allows for the determination of a microscopic model from first principles, with no fitting of free parameters [134]. In contrast, earlier methods for constructing microscopic models from DFT calculations relied on defining a tight-binding model with a series of hopping integrals, chosen by the user, and varying the magnitudes of these parameters to fit the calculated bandstructure, sometimes with as many as ten or more free parameters.

Koretsune and Hotta [130] were among the first to apply such methods to the BEDT-TTF based charge transfer salts, and to investigate how the parameters in an effective dimer model extracted from such methods relate to the general phase diagram of these materials. The authors compared two methods for determining these parameter sets for each material considered: by constructing a set of Wannier functions localised on each BEDT-TTF molecule and using the parameters of the resulting monomer model to construct a dimer model, and constructing a dimerised model directly by localising the Wannier functions on BEDT-TTF dimers rather than molecules. They found that the ground state properties of the materials were largely determined by the frustration of the effective dimer model (t'/t, see Fig. 4.1), with the largest magnitude $t'/t \sim 1$ found in the spin-liquid candidate κ-(BEDT-TTF)$_2$Cu$_2$(CN)$_3$. They also found that estimates of the frustration from the two methods disagreed, with the monomer approach underestimating the frustration t'/t in all materials studied.

More recently, Guterding *et al.* [62, 63] made use of these *ab initio* model construction techniques to parametrise microscopic models for several BEDT-TTF based materials with the ultimate goal of determining the form of the superconducting gap function. The gap symmetry was calculated by solving a self-consistent gap equation derived via the random phase approximation (RPA). On the basis of these calculations, the authors proposed a complicated 's+d$_{xy}$-wave' symmetry, with accidental nodes, for the majority of materials studied, though it was highlighted that the symmetry required 'd$_{x^2-y^2}$-wave' gap function was nearly degenerate with this more complicated symmetry. This approach was later extended using the two-particle self-consistent framework [78] to investigate the phase diagram of these materials in more detail, finding that the transition between these two symmetries occurs within a range of anisotropy and interaction strength relevant to the BEDT-TTF based superconductors. The authors again found that the s+d$_{xy}$-wave symmetry with accidental nodes was preferred in the framework of the monomer models, but also that the d$_{x^2-y^2}$-wave gap with symmetry required nodes was preferred in a dimer model constructed from these monomer parameters, consistent with the findings of Kuroki *et al.* [75]. This is interesting in light of the conclusion of Koretsune and Hotta [130], that dimer models constructed from molecular (monomer) model parameters underestimate the frustration of the material, which raises questions over the validity of such conclusions, particularly given the absence of a magnetic breakdown gap observed in any of the effective models found in Refs [62] and [78].

While the s+d$_{xy}$-wave gap proposed by Guterding *et al.* [63] predicts the observed tunnelling spectra with some accuracy, it has not yet been investigated in the context of data from other experiments. I will investigate how well this gap function, along with the other functions discussed in the previous chapter, reproduces experimental data for $1/T_1T$ in κ-(BEDT-TTF)$_2$Cu[N(CN)$_2$]Br. The superconducting parameters used have been determined largely from experiment, and the fit to the data has been performed solely by varying the magnitude of the interaction strength.

4.1.1 Dimer models

The most general (two band) dimer model for the κ-(BEDT-TTF)$_2X$ superconductors is given by the tight binding model shown in Fig. 4.1, with dispersion

$$\xi_{\boldsymbol{k},\pm} = t' \cos\left(k_x - k_y\right) + t'_2 \cos\left(k_x + k_y\right) \pm t\sqrt{\left[\cos\left(k_x\right) + \cos\left(k_y\right)\right]^2 + \left(\frac{\delta_t}{t}\right)^2 \left[\sin\left(k_x\right) + \sin\left(k_y\right)\right]^2}, \tag{4.1}$$

where, as in the previous chapter, $t = (t_1 + t_2)/2$, $\delta_t = (t_1 - t_2)/2$, and the material is half-filled. In Eq. (4.1) I have included the possibility of an additional (typically weaker) next nearest neighbour coupling t'_2, compared to Eq. (3.15) in Chapter 3. In this model, the frustration is controlled by t'/t (for $t'_2 \ll t'$) and the magnetic field leading to the breakdown cyclotron orbit is controlled by δ_t [125, 128], as is the degree of the nesting of the quasi-one-dimensional bands of the Fermi surface (see Fig. 3.7 in the previous chapter).

4.1.2 Monomer models

In the four band monomer models for κ-(BEDT-TTF)$_2X$ superconductors, the dispersion is given by the eigenvalues of the 4×4 Hamiltonian matrix, defined as

$$H_{\boldsymbol{k}} = \begin{bmatrix} -\mu & t_1 + t_3 e^{ik_x} & t_4\left(1 + e^{-ik_y}\right) & t_2\left(1 + e^{-ik_x}\right) \\ t_1 + t_3 e^{-ik_x} & -\mu & t_2 e^{-ik_y}\left(1 + e^{-ik_x}\right) & t_4 e^{-ik_x}\left(1 + e^{-ik_y}\right) \\ t_4\left(1 + e^{ik_y}\right) & t_2 e^{ik_y}\left(1 + e^{ik_x}\right) & -\mu & t_1 + t_3 e^{-ik_x} \\ t_2\left(1 + e^{ik_x}\right) & t_4 e^{ik_x}\left(1 + e^{ik_y}\right) & t_1 + t_3 e^{ik_x} & -\mu \end{bmatrix} \tag{4.2}$$

with the four basis states given by states localised to each of the four monomers in a single unit cell. The bandstructure is found by diagonalising $H_{\boldsymbol{k}}$ at the relevant momenta, with the model at 3/4 filling.

4.1.3 Superconducting parameters

Here, I review the various gap functions and superconducting parameters of the models before making a comparison between the experimental data and calculated values for $1/T_1$. As discussed in the previous chapter, for the κ-(BEDT-TTF)$_2X$ materials, the symmetry required gaps are given by the d$_{x^2-y^2}$-wave functions, with nodes on the boundary of the reduced Brillouin zone, given by

$$\Delta_{\boldsymbol{k}}^{(\mathrm{x}^2-\mathrm{y}^2)} = \Delta_0 \frac{\cos\left(2k_x\right) - \cos\left(2k_y\right)}{2}, \tag{4.3}$$

or without such nodes in the case of the gap predicted by Schmalian [74],

$$\Delta_{\boldsymbol{k},i}^{\left(\bar{x}^2-\bar{y}^2\right)} = \gamma_i \Delta_0 \frac{\cos\left(k_x\right) - \cos\left(k_y\right)}{2}, \tag{4.4}$$

where each gap is defined in the extended Brillouin zone, the factor of 2 in the cosine functions of Eq. (4.3) ensures the existence of nodes on the reduced Brillouin zone boundary, and $\gamma_i = \pm 1$ in Eq. (4.4) changes the sign of the gap dependent on the band index i. The simplest gap function with accidental nodes, which may mix freely with the isotropic s-wave gap, is given by

$$\Delta_{\boldsymbol{k}}^{(\mathrm{xy})}(\alpha) = \Delta_0 \left[\alpha + (1 - |\alpha|)\sin\left(k_x\right)\sin\left(k_y\right)\right], \tag{4.5}$$

where α controls the magnitude of the isotropic component, moving the accidental nodes around the Fermi surface and removing them entirely for $|\alpha| \geq 0.5$. In the limit $\alpha = 1$, this function reduces to the isotropic s-wave gap $\Delta_{\boldsymbol{k}} = \Delta_0$. Finally, the s+d$_{xy}$-wave mixed symmetry gap of Refs. [62, 63, 78] is given by

$$\Delta_{\boldsymbol{k}} = \Delta_0 \left\{c_{s_1}\left[\cos\left(k_x\right)\cos\left(k_y\right)\right] + c_{s_2}\left[\cos\left(2k_x\right) + \cos\left(2k_y\right)\right] + c_d\left[\sin\left(k_x\right)\sin\left(k_y\right)\right]\right\}, \tag{4.6}$$

and each coefficient c_i may vary with temperature and are fit from tunnelling spectra data.

The temperature dependence of the gap is given by the strong coupling Bardeen-Cooper-Schrieffer form in all following calculations

$$\Delta_0(T) = \frac{\Delta_0}{2}\tanh\left(3\sqrt{\frac{T_c}{T} - 1}\right) \tag{4.7}$$

with $\Delta_0/2 = 2.5 k_B T_c = 0.25t$, a magnitude consistent with experiments on κ-(BEDT-TTF)$_2$Cu[N(CN)$_2$]Br [82].

4.2 Reproducing experimental data

As can be seen in Fig. 4.3, while the dimer approximations reproduce the qualitative features of the bandstructure, they fail to agree quantitatively with the monomer model away from the Fermi energy. Close to the Fermi energy, however, the dimer models reproduce the features of the bandstructure reliably. The conclusion of Koretsune and Hotta [130], that the dimer model constructed from Wannier functions localised on dimer sites reproduces the bandstructure of the monomer model more reliably than a dimer model extracted from the monomer parameters, is supported by Fig. 4.3. Additionally, in the superconducting state, the dimer model of Koretsune and Hotta can again be seen to slightly more accurately reproduce the energy bands, in Fig. 4.4. For reference, the energy bands in the superconducting state for a number of different gap functions are shown in Fig. 4.5, showing the location of nodes in the Brillouin zone.

It is the aim of this chapter to examine which of the proposed superconducting gap structures, if any, are consistent with the behaviour observed experimentally in the $1/T_1$ relaxation rate [85]. To achieve this end, the parameters for the superconducting gap and its temperature dependence

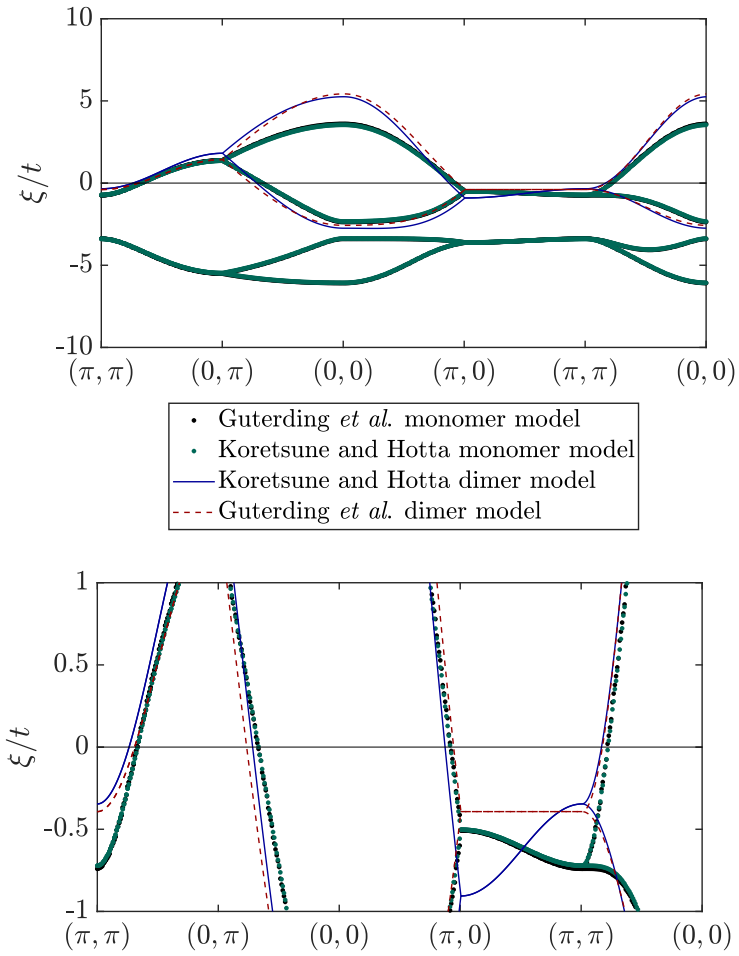

Figure 4.3: Comparison of bandstructures for κ-(BEDT-TTF)$_2$Cu[N(CN)$_2$]Br from monomer and dimer effective models. The monomer models are constructed from Wannier functions localised to molecular sites, and are in reasonable agreement with one another [62, 63, 130]. The dimer model presented by Guterding *et al.* was extracted from the monomer model parameters, while the model presented by Koretsune and Hotta arises from a Wannier construction localised to dimer sites rather than molecular (monomer) sites. In the top panel, it is clear that neither dimer model agrees consistently with the monomer model over the entire bandwidth, though the model of Koretsune and Hotta performes better than that of Guterding *et al.* Close to the Fermi energy (bottom) particularly, the dimer model of Koretsune and Hotta agrees considerably more closely to the monomer model than the dimer model constructed from the monomer parameters, as concluded by Koretsune and Hotta.

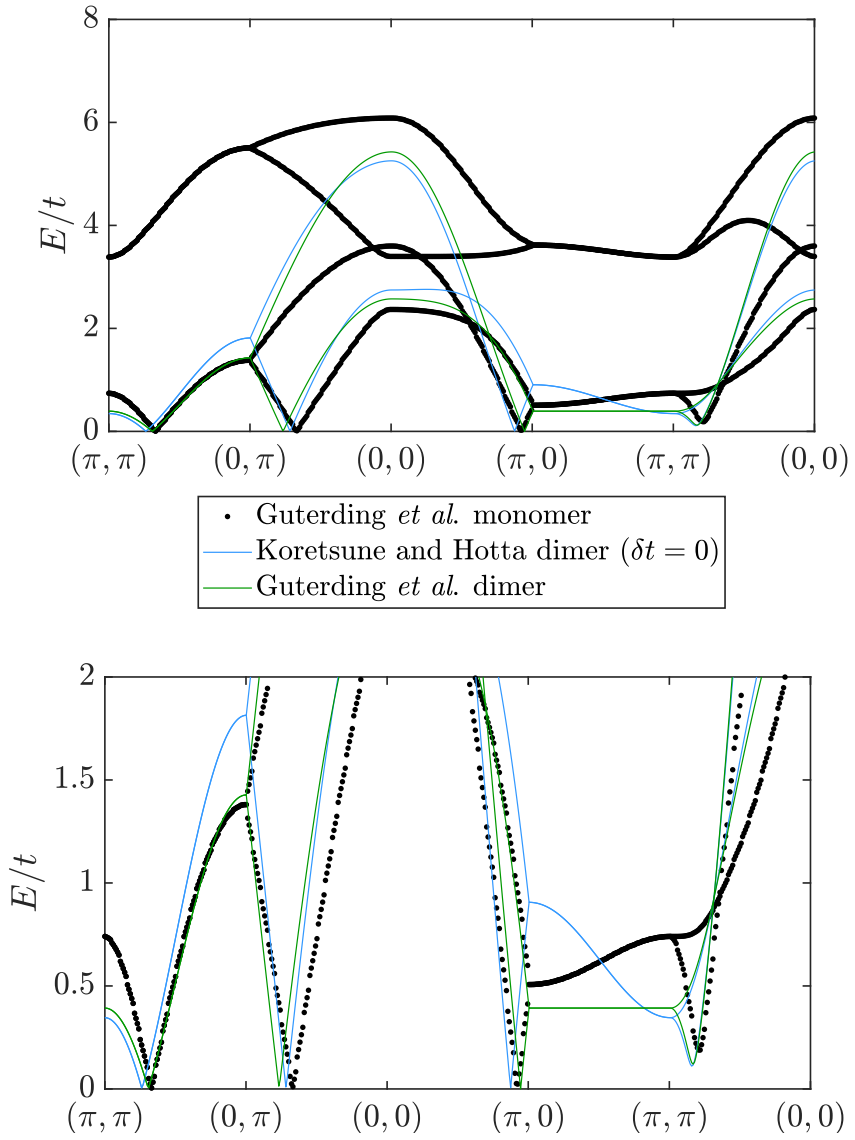

Figure 4.4: Comparison of the energy bands in the $d_{x^2-y^2}$ (symmetry required nodes) superconducting state of κ-(BEDT-TTF)$_2$Cu[N(CN)$_2$]Br from monomer and dimer effective models presented by Guterding *et al.* [62] and Koretsune and Hotta [130], with $\Delta_0/2 = 2.5k_BT_c = 0.25t$. As in the normal state bandstructure, Fig. 4.3, the bands of the monomer model are most accurately reproduced by the dimer model of Koretsune and Hotta, constructed from Wannier functions localised at dimer sites.

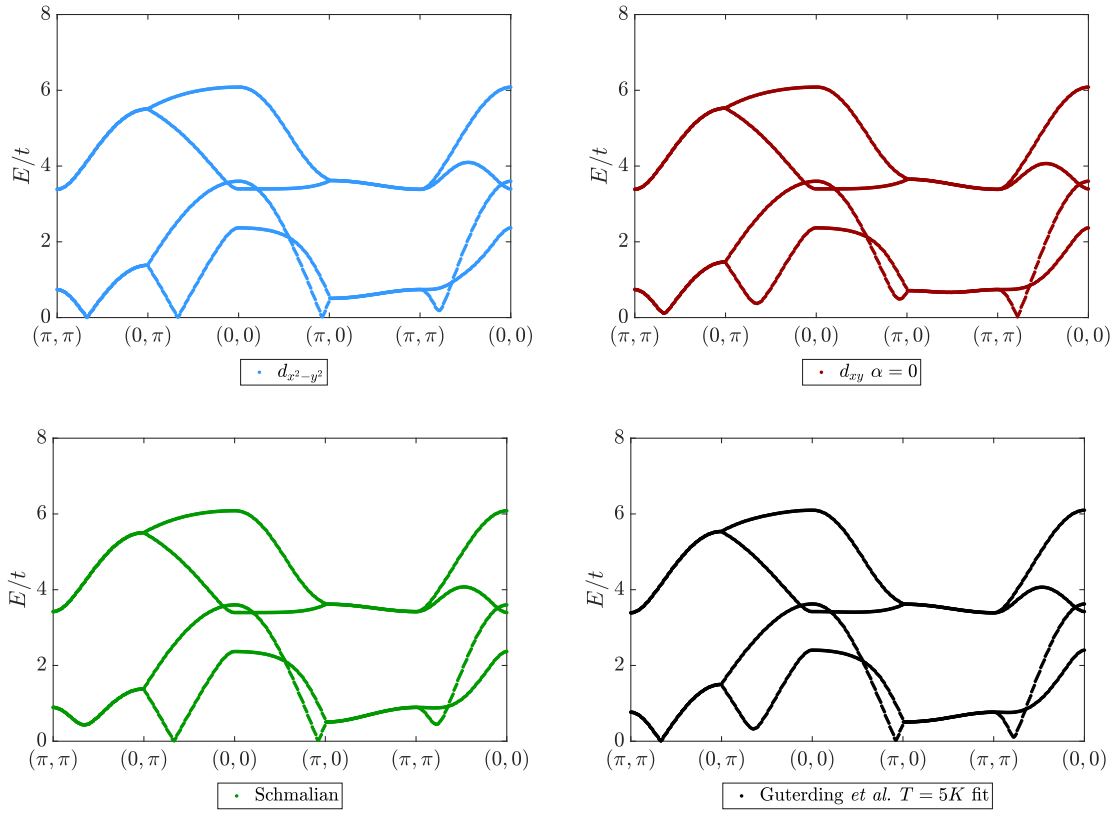

Figure 4.5: Energy bands in the superconducting state of κ-(BEDT-TTF)$_2$Cu[N(CN)$_2$]Br taking the monomer model of Guterding *et al.* [62], for a variety of gap symmetries. Top left: the d$_{x^2-y^2}$-wave state with symmetry required nodes. Top right: the d$_{xy}$-wave state with accidental nodes and no isotropic component. Bottom left: the gap function proposed by Schmalian [74], with symmetry required nodes. Bottom right: the gap function proposed by Guterding *et al.*, with accidental nodes. The nodes for the symmetry required states lie on the axes, while the accidental nodes lie on the diagonal. The d$_{x^2-y^2}$-wave gap has an additional node on the Brillouin zone boundary compared to the gap proposed by Schmalian, which has no such node but changes phase discontinuously as the band crosses the boundary. The gap proposed by Guterding *et al.* results in a node close to one high symmetry axis, between the origin and $(\pi, 0)$ while also exhibiting several nodes far from the high symmetry axes.

already discussed in this and the preceding chapters, extracted from other experiments [82], are used, with the interaction strength varied to find the best agreement with the experimental data. The experimental data is first fit to a polynomial function, and the interaction strength is varied to minimise the mean-squared error between the calculated values of $1/T_1T$ and those found from the fit to the data. This process was repeated for the variety of gap functions discussed in the previous section. For the material bandstructure, the two-band dimer model of Koretsune and Hotta was used, giving the greatest agreement with the more detailed, and less computationally tractable, monomer (four band) model[2]. The fit of Koretsune and Hotta has been used in order to avoid the possibility of the incorrect fitting highlighted by Koretsune and Hotta, wherein the anisotropy of the model is incorrectly reproduced [130]. This model neglects the small energy scale δ_t, approximating the nearest neighbour

[2]Reasonable variations in the effective parameters used to find the bandstructure are not expected to qualitatively alter the form of $1/T_1T$, and therefore the results of this chapter.

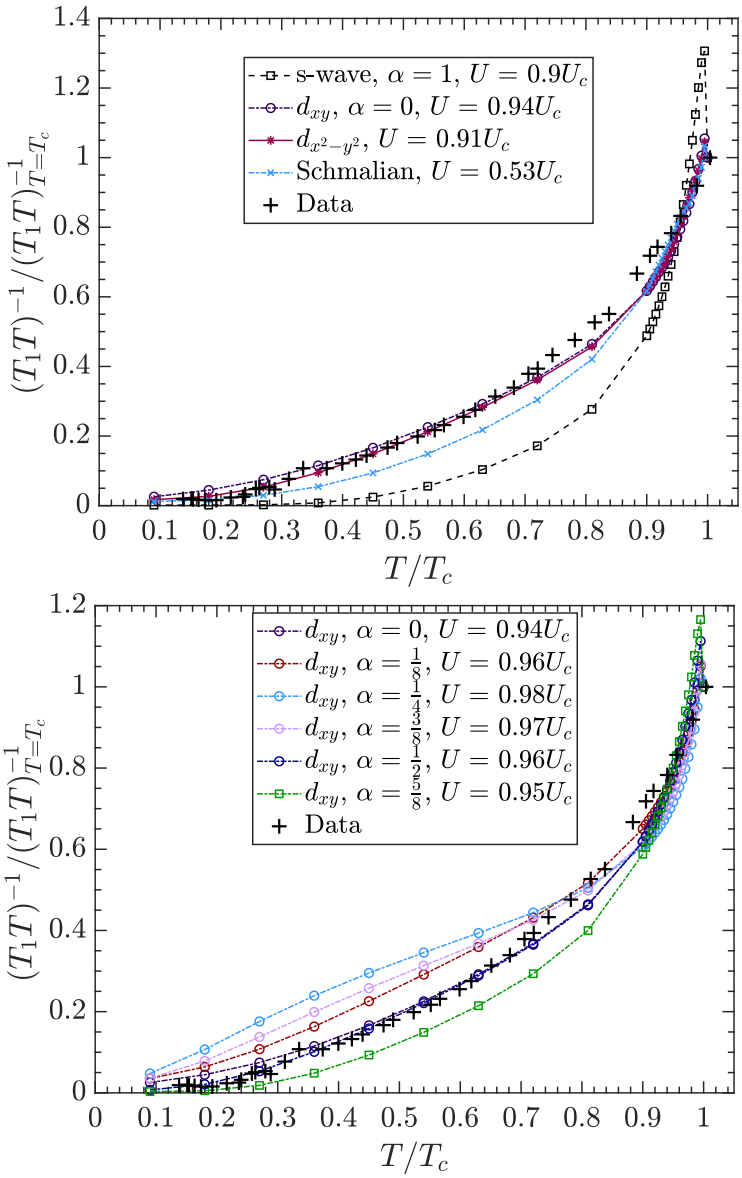

Figure 4.6: $1/T_1T$ for the dimer model proposed by Koretsune ane Hotta [130], for various gap functions, compared to experimental data from Ref. [85]. In these figures, the interaction strength has been varied to minimise the mean-squared error between the numerically generated relaxation rate and the experimental data. The top panel displays the relaxation rate for simple gaps and the gap proposed by Schmalian [74], while the lower panel shows the variation of the relaxation rate when a finite isotropic component is introduced to the d_{xy}-wave gap function. In this model, the mean-squared error is smallest for the gap function proposed by Schmalian, which also corresponds to a significantly smaller interaction strength than other gap functions. Such a low value for the interaction strength raises further questions about how realistic such a gap function can be, given κ-(BEDT-TTF)$_2$Cu[N(CN)$_2$]Br is known to be strongly correlated (i.e. $U \sim U_c$ in the RPA) [25, 135]. In these calculations, and those following, $U_c \sim 13.2t$, $\eta = 5 \times 10^{-3}t$, $N = 120^4$.

hopping integrals as constant, and is parametrised by $\left(t', t'_2, \delta_t\right) = (= 0.54t, 0.14t, 0)$. Additionally, for the purpose of discussion, I present calculations including a finite value for $\delta_t = 0.03t$, consistent with values estimated from the magnetic breakdown observed in the cyclotron orbits [74, 125, 128].

In Fig. 4.6, I present the results for a variety of gap functions and the dimer model of Koretsune and Hotta [130], with $\delta_t = 0$. The relaxation rates are plotted with the optimised (RPA) interaction

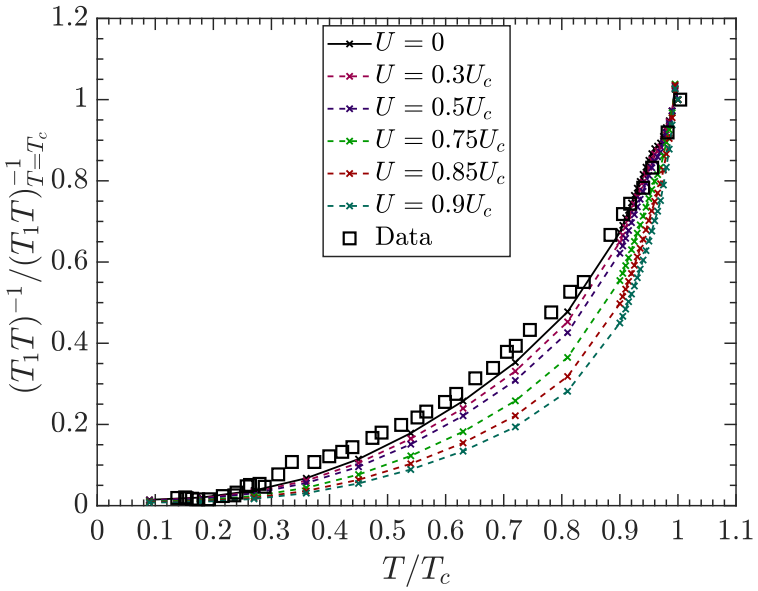

Figure 4.7: $1/T_1T$ for the gap proposed by Schmalian [74], in the dimer model proposed by Koretsune and Hotta [130]. For large interaction strengths, consistent with the observed strong correlations in κ-(BEDT-TTF)$_2$Cu[N(CN)$_2$]Br, the calculated relaxation rate fails to reproduce the experimental data.

strength found by the fit to the data. In this model, the gap proposed by Schmalian results in the lowest mean-squared relative error when compared to the fit to experimental data, with an unusually small interaction strength compared to the other gap functions. While this gap function provides the most accurate fit by this measure, the small interaction strength raises additional questions. The BEDT-TTF based superconductors are known to be close to a phase transition to a magnetically ordered Mott insulating state [6, 7, 25, 65, 67, 135], inconsistent with the small interaction strength observed for this gap function. As can be seen in Fig. 4.7, increasing the interaction strength to values more consistent with the strong correlations present in BEDT-TTF superconductors produces a relaxation rate in significantly worse agreement with the data, highlighting the incompatibility of such a gap function and strong electronic correlations.

Additionally, the mean-squared relative error is biased towards an accurate fit of the low temperature data. For a constant error, the mean-squared relative error will be larger for lower temperature data where the magnitude is smaller. A minimal value for the mean-squared relative error is then potentially due more to an accurate fit at low temperatures than across the whole temperature range, which is likely the case in this instance as can be seen in Fig. 4.6 where the Schmalian gap fits the low temperature data well.

The next closest fit to the data, with respect to the mean-squared relative error, is given by the $d_{x^2-y^2}$-wave gap function (with symmetry required nodes), at a much larger interaction strength, more consistent with the strong correlations observed in these materials. This gap also appears to fit the data more reliably over a wider temperature range. These two gap functions could potentially be further differentiated via pressure-dependent NMR. In the phase diagram of the BEDT-TTF based superconductors, increased pressure results in an effective reduction in the interaction strength. For the gap of Schmalian, the required interaction strength is relatively small, which in turn means that any

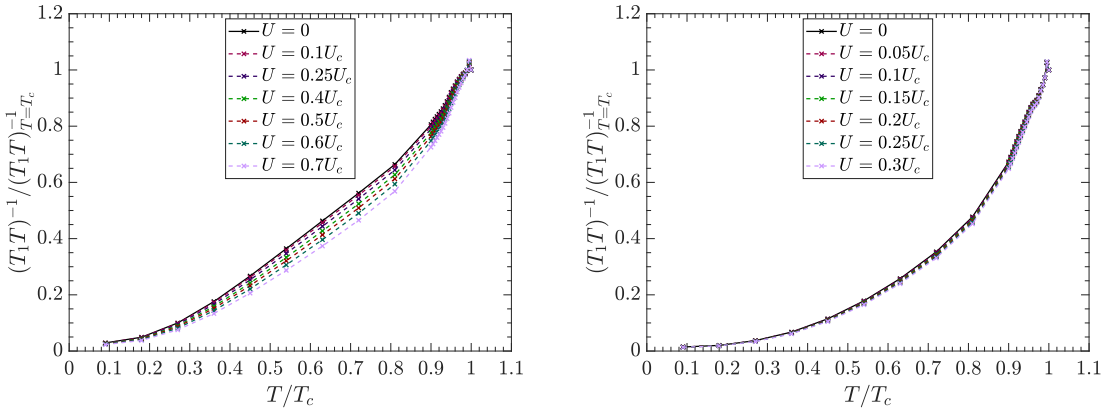

Figure 4.8: $1/T_1T$ for the $d_{x^2-y^2}$-wave gap (left) and the gap proposed by Schmalian [74] (right), in the dimer model proposed by Koretsune and Hotta [130], for interaction strengths smaller than that required to fit the data. As the interaction strength is lowered, which can be achieved experimentally by the application of pressure, the relaxation rate varies considerably more for the $d_{x^2-y^2}$-wave gap than that proposed by Schmalian, presenting a method to differentiate the two most likely gap functions experimentally.

changes in the relaxation rate under pressure will be minimal (see Fig. 4.8). The $d_{x^2-y^2}$-wave gap, on the other hand, requires a much larger value of U to fit the data, and as such the relaxation rate changes appreciably under the application of pressure.

Additionally, the gap proposed by Schmalian has the property discussed previously that, while remaining on a single sheet of the Fermi surface, the phase of the gap function changes discontinuously across the Brillouin zone boundary. Such behaviour is not unreasonable when the two Fermi surface sheets are intersecting (i.e. $\delta_t = 0$), and the gap is allowed to change phase between the bands. In such a case, the gap varies continuously over the large cyclotron orbit observed in real materials under large applied magnetic fields. In realistic materials, however, the two sheets of the Fermi surface do not intersect, and there is a finite magnetic field required to induce the large cyclotron orbit, corresponding to a nonzero δ_t in the dimer models discussed above. Interestingly, when a finite δ_t is introduced to the model, as in Fig. 4.9, the gap proposed by Schmalian remains the most accurate fit. The issues raised with this function remain, however, particularly the unexpectedly low interaction strength required to fit the experimental data.

For the anisotropic gaps with accidental nodes, the mean-squared error is generally significantly larger than that in either symmetry required case, and the calculated relaxation rate is clearly in worse agreement with the experimental data in Figs. 4.6 and 4.9. In some carefully chosen cases, the mean-squared error approaches that of the $d_{x^2-y^2}$-wave gap, however in all such cases the relaxation rate displays clear deviations from the data either close to $T = T_c$ (due to a Hebel-Slichter-like peak) or as $T \to 0$ (with the relaxation rate vanishing too slowly as the temperature is lowered). The relatively low mean-squared error in these states is therefore not necessarily an indicator of a realistic model for the data away from intermediate temperatures, and these gaps can be safely ruled out by the behaviour near $T = T_c$ and $T = 0$.

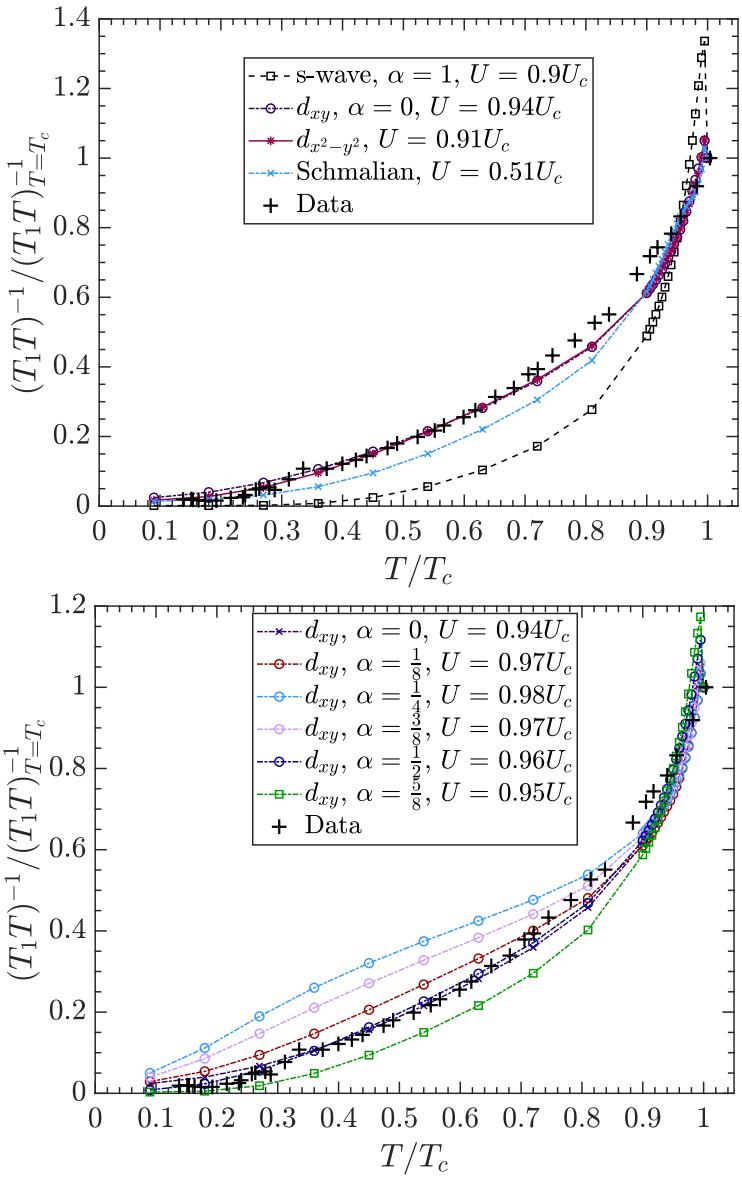

Figure 4.9: $1/T_1T$ for the dimer model proposed by Koretsune ane Hotta [130], including a finite δ_t, for various gap functions, compared to experimental data from Ref. [85]. The introduction of a finite magnetic breakdown energy scale $\delta_t = 0.03t$ does not alter the qualitative features of the relaxation rate, with the data again most closely reproduced by the gap function proposed by Schmalian, despite a much smaller interaction strength than expected in this material.

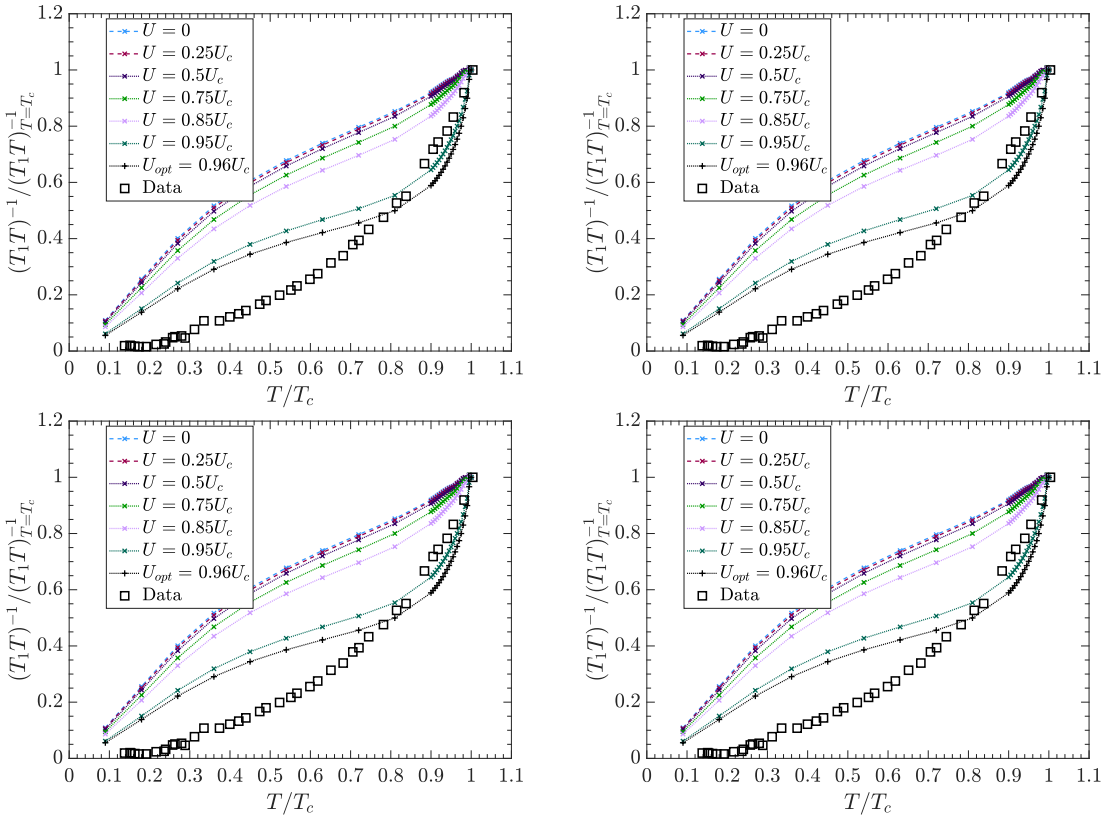

Figure 4.10: $1/T_1T$ for the dimer model proposed by Koretsune ane Hotta [130], including a finite $\delta_t = 0.03t$, with a superconducting gap proposed by Guterding *et al.* [63], compared to experimental data from Ref. [85]. Top left: gap parameters calculated at $T = 5K$. Top right: gap parameters calculated at $T = 7K$. Bottom left: gap parameters calculated at $T = 9K$. Bottom right: gap parameters calculated at $T = 11K$. In each figure, it is clear that, while the relaxation rate approaches that represented by the data as the interaction strength increases, it is never a convincing fit to the data.

4.2.1 The gap of Guterding *et al.*

Finally, I consider the complicated gap proposed by Guterding *et al.* [62, 63] with parameters extracted from measurements of the differential conductance (tunnelling density of states). In Fig. 4.10, I show the relaxation rate for the various parameter sets extracted by Guterding *et al.* from fits to the tunnelling spectra at different temperatures (fits with temperature dependent parameters are given in Appendix C). The relaxation rate agrees poorly with the experimental data in all cases. This is particularly noticeable at low temperatures, where the relaxation rate calculated for the gap function in question vanishes much more slowly than the observed relaxation rate. In terms of the mean-squared error, the closest fit to the data comes from the $T = 9K$ fit, but the error in this case is still a factor of two larger than that for any of the gaps considered in Figs. 4.6 and 4.9, including the s-wave gap, which shows a significant Hebel-Slichter peak.

4.3 Conclusions

On the basis of this comparison between numerical predictions via the RPA and experiment, the gap functions with symmetry required nodes are the only gaps consistent with experimental observations

of the $1/T_1$ relaxation rate over the entire temperature range. Gap functions belonging to the trivial representation of the point group (with or without accidental nodes) are unable to provide an accurate fit to the data, though the node positioning can in principle be finely tuned to agree with subsections of the temperature range. It is possible that more sophisticated approximations to the electronic interactions may alter these results, but such corrections aren't likely to fundamentally invalidate this analysis.

The extended $s + d_{xy}$ gap proposed by Guterding *et al.* fails to fit the data for any parameter set extracted from scanning tunnelling spectra in Ref [63]. The gap of Guterding *et al.*, in fact, performs less accurately than the simpler gap functions with accidental nodes, or even the isotropic s-wave gap function.

Of the two gaps with symmetry required nodes, the gap proposed by Schmalian provides the best fit, but requires an unreasonably small interaction strength, inconsistent with strong electronic correlations known to exist in κ-(BEDT-TTF)$_2$Cu[N(CN)$_2$]Br. The simpler $d_{x^2-y^2}$-wave gap requires an interaction strength much closer to the critical U_c found in the RPA, more consistent with other properties of BEDT-TTF based superconductors.

The two gaps with symmetry required nodes can be distinguished more definitively by future nuclear magnetic resonance experiments performed under external pressure, varying the effective interaction strength. The variation of the relaxation rate with respect to both temperature and interaction strength (via pressure) can give further indication of which state is responsible for the superconductivity.

Chapter 5

Quasiparticle scattering and relaxation mechanisms in unconventional superconductors

The previous chapters have focused on the analysis of the $1/T_1$ relaxation rate measured in nuclear magnetic resonance, and how it is influenced by the form of the superconducting gap, with a particular focus on the existence of Hebel-Slichter-like peaks due to certain gap symmetries. In this chapter, I turn to an alternative measurement, the penetration depth that characterises the Meissner effect in superconductors. The relationship between the penetration depth and the quasiparticle scattering rate allows for the use of the penetration depth as a probe of the momentum dependence of the low-energy excitations of the superconductor, and thus the gap structure.

5.1 The Meissner effect and the London penetration depth

The Meissner effect, the central signature of superconductivity, arises from the global phase coherence of the superconducting ground state. In a superconductor, magnetic flux is spontaneously expelled from the material on transition to the superconducting state. While a vanishing resistivity may arise in non-superconducting phases, the Meissner effect can only be seen as the result of such a phase coherence, sometimes referred to as the breaking of the gauge symmetry[1]. As the decay of the magnetic field must be continuous, in the superconducting state the magnetic field is suppressed exponentially as it enters the material, on a length scale given by the penetration depth λ_L, which also defines the superfluid density $\rho_s = 1/\lambda_L^2$, via the London equation [11, 12, 95, 136].

In the sperconducting state, there is then a combination of effects due to the superfluid ground state, which gives rise to both the infinite conductivity and the Meissner effect, and the quasiparticle excitations, which screen the collective superconducting behaviour. The magnitude of the penetration

[1] In truth, although the gauge symmetry is removed at the single particle level, collective effects act to restore this symmetry [19].

depth is determined by the superfluid density, which is reduced by the existence of quasiparticle excitations, the lifetime of which is given by the inverse of the scattering rate [70, 137, 138]. The influence of these excitations is dependent on both their lifetime and the availability of such states (given by the quasiparticle density of states). These properties can be probed in the temperature dependence of the penetration depth. For example, in a fully gapped superconductor, the quasiparticle excitations in the density of states are exponentially suppressed, and as the temperature is lowered below T_c, the penetration depth approaches its zero temperature value exponentially.

Similarly, in a superconductor with nodes in the gap function, and therefore low energy excitations in the density of states, it is often stated [70] that the penetration depth will behave as a power law at low temperatures. This picture is, however, complicated by the nature of the scattering rate due to quasiparticle interactions, as these scattering events determine the temperature dependence of the penetration depth.

There have been a number of recent studies investigating the quasiparticle scattering rate by measuring the surface impedance via microwave cavity resonance [45, 82, 139]. In these experiments, a sample of the superconducting material is placed in a dielectric resonant cavity and subjected to magnetic fields of various frequencies. The fields then induce screening currents in the sample, with the penetration of the field into the sample (on the length scale of the penetration depth) altering the effective volume of the resonator and therefore the resonant properties of the cavity. Such alterations can be related to the impedance within this region (i.e. within λ_L of the surface in a superconductor), and are then used to extract both the superfluid density and quasiparticle scattering rate.

In more detail, the penetration depth may be measured via the microwave conductivity, which is expressed, in a two-fluid model as [137, 138, 140]

$$\sigma(\omega,T) = \frac{1}{i\omega\mu_0\lambda_L^2(T)} + \sigma_{qp}(\omega,T) = \frac{i\omega\mu_0}{[Z_s(\omega)]^2}, \tag{5.1}$$

where μ_0 is the vaccuum permeability, σ_{qp} is the contribution due to quasiparticle excitations and $Z_s(\omega)$ is the (freqency-dependent) surface impedance, which can be measured in via microwave cavity perturbation techniques [45, 82, 137, 138, 141, 142]. The penetration depth can then be extracted in the zero frequency limit, in which the quasiparticle density of states vanishes and no excitations are present, by

$$\frac{1}{\lambda_L^2(T)} = \lim_{\omega\to 0} \omega\mu_0 \operatorname{Im}\{\sigma\}. \tag{5.2}$$

Away from the zero frequency limit, a frequency dependent superfluid density may be defined [45], taking into account the screening effect due to quasiparticle excitations,

$$\begin{aligned} \frac{1}{\delta^2(\omega,T)} &= \omega\mu_0 \operatorname{Im}\{\sigma(\omega,T)\} \\ &= \frac{1}{\lambda_L^2(T)} - \omega\mu_0 \operatorname{Im}\left\{\sigma_{qp}(\omega,T)\right\}, \end{aligned} \tag{5.3}$$

which can be explicitly related to the quasiparticle scattering rate, τ^{-1}, with σ_{qp} taking a Drude-like form,

$$\frac{1}{\delta^2(\omega,T)} = \frac{1}{\lambda_L^2(T)} - \mu_0 \frac{\omega^2 \tau(T)}{1-\omega^2[\tau(T)]^2}. \tag{5.4}$$

Clearly, as $\omega \to 0$, the second term, corresponding to the quasiparticle contribution, vanishes, while in the high frequency ($\omega\tau \gg 1$) limit $\delta(\omega,T) \propto \tau(T)$. This allows both the scattering rate and London penetration depth to be extracted from the surface impedance Z_s in an experimental setting.

In unconventional superconductors, electronic correlations are typically large, with the effects of such interactions dominating the physics of the materials. As such, the electron-electron scattering can be expected to account for a significant contribution to the quasiparticle scattering rate measured in the microwave conductivity. A distinction must be made however, between the rate for electron-electron scattering (which is an elastic process) and the rate of current relaxation due to these processes, which affects the conductivity and may differ dramatically from the rate of electron-electron scattering.

5.2 Quasiparticle scattering and relaxation mechanisms

In the context of Fermi liquid theory, there has long been debate regarding details of the origin of the quadratic temperature dependence, attributed to electron-electron scattering. The controversy arises due to the fact that the current, defined by the net velocity carried by electronic excitations, cannot relax due to elastic scattering, of which electron-electron scattering is an example. While it is true that electron-electron interactions cannot relax the current in a free, non-interacting system of electrons, there exist mechanisms in crystalline systems that allow electron-electron scattering to relax the current. The current is given by

$$J = \sum_{\boldsymbol{k}} e\boldsymbol{v}_{\boldsymbol{k}} c_{\boldsymbol{k}}^{\dagger} c_{\boldsymbol{k}}, \tag{5.5}$$

where e is the electronic charge, $\boldsymbol{v}_{\boldsymbol{k}}$ is the electronic (group) velocity at crystal momentum $\boldsymbol{k}$ (with momentum $\boldsymbol{p} = \hbar\boldsymbol{k}$), and $c_{\boldsymbol{k}}^{\dagger}$ ($c_{\boldsymbol{k}}$) is the creation (annihilation) operator at a given crystal momentum. A free electron gas is Galilean invariant, the velocity is proportional to the momentum,

$$v_{\boldsymbol{k}} = \frac{\hbar\boldsymbol{k}}{m} = \frac{\boldsymbol{p}}{m}, \tag{5.6}$$

and therefore the current cannot relax unless the momentum also relaxes.

Electron-electron scattering can, however, be responsible for current relaxation due to one of two effects: either the momentum is not truly conserved in the scattering process, or momentum conservation is not sufficient to conserve the total velocity, when the two are not necessarily proportional. The second of these possibilities has been discussed in a number of places [143–147], but the conditions to allow current relaxation via this mechanism are restrictive [143, 144]. Additionally, this mechanism has not been shown to be a relevant for current relaxation in unconventional superconductors thus far, as I shall discuss in the following sections.

5.2.1 Umklapp scattering in Fermi liquids

Momentum may not be conserved in crystalline systems due to 'umklapp' scattering, which arises due to the fact that the crystal momentum, $\boldsymbol{k}$, is only conserved up to a reciprocal lattice vector $\boldsymbol{G}$. In an umklapp scattering process, the momentum $\boldsymbol{p}$ is conserved, but the crystal momentum $\boldsymbol{k}$ is not, with the change in crystal momentum, an integer multiple of the reciprocal lattice vector, transferred to the lattice. As a result, the current, which depends on the crystal momentum, may relax due entirely to elastic scattering [102, 148–151].

In order for umklapp scattering to occur, at low energies, the Fermi surface must be larger than some minimum size. For a system with parabolic bands (and therefore a spherical Fermi surface), this amounts to a restriction that the Fermi wavevector k_F must be at least a quarter of the length of a reciprocal lattice vector, $k_F \geq |\boldsymbol{G}|/4$, corresponding to an at least quarter-filled band. This then allows, for certain momenta, the possibility of a net momentum transfer in an electron-electron scattering event (which involves four quasiparticle states) of $4k_F = |\boldsymbol{G}|$, thus allowing umklap scattering [144, 145, 148].

In a system with a more complicated bandstructure, the condition can no longer be reduced to a limitation on the filling. In this case, for umklapp processes to occur there must exist states on the Fermi surface with wavevector outside a minimum boundary for umklapp scattering (i.e. one of $|k_x| \geq |\boldsymbol{G}_x|/4$ or $|k_y| \geq |\boldsymbol{G}_y|/4$), as shown in Fig. 5.1. This allows a scattering process connecting two states on one boundary (e.g. at $k_x = |\boldsymbol{G}_x|/4$) with two states on the opposite boundary ($k_x = -|\boldsymbol{G}_x|/4$) such that the total change in momentum is exactly a reciprocal lattice vector. For such processes to be allowed in Fermi liquids, the Fermi surface must cross the boundary, with states on both sides, otherwise (i.e. if the Fermi surface is solely outside the minimum bound for umklapp scattering) there exists no process with a momentum transfer of exactly a reciprocal lattice vector.

In general, an umklapp scattering process must involve two quasiparticles within the umklapp boundary with two quasiparticles, with momentum in the opposite direction, outside the boundary. Such a process is possible, for example, in the x direction, for momenta

$$\begin{aligned}
\boldsymbol{k}_1 &= \pm\frac{\boldsymbol{G}_x}{4} - \delta_1 \\
\boldsymbol{k}_2 &= \pm\frac{\boldsymbol{G}_x}{4} - \delta_2 \\
\boldsymbol{k}_3 &= \mp\frac{\boldsymbol{G}_x}{4} + \delta_1 \\
\boldsymbol{k}_4 &= \mp\frac{\boldsymbol{G}_x}{4} + \delta_2,
\end{aligned} \tag{5.7}$$

which satisfy the momentum transfer condition for umklapp scattering,

$$\boldsymbol{k}_1 + \boldsymbol{k}_2 - \boldsymbol{k}_3 - \boldsymbol{k}_4 = \pm\boldsymbol{G}_x. \tag{5.8}$$

In general, the scattering rate for a particle of momentum $\mathbf{k}$ due to electron-electron interactions in a Fermi liquid is given by the Fermi golden rule expression, with spin indices suppressed for clarity,

$$\begin{aligned}
\tau^{-1}(\boldsymbol{k}_1) = \frac{2\pi}{\hbar}\frac{1}{N^2}\sum_{\boldsymbol{k}_2,\boldsymbol{k}_3,\boldsymbol{k}_4} &\left|V_{\{\boldsymbol{k}_i\}}\right|^2 f\left(\xi_{\boldsymbol{k}_2}\right)\bar{f}\left(\xi_{\boldsymbol{k}_3}\right)\bar{f}\left(\xi_{\boldsymbol{k}_4}\right) \\
&\times\delta\left(\xi_{\boldsymbol{k}_1} + \xi_{\boldsymbol{k}_2} - \xi_{\boldsymbol{k}_3} - \xi_{\boldsymbol{k}_4}\right)\delta\left(\boldsymbol{k}_1 + \boldsymbol{k}_2 - \boldsymbol{k}_3 - \boldsymbol{k}_4 + n_i\boldsymbol{G}_i\right),
\end{aligned} \tag{5.9}$$

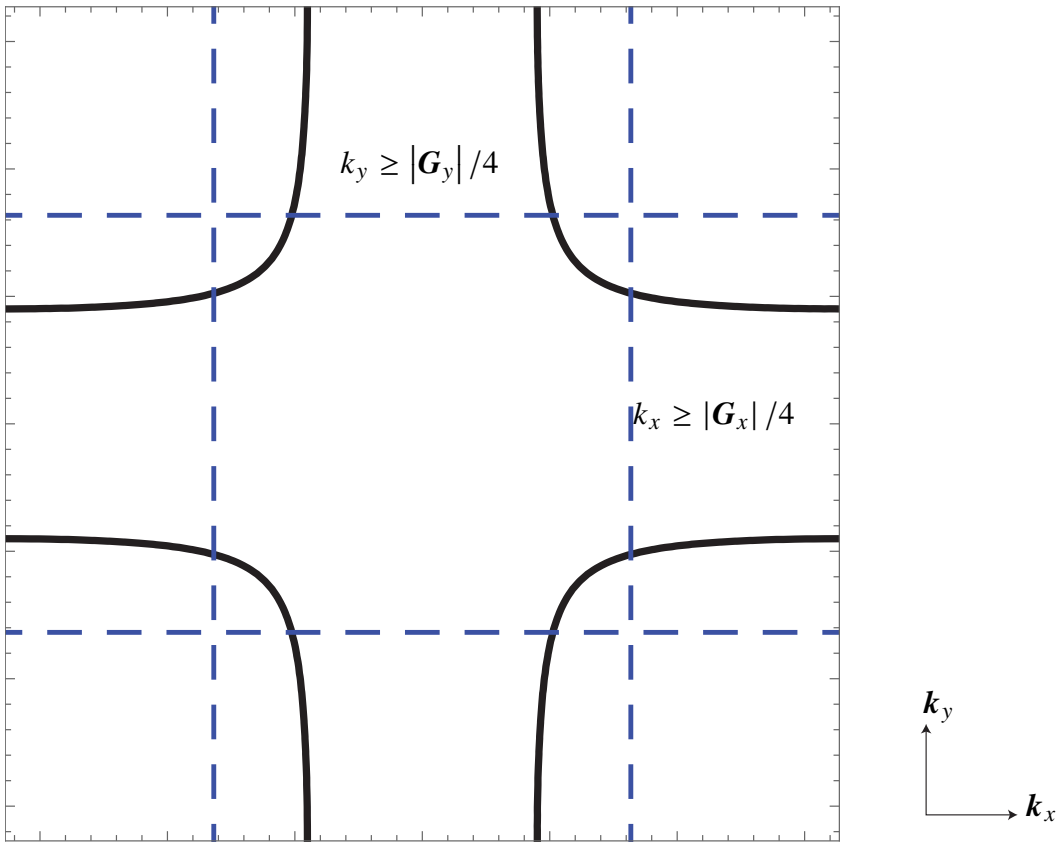

Figure 5.1: Fermi surface for a model of the high temperature superconductor $YBa_2Cu_3O_{6+x}$ [102, 151] (solid lines), and the minimum boundary in the first Brillouin zone for umklapp scattering (dashed lines), such that $k_x \geq |\boldsymbol{G}_x|/4$ or $k_y \geq |\boldsymbol{G}_y|/4$. For umklapp scattering to occur, two quasiparticle states outside the umklapp boundary must scatter with two inside the boundary. As can be seen, in this model the Fermi surface extends beyond this boundary, and umklapp scattering is therefore allowed in the Fermi liquid state of this material.

where $f(E)$ is the Fermi-Dirac distribution, $\bar{f}(E) = 1 - f(E)$, $V_{\{\boldsymbol{k}_i\}}$ is the scattering potential for the set of momenta $\{\boldsymbol{k}_i\}$, and the delta functions enforce energy and momentum conservation. In this expression, $n_i = 0$ corresponds to normal (non-umklapp) scattering processes in the i direction.

For a Fermi liquid, provided the Fermi surface extends beyond the minimum boundary for umklapp scattering, the scattering rate due to umklapp processes generally lacks any qualitative differences to the total electron-electron scattering rate. Generally, the two differ only by a constant overall factor, given by the ratio of the available phase space for umklapp processes to the phase space available for all scattering processes, with the same overall temperature dependence [144, 148]. The lack of further corrections to the scattering rate imposed by the phase space restriction is due to the fact that the Fermi surface is a constant energy surface, with no quasiparticle states at any point on the surface more energetically favourable than any other, and therefore no qualitative differences between momentum configurations contributing to the normal and umklapp scattering rates.

In a superconductor, however, the constant energy surfaces depend not only on the electron dispersion, but the quasiparticle gap. If the gap is anisotropic and possesses nodes, quasiparticles with momenta close to the node will be more easily excited at low temperatures than those away from the node, and the restricted phase space may then give rise to two distinct scattering rates with different

temperature dependences.

5.2.2 Superconductors, the superconducting gap and phase space restrictions

Unlike in a Fermi liquid, the restriction on the available phase space for umklapp scattering has additional consequences for the scattering rate in the superconducting state. The existence of the superconducting gap results in a more complicated relationship between energy and momentum than in a Fermi liquid, with an additional dependence on the position on the Fermi surface, which alters the observed scattering rate.

The Fermi golden rule scattering rate in this case is given by

$$\begin{aligned}\tau^{-1}(\boldsymbol{k}_1) &= \frac{2\pi}{\hbar}\frac{1}{N^2}\sum_{\boldsymbol{k}_2,\boldsymbol{k}_3,\boldsymbol{k}_4}\left|\tilde{V}_{\{\boldsymbol{k}_i\}}\right|^2 f\left(E_{\boldsymbol{k}_2}\right)\bar{f}\left(E_{\boldsymbol{k}_3}\right)\bar{f}\left(E_{\boldsymbol{k}_4}\right)\\ &\quad\times\delta\left(E_{\boldsymbol{k}_1}+E_{\boldsymbol{k}_2}-E_{\boldsymbol{k}_3}-E_{\boldsymbol{k}_4}\right)\delta\left(\boldsymbol{k}_1+\boldsymbol{k}_2-\boldsymbol{k}_3-\boldsymbol{k}_4+n_i\boldsymbol{G}_i\right),\end{aligned} \tag{5.10}$$

where the electron dispersion $\xi_{\boldsymbol{k}}$ has been replaced by the superconducting quasiparticle energy $E_{\boldsymbol{k}} = \sqrt{\xi_{\boldsymbol{k}}^2+\Delta_{\boldsymbol{k}}^2}$, and the scattering potential $\tilde{V}_{\{\boldsymbol{k}_i\}}$ must take quasiparticle coherence factors into account. As a result of these changes, both the total and umklapp scattering rates are changed significantly.

The constant energy contours of the superconductor are distinct from those of the Fermi liquid, and the low energy excitations are no longer located along the entire Fermi surface, but restricted to those sections for which the gap is small (or vanishes entirely). For a superconducting gap with (symmetry required) nodes, the energy can be expressed, close to the gap nodes, as

$$E_{\boldsymbol{k}} = \sqrt{\left[v_F\left(k_\perp-k_\perp^{\text{node}}\right)\right]^2+\left[v_\Delta\left(k_\parallel-k_\parallel^{\text{node}}\right)\right]^2}, \tag{5.11}$$

with elliptical constant energy contours at low energy. In such a system, the scattering rate for nodal quasiparticles has a cubic temperature dependence, which can be understood from the scaling of the momentum integrations[2] [151], with $E_{\boldsymbol{k}} \sim \left|\boldsymbol{k}-\boldsymbol{k}^{\text{node}}\right|$. For a fully gapped superconductor, low energy excitations are exponentially suppressed at low temperatures, leading to an exponential temperature dependence in the scattering rate [97].

Walker and Smith [151], showed that such an exponential temperature dependence may arise in the scattering rate of a superconductor even when there are nodes in the superconducting gap, as a result of the reduced phase space available for umklapp scattering. They found that, in a tight binding model for the high temperature superconductor $YBa_2Cu_3O_{6+x}$ (YBCO), the nodes of the gap function lie on a section of the Fermi surface within the boundary for umklapp scattering. As a result, the minimum energy configuration of quasiparticles giving rise to umklapp scattering required that at least some of the quasiparticles had a non-zero superconducting gap (see Fig. 5.2), and as such must be thermally

[2]For allowed scattering processes, the three momentum integrations each give a factor of E^2, while the energy and momentum conserving delta functions contribution E^{-1} and E^{-2}, respectively, leading to the overall result $\tau \sim E^3 \sim (k_B T)^3$. The scaling argument here was confirmed numerically for the total scattering rate of YBCO, with symmetry required nodes, by Duffy *et al.* [102].

activated. In the configuration they considered, two of the quasiparticles were located away from the nodes, at the minimum momentum consistent with umklapp scattering, resulting in a non-zero gap value for these two quasiparticles. The energy associated with each of these quasiparticles is then given by an expansion near this 'umklapp gap' value, $\Delta_{\boldsymbol{k}} = \Delta_U$,

$$E_{\boldsymbol{k}} = \Delta_U + v_2' \left(k_\parallel - k_\parallel^{\mathrm{U}}\right) + \frac{v_F'^2}{2\Delta_U}\left(k_\perp - k_\perp^{\mathrm{U}}\right), \tag{5.12}$$

with $\boldsymbol{k}^{\mathrm{U}}$ the minimum momentum for which umklapp scattering involving two nodal quasiparticles is allowed [satisfying Eq. (5.8)].

While the total quasiparticle scattering rate has the expected cubic temperature dependence, $\tau^{-1} \propto T^3$, the additional energy restrictions on the umklapp processes results in a umklapp scattering rate that becomes thermally activated,

$$\begin{aligned} \tau_{u,i}^{-1}(\boldsymbol{k}_1) &= \frac{2\pi}{\hbar}\frac{1}{N^2}\sum_{\boldsymbol{k}_2,\boldsymbol{k}_3,\boldsymbol{k}_4} \left|\tilde{V}_{\{\boldsymbol{k}_i\}}\right|^2 f\left(E_{\boldsymbol{k}_2}\right)\bar{f}\left(E_{\boldsymbol{k}_3}\right)\bar{f}\left(E_{\boldsymbol{k}_4}\right) \\ &\quad \times\delta\left(E_{\boldsymbol{k}_1} + E_{\boldsymbol{k}_2} - E_{\boldsymbol{k}_3} - E_{\boldsymbol{k}_4}\right)\delta\left(\boldsymbol{k}_1 + \boldsymbol{k}_2 - \boldsymbol{k}_3 - \boldsymbol{k}_4 + \boldsymbol{G}_i\right) \\ &\sim CT^2 f(\Delta_U)\bar{f}(\Delta_U), \end{aligned} \tag{5.13}$$

where C is a constant determined by the Fermi surface and gap function geometry, and the rate can be approximated by[3] $\tau_u^{-1} \propto T^2 \exp\{-\Delta_U/k_BT\}$. While such a configuration may not in fact be the lowest total energy configuration, it is sufficient to demonstrate the absence of any umklapp scattering process involving only nodal quasiparticles. In reality, a number of such processes will be possible for quasiparticles away from the nodes, each with a different energy required to activate the scattering (Δ_U), with the overall scattering rate dominated by the minimum energy process, giving the largest value for the exponential correction. Similarly, the umklapp (or normal) processes with non-zero energy momentum configurations will contribute to the total scattering rate, but it will be dominated by the nodal processes with $\tau^{-1} \propto T^3$. The result of Walker and Smith was further supported by numerical calculations involving a more detailed bandstructure and an electronic interaction given by the random phase approximation [102].

An activated temperature dependence in the scattering rate for umklapp processes will in general be present, to some degree, unless there exist nodes for which the net change in momentum is given by a reciprocal lattice vector ($\boldsymbol{k}_1 + \boldsymbol{k}_2 - \boldsymbol{k}_3 - \boldsymbol{k}_4 = \boldsymbol{G}$). If, for example, the nodes are outside the boundary for umklapp scattering processes, but separated by more than half a reciprocal lattice vector, then scattering cannot be solely between the nodal quasiparticles and still conserve momentum (see Fig. 5.3). This is of particular interest in light of recent experiments which have shown no such correction in several unconventional superconductors, including the organic superconductor κ-(BEDT-TTF)$_2$Cu[N(CN)$_2$]Br (κ-Br) [82] and the heavy fermion superconductor CeCoIn$_5$ [45]. Clearly, in these materials, the nodal

[3] Just as in the case for the normal scattering, the quadratic prefactor here is a result of the scaling of the momentum. For the quasiparticle at the node, the momentum integrations contribute a factor of E^2, while for the two away from the nodes the integrations contribute a factor of $E^{3/2}$ each, due to the anisotropic scaling of energy with momentum in Eq. (5.12). Energy and momentum conservation again contribute factors of E^{-1} and E^{-2}, respectively, for an overall result of $E^2 \sim (k_BT)^2$.

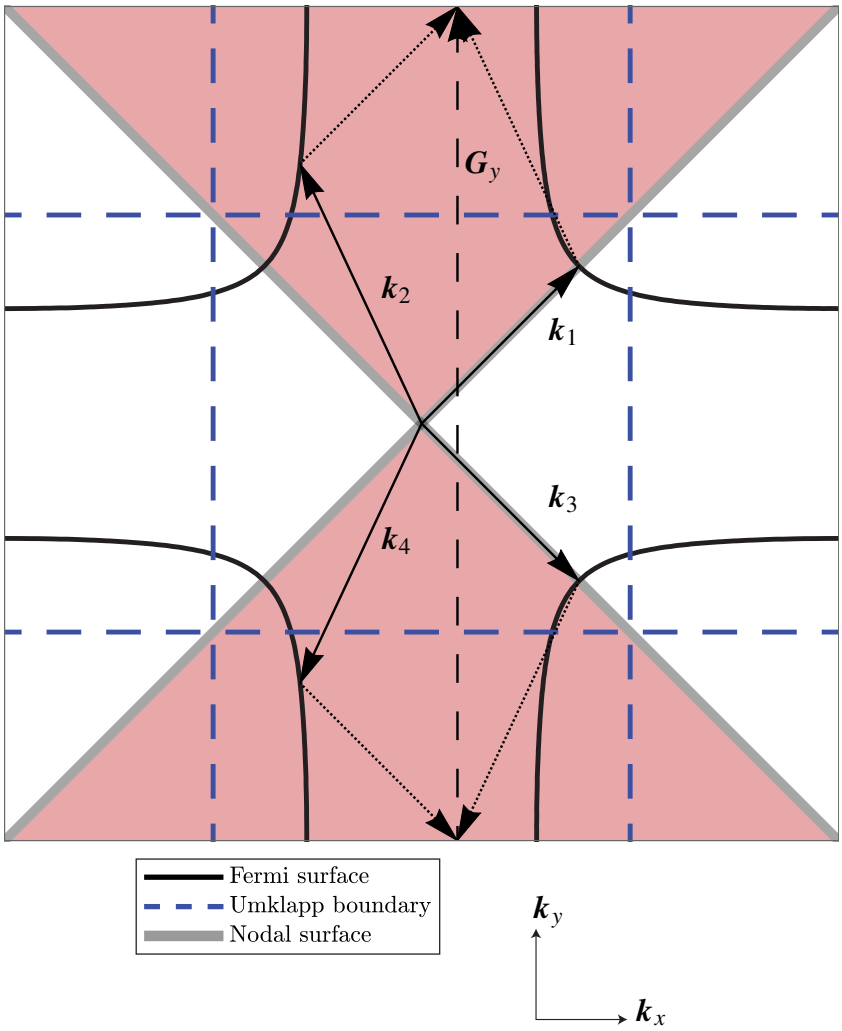

Figure 5.2: The momentum configuration giving rise to umklapp scattering in the high temperature superconductor $YBa_2Cu_3O_{6+x}$, as considered by Walker and Smith [151]. For a quasiparticle located at the node of the superconducting gap ($\boldsymbol{k}_1$), the minimum momentum state for which umklapp scattering is possible is located away from the node ($\boldsymbol{k}_2$), resulting in a non-zero activation energy (gap) for the scattering process, which introduces an exponential temperature dependence into the scattering rate, $\tau_u^{-1} \propto T^2 \exp\{-\Delta_U / k_b T\}$. The 'umklapp gap' Δ_U is given by the gap value for the quasiparticles located away from the nodes ($\boldsymbol{k}_2$ and $\boldsymbol{k}_4$), the minimum gap energy associated with the umklapp scattering. This parallelogram construction of the minimum momentum (and therefore energy) configuration for umklapp scattering is sufficient to prove the absence of umklapp processes involving only nodal quasiparticles, but not to uniquely define the minimum energy scale Δ_U. The solid vectors represent the quasiparticles involved in the scattering process, with the dashed vector the total momentum transfer (given by a reciprocal lattice vector). The dotted vectors are a guide to the eye to show the total momentum before and after the scattering process, and the background shading denotes the phase of the superconducting gap.

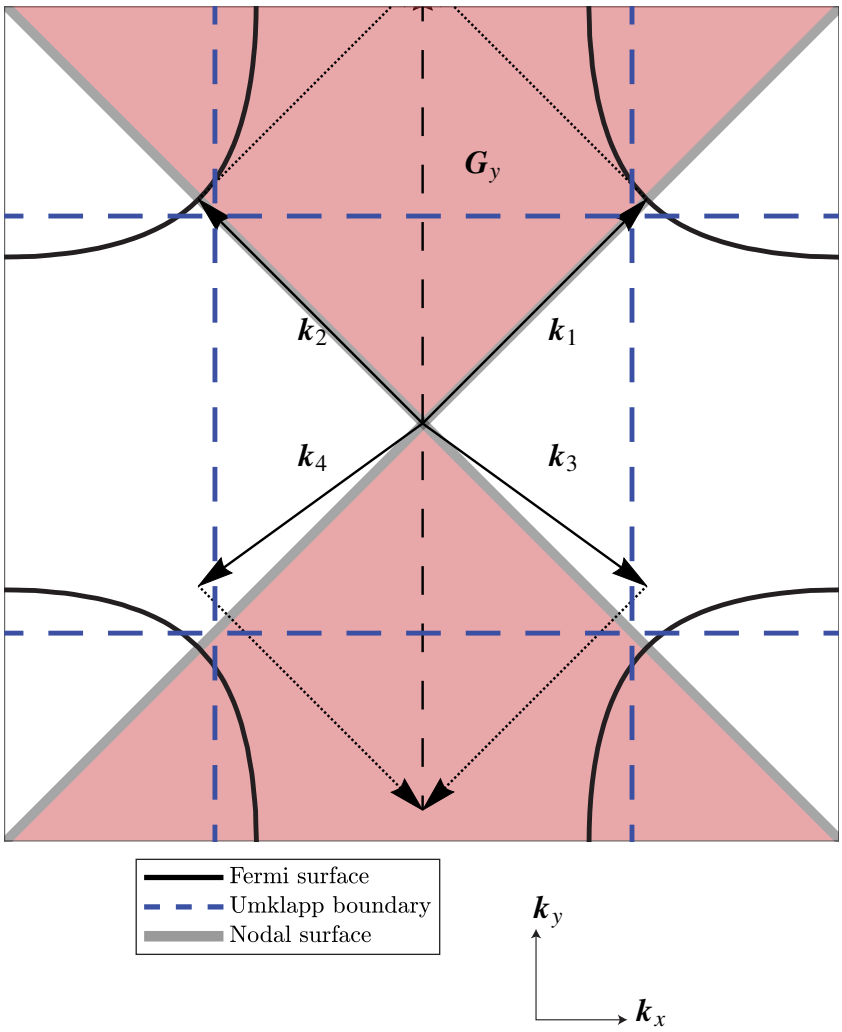

Figure 5.3: For a Fermi surface with nodes outside the minimum boundary for umklapp scattering, an umklapp scattering process involving only nodal quasiparticles is not possible. The umklapp scattering process involving two of the nodal quasiparticles, the states connected by a reciprocal lattice vector to these nodal states do not lie on the Fermi surface, forbidding this process due to energy conservation. It can be seen from this that, except for finely tuned bandstructures or gap functions, there will always be an exponential temperature dependence introduced into the scattering rate responsible for momentum relaxation due to umklapp scattering.

structure is either very finely tuned, or some mechanism other than umklapp scattering is responsible for the current relaxation.

Distinguishing between d-wave pairing symmetries in YBCO from penetration depth experiments

In the previous chapters, a great deal of discussion has been devoted to the $1/T_1$ relaxation rate in superconductors with gaps that have symmetry required or accidental nodes, and the qualitative differences between the two cases. Here, I highlight a possible application of the penetration depth (and quasiparticle scattering rate) measurements as a method to distinguish between different gaps with symmetry required nodes.

In a system without anisotropy in the tight binding parameters in the x and y directions, such

as the model of YBCO used by Walker and Smith, and Duffy *et al.* [102, 151], the nodes of both the '$d_{x^2-y^2}$' (i.e. $\Delta_{\boldsymbol{k}} \propto \cos[k_x] - \cos\left[k_y\right]$) and '$d_{xy}$' ($\Delta_{\boldsymbol{k}} \propto \sin[k_x]\sin\left[k_y\right]$) symmetry gaps lie on high-symmetry axes, making the nodes in both cases symmetry required. In such a case, measurements of $1/T_1$ would be insufficient to determine the gap symmetry, but the scattering rate may distinguish between the two. For the '$d_{x^2-y^2}$' symmetry gap, the umklapp scattering rate will have an exponential temperature dependence, as found by Walker and Smith [151]. In the 'd_{xy}' symmetry case, however, no such exponential temperature dependence is present. As shown in Fig. 5.4, there exists an electron configuration for which the quasiparticles at the nodes (on the Brillouin zone boundary) contribute to the umklapp scattering, with no umklapp gap, which would lead to a cubic temperature dependence of the scattering rate, rather than the observed $\tau_u^{-1} \propto T^2 \exp\{-\Delta_U/k_BT\}$. This suggests the possibility of using such measurements as a more direct probe of the detailed form of the superconducting gap than has been previously considered. Assuming that we know from other experiments that the pairing is d-wave, this then allows the gap symmetry to be determined without requiring the use of tunnelling experiments [60, 61], which have proved challenging in materials other than the cuprates.

5.3 Umklapp scattering and phase space restrictions in κ-Br

I will limit the discussion of specific relaxation mechanisms to κ-Br as, while the experimental properties of κ-Br and $CeCoIn_5$ are very similar, κ-Br has the simpler bandstructure. Additionally, I will only consider nodal gap functions, as the scattering rate shows no exponential temperature dependence, as would be expected for a nodeless state. The results discussed in this chapter help to reinforce the ideas of the preceding chapters, that the experimental properties of the material give a greater insight into the gap structure of the superconducting state than previously understood. More specifically, these results reinforce the identification of the superconducting gap in κ-Br as the symmetry required '$d_{x^2-y^2}$-wave' state.

Measurements of the penetration depth, via microwave cavity resonance, on both κ-Br and $CeCoIn_5$ have shown the presence of a cubic temperature dependence of the quasiparticle scattering rate, to the lowest temperatures measured [45, 82]. This is in sharp contrast to the case of YBCO discussed above, where the requirement for non-nodal quasiparticles to be involved in the umklapp scattering processes gave rise to the observed exponential temperature dependence of the scattering rate [151]. It is reasonable to assume, then, that umklapp scattering in κ-Br involving only nodal quasiparticles is possible and responsible for the cubic, rather than exponential, temperature dependence. It is this assumption that I will seek to confirm in the following.

Unlike YBCO, κ-Br has significant anisotropy, resulting in inequivalent conditions for umklapp scattering in the directions of the *a* and *c* crystal axes. As such, the two directions must be considered independently for each symmetry. I will consider momentum configurations similar to that of Walker and Smith [151], with two quasiparticles constrained to have momenta at the node of the superconducting gap and the remaining states determined by the minimum momentum for umklapp scattering, utilising the model parameters, in all cases, of Koretsune and Hotta [130], with a non-zero

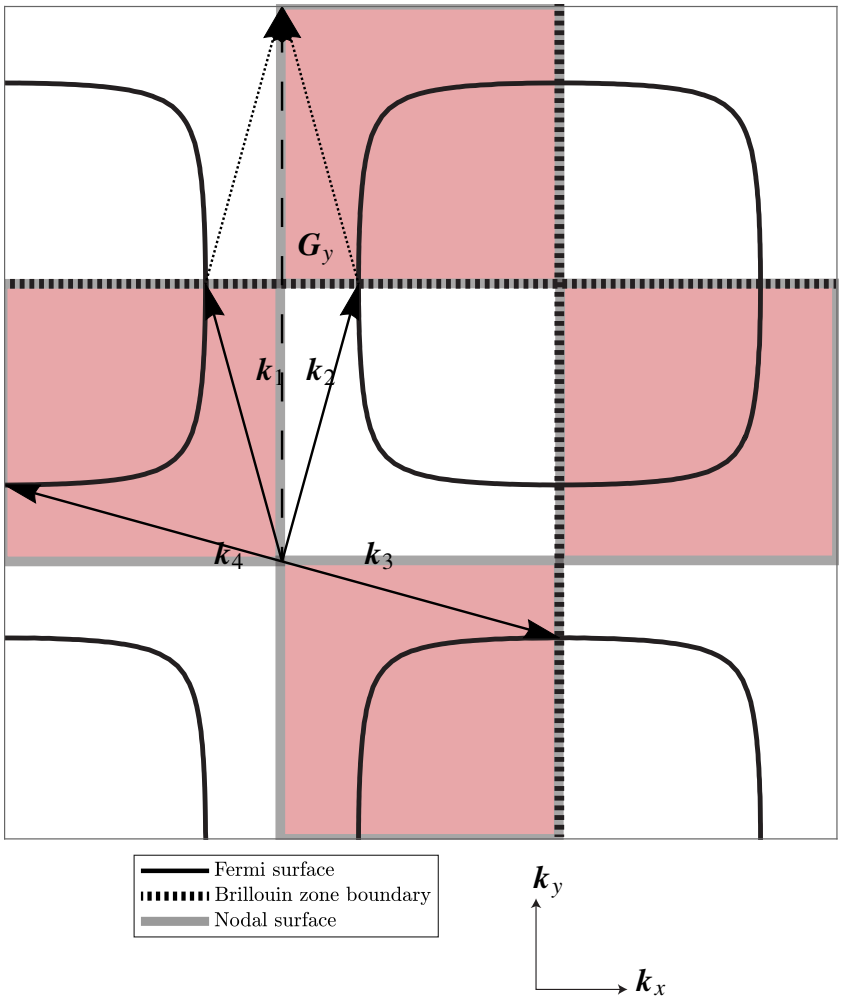

Figure 5.4: Umklapp scattering of nodal quasiparticles in a model for YBCO with a d_{xy}-wave gap, with nodes on the boundaries of the Brillouin zone. In this case, unlike that of Fig. 5.2, the scattering rate for umklapp processes lacks the exponential temperature dependence seen experimentally. The observed scattering rate, then, is sufficient to differentiate between $d_{x^2-y^2}$ and d_{xy} pairing.

magnetic breakdown gap ($\delta_t = 0.03t$). This will allow us to determine the existence or non-existence of umklapp scattering processes involving only nodal quasiparticles.

5.3.1 Symmetry required nodes

I will first discuss those gaps introduced in the preceding chapters that have symmetry required nodes, and are consistent with the NMR measurements, before considering the scattering rate for gaps with accidental nodes.

The gap of Schmalian

In a gap of the form proposed by Schmalian [74], there are nodes aligned with the crystal axes, but none on the boundary of the reduced Brillouin zone of the κ polymorph, as the gap is periodic over the extended Brillouin zone of the β polymorph.

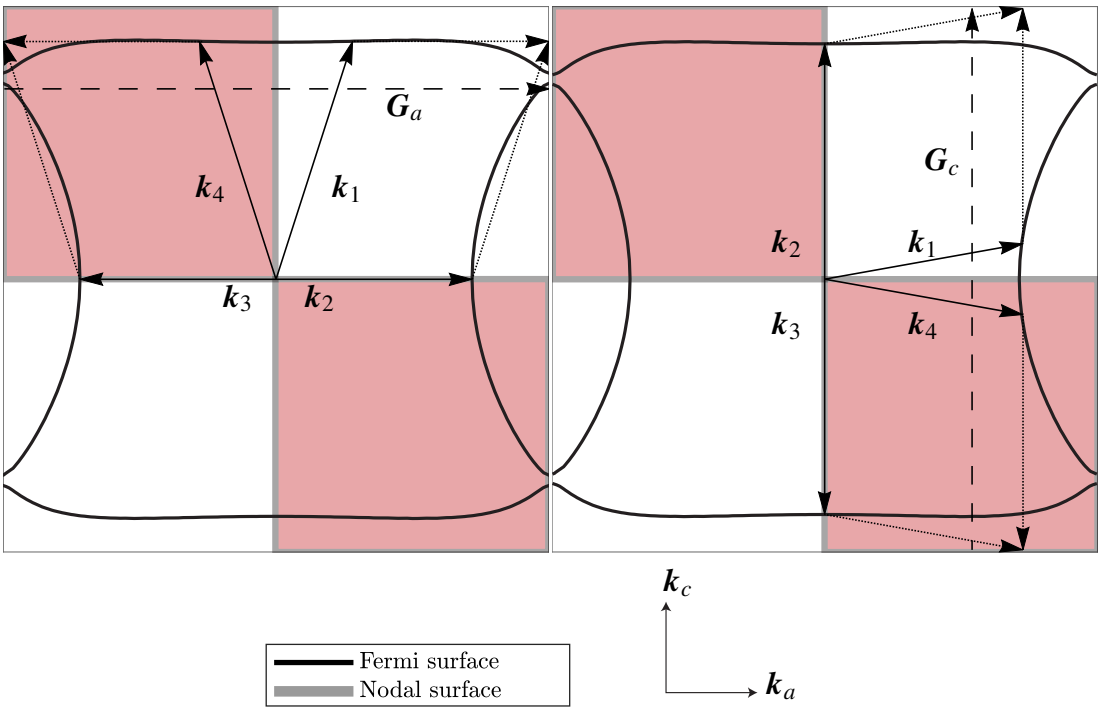

Figure 5.5: Umklapp scattering in κ-Br with a gap with symmetry required nodes of the type discussed by Schmalian [74], in the a (left) and c (right) directions (where a and c are the crystal axes of the material in the highly conducting plane), both of which require the inclusion of non-nodal quasiparticles. Since these processes involves states away from the nodes and therefore a non-zero umklapp gap Δ_U, they result in an exponentially activated temperature dependence in the scattering rate. This gap is then in disagreement with the experimentally observed cubic temperature dependence of the scattering rate measured via the penetration depth [82], despite being consistent with the NMR experiments discussed in earlier chapters.

The minimum energy momentum configurations with two quasiparticles constrained to the nodal positions, for scattering in each direction, are shown in Fig. 5.5. Clearly, in each case, there are quasiparticles away from the nodes involved in the scattering process and there will be a non-zero umklapp gap associated with the process. The scattering rate will then have the exponential temperature dependence ($\tau_u^{-1} \sim T^2 \exp\left[-\Delta_U / k_B T\right]$) seen in the microwave conductivity of YBCO, but not the cubic temperature dependence seen for κ-Br [82]. The gap proposed by Schmalian is therefore insufficient to explain the penetration depth experiments.

A gap with nodes on the boundary of the reduced Brillouin zone

As discussed in earlier chapters, a gap with symmetry required nodes and the periodicity of the reduced (κ) Brillouin zone must have additional nodes where the Fermi surface crosses the boundary of the Brillouin zone. A gap with such nodes will then have potential umklapp scattering processes involving these extra nodes, as well as the umklapp processes described in the previous section. The momentum configurations for umklapp scattering involving nodes on the Brillouin zone boundary are shown in Fig. 5.6.

The presence of nodes at the Brillouin zone boundary allows the possibility for umklapp scattering

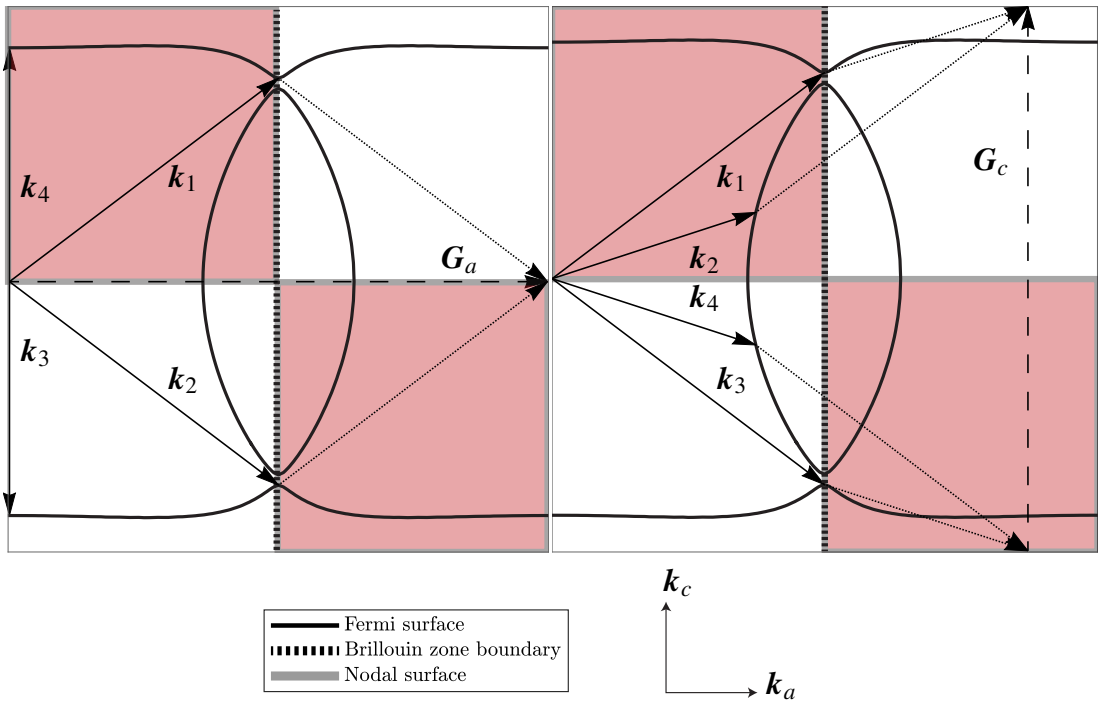

Figure 5.6: Umklapp scattering in κ-Br with a gap with symmetry required nodes, including nodes on the boundary of the reduced Brillouin zone, in the a (left) and c (right) directions, with the former involving only nodal quasiparticles. Unlike the case shown in Fig. 5.5, the nodes on the Brillouin zone boundary introduce the possibility of umklapp scattering in the a direction involving only nodal quasiparticles. This then leads to a cubic temperature dependence for the scattering rate in the a direction, while an exponential temperature dependence is still present for the scattering rate in the c direction. In the penetration depth measurements, however, the quasiparticles are excited into cyclotron orbits and the larger of the two scattering rates dominates the measured rate. The scattering rate is then dominated by the cubic temperature dependence, consistent with the experimental observations [82]. This case differs from that in Fig. 5.5 due to the presence of two separate sets of nodes, separated by $\boldsymbol{G}_a/2$ in the a direction, allowing umklapp scattering in this direction entirely due to nodal quasiparticles.

involving only nodal quasiparticles, unlike the gap proposed by Schmalian [74]. These processes are only possible in one direction, however, with a non-zero umklapp gap present for scattering in the perpendicular direction, resulting in an anisotropic temperature dependence of the microwave conductivity.

The total scattering rate measured in the microwave cavity resonance experiments will depend on the scattering rate in both directions in the highly conducting plane. In these experiments, the quasiparticles are excited into orbits, with scattering out of these orbits responsible for the measured scattering rate. The umklapp scattering rate will then be given by

$$\begin{aligned} \tau_u^{-1} &= \tau_{u,b}^{-1} + \tau_{u,c}^{-1} \\ &\propto CT^3 + DT^2 f\left(\Delta_{U,c}\right) \bar{f}\left(\Delta_{U,c}\right) \approx CT^3, \end{aligned} \tag{5.14}$$

which, for low temperatures, will be dominated by the cubic temperature dependence of the scattering rate in the a direction (unless $D \gg C$, due to a significantly larger phase space for scattering in the c

directions)

$$\lim_{T\to 0} \tau_u^{-1} \approx CT^3. \tag{5.15}$$

This gap is then consistent with both the NMR and penetration depth experiments, unlike the gap of Schmalian [74]. While the anisotropy in the scattering rates is not likely to be measurable via the penetration depth measurements (i.e. via microwave cavity resonance), directional microwave conductivity probes may be able to distinguish the two rates for current relaxation, providing further confirmation of the form of the superconducting gap in κ-Br.

5.3.2 Accidental nodes

In the previous chapters, it was found that superconducting gaps with accidental nodes were only capable of explaining the NMR experiments on κ-Br if very finely tuned, and generally were less consistent with experiment than the symmetry required gaps even when finely tuned. Here I will consider, for completeness, whether gaps with accidental nodes are capable of explaining the observed temperature dependence of the umklapp scattering rate.

For the simplest case, when the gap possesses nodes on the diagonals of the reduced Brillouin zone (typically referred to as d_{xy} symmetry, where the x and y axes are directed along the diagonals of the crystal axes), the momentum configurations giving rise to umklapp scattering are given in Fig. 5.7. As in the case of the gap of Schmalian, umklapp scattering involving only nodal quasiparticles is not possible, and an exponential temperature dependence must be evident for the scattering rate in both directions.

A gap of the form shown in Fig. 5.7 belongs to the same representation of the lattice point group as the s-wave superconducting gap, and the two may mix freely without a phase transition. This intermixing then shifts the position of the nodes of the gap around the Fermi surface, and may in principle be finely tuned to allow for umklapp scattering involving only nodal quasiparticles [i.e. satisfying Eq. (5.8)], provided that the positions of the nodes on the Fermi surface differ by half a reciprocal lattice vector (as is the case in the previous section, considering the symmetry required gap with nodes on the Brillouin zone boundary). Such a specific fine tuning of the isotropic component of the gap is unrealistic, however, and unlikely to simultaneously satisfy the restrictions enforced by the NMR data. A gap with accidental nodes is, therefore, inconsistent with both the NMR and penetration depth experiments.

The more detailed gap of Guterding *et al.*

Finally, I consider the complicated gap proposed by Guterding *et al.* [62, 63, 78], which has eight accidental nodes on the Fermi surface. The Fermi surface and nodal structure of this gap, for parameters fit by Guterding *et al.* to low temperature tunnelling spectra [63], are shown in Fig. 5.8.

For umklapp scattering involving only nodal quasiparticles to be possible, there must be nodes on the Fermi surface separated in one direction by half a reciprocal lattice vector in that direction[4]. As

[4]More rigorously, there exists no collection of nodes satisfying the requirements for umklapp scattering, e.g. Eq. (5.8).

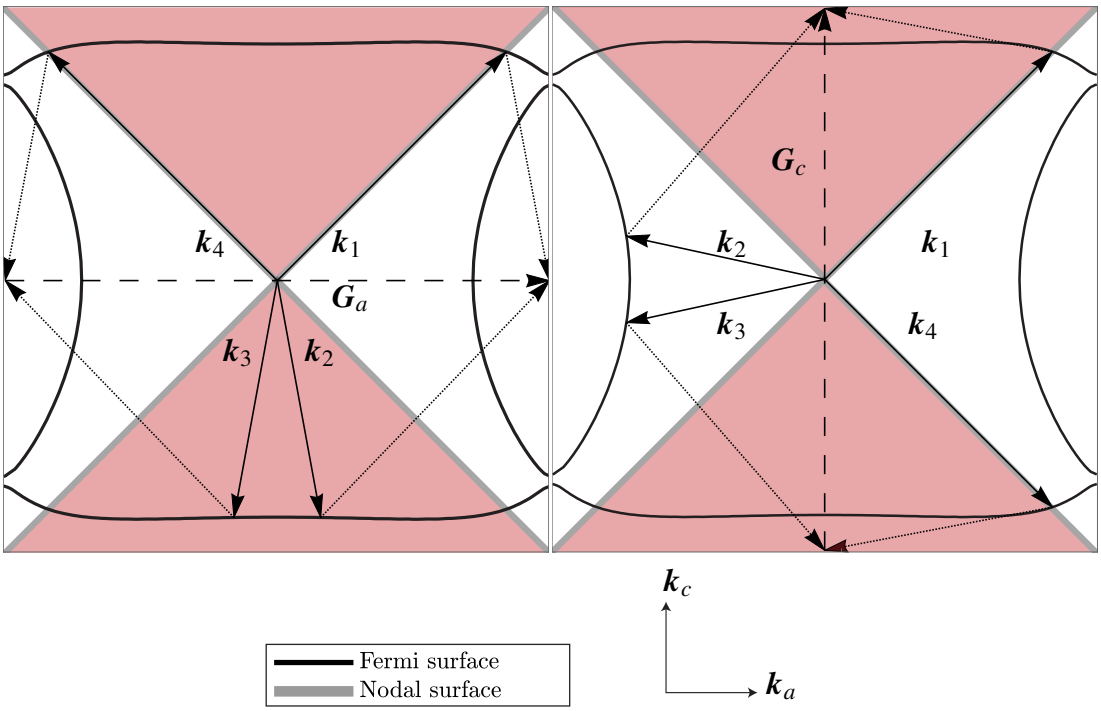

Figure 5.7: Umklapp scattering in κ-Br with a gap with accidental nodes, aligned with the diagonals of the crystal lattice, in the a (left) and c (right) directions. For umklapp scattering in either direction, there is a finite energy required to excite the quasiparticles located away from the node, resulting in a non-zero umklapp gap Δ_U and an expected exponential correction to the temperature dependence scattering rate. This gap can, however, freely mix with an isotropic gap, shifting the positions of the nodes around the Fermi surface, as discussed in the previous chapters. Despite this freedom in shifting the nodal positioning, unless the gap is very carefully tuned such that the nodal positions differ by $\boldsymbol{G}_a/2$ or $\boldsymbol{G}_c/2$, such a gap is inconsistent with the penetration depth experiments performed on κ-Br.

can be seen from this figure, no such combination of nodes is possible for this gap, indicating that an exponential temperature dependence will be present for the scattering rate in both directions. Like the simpler gap with accidental nodes in Fig. 5.7, this gap function is only consistent with the observed cubic temperature dependence for the scattering rate if the parameters for the gap are carefully fine tuned, and not consistent with the parameters extracted from the tunnelling density of states.

As discussed in the context of YBCO, the umklapp scattering rate has a potential use as a probe of the structure of the superconducting gap. Clearly, in κ-Br, a scattering rate that varies cubically with temperature (as has been observed [82]) is only possible due to umklapp scattering if the gap function has symmetry required nodes, with nodes at the Brillouin zone boundaries (as opposed to the symmetry required gap proposed by Schmalian, with no such nodes [74]).

5.4 Conclusions

I have identified a potential use of measurements of the quasiparticle scattering rate in superconductor as a probe of the detailed form of the superconducting gap. While the temperature dependence has, in the past, been seen as an indication of the presence of absence of nodes in the gap, I have argued that the lack of a minimum threshold energy (umklapp gap) in the scattering rate for κ-Br strongly

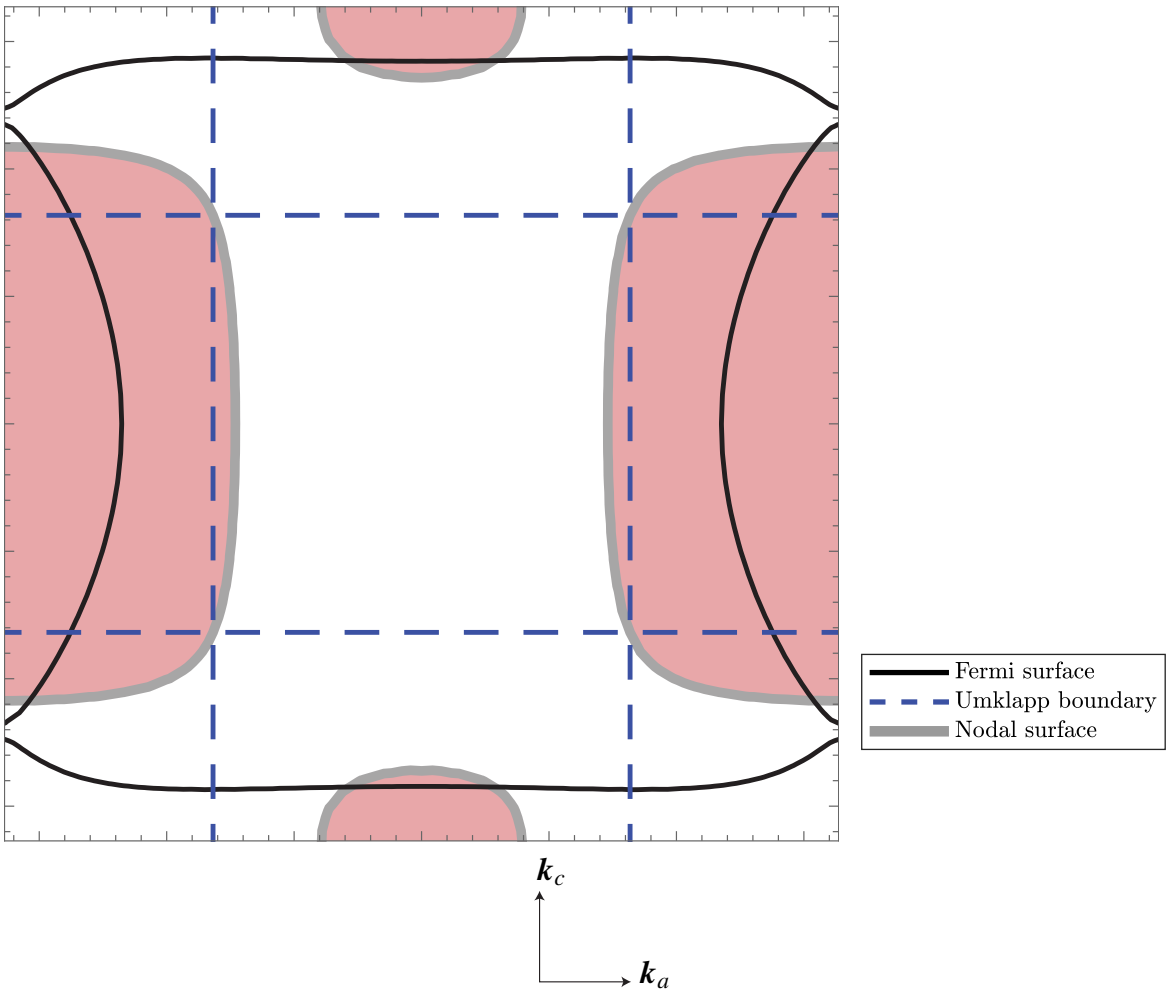

Figure 5.8: The Fermi surface and nodal structure of κ-Br with the complicated gap proposed by Guterding *et al*. [63], with accidental nodes. For umklapp scattering of nodal quasiparticles, there must be some collection of nodes satisfying, in one direction, the umklapp scattering condition Eq. (5.8). As in the case of the simpler gap with accidental nodes shown in Fig. 5.7, the positioning of the nodes fails to satisfy the conditions for umklapp scattering in either direction, unless there is careful fine tuning of the gap parameters (e.g., the parameters are tuned such that nodes are separated by half a reciprocal lattice vector, as in the case of Fig. 5.6). There is then no possible channel, for this gap function, to give rise to the cubic temperature dependence of the scattering rate seen experimentally.

hints at the presence of nodes on the boundary of the reduced Brillouin zone. This then allows a concrete determination of the gap structure, beyond the differentiation between symmetry required and accidental nodes discussed in the previous chapters. For further confirmation, I suggest directional microwave conductivity measurements, for which this analysis predicts an anisotropy in the temperature dependence of the scattering rate.

Chapter 6

Conclusions

In this work, I have examined on the use of experimental data to constrain the form of the superconducting gap, with the ultimate goal of resolving the open question of the gap symmetry in κ-(BEDT-TTF)$_2$Cu[N(CN)$_2$]Br. In the process, I have gained insight into how the form of the gap function in low symmetry superconductors influences both the nuclear magnetic relaxation rate, $1/T_1$, and the quasiparticle scattering rate, τ^{-1}, generally applicable to unconventional superconductors other than κ-Br.

One significant insight of this work has been to demonstrate the differences between nodal superconducting gaps with nodes constrained by symmetry requirements and those with accidental node placement. Many probes of the superconducting gap focus on the behaviour in the low temperature limit, which reflects the differences in the density of states due to the type of node present, or the absence of nodes entirely. Such probes, however, are unable to distinguish between gap functions with the same type of node. Identifying the gap function unambiguously has previously been the domain more complex probes, such as the tunnelling experiments used to identify the gap of the cuprates or directional probes of properties (e.g., the heat capacity). I have found that it is possible, in fact, to differentiate between symmetry required and accidental nodes using far less complicated probes.

In nuclear magnetic resonance, the influence of the coherence factors in the susceptibility is such that a peak, similar to that found by Hebel and Slichter, may be present immediately below the critical temperature for gaps that have accidental nodes. Formally such gap functions belong to the trivial representation of the lattice point group, as does the nodeless 's-wave' gap, and the $1/T_1$ relaxation rate reflects this similarity. Since the node placement is unconstrained by symmetry in such a gap, the nodes may move freely around the Fermi surface. I have examined this possibility by allowing an admixture of the isotropic 's-wave' gap and the anisotropic 'd-wave' gap with accidental nodes. In the low (D_{2h}) symmetry toy model examined in Chapter 2, the gap functions with symmetry required and accidental nodes are easily defined and examined, and it was found that while shifting the accidental nodes may reduce the magnitude of the peak, removing it entirely required a very finely tuned gap function not likely to be realistic for any material.

The peak seen in the nuclear magnetic relaxation rate can be controlled, but not removed entirely,

by the influence of bandstructure effects, particularly by the proximity of Van Hove singularities to the Fermi surface, as examined in Chapter 2. The peak is also affected by lifetime effects due to impurity scattering and electron-electron interactions. How a finite quasiparticle lifetime due to impurity scattering affected the relaxation rate was investigated in Chapter 2 and found to be relatively insignificant, while the influence of electron-electron interactions, particularly higher-order effects due to vertex corrections, formed the focus of Chapter 3. In this chapter, I found that sufficiently large interaction strengths, in the random phase approximation, may suppress the peak even in the case of an isotropic 's-wave' gap, and that the peak observed for a gap with accidental nodes was robust to interactions up to a similarly large interaction strength.

In Chapter 3, I also extended the treatment of $1/T_1$ from the toy model of Chapter 2 to more realistic models of BEDT-TTF based superconductors, again finding that gaps with accidental nodes display a Hebel-Slichter-like peak below T_c. The possibility of removing the Hebel-Slichter peak by the inclusion of strong interactions is of particular interest in κ-Br, for which an isotropic gap has been argued on the basis of heat capacity and thermal conductivity measurements. When interactions are significant enough to suppress the peak, it was also found that the low temperature behaviour of the relaxation rate still reflects the low energy density of states, however, and it is therefore necessary to consider the low temperature behaviour as well as the presence of absence of a Hebel-Slichter-like peak. In κ-Br, the low temperature behaviour of $1/T_1$ is indicative of a gap with line nodes, rather than an isotropic gap.

To more concretely compare the experimentally observed relaxation rate with the predictions based on the gap structure, I discussed the various effective models and proposed gap structures for κ-Br in Chapter 4, before making comparison with experimental data. For a realistic model bandstructure, the gap functions with symmetry required nodes provide the most accurate fit to the data. Of the two gaps with symmetry required nodes considered, with and without nodes on the Brillouin zone boundary. Of the two symmetry required gaps, the interaction strength which best fits the data for the gap without nodes on the Brillouin zone boundary is well below the expected magnitude for κ-Br, making it inconsistent with other experiments, and the proximity of the material to the Mott transition.

Differentiating between the two symmetry required gaps more definitively lead us to consider the scattering rate. In Chapter 5 I have reviewed how the scattering rate due to umklapp processes is influenced by both the geometry of the Fermi surface, in a Fermi liquid, and the nodal positioning, in a superconductor. The scattering rate measured in the penetration depth, in a superconductor with nodes in the gap function, was shown to vary with temperature as $T^2 \exp(-\Delta_U/T)$, unless the nodes are positioned such that umklapp processes involving only nodal quasiparticles are possible, in which case the scattering rate varies as T^3.

In the cuprate superconductor $YBa_2Cu_3O_7$, the observed exponential temperature dependence of the scattering rate is then sufficient to differentiate between the possible d_{xy} and $d_{x^2-y^2}$-wave gap functions. For κ-Br, the scattering rate is found experimentally to very cubically with temperature, which is only possible for the $d_{x^2-y^2}$-wave superconducting gap.

The results for all of the gap functions considered are shown in Table 6.1, and on the basis of the $1/T_1$ and scattering rate data, I conclude that κ-(BEDT-TTF)$_2$Cu[N(CN)$_2$]Br has a $d_{x^2-y^2}$-wave

Gap function	Irrep	Nodes	$1/T_1T$ peak	$1/T_1T$ fit to data	τ_U^{-1}
s	A_{1g}	None	Yes	$\approx 0.9U_c$	$\propto T^2 e^{(-\Delta_U/T)}$
s+d_{xy}	A_{1g}	Accidental	Yes	$\gtrapprox 0.94U_c$	$\propto T^2 e^{(-\Delta_U/T)}$
$d_{x^2-y^2}$	B_{2g}	Symmetry required	No	$\approx 0.91U_c$	$\propto T^3$
Schmalian [74]	B_{2g}	Symmetry required	No	$\approx 0.51U_c$	$\propto T^2 e^{(-\Delta_U/T)}$
Guterding [63]	A_{1g}	Accidental	Slight	$\approx 0.96U_c$	$\propto T^2 e^{(-\Delta_U/T)}$

Table 6.1: Summary of results regarding the form of the superconducting gap in κ-(BEDT-TTF)$_2$Cu[N(CN)$_2$]Br. Here 'Irrep' is the irreducible representation of the point group to which the gap function belongs, and green, red and yellow cell shading indicate agreement, disagreement and potential disagreement with experiment, respectively. While the anisotropic gaps in the trivial A_{1g} representation can potentially be finely tuned to fit the data for $1/T_1$ and the scattering rate temperature dependence, they cannot reproduce both simultaneously. On the basis of these results, I confirm that, of the considered gap functions, only the '$d_{x^2-y^2}$-wave' gap, with symmetry required nodes (and nodes of the boundary of the Brillouin zone), is capable of reproducing all of the experimental data with reasonable parameters.

superconducting gap (i.e. in the B_{2g} representation of the D_{2h} point group).

Bibliography

[1] D. C. Cavanagh and B. J. Powell. Nuclear magnetic resonance in low-symmetry superconductors. *Physical Review B*, 97(2):024509, Jan. 2018.

[2] D. C. Cavanagh, A. C. Jacko, and B. J. Powell. Breakdown of the universality of the Kadowaki-Woods ratio in multi-band metals. *Physical Review B*, 92(19):195138, Nov. 2015.

[3] J. Bardeen, L. N. Cooper, and J. R. Schrieffer. Microscopic theory of superconductivity. *Physical Review*, 106(1):162–164, July 1957.

[4] J. Bardeen, L. N. Cooper, and J. R. Schrieffer. Theory of superconductivity. *Physical Review*, 108(5):1175–1204, July 1957.

[5] J. F. Annett. Unconventional pairing in anomalous superconductors. *Physica C: Superconductivity*, 317-318:1–8, 1999.

[6] R. H. McKenzie. Similarities between organic and cuprate superconductors. *Science*, 278(5339):820–821, Oct. 1997.

[7] B. J. Powell and R. H. McKenzie. Quantum frustration in organic Mott insulators: from spin liquids to unconventional superconductors. *Reports on Progress in Physics*, 74(5):056501, 2011.

[8] D. J. Scalapino. A common thread: The pairing interaction for unconventional superconductors. *Reviews of Modern Physics*, 84(4):1383–1417, Oct. 2012.

[9] M. Sigrist and K. Ueda. Phenomenological theory of unconventional superconductivity. *Reviews of Modern Physics*, 63(2):239–311, Apr. 1991.

[10] J. F. Annett. Symmetry of the order parameter for high-temperature superconductivity. *Advances in Physics*, 39(2):83–126, Apr. 1990.

[11] J. B. Ketterson and S. N. Song. *Superconductivity*. Cambridge University Press, Cambridge, 1999.

[12] M. Tinkham. *Introduction to Superconductivity*. Dover, New York, 2004.

[13] J. F. Annett. *Superconductivity, Superfluids and Condensates*. Oxford University Press, 2004.

[14] L. N. Cooper. Bound electron pairs in a degenerate fermi gas. *Physical Review*, 104(4):1189–1190, July 1956.

[15] J. Bardeen and D. Pines. Electron-phonon interaction in metals. *Physical Review*, 99(4):1140–1150, July 1955.

[16] P. Coleman. *An Introduction to Many-Body Physics*. Cambridge University Press, Cambridge, 2015.

[17] M. N. Chernodub. *Electromagnetic Superconductivity of Vacuum Induced by Strong Magnetic Field*. Springer, 2013.

[18] N. Bulut and D. J. Scalapino. Weak-coupling model of spin fluctuations in the superconducting state of the layered cuprates. *Physical Review B*, 45(5):2371–2384, Feb. 1992.

[19] Y. Nambu. Quasi-particles and gauge invariance in the theory of superconductivity. *Physical Review*, 117(3):648–663, Feb. 1960.

[20] V. P. Mineev and K. V. Samokhin. *Introduction to Unconventional Superconductivity*. Gordon and Breach, Amsterdam, 1999.

[21] V. L. Ginzburg and L. D. Landau. On the theory of superconductivity. *Zh. Eksp. Teor. Fiz.*, 20:1064, 1950.

[22] L. P. Gor'kov. Microscopic derivation of the Ginzburg-Landau equations in the theory of superconductivity. *Sov. Phys. JETP*, 36:1364, 1959.

[23] E. Maxwell. Isotope effect in the superconductivity of mercury. *Physical Review*, 78(4):477–477, July 1950.

[24] Y. J. Uemura, L. P. Le, G. M. Luke, B. J. Sternlieb, W. D. Wu, J. H. Brewer, T. M. Riseman, C. L. Seaman, M. B. Maple, M. Ishikawa, D. G. Hinks, J. D. Jorgensen, G. Saito, and H. Yamochi. Basic similarities among cuprate, bismuthate, organic, chevrel-phase, and heavy-fermion superconductors shown by penetration-depth measurements. *Physical Review Letters*, 66(20):2665–2668, July 1991.

[25] B. J. Powell and R. H. McKenzie. Strong electronic correlations in superconducting organic charge transfer salts. *Journal of Physics: Condensed Matter*, 18(45):R827, 2006.

[26] Y. Cao, V. Fatemi, S. Fang, K. Watanabe, T. Taniguchi, E. Kaxiras, and P. Jarillo-Herrero. Unconventional superconductivity in magic-angle graphene superlattices. *Nature*, 556(7699):43–50, Apr. 2018.

[27] Y. Cao, V. Fatemi, A. Demir, S. Fang, S. L. Tomarken, J. Y. Luo, J. D. Sanchez-Yamagishi, K. Watanabe, T. Taniguchi, E. Kaxiras, R. C. Ashoori, and P. Jarillo-Herrero. Correlated insulator

behaviour at half-filling in magic-angle graphene superlattices. *Nature*, 556(7699):80–84, Apr. 2018.

[28] P. W. Anderson. More is different. *Science*, 177(4047):393–396, July 1972.

[29] M. R. Norman. The Challenge of Unconventional Superconductivity. *Science*, 332(6026):196–200, Apr. 2011.

[30] G. R. Stewart. Unconventional superconductivity. *Advances in Physics*, 66(2):75–196, Apr. 2017.

[31] G. R. Stewart. Superconductivity in iron compounds. *Reviews of Modern Physics*, 83(4):1589–1652, Dec. 2011.

[32] J. P. Carbotte. Properties of boson-exchange superconductors. *Reviews of Modern Physics*, 62(4):1027–1157, Oct. 1990.

[33] G. M. Eliashberg. Interactions between electrons and lattice vibrations in a superconductor. *Journal of Experimental and Theoretical Physics*, 12:1000, 1959.

[34] G. M. Eliashberg. Temperature green's function for electrons in a superconductor. *Journal of Experimental and Theoretical Physics*, 11:696, 1960.

[35] Z. F. Weng, M. Smidman, L. Jiao, X. Lu, and H. Q. Yuan. Multiple quantum phase transitions and superconductivity in Ce-based heavy fermions. *Reports on Progress in Physics*, 79(9):094503, 2016.

[36] G. R. Stewart. Heavy-fermion systems. *Reviews of Modern Physics*, 56(4):755–787, Oct. 1984.

[37] B. D. White, J. D. Thompson, and M. B. Maple. Unconventional superconductivity in heavy-fermion compounds. *Physica C: Superconductivity and its Applications*, 514:246–278, July 2015.

[38] Y. Yanase, T. Jujo, T. Nomura, H. Ikeda, T. Hotta, and K. Yamada. Theory of superconductivity in strongly correlated electron systems. *Physics Reports*, 387(1):1–149, Nov. 2003.

[39] H. Hosono and K. Kuroki. Iron-based superconductors: Current status of materials and pairing mechanism. *Physica C: Superconductivity and its Applications*, 514:399–422, July 2015.

[40] A. V. Chubukov, D. V. Efremov, and I. Eremin. Magnetism, superconductivity, and pairing symmetry in iron-based superconductors. *Physical Review B*, 78(13):134512, Oct. 2008.

[41] D. Vollhardt and P. Wolfe. *Superfluid Phases of Helium 3*. Taylor and Francis, London, 1999.

[42] B. J. Powell. Mixed order parameters, accidental nodes and broken time reversal symmetry in organic superconductors: a group theoretical analysis. *Journal of Physics: Condensed Matter*, 18(46):L575, 2006.

[43] G.-Y. Chen, X. Zhu, H. Yang, and H.-H. Wen. Highly anisotropic superconducting gaps and possible evidence of antiferromagnetic order in FeSe single crystals. *Physical Review B*, 96(6):064524, Aug. 2017.

[44] T. Hanaguri, S. Niitaka, K. Kuroki, and H. Takagi. Unconventional s-wave superconductivity in Fe(Se,Te). *Science*, 328(5977):474–476, Apr. 2010.

[45] C. J. S. Truncik, W. A. Huttema, P. J. Turner, S. Özcan, N. C. Murphy, P. R. Carrière, E. Thewalt, K. J. Morse, A. J. Koenig, J. L. Sarrao, and D. M. Broun. Nodal quasiparticle dynamics in the heavy fermion superconductor $CeCoIn_5$ revealed by precision microwave spectroscopy. *Nature Communications*, 4:2477, Sept. 2013.

[46] M. A. Tanatar, J. Paglione, S. Nakatsuji, D. G. Hawthorn, E. Boaknin, R. W. Hill, F. Ronning, M. Sutherland, L. Taillefer, C. Petrovic, P. C. Canfield, and Z. Fisk. Unpaired electrons in the heavy-fermion superconductor $CeCoIn_5$. *Physical Review Letters*, 95(6):067002, Aug. 2005.

[47] E. Bauer and M. Sigrist. *Non-centrosymmetric Superconductors: Introduction and Overview*. Springer-Verlag, Heidelberg, 2012.

[48] T. Ishiguro, K. Yamaji, and G. Saito. *Organic Superconductors*. Springer, Heidelberg, 1998.

[49] K. A. Kouznetsov, A. G. Sun, B. Chen, A. S. Katz, S. R. Bahcall, J. Clarke, R. C. Dynes, D. A. Gajewski, S. H. Han, M. B. Maple, J. Giapintzakis, J.-T. Kim, and D. M. Ginsberg. *c*-axis Josephson tunneling between $YBa_2Cu_3O_{7\delta}$ and Pb: Direct evidence for mixed order parameter symmetry in a high- T_c superconductor. *Physical Review Letters*, 79(16):3050–3053, Oct. 1997.

[50] A. Ono and Y. Ishizawa. Preparation and properties of three types of orthorhombic superconductor $Ba_2YCu_{3-x}O_{7-y}$. *Japanese Journal of Applied Physics*, 26(6A):L1043, June 1987.

[51] L. Zhao, C. A. Belvin, R. Liang, D. A. Bonn, W. N. Hardy, N. P. Armitage, and D. Hsieh. A global inversion-symmetry-broken phase inside the pseudogap region of $YBa_2Cu_3O_y$. *Nature Physics*, 13(3):250, Mar. 2017.

[52] J. Wu, A. T. Bollinger, X. He, and I. Božović. Spontaneous breaking of rotational symmetry in copper oxide superconductors. *Nature*, 547(7664):432, July 2017.

[53] G. M. Luke, Y. Fudamoto, K. M. Kojima, M. I. Larkin, J. Merrin, B. Nachumi, Y. J. Uemura, Y. Maeno, Z. Q. Mao, Y. Mori, H. Nakamura, and M. Sigrist. Time-reversal symmetry-breaking superconductivity in Sr_2RuO_4. *Nature*, 394(6693):558–561, Aug. 1998.

[54] L. Nie, A. V. Maharaj, E. Fradkin, and S. A. Kivelson. Vestigial nematicity from spin and/or charge order in the cuprates. *Physical Review B*, 96(8):085142, Aug. 2017.

[55] Y. Sato, S. Kasahara, H. Murayama, Y. Kasahara, E.-G. Moon, T. Nishizaki, T. Loew, J. Porras, B. Keimer, T. Shibauchi, and Y. Matsuda. Thermodynamic evidence for a nematic phase transition at the onset of the pseudogap in $YBa_2Cu_3O_y$. *Nature Physics*, 13(11):1074, July 2017.

[56] S. Kasahara, H. J. Shi, K. Hashimoto, S. Tonegawa, Y. Mizukami, T. Shibauchi, K. Sugimoto, T. Fukuda, T. Terashima, A. H. Nevidomskyy, and Y. Matsuda. Electronic nematicity above the structural and superconducting transition in $BaFe_2(As_{1x}P_x)_2$. *Nature*, 486(7403):382, June 2012.

[57] R. M. Fernandes and A. J. Millis. Nematicity as a probe of superconducting pairing in iron-based superconductors. *Physical Review Letters*, 111(12):127001, Sept. 2013.

[58] A. E. Böhmer, F. Hardy, F. Eilers, D. Ernst, P. Adelmann, P. Schweiss, T. Wolf, and C. Meingast. Lack of coupling between superconductivity and orthorhombic distortion in stoichiometric single-crystalline FeSe. *Physical Review B*, 87(18):180505, May 2013.

[59] F. Ronning, T. Helm, K. R. Shirer, M. D. Bachmann, L. Balicas, M. K. Chan, B. J. Ramshaw, R. D. McDonald, F. F. Balakirev, M. Jaime, E. D. Bauer, and P. J. W. Moll. Electronic in-plane symmetry breaking at field-tuned quantum criticality in $CeRhIn_5$ <. *Nature*, 548(7667):313, Aug. 2017.

[60] D. A. Wollman, D. J. Van Harlingen, W. C. Lee, D. M. Ginsberg, and A. J. Leggett. Experimental determination of the superconducting pairing state in YBCO from the phase coherence of YBCO-Pb dc SQUIDs. *Physical Review Letters*, 71(13):2134–2137, Sept. 1993.

[61] C. C. Tsuei, J. R. Kirtley, C. C. Chi, L. S. Yu-Jahnes, A. Gupta, T. Shaw, J. Z. Sun, and M. B. Ketchen. Pairing symmetry and flux quantization in a tricrystal superconducting ring of $YBa_2Cu_3O_{7-\delta}$. *Physical Review Letters*, 73(4):593–596, July 1994.

[62] D. Guterding, M. Altmeyer, H. O. Jeschke, and R. Valentí. Near-degeneracy of extended $s + d_{x^2-y^2}$ and d_{xy} order parameters in quasi-two-dimensional organic superconductors. *Physical Review B*, 94(2):024515, July 2016.

[63] D. Guterding, S. Diehl, M. Altmeyer, T. Methfessel, U. Tutsch, H. Schubert, M. Lang, J. Müller, M. Huth, H. O. Jeschke, R. Valentí, M. Jourdan, and H.-J. Elmers. Evidence for eight-node mixed-symmetry superconductivity in a correlated organic metal. *Physical Review Letters*, 116(23):237001, June 2016.

[64] K. Hashimoto. *Non-Universal Superconducting Gap Structure in Iron-Pnictides Revealed by Magnetic Penetration Depth Measurements*. Springer Japan, 2013.

[65] J. Wosnitza. Quasi-two-dimensional organic superconductors. *Journal of Low Temperature Physics*, 146(5-6):641–667, Mar. 2007.

[66] I. Askerzade. *Unconventional Superconductors: Anisotropy and Multiband Effects*. Springer Series in Materials Science. Springer-Verlag, Berlin Heidelberg, 2012.

[67] J. Wosnitza. Superconductivity in layered organic metals. *Crystals*, 2(2):248–265, Apr. 2012.

[68] K. Izawa, H. Yamaguchi, T. Sasaki, and Y. Matsuda. Superconducting gap structure of $\kappa - (\mathrm{BEDT-TTF})_2\mathrm{Cu(NCS)}_2$ probed by thermal conductivity tensor. *Physical Review Letters*, 88(2):027002, Dec. 2001.

[69] K. Izawa, H. Takahashi, H. Yamaguchi, Y. Matsuda, M. Suzuki, T. Sasaki, T. Fukase, Y. Yoshida, R. Settai, and Y. Onuki. Superconducting gap structure of spin-triplet superconductor Sr_2RuO_4 studied by thermal conductivity. *Physical Review Letters*, 86(12):2653–2656, Mar. 2001.

[70] R. Prozorov and R. W. Giannetta. Magnetic penetration depth in unconventional superconductors. *Superconductor Science and Technology*, 19(8):R41, June 2006.

[71] Ø. Fischer, M. Kugler, I. Maggio-Aprile, C. Berthod, and C. Renner. Scanning tunneling spectroscopy of high-temperature superconductors. *Reviews of Modern Physics*, 79(1):353–419, Mar. 2007.

[72] F. Giubileo, D. Roditchev, W. Sacks, R. Lamy, and J. Klein. Strong coupling and double-gap density of states in superconducting MgB_2. *EPL (Europhysics Letters)*, 58(5):764, June 2002.

[73] H. Kotegawa, K. Ishida, Y. Kitaoka, T. Muranaka, N. Nakagawa, H. Takagiwa, and J. Akimitsu. Evidence for strong-coupling s-wave superconductivity in MgB2: 11B-NMR study of MgB2 and the related materials. *Physica C: Superconductivity*, 378-381:25–32, Oct. 2002.

[74] J. Schmalian. Pairing due to spin fluctuations in layered organic superconductors. *Physical Review Letters*, 81(19):4232–4235, Nov. 1998.

[75] K. Kuroki, T. Kimura, R. Arita, Y. Tanaka, and Y. Matsuda. $d_{x^2-y^2}$ versus d_{xy}- like pairings in organic superconductors κ-(BEDT-TTF)$_2X$. *Physical Review B*, 65(10):100516, Mar. 2002.

[76] B. J. Powell and R. H. McKenzie. Dependence of the superconducting transition temperature of organic molecular crystals on intrinsically nonmagnetic disorder: A signature of either unconventional superconductivity or the atypical formation of magnetic moments. *Physical Review B*, 69(2):024519, Jan. 2004.

[77] B. J. Powell and R. H. McKenzie. Symmetry of the superconducting order parameter in frustrated systems determined by the spatial anisotropy of spin correlations. *Physical Review Letters*, 98(2):027005, Jan. 2007.

[78] K. Zantout, M. Altmeyer, S. Backes, and R. Valentí. Superconductivity in correlated BEDT-TTF molecular conductors: Critical temperatures and gap symmetries. *Physical Review B*, 97(1):014530, Jan. 2018.

[79] J. Wosnitza, S. Wanka, J. Hagel, M. Reibelt, D. Schweitzer, and J. A. Schlueter. Thermodynamic properties of quasi-two-dimensional organic superconductors. *Synthetic Metals*, 133-134:201–203, Mar. 2003.

[80] H. Elsinger, J. Wosnitza, S. Wanka, J. Hagel, D. Schweitzer, and W. Strunz. κ – (BEDT – TTF)$_2$Cu[N(CN)$_2$]Br: A fully gapped strong-coupling superconductor. *Physical Review Letters*, 84(26):6098–6101, June 2000.

[81] S. Kühlmorgen, R. Schönemann, E. L. Green, J. Müller, and J. Wosnitza. Investigation of the superconducting gap structure in κ-(BEDT-TTF)$_2$Cu(NCS)$_2$ and κ-(BEDT-TTF)$_2$Cu[N(CN)$_2$]Br by means of thermal-conductivity measurements. *Journal of Physics: Condensed Matter*, 29(40):405604, 2017.

[82] S. Milbradt, A. A. Bardin, C. J. S. Truncik, W. A. Huttema, A. C. Jacko, P. L. Burn, S.-C. Lo, B. J. Powell, and D. M. Broun. In-plane superfluid density and microwave conductivity of the organic superconductor κ-(BEDT-TTF)$_2$Cu[N(CN)$_2$]Br: Evidence for d-wave pairing and resilient quasiparticles. *Physical Review B*, 88(6):064501, Aug. 2013.

[83] M. Dumm, D. Faltermeier, N. Drichko, M. Dressel, C. Mézière, and P. Batail. Bandwidth-controlled Mott transition in κ-(BEDT-TTF)$_2$Cu[N(CN)$_2$]Br$_x$Cl$_{1-x}$: Optical studies of correlated carriers. *Physical Review B*, 79(19):195106, May 2009.

[84] H. Mayaffre, P. Wzietek, D. Jérome, C. Lenoir, and P. Batail. Superconducting state of κ-(ET)$_2$CU[N(CN)$_2$]Br studied by13 C NMR: Evidence for vortex-core-induced nuclear relaxation and unconventional pairing. *Physical Review Letters*, 75(22):4122–4125, Nov. 1995.

[85] K. Kanoda, K. Miyagawa, A. Kawamoto, and Y. Nakazawa. NMR relaxation rate in the superconducting state of the organic conductor κ-(BEDT-TTF)$_2$Cu[N(CN)$_2$]Br. *Physical Review B*, 54(1):76–79, July 1996.

[86] J. Müller, M. Lang, R. Helfrich, F. Steglich, and T. Sasaki. High-resolution ac-calorimetry studies of the quasi-two-dimensional organic superconductor κ – (BEDT – TTF)$_2$Cu(NCS)$_2$. *Physical Review B*, 65(14):140509, Mar. 2002.

[87] Y. Nakazawa and K. Kanoda. Low-temperature specific heat of κ-(BEDT-TTF)$_2$Cu[N(CN)$_2$]Br in the superconducting state. *Physical Review B*, 55(14):R8670–R8673, Apr. 1997.

[88] O. J. Taylor, A. Carrington, and J. A. Schlueter. Specific-heat measurements of the gap structure of the organic superconductors κ–(ET)$_2$Cu[N(CN)$_2$]Br and κ–(ET)$_2$Cu(NCS)$_2$. *Physical Review Letters*, 99(5):057001, July 2007.

[89] L. Malone, O. J. Taylor, J. A. Schlueter, and A. Carrington. Location of gap nodes in the organic superconductors κ–(ET)$_2$Cu(NCS)$_2$ and κ–(ET)$_2$Cu[N(CN)$_2$]Br determined by magnetocalorimetry. *Physical Review B*, 82(1):014522, July 2010.

[90] M. Lang, N. Toyota, T. Sasaki, and H. Sato. Magnetic penetration depth of \ensuremath{\kappa}-(BEDT-TTF${)}_{2}$Cu[N(CN${)}_{2}$]Br, determined from the reversible magnetization. *Physical Review B*, 46(9):5822–5825, Sept. 1992.

[91] N. Yoneyama, A. Higashihara, T. Sasaki, T. Nojima, and N. Kobayashi. Impurity Effect on the In-plane Penetration Depth of the Organic Superconductors Îž-(BEDT-TTF)2x (X = Cu(NCS)2 and Cu[N(CN)2]Br). *Journal of the Physical Society of Japan*, 73(5):1290–1296, May 2004.

[92] A. Carrington, I. J. Bonalde, R. Prozorov, R. W. Giannetta, A. M. Kini, J. Schlueter, H. H. Wang, U. Geiser, and J. M. Williams. Low-Temperature Penetration Depth of $\mathit{\ensuremath{\kappa}}\ensuremath{-}(\mathrm{ET}{)}_{2}\mathrm{Cu}[N(\mathrm{CN}{)}_{2}]\mathrm{Br}$ and $\mathit{\ensuremath{\kappa}}\ensuremath{-}(\mathrm{ET}{)}_{2}\mathrm{Cu}(\mathrm{NCS}{)}_{2}$. *Physical Review Letters*, 83(20):4172–4175, Nov. 1999.

[93] B. J. Powell, E. P. Kenny, and J. Merino. Dynamical reduction of the dimensionality of exchange interactions and the "spin-liquid" phase of κ-(BEDT$-$TTF)$_2X$. *Physical Review Letters*, 119(8):087204, Aug. 2017.

[94] M. Dion, D. Fournier, M. Poirier, K. D. Truong, and A.-M. S. Tremblay. Mixed pairing symmetry in $\kappa-$(BEDT-TTF)$_2$X organic superconductors from ultrasonic velocity measurements. *Physical Review B*, 80(22):220511, Dec. 2009.

[95] G. D. Mahan. *Many-Particle Physics*. Springer US, New York, 2000.

[96] A. B. Migdal. Interaction between electrons and lattice vibrations in a normal metal. *Journal of Experimental and Theoretical Physics*, 7:996, 1958.

[97] S. B. Kaplan, C. C. Chi, D. N. Langenberg, J. J. Chang, S. Jafarey, and D. J. Scalapino. Quasiparticle and phonon lifetimes in superconductors. *Physical Review B*, 14(11):4854–4873, May 1976.

[98] R. J. Abraham, J. Fisher, and P. Loftus. *Introduction to NMR Spectroscopy*. Wiley, Michigan, 1988.

[99] C. P. Slichter. *Principles of Magnetic Resonance*. Springer-Verlag, Heidelberg, 1978.

[100] G. F. Giuliani and G. Vignale. *Quantum Theory of the Electron Liquid*. Cambridge University Press, New York, 2005.

[101] A. A. Abrikosov and L. P. Gor'kov. Spin-orbit interaction and the Knight shift in superconductors. *Journal of Experimental and Theoretical Physics*, 1962.

[102] D. Duffy, P. J. Hirschfeld, and D. J. Scalapino. Quasiparticle lifetimes in a $d_{x^2-y^2}$ superconductor. *Physical Review B*, 64(22):224522, Nov. 2001.

[103] S. M. Quinlan, D. J. Scalapino, and N. Bulut. Superconducting quasiparticle lifetimes due to spin-fluctuation scattering. *Physical Review B*, 49(2):1470–1473, Jan. 1994.

[104] N. Bulut and D. J. Scalapino. Analysis of NMR data in the superconducting state of $YBa_2Cu_3O_7$. *Physical Review Letters*, 68(5):706–709, Feb. 1992.

[105] L. C. Hebel and C. P. Slichter. Nuclear spin relaxation in normal and superconducting aluminum. *Physical Review*, 113(6):1504–1519, Mar. 1959.

[106] L. C. Hebel and C. P. Slichter. Nuclear relaxation in superconducting aluminum. *Physical Review*, 107(3):901–902, Aug. 1957.

[107] E. Yusuf, B. J. Powell, and R. H. McKenzie. Vertex corrections and the Korringa ratio in strongly correlated electron materials. *Journal of Physics: Condensed Matter*, 21(19):195601, 2009.

[108] G. B. Arfken and H. J. Weber. *Mathematical Methods for Physicists (6e)*. Academic Press, Oxford, 6 edition, 2005.

[109] K. V. Samokhin and B. Mitrović. NMR relaxation time in a clean two-band superconductor. *Physical Review B*, 72(13):134511, Oct. 2005.

[110] J. G. Analytis, A. Ardavan, S. J. Blundell, R. L. Owen, E. F. Garman, C. Jeynes, and B. J. Powell. Effect of irradiation-induced disorder on the conductivity and critical temperature of the organic superconductor $\kappa-(BEDT-TTF)_2Cu(SCN)_2$. *Physical Review Letters*, 96(17):177002, May 2006.

[111] S. Doniach and E. H. Sondheimer. *Green's Functions for Solid State Physicists*. Imperial College Press, London, 1998.

[112] A. C. Jacko, J. O. FjÃęrestad, and B. J. Powell. A unified explanation of the Kadowaki-Woods ratio in strongly correlated metals. *Nature Physics*, 5(6):422, June 2009.

[113] U. Rössler. *Solid State Theory: An Introduction*. Springer-Verlag, Heidelberg, 2009.

[114] G. Baym and L. P. Kadanoff. Conservation laws and correlation functions. *Physical Review*, 124(2):287–299, Oct. 1961.

[115] G. Baym. Self-consistent approximations in many-body systems. *Physical Review*, 127(4):1391–1401, Aug. 1962.

[116] M. Revzen, T. Toyoda, Y. Takahashi, and F. C. Khanna. Baym-Kadanoff criteria and the Ward-Takahashi relations in many-body theory. *Physical Review B*, 40(1):769–771, July 1989.

[117] H. Kontani. Anomalous transport phenomena in Fermi liquids with strong magnetic fluctuations. *Reports on Progress in Physics*, 71(2):026501, 2008.

[118] H. Monien and D. Pines. Spin excitations and pairing gaps in the superconducting state of $YBa_2Cu_3O_{7-\delta}$. *Physical Review B*, 41(10):6297–6305, Apr. 1990.

[119] R. Akis, C. Jiang, and J. P. Carbotte. Quasiparticle damping, anisotropy and Fermi liquid corrections to NMR in superconductors. *Physica C: Superconductivity*, 176(4):485–495, June 1991.

[120] B. W. Statt. Anisotropic gap and quasiparticle-damping effects on NMR measurements of high-temperature superconductors. *Physical Review B*, 42(10):6805–6808, Oct. 1990.

[121] R. Akis and J. P. Carbotte. Damping effects on NMR in superconductors. *Solid State Communications*, 78(5):393–396, May 1991.

[122] R. Akis and J. P. Carbotte. Strong coupling effects on the low frequency conductivity of superconductors. *Solid State Communications*, 79(7):577–581, Aug. 1991.

[123] L. Hedin. New method for calculating the one-particle Green's function with application to the electron-gas problem. *Physical Review*, 139(3A):A796–A823, Aug. 1965.

[124] N. E. Bickers and D. J. Scalapino. Conserving approximations for strongly fluctuating electron systems. I. formalism and calculational approach. *Annals of Physics*, 193(1):206–251, July 1989.

[125] J. Caulfield, W. Lubczynski, F. L. Pratt, J. Singleton, D. Y. K. Ko, W. Hayes, M. Kurmoo, and P. Day. Magnetotransport studies of the organic superconductor kappa-(BEDT-TTF)$_2$Cu(NCS)$_2$ under pressure: the relationship between carrier effective mass and critical temperature. *Journal of Physics: Condensed Matter*, 6(15):2911, 1994.

[126] H. Kino and H. Fukuyama. Electronic States of Conducting Organic Îž-(BEDT-TTF)2x. *Journal of the Physical Society of Japan*, 64(8):2726–2729, Aug. 1995.

[127] H. Kino and H. Kontani. Phase Diagram of Superconductivity on the Anisotropic Triangular Lattice Hubbard Model: An Effective Model of Îž-(BEDT-TTF) Salts. *Journal of the Physical Society of Japan*, 67(11):3691–3694, Nov. 1998.

[128] J. Merino and R. H. McKenzie. Cyclotron effective masses in layered metals. *Physical Review B*, 62(4):2416–2423, July 2000.

[129] H. Kondo and T. Moriya. Spin Fluctuation-Induced Superconductivity in Organic Compounds. *Journal of the Physical Society of Japan*, 67(11):3695–3698, Nov. 1998.

[130] T. Koretsune and C. Hotta. Evaluating model parameters of the κ- and β'-type Mott insulating organic solids. *Physical Review B*, 89(4):045102, Jan. 2014.

[131] H. Aizawa, T. Koretsune, K. Kuroki, and H. Seo. Electronic structure calculation and superconductivity in λ-(BETS)$_2$GaCl$_4$. *Journal of the Physical Society of Japan*, 87:093701, 2018.

[132] H. Urayama, H. Yamochi, G. Saito, K. Nozawa, T. Sugano, M. Kinoshita, S. Sato, K. Oshima, A. Kawamoto, and J. Tanaka. A new ambient pressure organic superconductor based on bedt-ttf with tc higher than 10 k (tc=10.4 k). *Chemistry Letters*, 17(1):55–58, Jan. 1988.

[133] D. Chasseau, J. Gaultier, M. Rahal, L. Ducasse, M. Kurmoo, and P. Day. Pressure dependence of the structural and electronic properties of the molecular superconductor, (bedt-ttf)2cu(ncs)2. *Synthetic Metals*, 42(1):2039–2042, May 1991.

[134] A. C. Jacko. Deriving *ab initio* model Hamiltonians for molecular crystals. *arXiv:1508.07735 [cond-mat]*, Aug. 2015.

[135] R. H. McKenzie. A strongly correlated electron model for the layered organic superconductors kappa-(bedt-ttf)2x. *Comments on Condensed Matter Physics*, 18:309, 1998.

[136] N. W. Ashcroft and N. D. Mermin. *Solid State Physics*. Holt-Saunders, Philadelphia, 1976.

[137] W. A. Huttema, B. Morgan, P. J. Turner, W. N. Hardy, X. Zhou, D. A. Bonn, R. Liang, and D. M. Broun. Apparatus for high-resolution microwave spectroscopy in strong magnetic fields. *Review of Scientific Instruments*, 77(2):023901, June 2006.

[138] O. Klein, S. Donovan, M. Dressel, and G. GrÃijner. Microwave cavity perturbation technique: Part i: Principles. *International Journal of Infrared and Millimeter Waves*, 14(12):2423–2457, June 1993.

[139] M. Li, N. R. Lee-Hone, S. Chi, R. Liang, W. N. Hardy, D. A. Bonn, E. Girt, and D. M. Broun. Superfluid density and microwave conductivity of FeSe superconductor: ultra-long-lived quasiparticles and extended s -wave energy gap. *New Journal of Physics*, 18(8):082001, 2016.

[140] D. A. Bonn and W. N. Hardy. *Microwave electrodynamics of high temperature Superconductors*, pages 145–214. Springer, 2007.

[141] S. Donovan, O. Klein, M. Dressel, K. Holczer, and G. Grüner. Microwave cavity perturbation technique: Part ii: Experimental scheme. *International Journal of Infrared and Millimeter Waves*, 14(12):2459–2487, June 1993.

[142] M. Dressel, O. Klein, S. Donovan, and G. Grüner. Microwave cavity perturbation technique: Part iii: Applications. *International Journal of Infrared and Millimeter Waves*, 14(12):2489–2517, June 1993.

[143] H. K. Pal, V. I. Yudson, and D. L. Maslov. Resistivity of non-Galilean-invariant Fermi- and non-Fermi liquids. *Lithuanian Journal of Physics*, 52(2), Aug. 2012.

[144] A. Rosch and P. C. Howell. Zero-temperature optical conductivity of ultraclean Fermi liquids and superconductors. *Physical Review B*, 72(10):104510, May 2005.

[145] A. Rosch. Optical conductivity of clean metals. *Annalen der Physik*, 15(7-8):526–534, May 2006.

[146] W. G. Baber. The contribution to the electrical resistance of metals from collisions between electrons. *Proc. R. Soc. Lond. A*, 158(894):383–396, May 1937.

[147] T. Giamarchi and B. S. Shastry. Baber scattering and resistivity of a two-dimensional two-band model. *Physical Review B*, 46(9):5528–5535, May 1992.

[148] K. Yamada, M. Nakano, K. Yoshida, K. Hanzawa, and A. Sakurai. T -square term of electrical resistivity. *Progress of Theoretical Physics*, 82(4):689–701, Oct. 1989.

[149] H. Maebashi and H. Fukuyama. Electrical conductivity of interacting fermions. i. general formulation. *Journal of the Physical Society of Japan*, 66(11):3577–3590, Nov. 1997.

[150] H. Maebashi and H. Fukuyama. Electrical conductivity of interacting fermions. ii. effects of normal scattering processes in the presence of umklapp scattering processes. *Journal of the Physical Society of Japan*, 67(1):242–251, Jan. 1998.

[151] M. B. Walker and M. F. Smith. Quasiparticle-quasiparticle scattering in high-T_c superconductors. *Physical Review B*, 61(17):11285–11288, May 2000.

Appendix A

Calculation details

Here, I reproduce the interaction parameters for the models discussed in Chapter 3. All calculations were performed on a discretised $\boldsymbol{k}$-space grid of 120 sites per dimension (for a total of $N = 120^4$ momentum configurations), with a (Lorentzian) broadening of $\eta = 10^{-3}t$. The critical interaction parameters found for each of the models are given in Table A.1, while Table A.2 provides a reference for the labelling of gap functions with accidental and symmetry required nodes.

Model	Parameters	$U_c = 1/\max\left[\chi_0'(\boldsymbol{q},\omega)\right]$
Orthorhombic	$\left(t_y/t_x,\ \langle n\rangle\right) = (1, 1)$	$U_c \approx 6.2t$
	$\left(t_y/t_x,\ \langle n\rangle\right) = (1, 0.85)$	$U_c \approx 9.2t$
	$\left(t_y/t_x,\ \langle n\rangle\right) = (1, 0.5)$	$U_c \approx 18.9t$
	$\left(t_y/t_x,\ \langle n\rangle\right) = (0.9, 0.5)$	$U_c \approx 17.7t$
	$\left(t_y/t_x,\ \langle n\rangle\right) = (0.8, 0.5)$	$U_c \approx 16.5t$
	$\left(t_y/t_x,\ \langle n\rangle\right) = (0.6, 0.5)$	$U_c \approx 14.0t$
	$\left(t_y/t_x,\ \langle n\rangle\right) = (0.4, 0.5)$	$U_c \approx 11.7t$
	$\left(t_y/t_x,\ \langle n\rangle\right) = (0.1, 0.5)$	$U_c \approx 10.4t$
β-(BEDT-TTF)$_2X$	$(t'/t,\ \langle n\rangle) = (1, 1)$	$U_c \approx 8.7t$
	$(t'/t,\ \langle n\rangle) = (0.7, 1)$	$U_c \approx 7.3t$
	$(t'/t,\ \langle n\rangle) = (0.5, 1)$	$U_c \approx 6.0t$
	$(t'/t,\ \langle n\rangle) = (0.2, 1)$	$U_c \approx 4.5t$
κ-(BEDT-TTF)$_2X$	$(t'/t, \delta_t/t,\ \langle n\rangle) = (0.5, 0.01, 1)$	$U_c \approx 12.4t$
	$(t'/t, \delta_t/t,\ \langle n\rangle) = (0.5, 0.05, 1)$	$U_c \approx 12.4t$
	$(t'/t, \delta_t/t,\ \langle n\rangle) = (0.5, 0.1, 1)$	$U_c \approx 12.4t$
	$(t'/t, \delta_t/t,\ \langle n\rangle) = (0.7, 0.05, 1)$	$U_c \approx 13.2t$
κ-Br, Koretsune [130]	$\left(t'/t, \delta_t/t, t_2'/t,\ \langle n\rangle\right) = (0.54,\ -0.14, 0.04, 1)$	$U_c \approx 13.2t$

Table A.1: Bandstructure parameters and critical interaction strengths (in the RPA) for the models considered in this thesis.

Model	Symmetry Required Nodes	Accidental Nodes
Orthorhombic	d_{xy}	s, $d_{x^2-y^2}$
β-(BEDT-TTF)$_2X$	$d_{x^2-y^2}$	s, d_{xy}
κ-(BEDT-TTF)$_2X$	$d_{x^2-y^2}$, 'Schmalian'	s, d_{xy}, 'Guterding'
κ-Br, Koretsune [130]	$d_{x^2-y^2}$, 'Schmalian'	s, d_{xy}, 'Guterding'

Table A.2: Identification of gaps with accidental and symmetry required nodes in the models considered in this thesis.

Appendix B

Vertex Corrections and NMR in Low-Symmetry Superconductors: Further random phase approximation calculations

In this appendix, I present some ancillary calculations for the nuclear magnetic relaxation rate in the random phase approximation.

B.0.1 Fully gapped superconductors

Fig. B.1 displays the influence of anisotropy and the proximity of Van Hove singularities on the relaxation rate, by varying the parameters of an orthorhombic tight binding model (as described in Chapter 2), for an isotropic s-wave gap. These effects influence the specific values of the relaxation rate, but not the broader trends. Figs. B.2 and B.3 show the detailed behaviour of the relaxation rate for various interaction strengths in simple dimer models of β-(BEDT-TTF)$_2X$ and κ-(BEDT-TTF)$_2X$, respectively, for an isotropic superconducting gap.

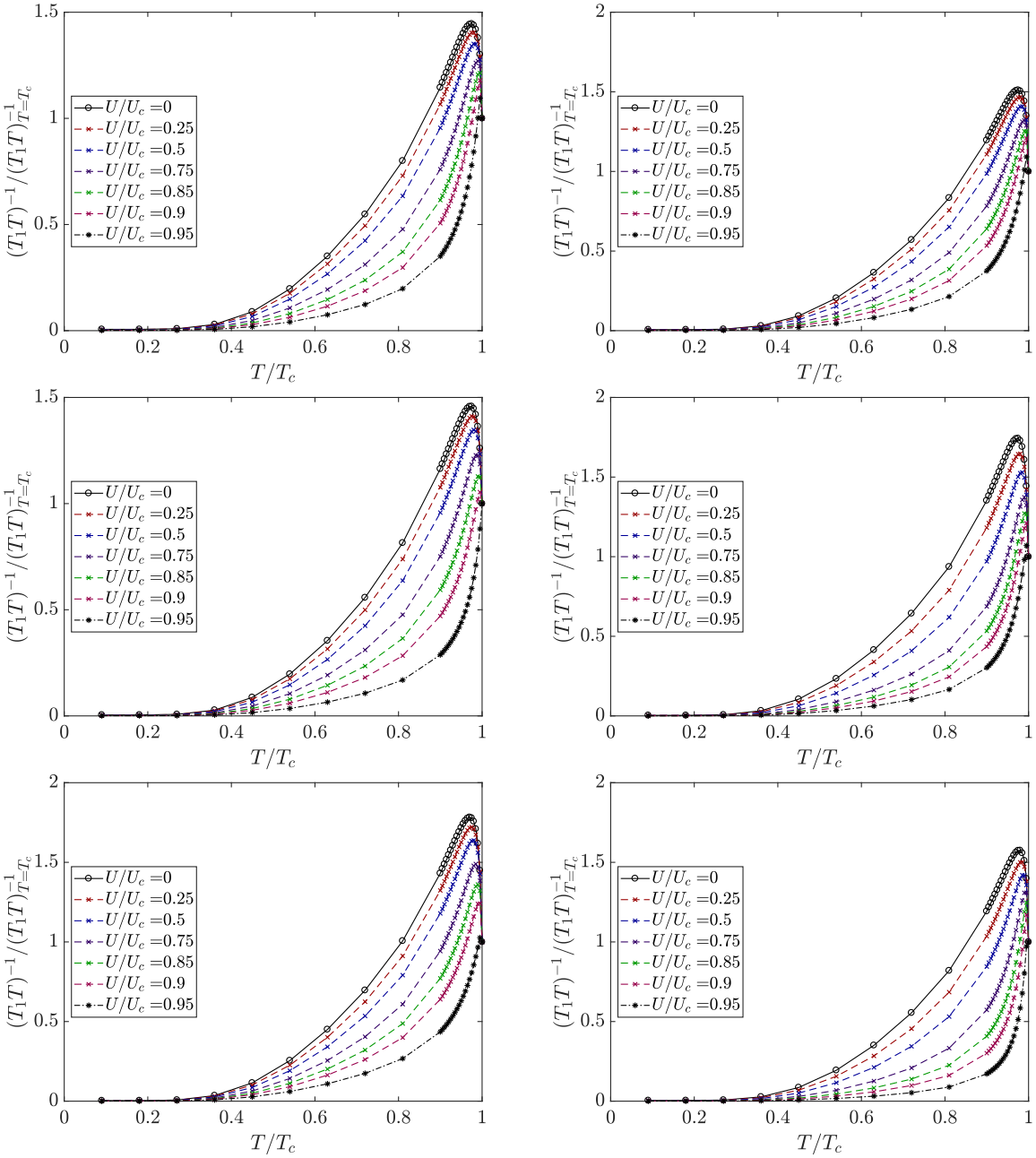

Figure B.1: The influence of anisotropy and Van Hove singularities on the $1/T_1$ relaxation rate in a fully gapped superconductor, in the presence of vertex corrections. The left column above shows the relaxation rate calculated for a square lattice at various fillings. Top: $\langle n \rangle = 0.5$. Middle: $\langle n \rangle = 0.85$. Bottom: $\langle n \rangle = 1$, at which point the Van Hove singularity is at the Fermi energy. The right column shows the relaxation rate for the orthorhombic model with $\langle n \rangle = 0.5$ at various levels of anisotropy. Top: $t_y = 0.8t_x$. Middle: $t_y = 0.4t_x$. Bottom: $t_y = 0.1t_x$.

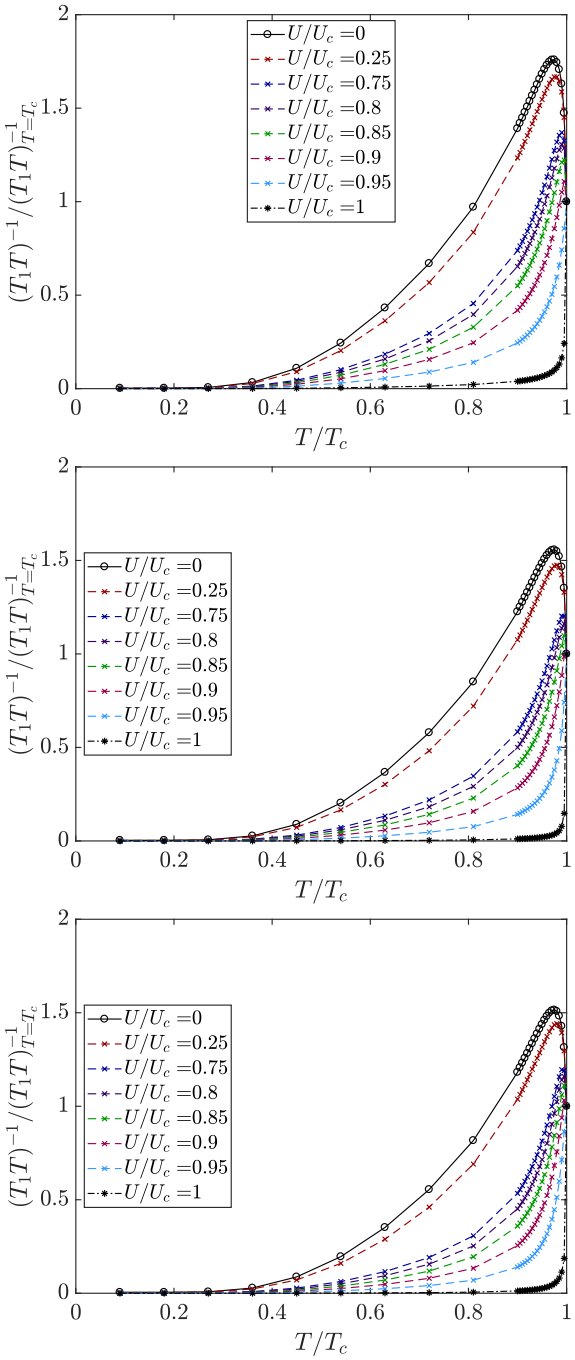

Figure B.2: $1/T_1T$, with increasing interaction strength in a dimerised model of s-wave superconductivity in β-(BEDT-TTF)$_2X$ for various model parameters. Top: $t' = 0.2t$. Middle: $t' = 0.5t$. Bottom: $t' = t$, the isotropic triangular lattice.

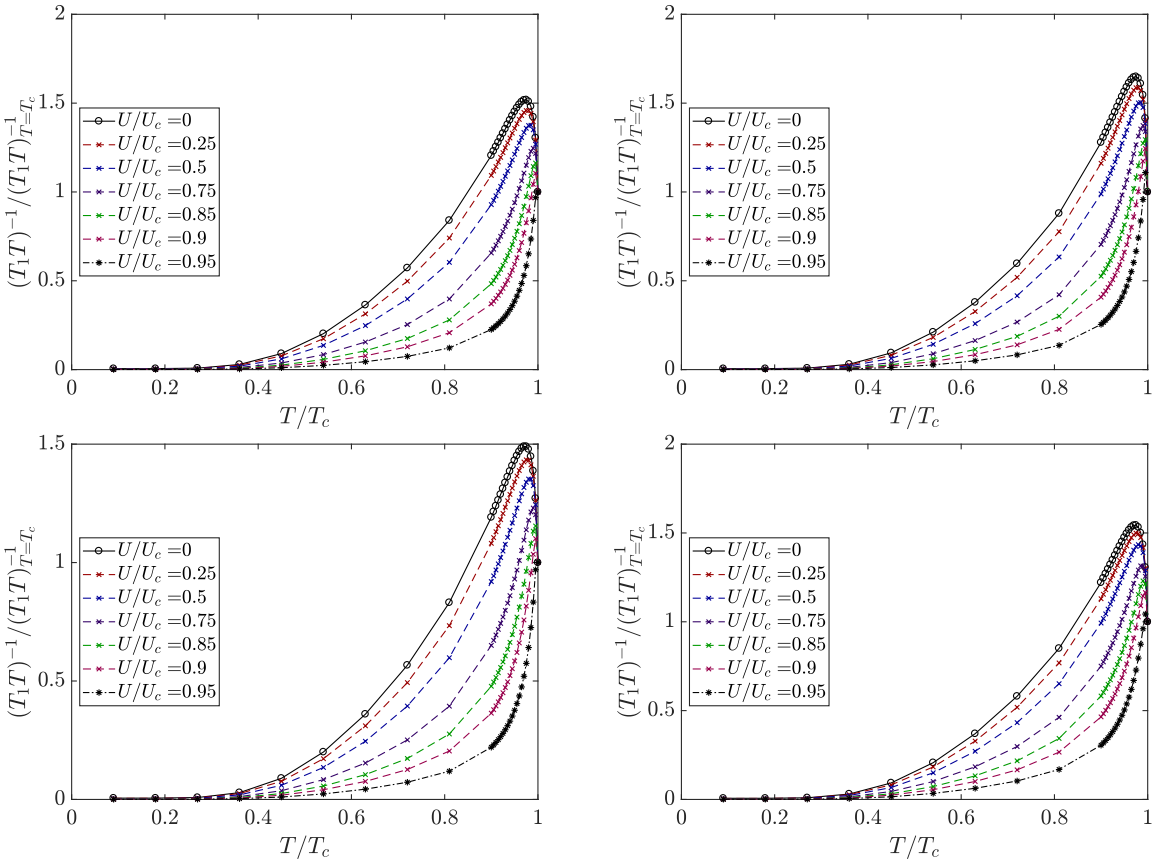

Figure B.3: $1/T_1T$, with increasing interaction strength in a dimerised model of s-wave superconductivity in κ-(BEDT-TTF)$_2X$. Top left: $t' = 0.5t$, $\delta_t = 0.01t$. Top right: κ-(BEDT-TTF)$_2X$ $t' = 0.5t$, $\delta_t = 0.1t$. Bottom left: κ-(BEDT-TTF)$_2X$ $t' = 0.5t$, $\delta_t = 0.05t$. Bottom Right: κ-(BEDT-TTF)$_2X$ $t' = 0.7t$, $\delta_t = 0.05t$.

B.0.2 Anisotropic gaps with accidental nodes

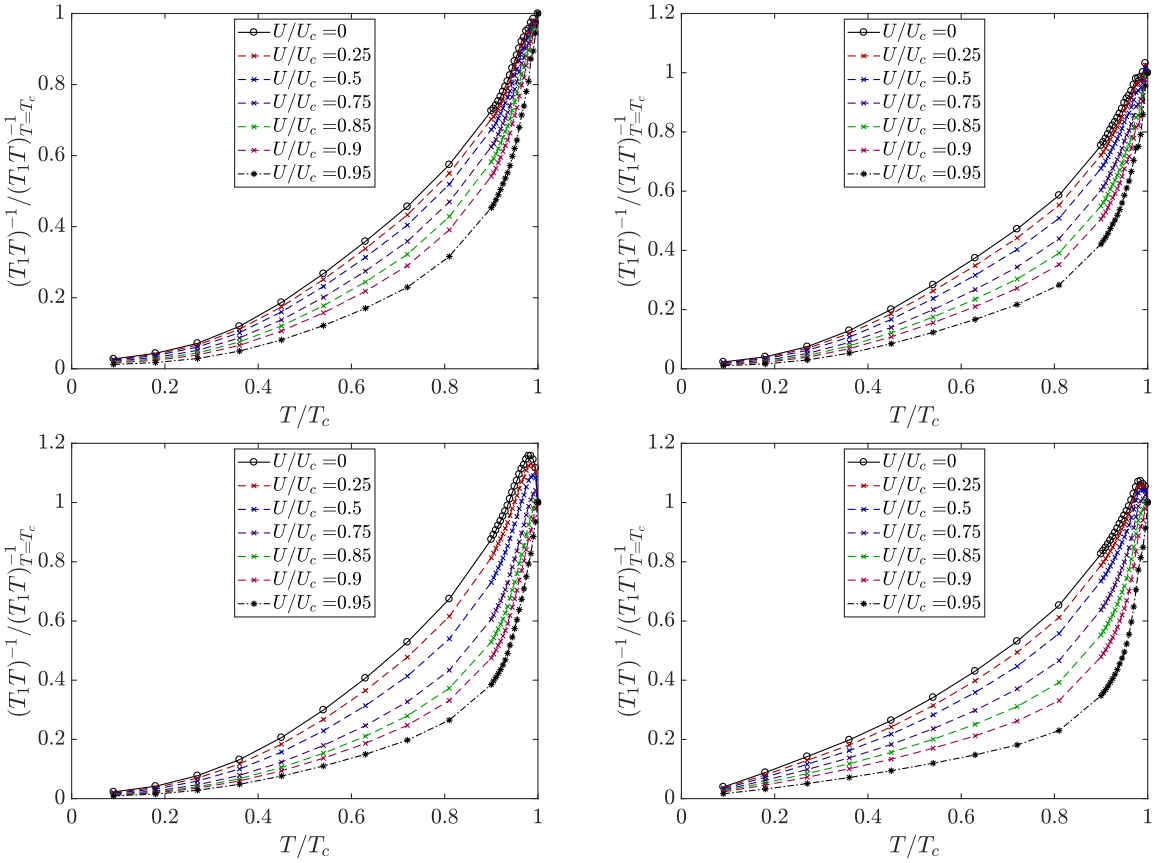

Figure B.4: $1/T_1T$ in an orthorhombic superconductor with accidental nodes, for various levels of anisotropy. Top left: $t_y = 0.8t_x$. Top right: $t_y = 0.6t_x$. Bottom left: $t_y = 0.4t_x$. Bottom right: $t_y = 0.1t_x$.

Fig. B.4 displays the influence of anisotropy on the relaxation rate, by varying the parameters of an orthorhombic tight binding model (as described in Chapter 2), for a gap with accidental nodes. These effects influence the specific values of the relaxation rate, but not the broader trends. Figs. B.5 and B.6 show the detailed behaviour of the relaxation rate for various interaction strengths in models of β-(BEDT-TTF)$_2X$ and κ-(BEDT-TTF)$_2X$, respectively, for a gap with accidental nodes and zero isotropic component. Figs. B.7 and B.8 show the relaxation rate in the model for κ-(BEDT-TTF)$_2X$ with a gap with accidental nodea and nonzero isotropic gap component, at various interaction strengths, for two values of the bandstructure parameters.

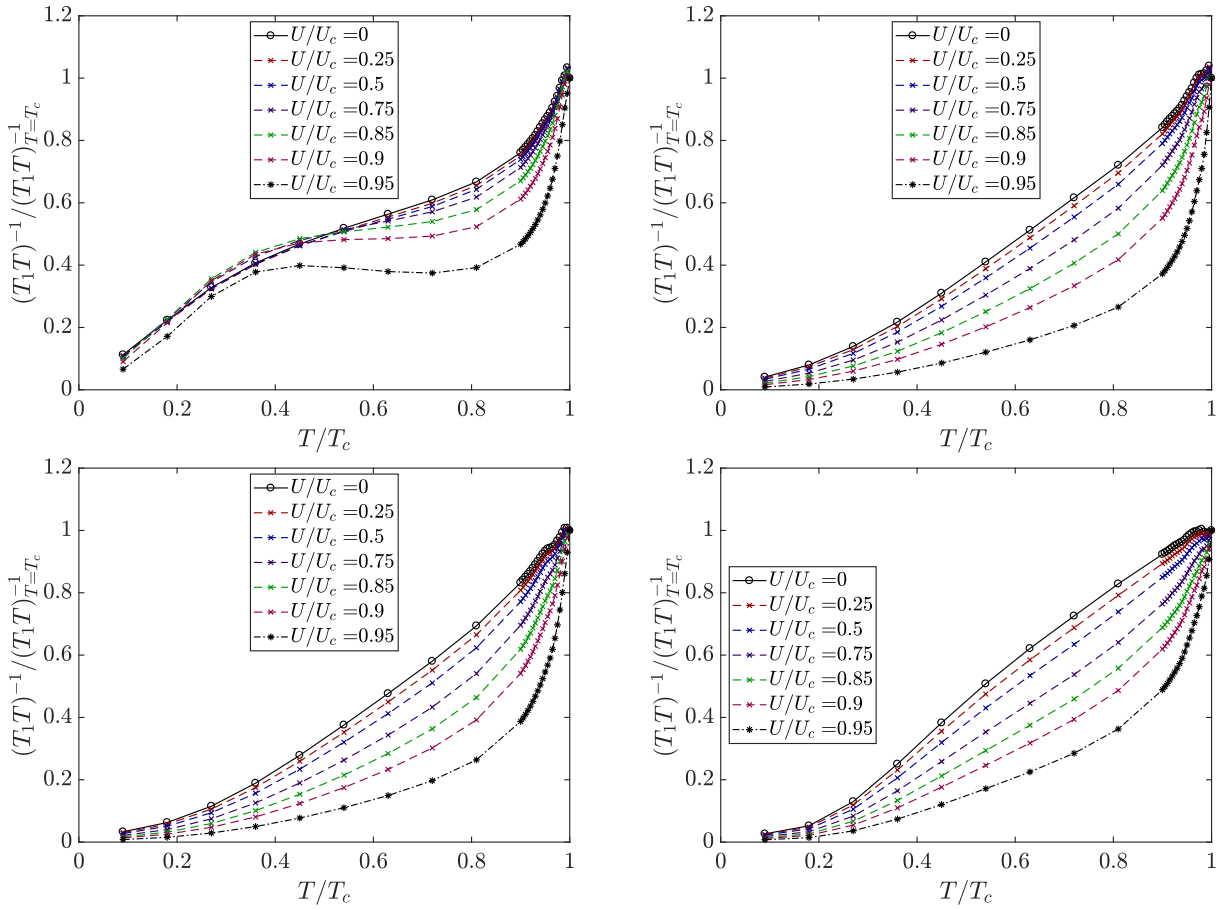

Figure B.5: $1/T_1T$ in a dimerised model of superconductivity with accidental nodes in β-(BEDT-TTF)$_2X$ for various model parameters. Top left: $t' = 0.2t$. Top right: $t' = 0.5t$. Bottom left: $t' = 0.7t$. Bottom right: $t' = t$.

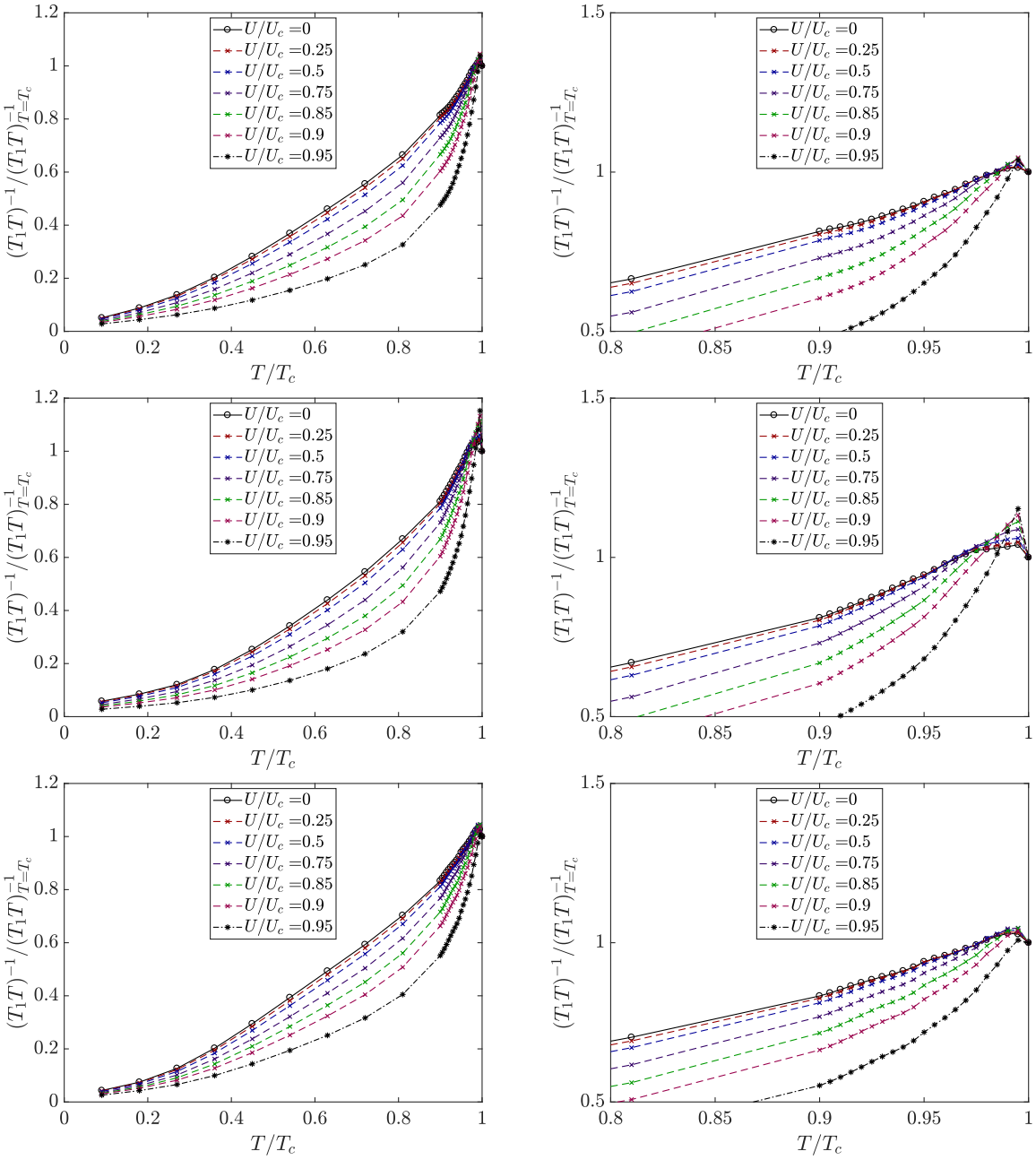

Figure B.6: $1/T_1T$, with increasing interaction strength in a dimerised model of superconductivity with accidental nodes in the two band κ-(BEDT-TTF)$_2X$ for various model parameters. Top: $t' = 0.5t$, $\delta_t = 0.05t$. Middle: $t' = 0.5t$, $\delta_t = 0.1t$. Bottom: $t' = 0.7t$, $\delta_t = 0.05t$.

B.0.3 All gaps, κ-(BEDT-TTF)$_2X$

Fig. B.9 displays the nuclear magnetic relaxation rate for a simple model of κ-(BEDT-TTF)$_2X$ with various interaction strengths, with the relaxation rates due to all discussed gap functions plotted on the same axes, to better compare how interactions influence the various relaxation rates.

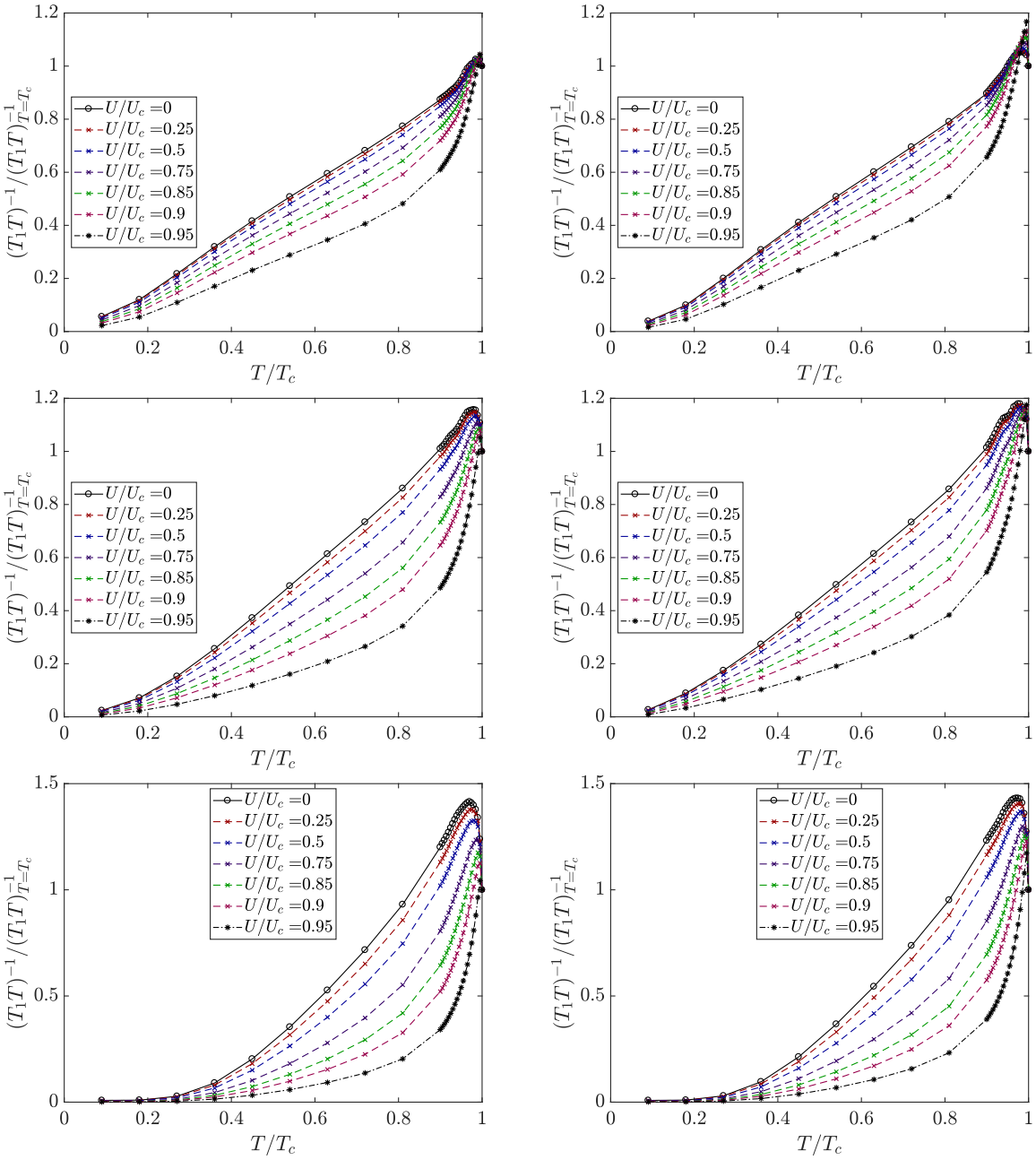

Figure B.7: Evolution of the relaxation rate, $1/T_1T$, with increasing interaction strength in a dimerised model of superconductivity with accidental nodes and non-zero s-wave gap component in the two band κ-(BEDT-TTF)$_2X$ for various model parameters. Left column: $t' = 0.5t$, $\delta_t = 0.05t$. Right column: $t' = 0.5t$, $\delta_t = 0.1t$. Top: $\alpha = 0.25$. Middle: $\alpha = 0.5$. Bottom: $\alpha = 0.75$.

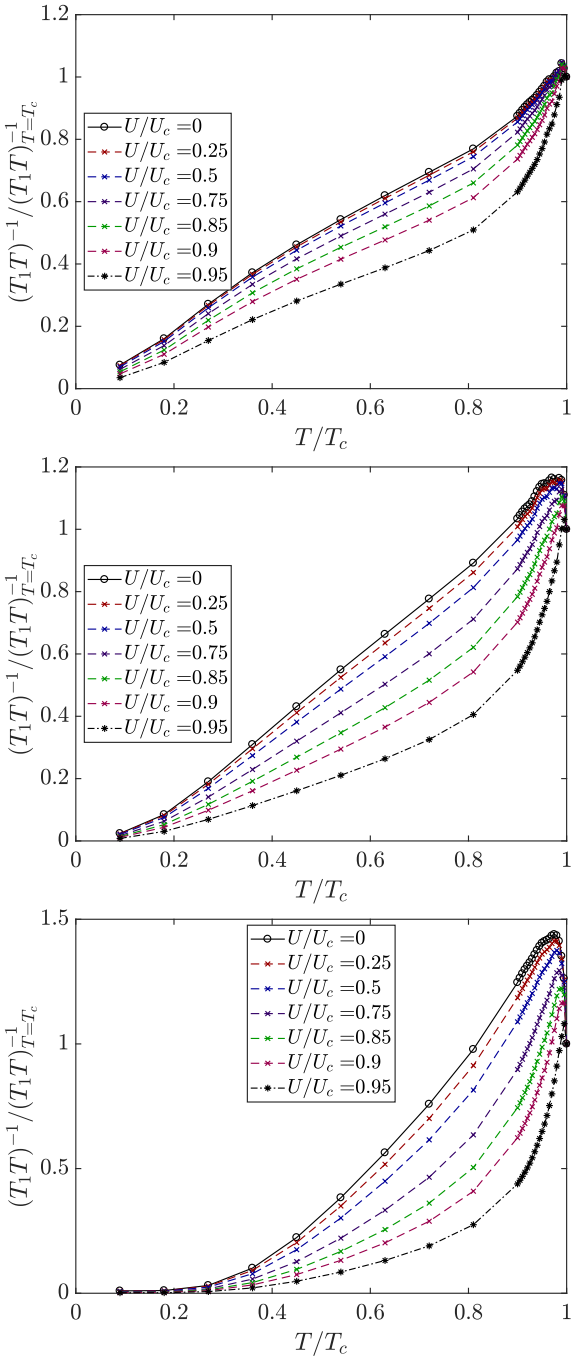

Figure B.8: Evolution of the relaxation rate, $1/T_1T$, with increasing interaction strength in a dimerised model of superconductivity with accidental nodes and non-zero s-wave component in κ-(BEDT-TTF)$_2X$ with $t' = 0.7t$, $\delta_t = 0.05t$. Top: $\alpha = 0.25$. Middle: $\alpha = 0.5$. Bottom: $\alpha = 0.75$.

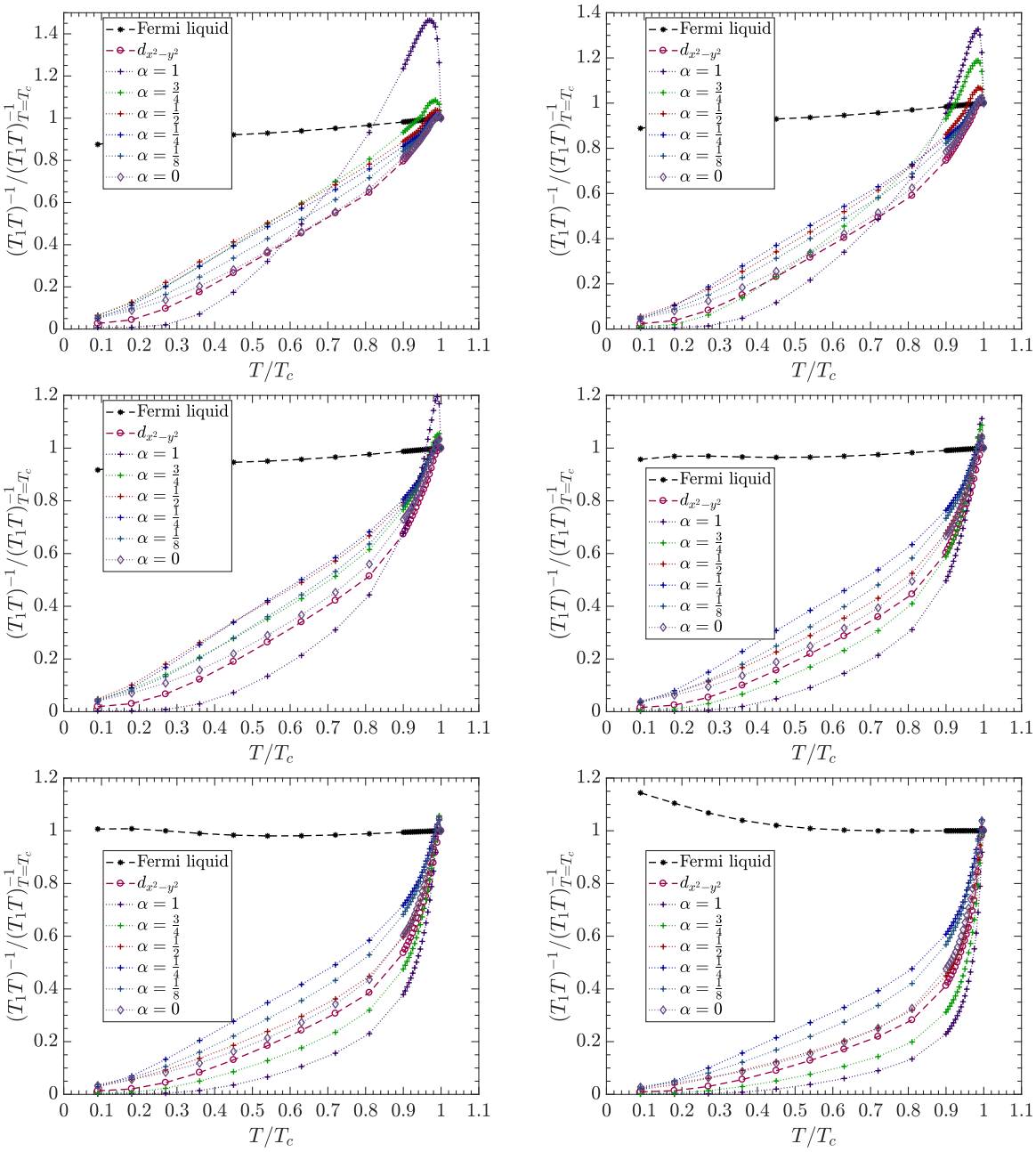

Figure B.9: $1/T_1T$ in a dimerised model of superconductivity in the two band κ-(BEDT-TTF)$_2X$ for various gap symmetries, with $t' = 0.5t$, $\delta_t = 0.05t$. Top left: $U = 0$. Top right: $U = 0.5U_c$. Middle left: $U = 0.75U_c$. Middle right: $U = 0.85U_c$. Bottom left: $U = 90$. Bottom right: $U = 0.95U_c$.

B.0.4 More complicated symmetry

In Fig. B.10, I display the nuclear magnetic relaxation rate calculated in the random phase approximation for a simple model of κ-(BEDT-TTF)$_2X$, with the complicated gap function of Guterding *et al.* [62], for gap parameters fit to scanning tunnelling spectroscopy experiments at both low temperatures and close to $T = T_c$.

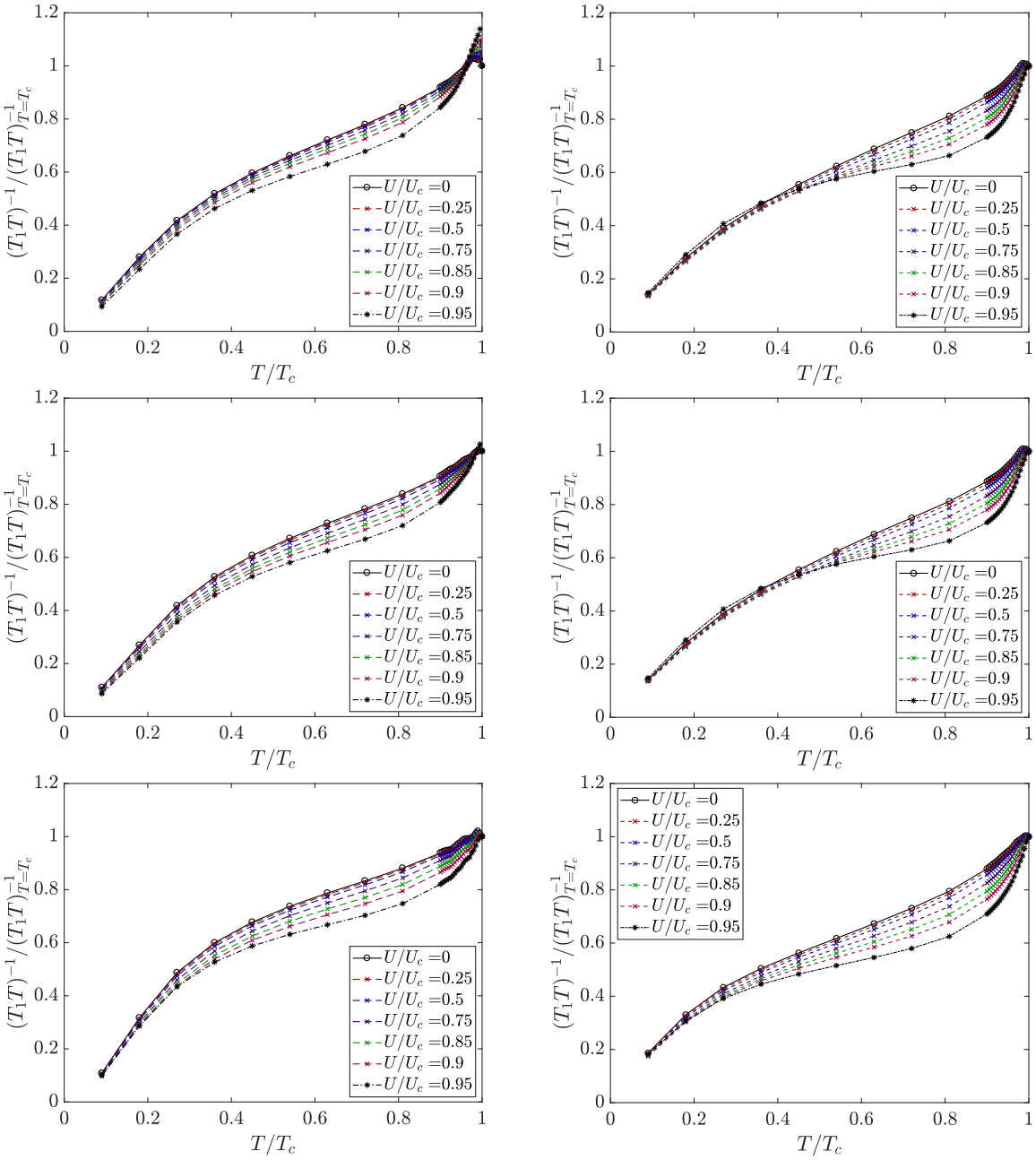

Figure B.10: $1/T_1T$ in a dimerised model of superconductivity in the two band κ-(BEDT-TTF)$_2X$ for various model parameters, and the mixed symmetry gap proposed in [62]. Top: $t' = 0.5t$, $\delta_t = 0.1t$. Middle: $t' = 0.5t$, $\delta_t = 0.05t$. Bottom: $t' = 0.7t$, $\delta_t = 0.05t$. The plots on the left use parameters calculated at low temperatures, while those on the right use parameters calculated just below T_c.

Appendix C

Comparison with experimental data: Extended accidental nodes and temperature dependent gap parameters

I present here nuclear magnetic relaxation rates, calculated in the random phase approximation, including the variation of the gap parameters with temperature, as extracted by Guterding *et al* from scanning tunnelling spectroscopy experiments [62]. Fig. C.1 displays fits to the experimental data (as described in Chapter 4) using the four sets of parameters listed in Ref. [**?**], while Fig. C.2 displays calculations including a linear interpolation of the parameters between the stated temperatures.

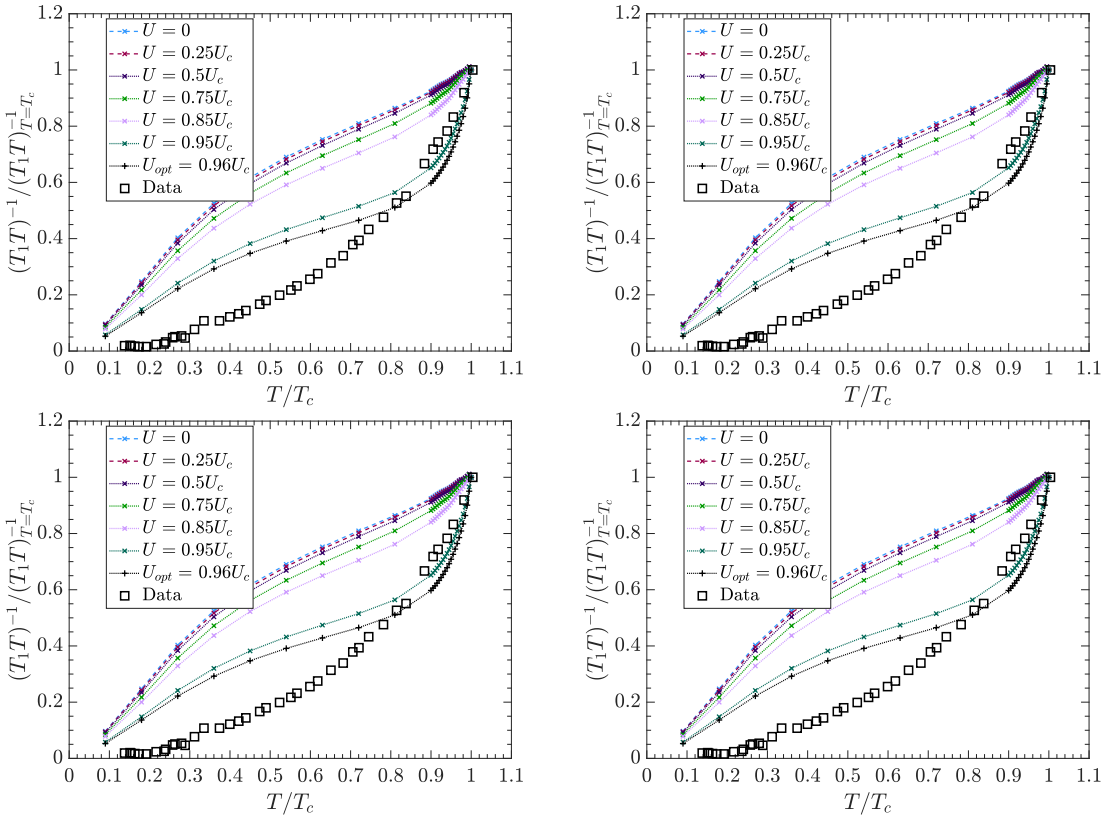

Figure C.1: $1/T_1T$ for the dimer model proposed by Koretsune ane Hotta [130], with $\delta_t = 0$ and a superconducting gap proposed by Guterding *et al.* [63], compared to experimental data from Ref. [85]. Top left: gap parameters calculated at $T = 5K$. Top right: gap parameters calculated at $T = 7K$. Bottom left: gap parameters calculated at $T = 9K$. Bottom right: gap parameters calculated at $T = 11K$. As in the model considered in the main text, none of the parameter sets accurately reproduce the observed relaxation rate. In these calculations, $U_c \sim 6.2t$

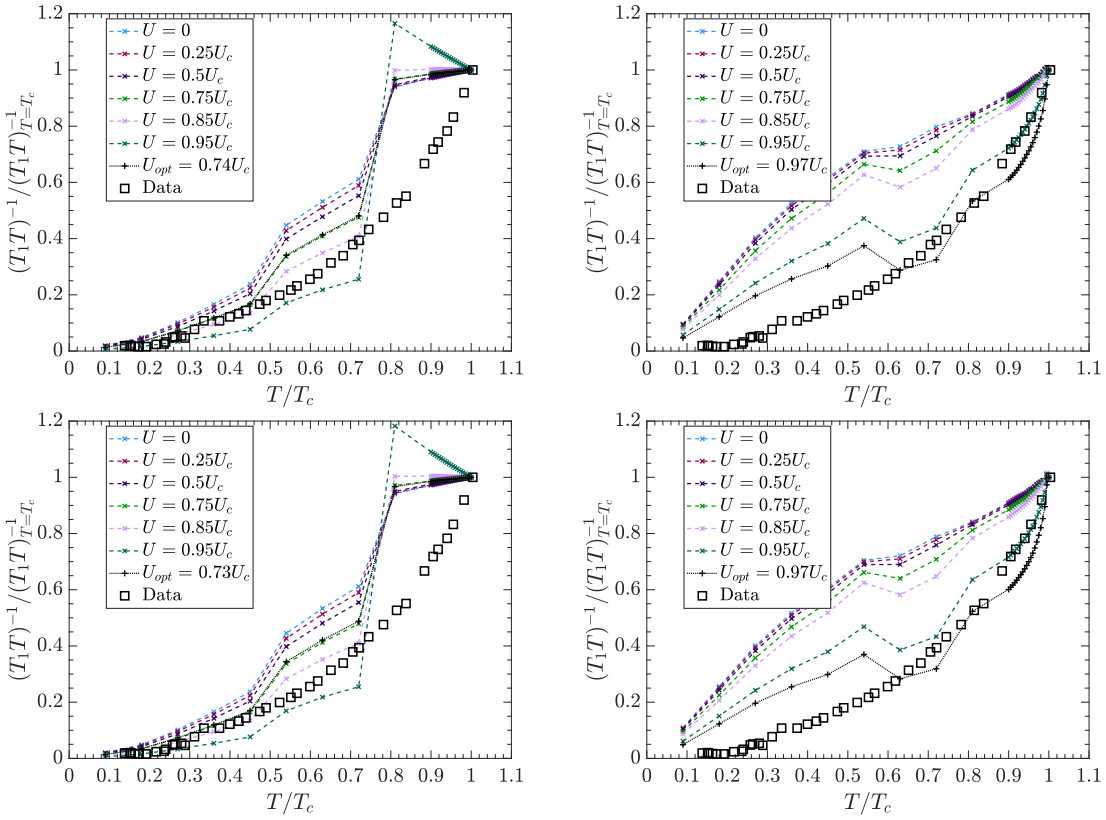

Figure C.2: $1/T_1T$ for the dimer model proposed by Koretsune ane Hotta [130], with a superconducting gap proposed by Guterding *et al.* [63], compared to experimental data from Ref. [85]. The gap parameters in these figures are allowed to vary with temperature, as in Ref. [63], and the figures in the right hand column also use the gap magnitude found by Guterding *et al.* from the tunnelling data, which is a factor of two larger than that determined from other experiments [82]. Top: $\delta_t = 0$. Bottom: $\delta_t = 0.03t$. In these calculations, $U_c \sim 6.2t$